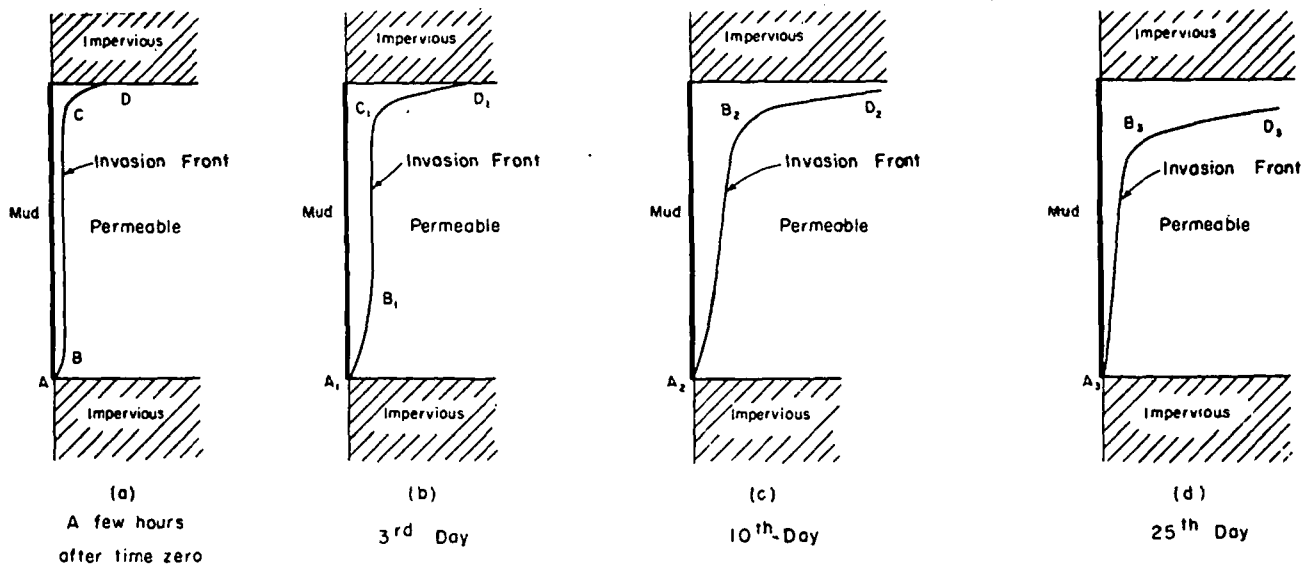

FIG. 1. Filtrate density less than connate water density. Time zero: Beginning of invasion. (Times shown are merely illustrative.)

A STUDY

Filtrate Invasion in Highly Permeable Sands

Depth of invasion often appears less in base than in upper portion of highly permeable sands. Conclusion is that filtrates rise in sand after passing filter cake barrier at hole wall.

H. G. DOLL

IT has often been observed in salt-water bearing sands of high permeability that the depth of invasion by mud filtrate is quite small near the bottom boundaries of the beds, whereas the top parts of the beds are deeply penetrated. This feature was brought to light by the resistivity logs, in which the shallow investigation curve (short normal) gives the same very low readings as the deep investigation curves (long normal and/or lateral) over the lower part of the beds, and an appreciably higher reading over the upper part.

Further evidence isprovided by the micrologs, which show respectively negative and positive separations opposite the lower and the upper portions of the beds. Examples of this behavior are exhibited in Figs. 12 and 13.

This observation has suggested the idea that, in this kind of formation, after the mud filtrate has been forced through the mud cake, it does not flow horizontally into the formation, but has a tendency to rise.

The mud filtrate is most often much less saline than the interstitial water originally located in the pores and its density is therefore appreciably smaller. As a result of this difference in densities, the mud filtrate is submitted to an ascensional force. Its velocity is the resultant of two components: One vertical (upward) component, caused by the ascensional force, and one horizontal (radial) component, due to the rate of filtration.

Considering a permeable bed, bounded by impervious formations, and thick enough that the upward movement of mud filtrate in the lower part of the bed is not affected too much by the presence of the upper impervious boundary, the vertical component of filtrate velocity in the lower part is essentially proportional to the ascensional force and to the vertical permeability of the formation. So, when this latter is great, the vertical component may be substantially larger than the horizontal component, which itself is comparatively small because the sealing properties of the mud cake limit the rate at which filtrate can enter the formation from the hole. Actually, as will be shown in more detail in the Appendix, a value of the order of 2 ft per day seems a reasonable figure for the vertical component in high per-

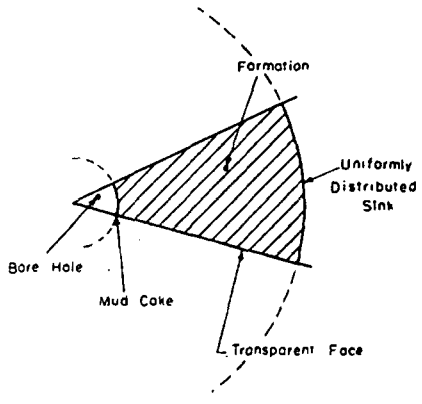

FIG. 2. Schematic view of horizontal cross section of laboratory model.

Reprinted from THE PETROLEUM ENGINEER, January, 1955

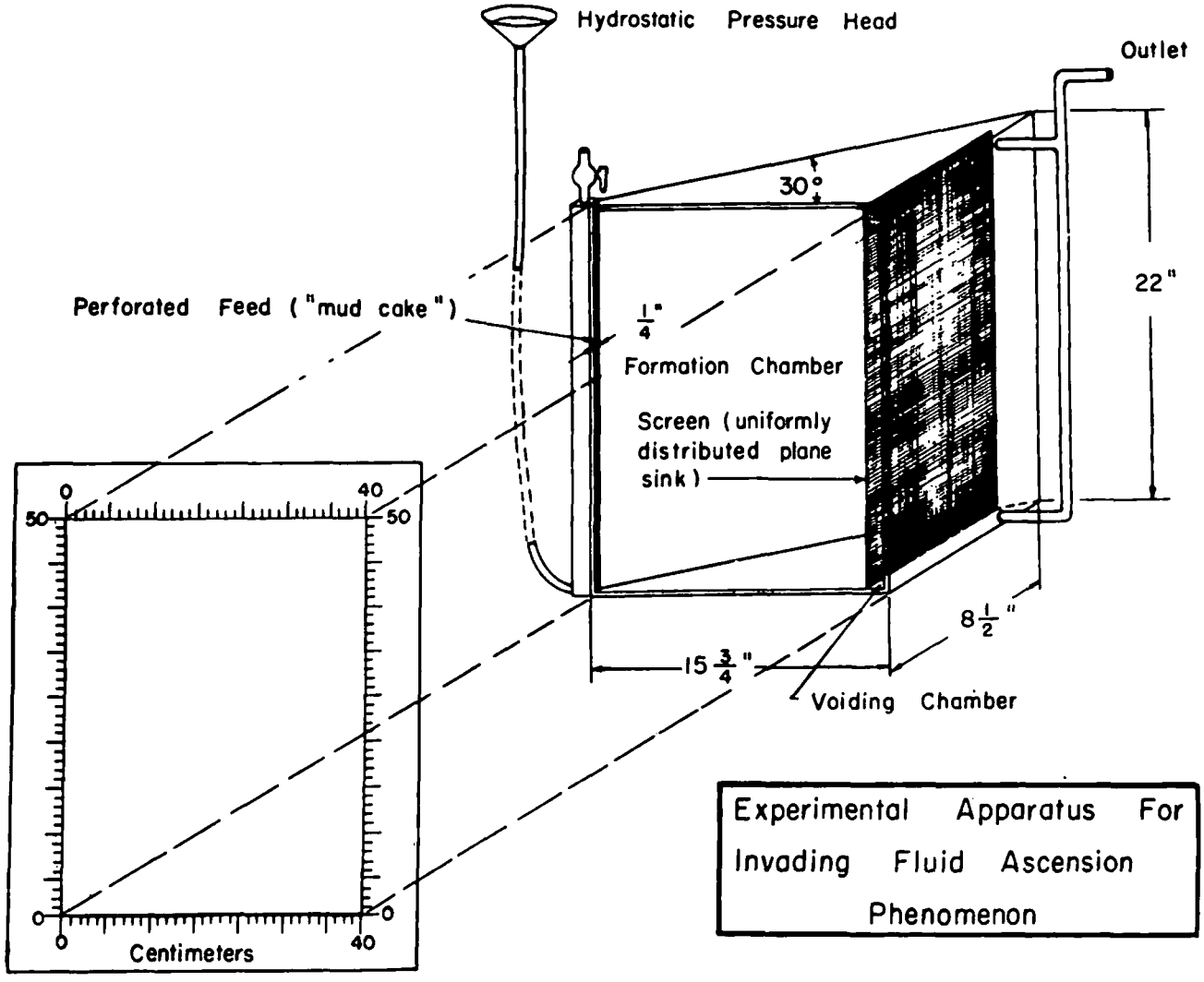

FIG. 3.

meability formations, with the usual differences between mud filtrate and connate water densities, whereas the horizontal component of filtrate velocity radially out from the hole wall is known to be of the order of a few inches per day at the most.

Consequently, in the lower part of the formation, the mud filtrate rises obliquely from the wall of the hole, and the invasion is shallow; in the upper part, the mud filtrate accumulates below the upper boundary, and the invasion is deep. By analogy with the displacement of the fluids contained in a vessel under the action of temperature differences, this ascensional movement of mud filtrate will be called a "convection current."

The invasion process in a permeable, homogeneous and salt-water-bearing bed, bounded by impervious formations, is shown schematically on Fig. 1.

In tracing the figure, it has been assumed that there is no transition zone between the invaded and non-invaded parts of the bed, which means that the diffusion from connate water into filtrate can be taken as negligible. It has been furthermore assumed that the drilling speed is so great with respect to the speed of filtration that invasion begins substantially at the same time throughout the whole permeable formation. The time of the beginning of invasion will be taken as time "zero" in the following discussion.

Shortly after time zero, say a few hours, the surface separating the invaded and the non-invaded zones, which will be referred to in the following as the "invasion front," is still quite close to the wall of the hole, and its shape, as indicated in Fig. 1a by the line ABCD, includes a central vertical section BC*. As the invasion front moves forward the vertical portion shrinks, as shown for example by the curve $A_1B_1C_1D_1$ of Fig. 1b, representing the conditions existing on the third day after time zero. Still later, for example on the 10th day, all the filtrate that had penetrated the bed at time zero has had time to reach the top boundary. At that time the invasion front no longer contains a vertical section, but has assumed the shape qualitatively shown by curve $A_2B_2D_2$ in Fig. 1c.

Furthermore, the rate of filtration, and hence the radial component of filtrate velocity, decreases progressively with time as the mud cake becomes thicker, whereas the vertical component should be constant with respect to time and to space (see Appendix). The result is that the direction of the lines of flow have a tendency to come closer and closer with time to the vertical. The invasion front therefore moves forward for several days after time zero until a maximum extension of invasion is attained, (for example, until the 10th day, as shown in Fig. 1c), and then, in the lower part of the bed, it recedes progressively, whereas in the upper part it continues to expand below the upper boundary (Fig. 1d — curve $A_3B_3D_3$: 25th day).

This qualitative description will be elaborated by the results of laboratory

*To simplify the wording, terms like ABCD, which designate the intersection of a surface of revolution with the plane of the figure, are used in this article to denote the surface itself.

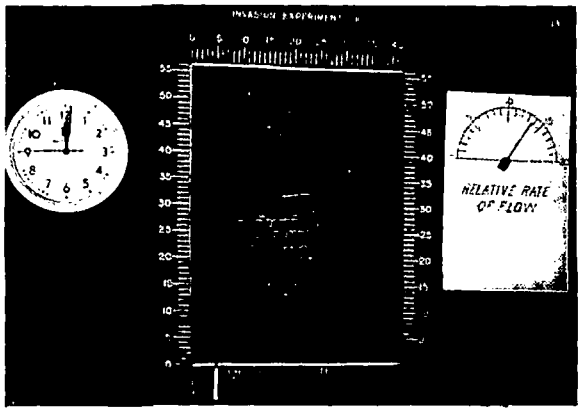

FIG. 4.

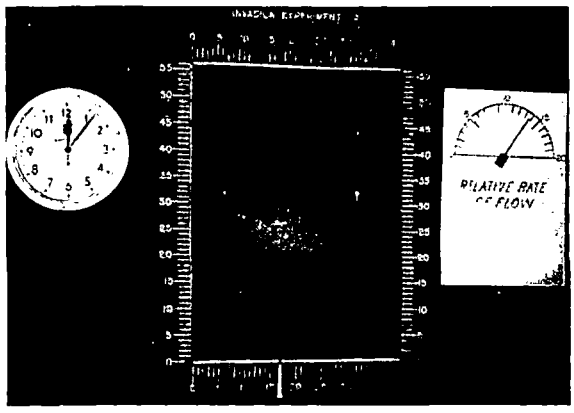

FIG. 5.

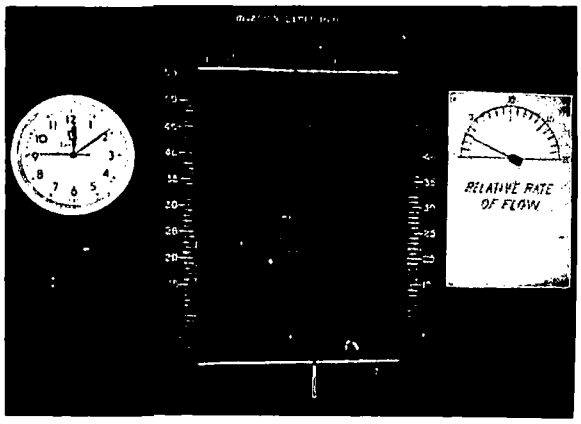

FIG. 6.

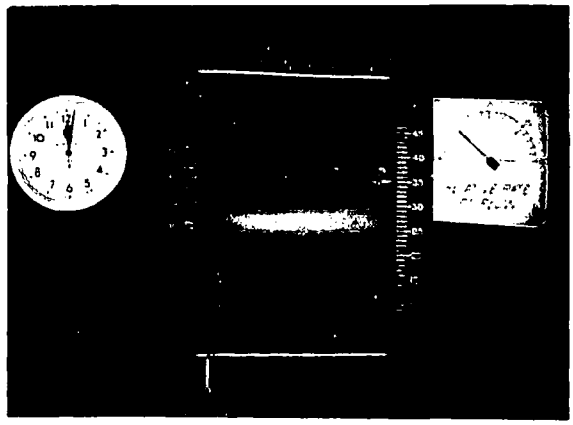

FIG. 7.

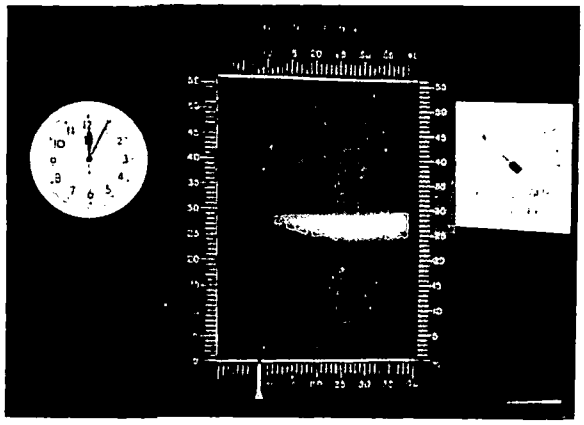

FIG. 8.

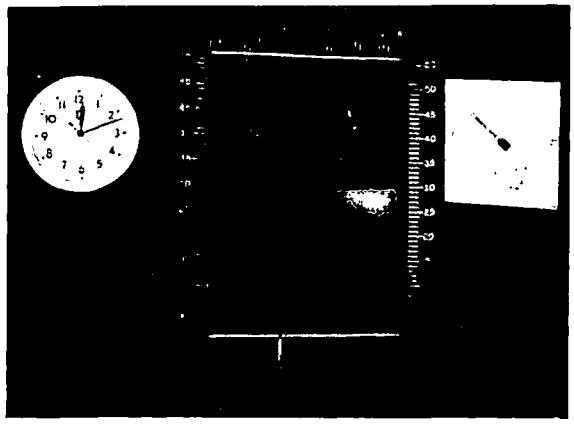

FIG. 9.

FIGS. 4, 5, and 6. Invasion process in homogeneous formation of 4500 darcies.

FIGS. 7, 8, 9, and 10. Invasion process in permeable formation (4500 darcies) including a less permeable section (230 darcies).

(The pointer at bottom indicates depth of uniform invasion.)

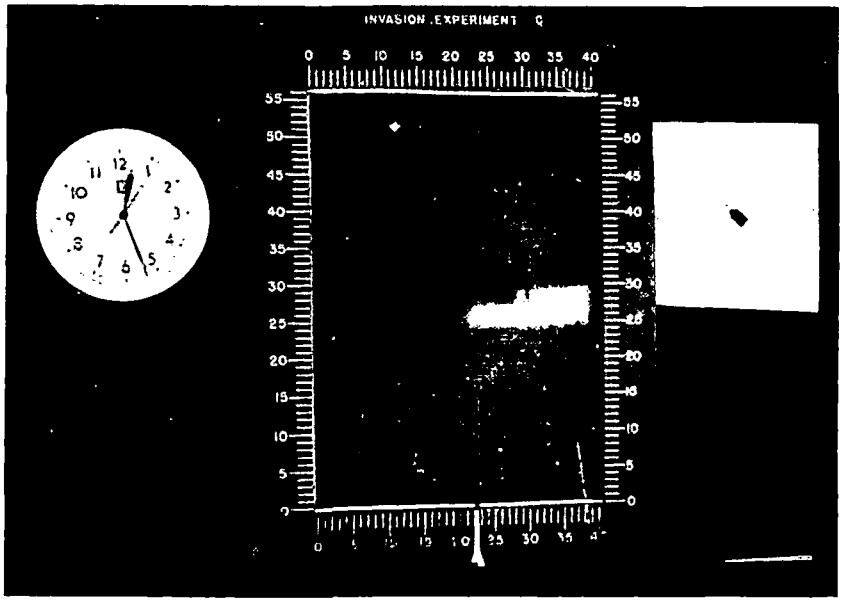

FIG. 10.

The Author

Henri-Georges Doll was graduated from the University of Lyon, France, with a bachelor of science. He did graduate work at the Ecole Polytechnique and the Ecole Nationale Supérieure des Mines de Paris. He was first employed as research engineer for the Société de Prospection Electrique (Procedes Schlumberger), Paris, France, from 1926 to 1939. From 1934 to 1939, he was technical consultant for Schlumberger Well Surveying Corporation, Houston, Texas. In 1940, he became director of research for Schlumberger, and in 1941 chairman of the board of directors.

Doll was awarded a Certificate of Appreciation by the U. S. Government for his work on mine detectors, and the Legion of Honor Medal by the French Government for his technical achievements.

tests and of mathematical computations to be explained hereafter.

Laboratory Experiments

Procedure. The invasion process in highly permeable formations was studied by means of a laboratory model, consisting essentially of a chamber that could allow radial invasion. To this end, the model approximated a "pie-shaped" sector cut from a cylinder, as shown in Fig. 2. To represent the mud cake use was made of a metal strip closing the narrow edge of the "pie-shaped" cavity. This strip was perforated with many evenly distributed capillary apertures through which "mud filtrate" could be forced into the "formation." The permeable formation was made of spherical glass beads of uniform diameter. In order to make possible free radial invasion the outer periphery of the model was terminated by a screen, which served as a uniformly distributed sink for the flow of fluids (Fig. 3). The top and bottom boundaries of the pie-shaped box represented impervious beds above and below the glass bead formation.

The permeabilities of the mud cake and of the formations were chosen quite large, at least one thousand times larger than in usual field conditions. This was done because it was difficult to build a simulated "mud cake" with a low enough permeability. Also, for lower permeabilities the time required for the phenomenon to develop in the laboratory would have been excessive. In fact, the time in the laboratory tests was counted in minutes, whereas in actual conditions it is a matter of days.

One plane face of the model was transparent, which enabled the recording of the evolution of the phenomenon by means of photographs taken at proper intervals of time. To this end, and also to facilitate the visual inspection of the experiment, a special dye (potassium permanganate) was used to color the filtrate water.

The pressure needed to cause the flow of the filtrate into the invasion chamber was provided by a water column, the hydrostatic head of which could be varied at will. It was verified that the rate of flow of the filtrate into the chamber was proportional to this pressure, as measured by a mercury manometer connected at the lower inlet of the simulated mud cake.

A dial, the reading of which was proportional to the pressure on the filtrate, is shown in the accompanying photographs to indicate the "relative rate of flow."

In all experiments, the specific gravities of the connate water and of the filtrate were respectively 1.04 and 1.

Results. Figs. 4, 5, and 6 illustrate the case of a homogeneous formation, with a permeability of 4500 darcies.

On each photograph, the pointer at the bottom of the frame indicates the depth of uniform invasion, i.e. the depth to which invasion would have extended in the same time, were it not for the convection currents.

The times after the beginning of invasion are shown on the clock: Each minute of time elapsed corresponds to about 3 days for a formation with a usual permeability of 1000 md (1 darcy).

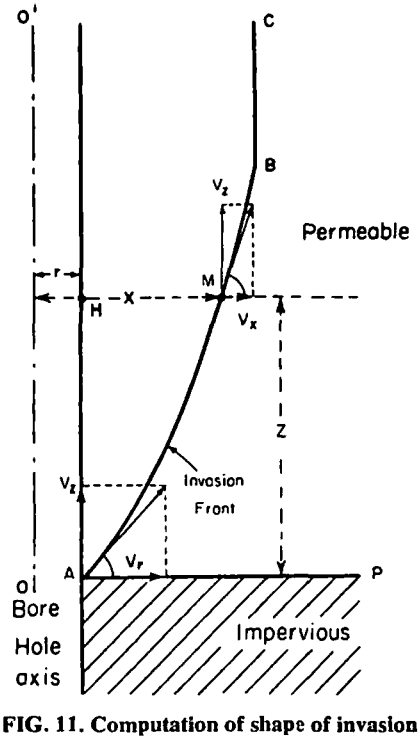

FIG. 11. Computation of shape of invasion front in salt water bearing sand of high porosity (upper boundary at great distance).

In Fig. 4, invasion is just beginning, and the invasion front is substantially vertical between altitudes 10 and 50. The distance of this vertical front from the wall of the hole is substantially equal to the depth of uniform invasion, as shown by the pointer (except for some diffusion).

Fig. 5 shows the invasion front, six minutes after the beginning of invasion (18 days for a 1000-md formation). As the rate of invasion has been kept constant, an equilibrium position has been established. In the lower part, the depth of invasion is much smaller than would be in case of uniform penetration, as is clearly shown by the position of the pointer. Above altitude 37 the filtrate has accumulated, and the invasion is quite deep. Between altitudes of about 25 and 35, the photograph shows a portion that looks approximately vertical: this is likely to be caused by some lack of homogeneity in the glass bead formation.

Fig. 6 shows the situation after 9 minutes (equivalent to 27 days for 1000 md). In the meantime, the rate of invasion had been reduced (the relative flow of rate, shown by the meter, reads 3 instead of 14, as in the previous views). As could be expected, a recession of the invasion front, with respect to its position in Fig. 4, is noticeable.

Further experiments were made to investigate the effect of variations of permeability within a bed.

To illustrate the results, Figs. 7, 8, 9, and 10 show the evolution of the phenomenon in a model containing a permeable bed, 4500 darcies divided by a horizontal section with a lower permeability (230 darcies).

In Fig. 7, just after the beginning of the invasion, mud filtrate shows a tendency to accumulate underneath the boundary between the lower more permeable portion and the less permeable section. The same tendency is observed also near the top boundary of the model.

Fig. 8 shows the invasion after 4 minutes (12 days for 1000 md). Some vertical channeling is visible within the intermediate section.

After 12 minutes (36 days), the channeled filtrate has extended into the upper more permeable part of the bed (Fig. 9).

Finally, as the rate of filtration has been kept constant, an equilibrium position is practically reached after 26 minutes (i.e. 78 days), as shown in Fig. 10. The invasion appears to be very shallow throughout most of the lower permeable part of the bed, then an abrupt increase occurs near and

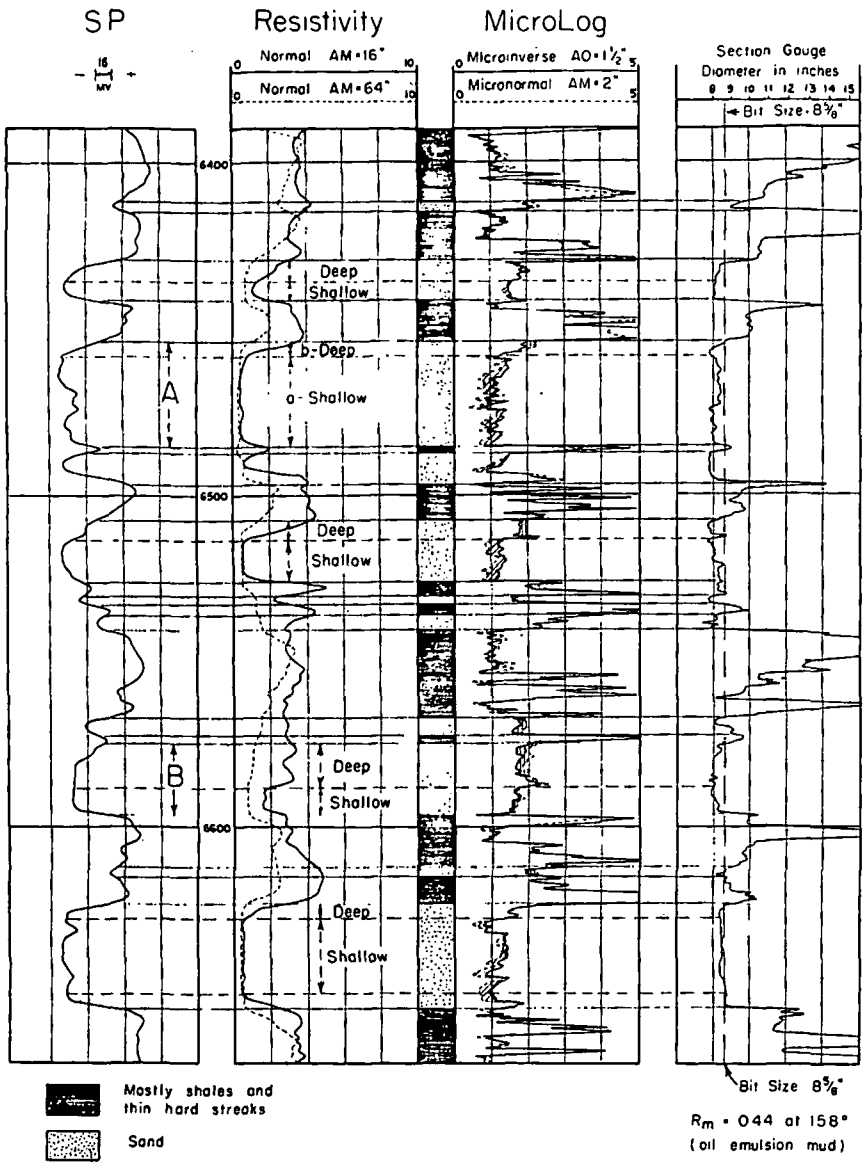

FIG. 12. Example showing effect of convection currents in salt water bearing sands of high permeability: Shallow invasion at bottom and deep invasion at top.

below the lower boundary of the less permeable section. From this level the invasion remains approximately at the same depth, and then increases again near the top boundary of the upper permeable part of the bed.

Of course, in the upper half of the model, the invasion front is not clearly defined because of the influence of channeling. The invaded zone actually does not contain only mud filtrate, but a mixture of filtrate and connate water.

The experiment seems to show that when a high permeability bed includes a section with a lower permeability, a regime of convection currents builds up such that the invasion is shallow only below the less permeable section.

Computations

The shape of the invaded front can be computed approximately for the lower portion of a homogeneous permeable bed again supposed to be thick enough that the presence of the impervious upper boundary has a negligible influence on the circulation of the fluids in the lower part.

Fig. 11 represents the vertical cross-section of the lower part of such a permeable bed. In this figure, the vertical distances, z, are measured from the lower boundary AP, and the horizontal distances, x, are measured from the axis 0 0′ of the bore hole.

Considering a certain point M of altitude AH = z on the invasion front, the computations were made supposing that all the mud filtrate, which had crossed the wall between A and H at time zero, has already ascended above the level of M. In other words, the vertical portion of the invasion front (such as A_1B_1 in Fig. 1 b for example), if any such still exists, has, at the time being considered, passed above M. On Fig. 11, such a vertical position is shown in BC.

The volume of filtrate flowing across the horizontal plane through point M between times t and $t + dt$, is equal to $\pi(x^2 - r^2)\, v_z\, \phi\, dt$, r being the radius of the hole, ϕ the porosity, and v_z the vertical velocity, which, in a homogeneous bed, is constant with respect to space and to time. The volume of filtrate that crosses the wall of the hole in the section between the bottom of the bed and the level of point M (section AH with AH = z), between the same times t and $t + dt$, is equal to $2\pi rz\, v_r\, \phi\, dt$, where v_r is the radial velocity at the wall of the hole (v_r, at a given time, can be taken as being substantially constant).

If it is assumed further that v_r is constant with time, the portion AMB of the invasion front is at an equilibrium position, and these two volumes must be equal. It follows:

$$\pi(x^2 - r^2)\, v_z\, \phi\, dt = 2\pi rz\, v_r\, \phi\, dt \quad . \quad . \quad . \quad . \quad . \quad . \quad . \quad . \quad . \quad . \quad (1)$$

Hence:

$$x = \sqrt{2\, rz \frac{v_r}{v_z} + r^2} \quad . \quad . \quad (2)$$

Equation (2) shows that the shape of the invasion front over section AMB is a paraboloid of revolution around the axis of the hole.*

In fact, the radial velocity v_r is not constant, but decreases progressively with time as the mud cake thickness increases. Accordingly, x decreases also with time. In other words, at any given level HM in a bed, the invasion front recedes toward the hole after the instant when the filtrate that had penetrated at level A at time zero has risen to level M**. Up to that time, M had been in a vertical part of the front, moving out from the hole. The evolution of the invasion front at any level in the lower part of a bed is therefore first a progression, then a recession. The higher the level, the later the recession starts, and this up to a distance sufficiently near the top boundary, where filtrate accumulates and where

*Curve AMB is a line of flow, and, accordingly, the filtrate velocity at points along AMB is tangent to this curve. It is thus possible to write for points along AMB:

$$\frac{\partial z}{\partial x} = \frac{v_z}{v_x}$$

v_x being the radial velocity at each point along AMB, which in turn is related to v_r through:

$$\frac{v_x}{v_r} = \frac{r}{x}$$

Hence:

$$\frac{\partial z}{\partial x} = \frac{v_z \cdot x}{v_r\, r}$$

Integrating this equation leads again to equation (2).

**The slope of the tangent to curve AMB at point A is v_z/v_r; this shows that, at the bottom of the bed, the tangent to the curve approaches the vertical with time, or, in other words, that the invasion front approaches the wall of the hole.

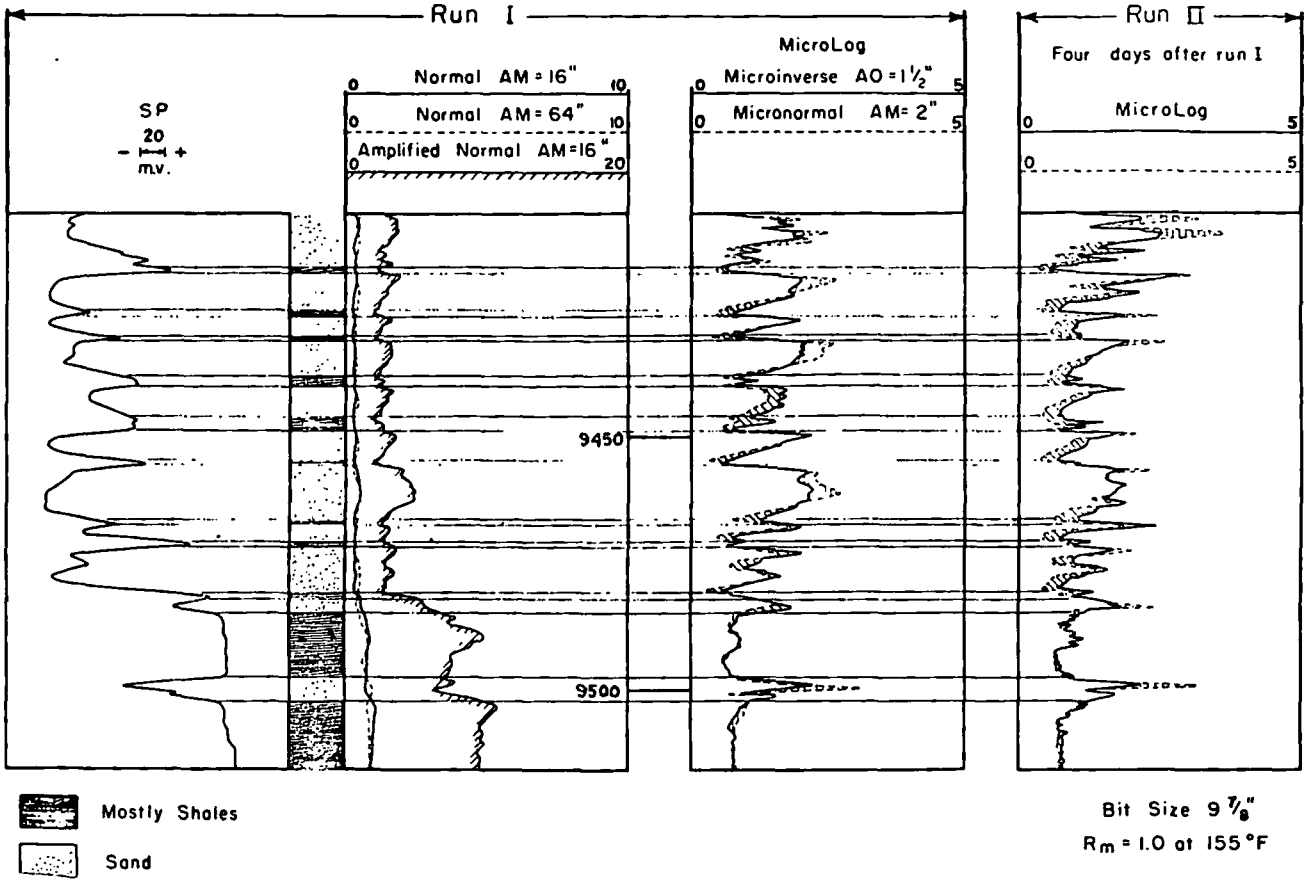

FIG. 13. Example showing effect of convection currents in salt water bearing sands of high permeability: shallow invasion at botton and deep invasion at top.

the depth of invasion continues to increase without limit.

If filtration stops completely, all the filtrate eventually will gather along the upper boundary and the invaded condition will disappear elsewhere in the bed.

Field Examples

In addition to their possible interest in drilling and production practice, the above concepts account for the behavior of electrical logs in salt-water-bearing sands of high permeability.

Fig. 12 shows the conventional ES, microlog, and section gage recorded over a sequence of sands, shales, and thin tight streaks. The sands have a high permeability and are all salt-water-bearing. The drilling mud is appreciably fresher than the connate water.

Section A will be examined in detail as an example. This section can be divided into two parts, a and b, according to the resistivity curves and the microlog.

In sub-section a, both short and long normal curves track practically together, which is indicative of a very shallow invasion. On the other hand, the microlog shows a negative separation. In a permeable bed of low resistivity, this means that R_{xo}, resistivity of the formation close to and behind the wall of the hole, is smaller than R_{mc}, the resistivity of the mud cake. If the depth of invasion were at least equal to the average radius of investigation of the microlog (i.e. about 3-in. from the wall), R_{xo} would be approximately equal to the mud filtrate resistivity multiplied by the formation factor, i.e. would be greater than R_{mc}, and a positive separation would be observed. The fact that R_{xo} is smaller than R_{mc} is due to the presence of the uncontaminated zone, whose resistivity is very low (0.4 ohmmeter, according to the normal curves), within the radius of investigation of the microlog, i.e. at very close distance from the wall. The negative separation observed on the microlog therefore confirms that the invasion is very shallow in this sub-section.

In sub-section b, just below the tight adjacent bed, the greater values recorded on both curves indicate a deeper invasion. This is confirmed by the higher values and the positive separation observed on the microlog.

The SP curve and the microlog show that the bed is not homogeneous and contains variable amounts of shale (although the variations on the microlog curves may correspond partly to changes in mud cake thickness). It appears that, despite the presence of interstitial shale, the vertical permeability of the bed is nevertheless great enough for the convection currents to be appreciable.

Similar considerations apply to the other permeable sections. The feature is slightly different in bed B. The lower part, with shallow invasion, is clearly differentiated from the upper part, with deep invasion; however, in the lower part, the short normal curve stays higher than the long normal, which shows that the invasion is not so shallow as in the case of bed A, section a, for example. Correspondingly, the separation between microlog curves, instead of being negative, is slightly positive.

The section gage log indirectly confirms the existence of convection currents. Considering each individual sand, the log shows that the mud cake thickness has no tendency to increase from the bottom to the top. This indicates that the rate of filtration should be substantially the same at all levels of the same bed. As the porosity is known to be constant on the average, the depth of invasion would be also the same, if there were no convection currents.

Fig. 13 is another example of a similar sequence of formations. The point

of interest is that the microlog was recorded twice: In run I, at the same time as the conventional log; in run II, four days later. The comparison of the amplified short normal curve and of the microlog run I again shows the effect of the convection currents on the behavior of the invaded zone. Furthermore, on microlog run II, the amplitudes of the negative separations and their vertical extensions are more accentuated than in run I, whereas the sections with positive separations are narrower. This shows that the invasion front receded between run I and run II, except at a very close distance below the upper boundaries where filtrate continued to accumulate.

Case of Oil Bearing Formations

The mathematical analysis of the problem of invasion in case of oil bearing formations seem to be very involved. The problem, accordingly, was studied only in the laboratory, and with simple equipment. The model consisted of two identical burettes filled with glass beads and water of 1.04 specific gravity. Oil was poured into the burettes from above until about one-half the formation was oil invaded. Then dyed filtrate water of 1.00 specific gravity was introduced in each system through a glass tube. In one burette the tube outlet was in the oil-bearing portion above the oil-water interface, in the other burette the tube outlet was in the water portion.

It was found, in the first case, that the fresh filtrate water sank through the oil to the oil-water interface and floated on the top of the salty formation water without appreciable mixing. In the second case, the fresh water rose through the salty water up to the oil-water interface and concentrated at this level, with some mixing between the fresh and salty water.

This experiment suggests the idea that in a high permeability formation supposed substantially homogeneous, which is oil-bearing at the top and salt-water-bearing at the bottom, the mud filtrate would tend to flow downward in the oil-bearing part and upward in the water-bearing part. This process would create a zone of deep invasion near the oil-water level, whereas invasion would be shallower everywhere else.

The conditions of the laboratory experiments, however, were so different from the actual conditions prevailing in the formations that the above suggestion should be considered with great caution. It is certain, in particular, that the permeability of the formation in the laboratory model was enormous in comparison with the highest permeabilities encountered in practice. Although this circumstance was acceptable for

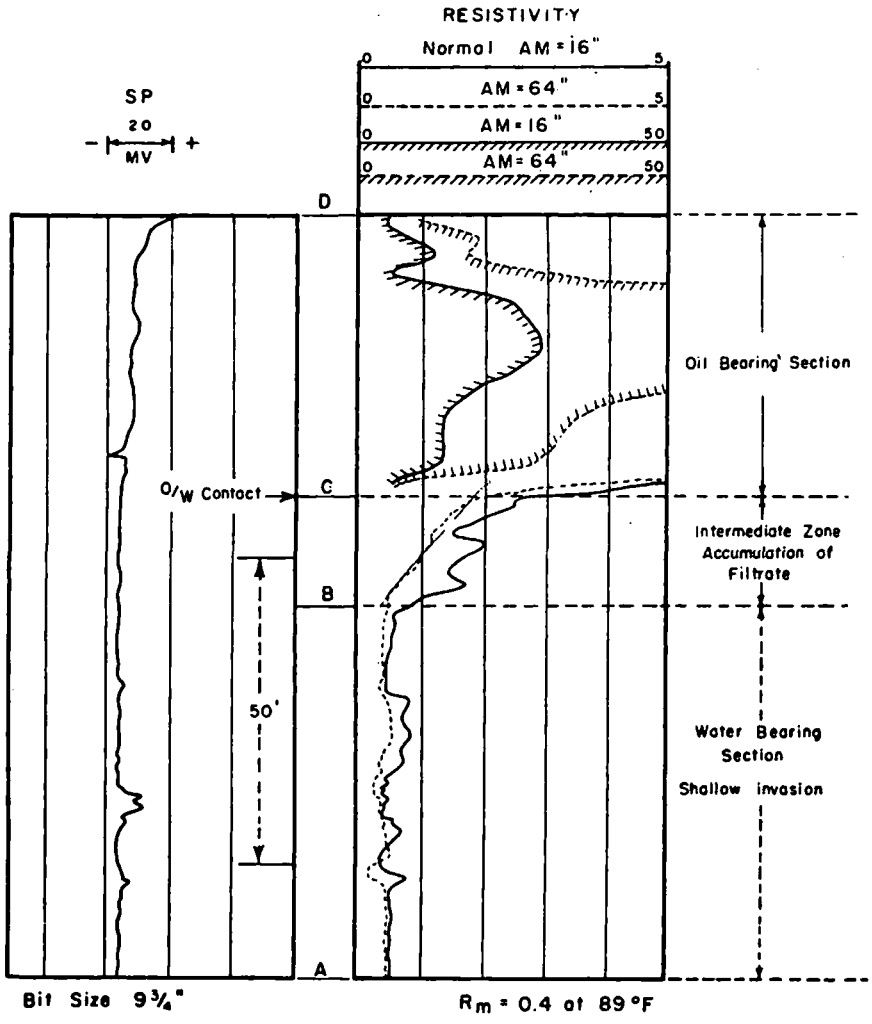

FIG. 14. Invasion in thick high permeability sand, oil bearing on top, salt water bearing at bottom. Porosity: about 30 per cent. Vertical permeability: about 100 md.

the investigation of water-bearing formations, it may give a completely false representation of the actual phenomenon in the case of oil-bearing formations, if only because the effect of capillary forces was practically negligible in the laboratory model.

On the other hand, it has been difficult thus far to find definite experimental evidence of the phenomenon on actual electrical logs. The deep invasion zone, if such really exists at the oil-water contact, would have a limited vertical extension and, with the present measuring devices, could not be easily differentiated from the oil-bearing zone. Furthermore, to ascertain from the electrical logs available at present whether invasion is shallow or deep is generally difficult, and even impossible in oil-bearing sections, because the values of R_{xo} and R_t are not very different.

An example is shown, nevertheless, in Fig. 14, which seems to confirm the assumption that filtrate accumulates near the oil-water contact. The log was run in a thick, fairly homogeneous, high permeability sand (porosity about 30 per cent and vertical permeability about 1000 md). The resistivity of the mud was 0.4 at 89 F, much higher than that of the connate water, which was known to be quite salty.

The invasion is extremely shallow over the interval AB where low readings are observed on the two normal curves (about 0.5 ohms). The upper section CD is known as oil-bearing, and corresponds to high resistivity values on both curves (10-15 ohms). In the transition zone BC, intermediate resistivities are observed, with the short normal reading higher than the long normal. It does not seem that the transition is caused by a progressive decrease of water saturation, corresponding to a progressive increase of R_t, since for so high a permeability the oil-water contact should be sharp. The possibility of lithologic variations is also excluded, according to what is known about the formation. As the filtrate is more resistive than the connate water, it is therefore likely that the feature observed in zone BC corresponds to a progressive increase of the depth of the invaded zone, as a result of convection

currents, below the oil-water contact.

Whether the invasion is deep or shallow in the oil-bearing zone is difficult to decide from the logs.

The use of new methods such as laterolog and induction log, which have a better resolving power and which furthermore should permit the evaluation of the depth of invasion, perhaps will provide some more accurate data on this phenomenon in oil-bearing formations.

It is actually easier for water to flow through a porous diaphragm when this diaphragm is completely filled with water than when it is filled with both oil and water, all other conditions being the same. In the latter case, the water has to displace the oil and its movement is responsive to the effective permeability of the diaphragm to oil, which, of course, is smaller than the single-phase permeability to water, and to the viscosity of the oil, which generally is greater than the viscosity of water.

Accordingly, when mud filtrate penetrates into a formation that is oil-bearing at top and water-bearing at bottom, it may find a greater resistance to flow radially across the oil-bearing pores, than when it descends toward the water table. This consideration would support the hypothesis that mud filtrate tends to flow downward in the oil-bearing part of a permeable bed. It would even seem that this tendency should prevail whatever the permeability of the bed.

All this, of course, is merely speculative and has not been checked by any experiment or theoretical analysis.

Conclusion

1. The hypothesis has been advanced that in salt-water-bearing sands of high permeability, drilled through with comparatively fresh mud, convection currents occur due to the difference in density between mud filtrate and connate water. The effect of these convection currents is to drive mud filtrate toward the upper boundary of the bed, so that the invasion is shallow in the lower part and deep in the upper part.

2. Corresponding laboratory tests have been described, and a computation of the phenomenon discussed. It has been shown that both studies confirm the above hypothesis, and also provide data on the shape of the invasion front, and on its evolution with time.

3. It has been shown that the concept of convection currents accounts for the behavior of the electrical logs run in the formations in question.

4. The investigation of the case of permeable beds containing oil at top and salt-water at bottom is still very incomplete. It is, nevertheless, suggested that mud filtrate flows downward in the oil-bearing part and upward in the water-bearing part, thus accumulating around the oil-water contact.

APPENDIX

Vertical Component of Mud Filtrate Velocity

Briefly stated, the theory is that after the filtrate penetrates the mud cake sheath it acquires a vertical velocity v_z due to the difference between the specific gravities of the filtrate and formation waters. The vertical velocity can be evaluated from Darcy's law:

At a point of altitude z, the volume of fluid in cubic centimeters flowing in the vertical direction across 1 square centimeter of cross-sectional area per second is $v_z \phi$, ϕ being the porosity.

Hence:

$$v_z = -\frac{k_z}{\mu\phi} \cdot \frac{\partial p}{\partial z}$$

Where:

k_z = permeability in the vertical direction in darcies,

μ = viscosity of the fluid in centipoises, and

p = pressure in atmospheres

Using practical units, the vertical components will thus be given by the equation:

$$v_z \text{ (feet-day)} = 2.74 \frac{(\rho w - \rho mf)\, k_z}{\phi\mu}$$

This equation shows that the vertical velocity is independent of time, and is constant everywhere in a homogeneous formation.

Taking the following numerical values:

$$\text{Porosity } \phi = 0.25,$$

$\rho w - \rho mf = 0.05$ (this corresponds to a salt content in the connate water exceeding that in the filtrate by about 100,000 ppm, which is a usual case),

Temperature: 200 F, which gives for μ, viscosity of water, a value of about 0.30 centipoises.

The value found for the vertical component would be about 2 ft per day if $k_z = 1000$ md.

Acknowledgments

The writer expresses his appreciation to A. Poupon for his valuable assistance in the computations, to F. Segesman for his most important part in designing the laboratory model and in conducting the experiments, and to M. Martin for his help in preparing the manuscript.

Acknowledgement is also due to J. P. Causse for his mathematical studies involved in the design of the model, and to the oil companies who released the logs for the illustration of this article. * * *

How downhole temperatures, pressures affect drilling

PART 5: Predicting hydrocarbon environments with wireline data

Donald J. Timko, Supervisor-Formation Evaluation Group, Production Engineering Services, Continental Oil Co., Houston, and **Walter H. Fertl,** Research Scientist, Production Research Department, Continental Oil Co., Ponca City, Okla.

15-second summary

It is possible to predict the probability that commercial reservoirs exist in a geographical area of investigation —and even to estimate whether production will be gas or oil. Methods used involve comparing log derived reservoir data to statistical properties of hydrocarbon environments.

WIRELINE DATA combined with knowledge of the origin of petroleum provide important information used in estimating regional probability of commercial hydrocarbon deposits and physical state of gas-oil systems at different depths.

Many world-wide studies have been made of the origin of petroleum (Hedberg, 1969; Dott, 1969; Vassoyevich, 1969; Andreev, 1968; and Al'tovskii, 1958). Investigators relate distribution of gas and oil to single parameters, or their various combinations, such as depth, geologic time, temperature, pressure, clay diagenesis, dissolved gases, sand-shale ratios, etc. Many of these important factors can be ascertained from wireline data.

Depth. Depending on thermodynamic conditions, hydrocarbon systems may occur as solids, liquids, gases or mixtures. Generally, regional distribution of hydrocarbons versus depth shows that gas reserves exceed oil reserves, with increasing depth, for both normal and abnormal pressure reservoirs. Since 1964, all record holders for deepest producers are gas wells (Please see table, WORLD OIL, Feb. 15, 1972, Page 58).

Gas and oil distribution in the Persian Gulf basin, (Zvereva and Selitskii 1970) is characteristic of other basins. About 80% of the oil reserves is concentrated on platform basin edges, and more than 98% of free gas reserves is associated with the leading depression (folded edge of the basin).

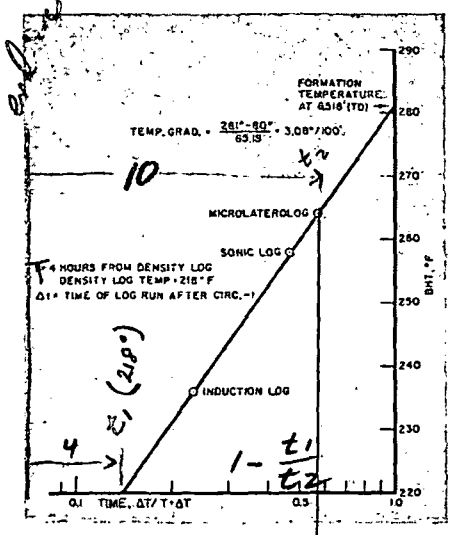

FIG. 20—How to obtain true BHT. Well was drilled in an area with high temperature gradients. Four trips were made with logging tools to 6,518 feet. Density log was on bottom 4 hours after mud circulation stopped and recorded temperature of 218°F. Microlaterolog, on bottom some 6 hours later, recorded 264°F. Straight line extrapolation to infinite time indicates BHT of 281°F. Actual stabilized temperature was 280°F.

Vertically, oil and gas accumulations in the basin are distributed in three zones:

1. Oil-gas and oil pools in the interval 250-2,500 meters. More than 50% of oil reserves and nearly 100% of dry gas reserves are concentrated there.

2. Oil and gas condensate pools at depths of 2.5 to 4 km, where substantial gas condensate deposits are concentrated.

3. Probable zone of gas condensate and gas deposits at depths exceeding 4 km.

Presence of the first two zones has been confirmed by exploratory drilling, but the third zone has not been penetrated.

Distribution patterns were governed mainly by direction and magnitude of vertical tectonic movements during geologic evolution of the basin.

Temperatures. Reasonably accurate formation temperatures can be obtained from well logs. Maximum recording thermometers should be used on each logging device. Generally, maximum recorded temperature is assumed to be bottom hole temperature, BHT. And temperature usually increases with depth.

However, measured temperature is not necessarily absolute BHT unless

→

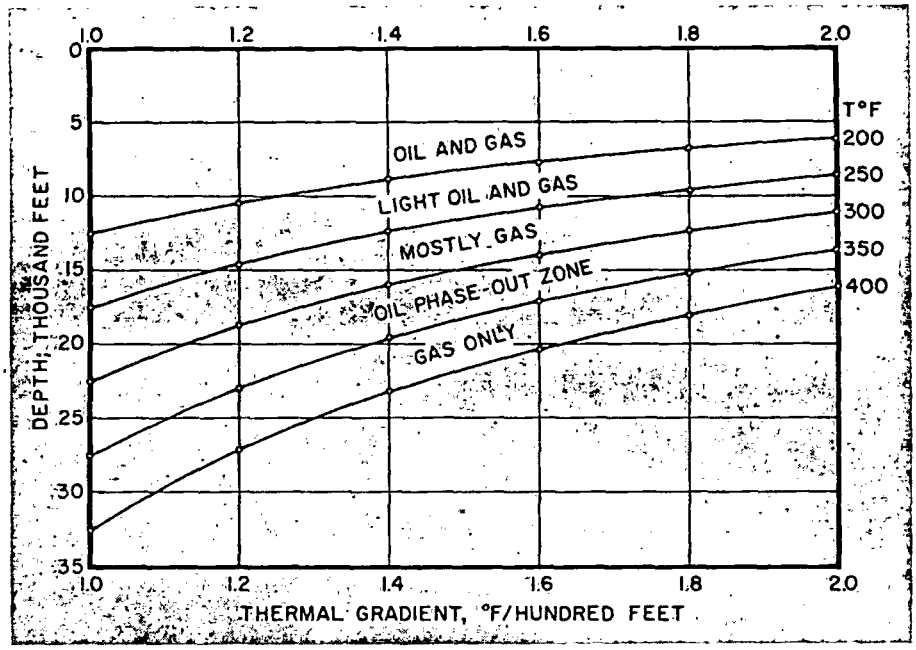

FIG. 21—Universal relations of physical state of oil and gas are shown as a function of depth and thermal gradient (after Landes, 1967). Chart has been checked with known production versus depth and temperature in several world areas, and general agreement is noted except for areas of overpressure.

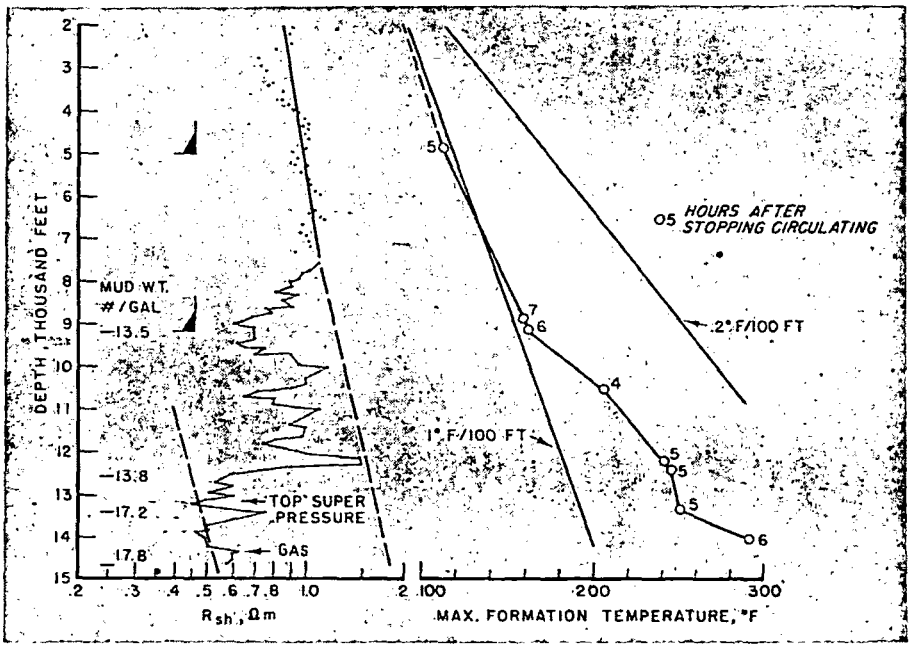

FIG. 22—Conventional Short Normal shale plot indicates abnormal pressure below about 8,000 feet, and super pressures (Timko and Fertl, 1970) below 13,000 feet, as characterized by a very high shale-sand ratio and 17 + ppg mud weight. Plot of log derived formation temperature suggests an "elbow" region which corresponds closely to the high pressure.

the well has been static long enough so that borehole and adjacent formations temperatures stabilize. Unfortunately, stabilized temperature is rarely reached by the time logs are run. Therefore, log BHT will be less than actual formation temperature. Difference depends on several factors, and can range from 15° F-80° F.

To get true temperature, an extrapolation technique must be used whenever multiple log runs are made at any particular depth. Besides temperature measurement on each run, it is necessary to record time, after mud circulation, that the sonde was last on bottom. Fig. 20 illustrates this method.

Terrestrial heat field distribution studies in potential hydrocarbon provinces around the world indicate fields are generally confined to temperature zones, while gas fi occur in higher temperature zone

Landes (1967) proposed a unive relationship of gas and oil distribu with depth and temperature (21). This chart agrees fairly when compared with known gas oil production versus depth and t perature in several places in the wc However, we have reservations at the author's general observation most temperature gradient curves come straight lines below 3,000-4 feet and that rate of temperature crease with depth, once stabilized, be extrapolated downward dur drilling to forecast content of pros tive reservoirs.

The chart should be used cautic in regions of known or suspected c pressure, since recent experiences i cate steeper than normal tempera gradients will occur (George, 1 Lewis and Rose, 1970; Jones, 1 Fertl and Timko, 1970). Fig. 22 sl such a case from offshore Louisia

Klemme (1972) also recently cussed influence of heat with re to size of oil giants, the migration formation of hydrocarbons and t of tectonic basins.

Clay diagenesis. Burst (1969) cently related clay diagenesis to hy carbon distribution on the U.S. Coast. He proposed a three-s water escape curve and sugge "The amount of water in moven during the second stage, is 10-15 compacted bulk volume and r sents a significant fluid displace capable of redistributing any m subsurface component. The move occurs in a relatively restricted, d dependent temperature zone in w average dehydration temperatu the points measured is 221° F."

Based on empirically derived curves and a geothermal grad map, Burst constructed regional surface dehydration contour map concluded that hydrocarbon pr tion depths are distributed in a s tically consistent relation to calcu clay-dehydration contour sur Production versus dehydration also were given as functions of logic age and field size.

Analysis of production versus dration data shows that concl

Continued on F

TWELFTH INTERSOCIETY ENERGY CONVERSION ENGINEERING CONFERENCE
SHERATON PARK HOTEL, WASHINGTON, D. C. AUGUST 28 – SEPTEMBER 2, 1977

THE HELICAL SCREW EXPANDER EVALUATION PROJECT

Richard A. McKay

Jet Propulsion Laboratory, Pasadena, California

Abstract

A positive-displacement helical-screw expander of the Lysholm type has been adapted for geothermal service by the Hydrothermal Power Co., Ltd. (HPC) and successfully demonstrated in a 50 kW prototype power system. With ERDA support, the Jet Propulsion Laboratory (JPL) and HPC are preparing to evaluate the expander by testing a new model in a 1 MW power system under wellhead conditions in selected liquid-dominated geothermal fields. The objectives are to determine the performance characteristics of the expander and power system over a broad range of operating conditions and also to examine the concept of wellhead power plants. Throttling and fractionation of the fluids from the test wells is planned to simulate a wide range of wellhead pressures and steam fractions. Provision is also planned to vary the expander exhaust pressure. The investigation will include expander efficiency, corrosion, erosion, scale formation and control, and endurance testing. Interaction studies with the wells and an electric grid are also proposed.

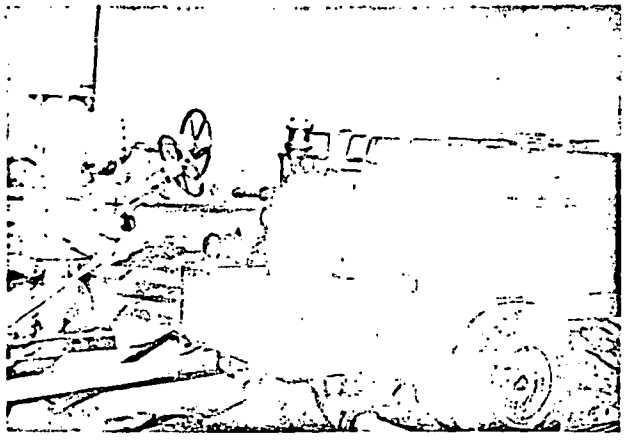

Figure 1. Geothermal Power System (50 kW Prototype) Complete with Helical-Screw Expander, Speed Reducer, Electric Generator, Forced Lubrication System, Governor, and Instrument Panel, Operating at Well M7, Cerro Prieto, Mexico. (Courtesy of Hydrothermal Power Co., Ltd.)

INTRODUCTION

The prospects of geothermal energy utilization around the world could be enhanced by an expander which operates directly on the hot mineralized water and vapor produced in liquid-dominated geothermal fields.

A positive-displacement mixed flow expander based on the design of Lysholm (Sweden) has been adapted for geothermal service and incorporated into a 50 kW prototype electric power plant module by the Hydrothermal Power Co., Ltd., shown in Figure 1. This prototype system was successfully demonstrated in three geothermal fields in southwestern United States and Mexico using brines having mineral content ranging from 1.7 to 33 weight percent dissolved solids.

However, inherent limitations in size and construction details of the prototype precluded establishing commercial credibility. The need to test a larger machine designed and built for geothermal service was evident.

EXPANDER OPERATION

The principle of operation of the expander can be described with the aid of Figure 2. The geothermal fluid at wellhead pressure flows through the throttle valve T and at high velocity enters the high pressure pocket formed by the meshed rotors, the rotor case bores, and the case end face. This pocket, designated by A in the figure, is mostly hidden by the rotor lobes, but can be seen in the plan section view. As the rotors turn, the pocket elongates, splits into a V, and moves away from the inlet port to form the region designated by B. With continued rotation, the V lengthens, expanding successively to C, D, and E as the point of meshing of the rotors appears to retreat from the expanding fluid. The expanded fluid at low pressure is then discharged into the exhaust port. Within the machine, vapor is continuously being produced from the hot liquid phase as it decreases in pressure during its passage through the expander. The effect is that of an infinite series of steam flashers, all within the prime mover. Thus, the mass flow of vapor increases continuously as the pressure drops throughout the expansion process, and the total energy stream from the well is carried all the way to the lowest expansion pressure.

During operation of the prototype, the buildup of scale within the expander was limited by the sweeping action of the two meshing helical screw rotors on each other and on all other internal surfaces. The scale deposit provided corrosion protection for otherwise exposed surfaces and

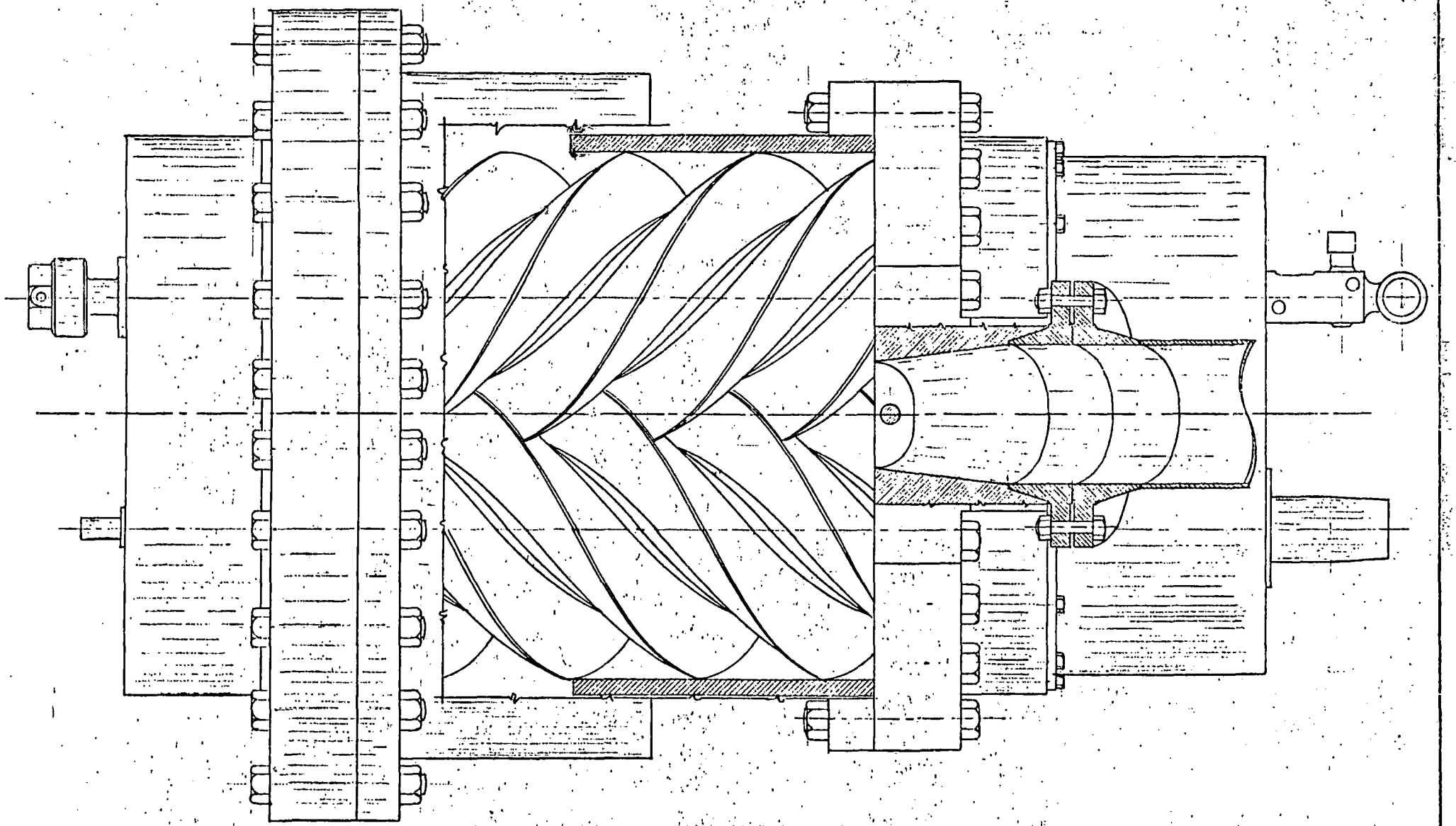

HYDROTHERMAL POWER CO. LTD.
PASADENA CALIFORNIA

SCALE:	APPROVED BY:	DRAWN BY: [illegible]
DATE: 3-6-77		REVISED

HPC POWER SYSTEM
1250 KVA MODEL PG-1

DRAWING NUMBER
A-55

Text

FOREWORD

This pamphlet has been prepared for the benefit of the Sales and Field Engineer.

It describes practical methods for determining water saturation from TDT logs. With special emphasis on TDT-K, it shows how porosity and nature of hydrocarbon can also be determined and how confident one can be in the results.

The various methods and observations presented in this pamphlet have been proposed, used, and analyzed during the last eighteen months by SDRC, Interpretation Development, and the Field. They represent our experience in TDT interpretation today.

DETERMINATION OF WATER SATURATION

Thermal Neutron Decay Time measurements can be used to calculate water saturation. The Thermal Neutron Decay Time constant of the formation (τ) is related to the Neutron capture cross section of the formation (Σ) as follows:

$$\tau_{\mu sec} = \frac{4550}{\Sigma_{cu}} \qquad (1)$$

- The units of τ are microseconds
- The units of Σ are capture units ($10^{-3} cm^2/cm^3$)

A typical Dual Spacing TDT log is shown in Fig. 1. This log differs from those made by previous tools in that the additional detector provides a ratio curve similar to that of the CNL. Porosity can be derived from this Ratio. Another feature of the tool is the recording of the Gate 1 counts per second for near and far detectors. Under favorable conditions these curves can indicate gas in the formation.

Fig. 2 is a schematic (representation) of an earth formation. Each component of the formation has a specific capture cross section. The log response can be written as follows:

$$\Sigma_{log} = (1-\phi_e-V_{sh})\Sigma_{ma} + V_{sh}\,\Sigma_{sh} + \phi_e\,S_w\,\Sigma_w + (1-S_w)\,\phi_e\,\Sigma_{hy} \qquad (2)$$

Note that Eq. 2 is linear and independent of formation factor and saturation exponents. Once the log has been run, we need to determine as many as six additional parameters in order to solve Eq. 3 for the formation water saturation.

$$S_w = \frac{(\Sigma_{log}-\Sigma_{ma}) - \phi_e\,(\Sigma_{hy}-\Sigma_{ma}) - V_{sh}\,(\Sigma_{sh}-\Sigma_{ma})}{\phi_e\,(\Sigma_w - \Sigma_{hy})} \qquad (3)$$

Fig. 3 shows the information required to solve for S_w. The inner circle applies to clean formations. The outer circle is additional information required when the formations are shaly. Part of this report is devoted to determining these parameters.

CONDITIONS FOR TDT-S_w DETERMINATION — CONFIDENCE FACTOR

The TDT, as with all logging tools gives better answers with certain formation parameters than with others. Interpretation is enhanced with the TDT when:

1) Sigms water is high,
2) Porosity is high,
3) Shale content is low.

If any of the characteristics are not met, the chance of error affecting the calculation becomes larger.

Since the TDT is a radioactivity device, it is affected by statistics. Statistical error can be a problem when the resolution of a tool is poor. This is the case with the TDT in certain areas. However, new logging procedures have been developed to reduce these statistics to a minimal level. This allows reliable answers to be determined from the TDT even in fresh water or low porosity.

A method of determining the reliability of these answers has been devised such that we can put a quality rating on each interval of the log. The reliability is calculated by determining what the statistical error is and calculating how much effect on saturation the error will have. If the parameters are such that the normal errors associated with the tool yield a poor quality rating, then new logging procedures can be used to improve the reliability. By making multiple passes and computer averaging of the data, statistical variation can be brought to a minimal level. This improves the resolution of the tool and allows a greater degree of confidence.

Delta $S_w(\Delta S_w)$ is the amount of variance in water saturation seen due to statistical sensitive data. S_w is calculated by taking the basic TDT equation (3) and rewriting it for the possible error in each measurement (4).

$$\Delta S_w = \frac{\sqrt{\phi_E^2 \Delta\Sigma_{log}^2 + \Delta\phi^2 \left[\Sigma_{log} - \Sigma_{ma} - V_{cl}(\Sigma_{cl} - \Sigma_{ma})\right]^2 + \Delta V_{cl}^2 \phi_E^2 (\Sigma_{cl} - \Sigma_{ma})^2}}{\phi_E^2 (\Sigma_w - \Sigma_{hy})} \qquad (4)$$

where:

$\Delta\Sigma_{log}$ = Accuracy of Sigma

$\Delta\phi$ = Accuracy of Porosity

ΔV_{cl} = Accuracy of Volume of Clay

The accuracy of sigma can be determined by an empirical method shown below:

$$\Delta\Sigma_{log} = \frac{(\Sigma_{log})*.96\sqrt{N_1+N_3}}{\sqrt{P.T.\ \ N_1-\left(\frac{N_3}{3}\right)}} \qquad (5)$$

where:
- N_1 = Count Rate of Near Detector Gate I
- N_3 = Count Rate of Gate 3
- T = Logging Time Constant
- P = Number of Passes

If the count rates are not available, N_1 and N_3 can be related to total porosity by equation (6).

$$\begin{aligned} N_1 &= 8700 + 800\ (cps) \\ N_3 &= 600\ (cps) \end{aligned} \qquad (6)$$

A ΔS_w of $\pm$ 10 was taken to give a confidence representing the lower limit for quantitative determination and ΔS_w of $\pm$ 20 for qualitative determination. Fig. 4 is a plot of the lower limit of confidence for varying porosity and sigma water with $V_{cl} = 0$. Note the effect of multiple passes on confidence. Fig. 5 is the same plot with $V_{cl} = .2$. It can be seen from these figures that by multiple passes and computer application, reliability of TDT answers is increased.

DETERMINATION OF POROSITY FROM TDT-K (ϕ_K)

Soft Rock--Clean Formations

The ratio curve is essentially a dual-spaced Neutron. Unlike the CNL, it responds to gamma rays of capture. Because of this, the Ratio must be corrected for the salinity of the borehole and formation fluids. Fortunately, sigma is a measure of the formation salinity. Crossplotting ratio and sigma yields porosity. To date, there are six such crossplots for varying borehole sizes and salinities. These are Figs. 6, 7, 8, 9, 10 and 11. The charts were derived from lab measurements. The measurements were taken for porosities of .18 and .36. The charts are based on $\Sigma_{ma} = 10$.

Ratio and Sigma values are entered in the chart that matches the hole size, casing size, and borehole salinity of the well. Porosity is read from the chart. Fig. 12 shows ϕ_K compared to open-hole FDC and CNL logs. For situations where the hole conditions differ from the chart, the porosities determined may be systematically in error. Experience to date shows that ϕ_K may be adjusted to fit the known porosity in a specific zone, and this correction can then be applied to the rest of the log. If hole conditions change, ϕ_K must be renormalized.

As well as porosity, the crossplot yields the apparent water salinity of the formation--WSa. WSa is analagous to R_{wa}. Water zones plot such that WSa is relatively high (low R_{wa}). Oil zones give relatively low WSa values (fresh water zones too). Because ϕ_K is a Neutron log, gas zones plot as low porosity zones with moderate to high WSa values. Like the CNL, the TDT-K ratio does not work in gas-filled holes.

Soft Rock--Shaly Formations

The accepted procedure for shale correction is to correct the data before entering the Sigma vs. Ratio chart. This is done as follows:

$$R_{corr} = R_{log} - V_{sh}(R_{sh}-1.) \qquad (7)$$

$$\Sigma_{corr} = \Sigma_{log} - V_{sh}(\Sigma_{sh}-\Sigma_{ma}*) \qquad (8)$$

Crossplotting the corrected values gives $\phi_K \simeq \phi_e$.

This method is used by TCD. LID plots Σ_{corr} vs uncorrected ratio; that is, they only correct sigma for shale.

---

* For this equation, Σ_{ma} can be taken as 10.

Hard Rock

All experience with TDT-K as a porosity device in carbonates or low porosities comes from the field. No charts based on lab experience were ever built around ratio conversion to porosity in formations other than sandstone or lower than 15% (other than 0%).

Since the TDT-K porosity is similar to a CNL in response, it can be corrected for matrix the same way. Fig. 14 is a chart for converting CNL or TDT-K sandstone porosity for matrix effects.

Often, it is found necessary to calibrate the ratio to open-hole porosity. It should be remembered in old wells, especially carbonates, the apparent porosity may have changed. In limestone, wells are routinely acidized with the net effect of increasing the porosity around the well bore. The TDT-K sees this porosity change and any water saturation calculation must be treated accordingly. Also as gas wells pressure deplete, the Neutron porosity is lowered as the hydrogen index of the fluid lessens. This also must be taken into account as with any Neutron device.

DETERMINATION OF SHALE VOLUME (V_{sh} or V_{clay})

Of all the necessary parameters used to compute S_w from TDT, tne volume of shale is the most critical. The terms clay and shale are used interchangeably in most of the literature on TDT and in this report. S_w calculations made using SARABAND answers show that best results are obtained using V_{clay} as the input. This is not surprising because logically, the silt component of the shale should have a sigma value similar to that of the matrix.

There are no universal relationships that can be applied to an SP or GR to determine V_{sh}. Local relationships must be developed to determine V_{sh} as accurately as possible. Following are some of the methods used:

1. SP
   The TCD uses the SP almost exclusively to derive V_{sh}. Fig. 15 shows the relationship between SP reduction (α) and V_{sh} developed by TCD. The chart is based on a dispersed clay model and assumes hydrocarbon-bearing sands, where the SP reduction is larger than in water-bearing shaly sands. If the zone is really water

bearing, the value of V_{sh} is too small; thus, the resulting S_w is fail-safe. If no other source of V_{sh} is available, the analyst's experience and good judgement are the only recourse for determination of V_{sh}. It is noteworthy that the maximum V_{sh} that TCD will use is .2.

Recommended reading for the use of SP to get V_{sh} is an article in the Technical Review, Vol. 20, No. 1, p20.

2. GR
As in the case of the SP, local relationships must be developed to relate GR deflection to V_{sh}. Fig. 16 shows two relationships. The curve labeled "1" was proposed by C. Clavier. The curve labeled "2" was derived by J. Stieber of Shell Oil for use in South Louisiana shaly sand formations.

3. Sonic & Density
If open-hole Sonic and Density logs are available, the dispersed clay model may be used for determining V_{clay} where

$$q = \frac{\phi_S - \phi_D^*}{\phi_S}$$

$$\text{and } V_{clay} = q\,\phi_z \qquad (9)$$

4. Sigma
The TDT has been run in Surenco as a shale indicator. For the special case where $\Sigma_{hy} \simeq \Sigma_w$ (oil and fresh water), sigma does not respond to changes in water saturation. In these cases it responds only to changes in clay content.

$$V_{cl} = \frac{\Sigma_{log} - \Sigma_{min}}{\Sigma_{cl} - \Sigma_{min}} \qquad (10)$$

$$\text{where } \Sigma_{min} = \phi \times \Sigma_{hy} + (1-\phi)\,\Sigma_{ma} \qquad (11)$$

This set of conditions is not usually met in NAM and the sigma curve reflects the variation of S_w. However, sigma can indicate if there is a need to make shale corrections in hydrocarbon zones.

PARAMETER SELECTION

Sigma Hydrocarbon - Σ_{hy}

For the case of oil, the GOR and API gravity should be known. These values are entered in Fig. 17 and Σ_{hy} read in the ordinate. If the GOR and API gravity are unknown, Σ_{hy} = 21. is used for oil.

---

* ϕ_S has to be corrected for compaction.

For the case of gas, the reservoir pressure and temperature as well as the gas gravity must be known. The sigma of methane is determined from Fig. 18. Sigma hydrocarbon for gas is calculated as follows:

$$\Sigma_g = \Sigma_{methane} \times (.23 + 1.4\ \gamma_g)^* \qquad (12)$$

where γ_g is the gravity of the gas at standard conditions ($\gamma_{air} = 1.$)

Sigma Shale (Clay) Σ_{sh}

This parameter is picked from the log.

If a caliper log is available, choose an interval where the shales are not excessively caved.

The N_1-F_1 count rate curves can also be used to monitor excessively caved intervals. This will be discussed later.

If the sigma readings in a shale zone are varying over an appreciable range ($\simeq$ 6 c.u.), pick the higher readings. This presumes that the variation is due to varying silt content and not to hole conditions.

Note that of all the parameters influencing the S_w calculation Σ_{sh} is the least critical whereas V_{sh} is the most critical.

Sigma Matrix (Σ_{ma}) and Sigma Water (Σ_w)

These parameters will be treated together since the determination of one often depends on the other. The preferred technique for determining these parameters is through the use of crossplots. For shaly zones the accepted procedure is to make shale corrections to the data (Σ_{log} and ϕ) before plotting the points.

1. Sigma vs. ϕ Crossplot

   Since sigma varies linearly with porosity, a sigma vs. porosity crossplot is very useful. This plot will be discussed for two situations:

   - The well has zones of varying porosity. Fig. 19 is a sigma vs. porosity crossplot for a hypothetical well. The most northwesterly points on the plot are water bearing. A line drawn through these points will be the $S_w = 1.$ line. The line intersects the ordinate ($\phi = 0.$) at the value of Σ_{ma}; in this case $\Sigma_{ma} = 10$. This

---

* $\gamma_g = \frac{\text{Mol. Wt.}}{28.95}$

particular line also intersects the $\emptyset = .5$ ordinate at $\Sigma = 45$. For the condition of $\emptyset = .5$ and $S_w = 1.$, $\Sigma = 45$. Using $\Sigma_{ma} = 10$ (from the plot), we can solve for Σ_w:

$$\Sigma = (1-\emptyset)(\Sigma_{ma}) + \emptyset(\Sigma_w) \qquad (13)$$

$$45 = .5(10) + .5(\Sigma_w)$$

$$\Sigma_w = 80$$

- The porosity in the zones of interest is essentially constant. For this situation the water points occur as a lump with no definable trend to a value of Σ_{ma}. For this case either Σ_{ma} or Σ_w must be known in order to calculate the other. Fig. 20 shows a typical cluster of water points. In this example, the center of the cluster is at $\Sigma = 30$ c.u., and $\emptyset = .3$. Suppose Σ_w derived from water analysis = 71. c.u.

$$\Sigma = (1-\emptyset)(\Sigma_{ma}) + \emptyset(\Sigma_w) \qquad (13)$$

$$30 = .7(\Sigma_{ma}) + .3(71)$$

$$\Sigma_{ma} = 12.4$$

The $S_w = 1.$ line can now be drawn as shown in Fig. 20.

2. Sigma vs. Resistivity Crossplot

This plot is made using the conventional Resistivity vs. Porosity charts on pages 80 and 81 of the Chart Book. It can be used to derive Σ_{ma}. Fig. 21 shows an example of this plot. It is used for the cases where the porosities in the water and hydrocarbon zones are fairly constant. Table I shows the log values used in Fig. 21. Two zones are shown. The readings were averaged over several feet. Points 5 and 9 are gas sands having $\Sigma_{hy} = 7.$ c.u. The other points are water sands. After plotting the points on the chart a straight line can be drawn between the water and hydrocarbon sands. Extrapolating the line to zero conductivity yields a value for sigma ($\Sigma_{o.o}$). $\Sigma_{o.o}$ represents the formation comprising only matrix and hydrocarbon. Σ_{ma} can be solved knowing $\emptyset$ and Σ_{hy}.

$$\Sigma_{o.o} = (1-\emptyset)\Sigma_{ma} + \emptyset(\Sigma_{hy}) \qquad (14)$$

Caution: When determining Σ_{ma} in this manner, the sands must be clean. If the sands are shaly, Σ_{ma} determined will be too high. The effect of the shale will be included in $\Sigma o.o$; that is,

$$\Sigma_{o.o} = (1-\emptyset-V_{sh})\ \Sigma_{ma} + \emptyset\ (\Sigma_{hy}) + V_{sh}\ \Sigma_{sh} \qquad (15)$$

After determination of Σ_{ma}, a Sigma vs. Porosity plot is made to determine Σ_w. This is shown by Fig. 22.

METHODS FOR SOLVING THE S_w EQUATION

Nomogram--Chart Sw-12, Fig. 23

1. Clean Formations

   - Join Σ_{ma} with Pivot Point B. This gives a line (a) which crosses the vertical $\emptyset$ lines.
   - Extrapolate a line (b) from Σ_{log} through the intersection of line (a) and the appropriate $\emptyset$ to a point on the Σ_f column.
   - Determine the intersection of Σ_w and Σ_{hy} for the appropriate conditions.
   - Extrapolate a line (5) from the point on the Σ_f column through the intersection of Σ_w and Σ_{hy} to the S_w column.

   Notes

   - Construct a new line (a) when Σ_{ma} changes.
   - Obviously, the intersection of Σ_w and Σ_{hy} will vary with changes in either or both of these parameters. Care must be taken with this point as S_w is very sensitive to these parameters. (Also true for shaly formations)

2. Shaly Formations

   - Construct line (1) by joining Pivot Point A with Σ_{ma} of the clean formation. This gives a line crossing the vertical V_{sh} lines.
   - Extrapolate a line (2) from the Σ_{sh} value through the intersection of the appropriate V_{sh} value and line (1) to Column 2. This gives Σ_{corr} which is Σ_{ma} + the effect of shale.

- Line (3) is constructed between Σ_{corr} and Σ_{ma} (for the clean formation). Line (3) is used in the same manner as line (a) was for clean formations.

- Line (4) is extrapolated from the log reading (for the zone of interest) through the intersection of line (3) and the porosity--which has been shale corrected--to column 3.

- Line 5 is made using the same procedure as in the case of clean formations.

Notes

- Line (1) must be changed if Σ_{ma} changes.

- Line (2) must be changed if V_{sh} and/or Σ_{sh} changes.

- Line (3) changes if line (2) and/or Σ_{ma} changes.

- The porosity used to locate line (4) must be shale corrected. For this reason, porosity from a synergetic log is most desirable. For a single porosity log, use:

$$\phi = \phi_{log} - V_{sh} (\phi_{sh}) \qquad (16)$$

where ϕ_{log} = porosity log reading

ϕ_{sh} = apparent porosity of shale as seen by the tool.

V_{sh} = volume of shale determined from GR or SP.

Sigma vs. Porosity Crossplot

The use of this plot to find Σ_w and Σ_{ma} has been covered. The plot can be scaled to determine the water saturation of hydrocarbon zones. After locating the S_w = 1. line, the S_w = 0. line is located using Σ_{ma} and Σ_{hy}. If S_w = 0., then:

$$\Sigma = (1-\phi)(\Sigma_{ma}) + (\phi)(\Sigma_{hy}) \qquad (17)$$

For Σ_{ma} = 11.3, Σ_{hy} = 7, and ϕ = .5

$$\Sigma = (.5)(11.3) + (.5)(7)$$

$$\Sigma = 9.2$$

Σ = 9.2 is plotted on the chart at ϕ = .5

The S_w = 0 line is drawn between this point and Σ_{ma} (ϕ = 0.)

To construct lines for S_W = .1, S_W = .2, etc., simply divide any vertical line (between the S_W = 0 and S_W = 1. lines) into 10 equal segments of sigma. Fig. 24 shows a sigma vs. porosity crossplot scaled in water saturation.

Computer-Derived Water Saturation

Basically, the TDT computer program solves Eq. 3 for S_W. The advantage of using the computer is that a detailed analysis can be presented in an appealing and useful format.

Fig. 25 shows the output of the TDT computer program. The TDT was run to monitor the sand after several years' production. This particular well is somewhat unique in that there is a veritable wealth of open-hole information. The logs on the well are shown in Fig. 26. ϕ_K was derived from Ratio and Sigma. The GR, SP, Induction, and FDC readings, together with ϕ_K (actually a Neutron porosity), were used in the SARABAND program and V_{clay} and ϕ_e were computed. Then, V_{clay} and ϕ_e together with Sigma were used in the TDT program to obtain the results in Fig. 25.

The TDT can be a valuable tool when planning a recompletion. Fig. 27 is a computer output made on a carbonate well in Canada. The well was producing with a high water cut at the time the TDT-K was run. The open-hole porosity, permeability, and water saturation were computed from IES and Sonic logs. The cased-hole porosity and water saturation were derived from the TDT-K.

The well has been acidized and the effects of the acid are reflected on the ratio curve and sigma. Currently, we can not compute a reliable water saturation across the acidized interval.

Analyzing the open-and cased-hole interpretations, it can be seen that recompleting the well in the upper zones will yield more oil. Note that the zone from 8926-8934 should not be perforated. The cased-hole bulk-volume water curve shows that this zone is no longer at irreducible water saturation and will produce with some water cut.

QUALITATIVE ANALYSIS

Sigma vs. Resistivity Crossplot

Very often the only additional information on an old well is a resistivity log. The sigma vs. resistivity plot is an effective tool in this circumstance. If the formations are fairly clean and have similar porosities this plot can distinguish depleted zones. Formations whose saturation has not changed during the life of the well plot on a straight line. This line can be scaled in water saturation. Fig. 28 is an example of this plot. The points on the plot are taken from the logs shown in Fig. 26. Although the example deals with one large sand, the plot works equally as well for a series of sands if the type of hydrocarbon is the same. Gas zones plot to the left of oil zones. Increasing shaliness moves the points

to the right toward the shale point. Point 3 is a slightly shaly hydrocarbon interval. Thief zones, oil zones that have developed secondary gas caps, and water zones that are still invaded with mud filtrate plot to the left of the line.

Parameter Selection

There are occasions when the expected values for the parameters do not yield reasonable answers. For these occasions the parameters have to be determined empirically. Fig. 29 is an example of a sigma vs. porosity crossplot developed for the Beaver Hill Lake formation in Canada. This chart was developed from a study of 21 wells in this formation. The wells produce oil. Using conventional values of Σ_{ma} = 12., Σ_w = 100., and Σ_{hy} = 21. yields TDT values of water saturation that are negative.

After plotting the points on the Σ vs. ϕ crossplot, the saturation lines were located from corresponding open-hole saturation data. The parameters that relate TDT data to open-hole saturations for this field are Σ_{ma} = 10., Σ_{hy} = 10., and Σ_w = 120.

Quick Look S_w Determination

The sigma vs. ratio crossplot can be used to derive water saturation. This is a reconnaissance technique to pick out zones for detailed analysis. For oil zones:

$$S_{wa} \simeq \frac{\text{WSa in the oil zone}}{\text{WSa in a nearby water zone}} \qquad (18)$$

For gas zones:

$$S_{wa} \simeq \frac{\phi_K \text{ in the gas zone}}{\phi_K \text{ in a nearby water zone}} \qquad (19)$$

S_{wa} in shaly oil and gas zones will be too high.

1. Look for zones with low sigma; check shale indicators so as not to overlook shaly hydrocarbons where sigma may be high.
2. Look at N_1F_1 to determine if the zone is gas bearing.
3. Determine ϕ_K and WSa in cleanest water zones.
4. Determine ϕ_K and WSa in zones of interest.
5. For oil zones use Eq. 18; for gas zones use Eq. 19.

ANALYSIS OF N_1-F_1 COUNT RATES

During the field test of the TDT-K, it was found that the near detector and far detector Gate I count rates could be used to locate gas. TCD has been the leader in developing interpretation guidelines in the analysis of these curves.

It was determined that if the count rates were displayed such that the scale of N_1 with respect to F_1 was in the ratio of 6:1, then the curves would overlay in water sands. In gas sands the curves separate. The exact explanation for this phenomenon is unknown. The most plausible theory is that the N_1 and F_1 count rates behave as short- and long-spacing neutrons, respectively. This behavior has been noted with the CNL count rates as well.

The count rates are sensitive to changes in porosity. Best results to date have been obtained in high porosity sand/shale sequences. For lower porosities the ratio of the count rate scales may have to be lowered. After rescaling the count rates a similar separation may occur when gas is present. However, the zones must have fairly constant low porosity.

Fig. 30 shows typical responses of the N_1-F_1 count rate curves:

- Zone A is the response in water sands and uncaved shales.
- Zone B is an oil zone and shows slight separation--F_1 to the left of N_1.
- Zone C is a gas zone w/large separation. F_1 can be 1 to 3 large divisions to the left of N_1. Note the decrease in ratio curve.

The shale above Zone C is typical of a caved shale with so-called reverse or negative separation between N_1 and F_1.

The amount of gas separation in shaly zones is attenuated due to the shale content. Fig. 31 shows this.

Fig. 32 shows two zones. Zone A is a gas zone. The response of Zone B is typical of the response in some zones of low porosity. Note that sigma and ratio values are about the same for these zones; however, the N_1-F_1 signature is quite different. For Zone B, both count rates decrease whereas Zone A has the gas signature. TCD postulates that the response of Zone B applies to low porosity sandstones with little or no calcareous infilling.

Fig. 33 exhibits gas separation in Zones A, D, and C. Zone B is a water sand. Zone A is limestone. Zones D and C are limestone or limy sands. It is impossible to distinguish these zones from gas zones without other information. GR and SP response may help. Ideally, open-hole Sonic, Density, or core information is available.

Zone A of Fig. 34 shows super gas saturation. The Ratio is very much attenuated, reading close to 1. in the upper part of the sand. The reservoir is a depletion drive reservoir with gravity drainage as the production mechanism. The "super separation" of N1-F1 is indicative of low pressure gas in the depleted sand. Zone B is a hydrocarbon zone showing a gas/oil contact.

Fig. 35 shows a gas-liquid contact in the casing. N1 and F1 both increase and the Ratio drops to a low value. The TDT-K Ratio can not be used when there is gas in the casing.

Fig. 36 shows the response of N1-F1 curves with gas trapped below a packer. Again, both count rates increase and the Ratio is attenuated.

Fig. 37 is another example that appears to show trapped gas. Since there is no packer, the gas is presumed to be in the casing/borehole annulus. Sigma indicates that the formation is water bearing.

Fig. 38 shows two zones with gas separation on N1-F1. The upper zone is gas. The separation in the lower zone is caused by a "hot spot" on the casing or tubing. These "hot spots" are caused by deposits of radioactive salts accumulating in or near the well bore during production. The far Gate 3 count rate (F3) measures the background counts at the far detector. Subtracting the background (1/3 F3 cps) from F1 eliminates the separation in these "hot spots." Note that the Ratio curve is unaffected since Ratio is computed after background subtraction.

Fig. 39 is another example of high background causing false separation. Two logging runs are presented--one with the well flowing--the other with the well shut in. The response of count rate curves indicate that with the well flowing gas is channeling down the casing formation annulus.

JMH:kb
5-17-74 (Updated by J. T. Watson, 4-1-77)

REFERENCES

1. Clavier, C., Hoyle, W., Meunier, D.: "Quantitative Interpretation of TDT Logs," J. Pet. Tech. (June 1971).

2. Dewan, J., Johnstone, C., Jacobson, L., Wall, W., and Alger, R.: "Thermal Neutron Decay Time Logging Using Dual Detection," presented at the annual meeting of the SPWLA (May 1973).

3. Robinson, J., Bufton, W., Hamilton, J., Tixier, M.: Improving Producibility with Cased-Hole Wirline Techniques," presented at 25th Annual Technical Meeting of the Petroleum Society of CIM (June 1974).

4. McGhee, B., McGuire, J., and Vacca, H.: "Field Applications of Dual Spacing TDT in Texas Gulf Coast," presented at the annual meeting of the SPWLA (June 1974).

5. Stieber, S.: "Pulsed Neutron Capture Log Evaluation--Louisiana Gulf Coast," presented at the annual SPE of AIME Symposium (Oct. 1970).

6. "Schlumberger Log Interpretation Charts," Schlumberger Limited (1972).

Figures

DUAL SPACING TDT

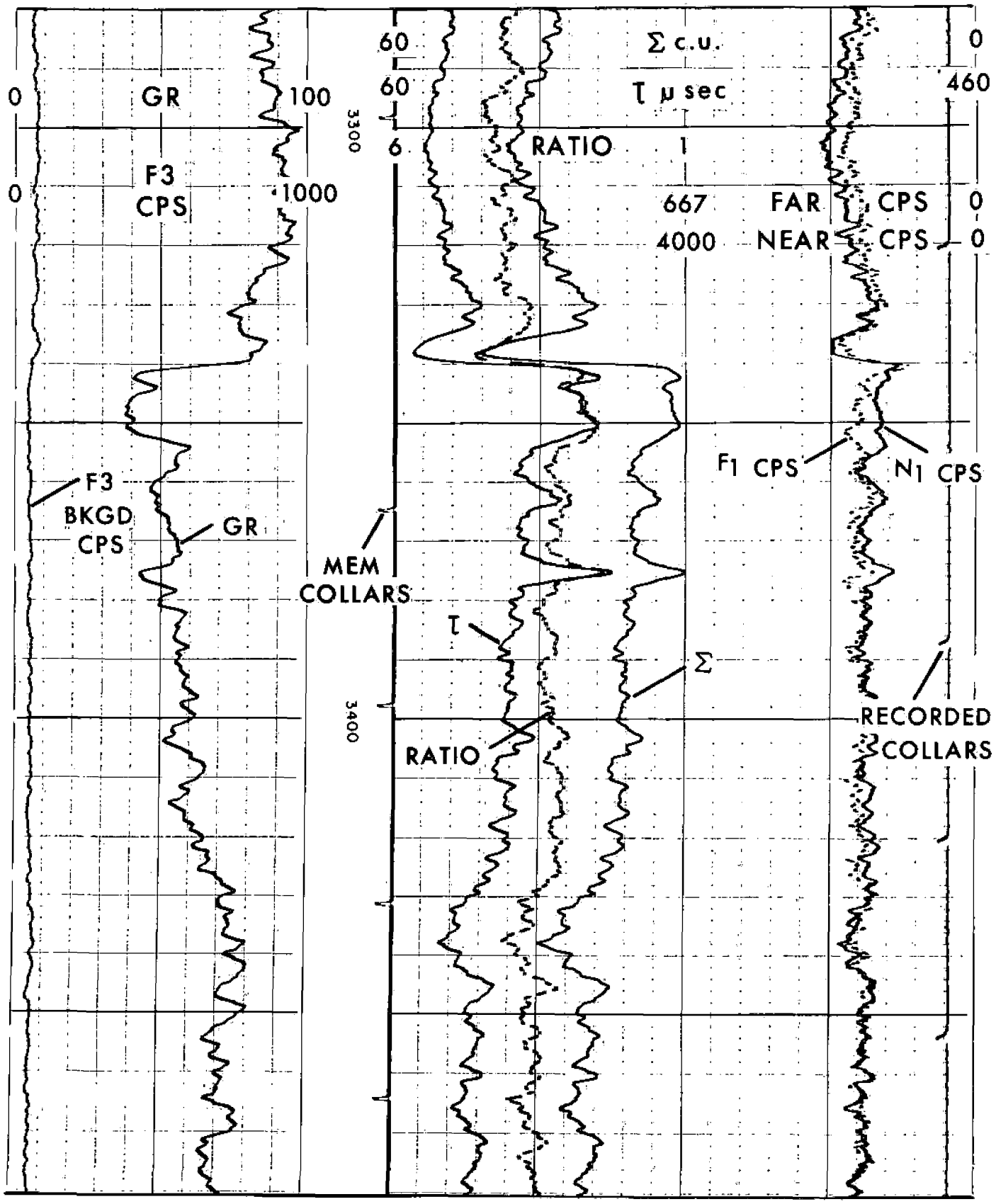

Fig. 1

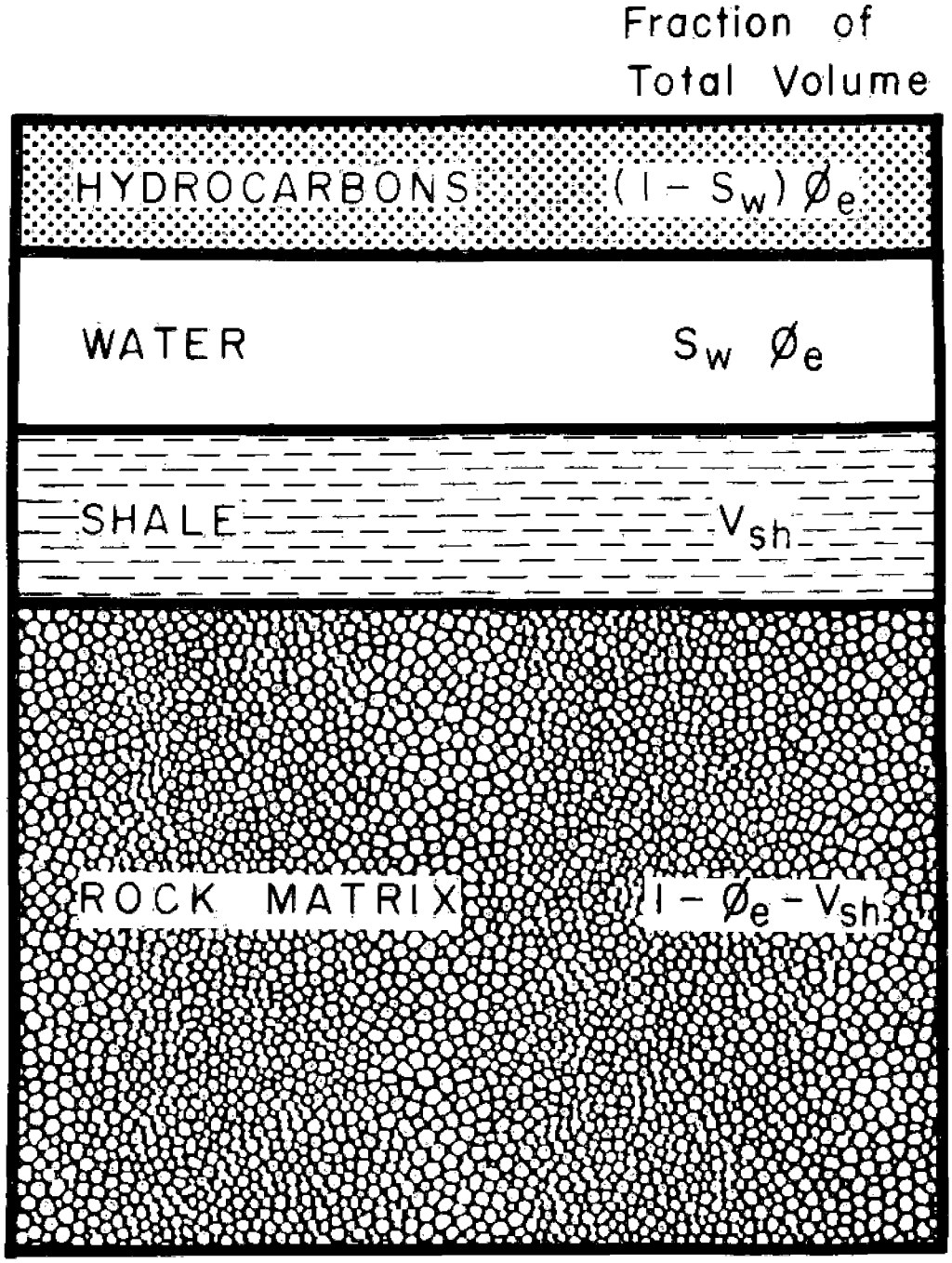
Fraction of
Total Volume
HYDROCARBONS
$(1 - S_w)\,\phi_e$
WATER
$S_w\,\phi_e$
SHALE
V_{sh}
ROCK MATRIX
$1 - \phi_e - V_{sh}$

Fig. 2

INFORMATION NECESSARY TO DETERMINE WATER SATURATION FROM TDT

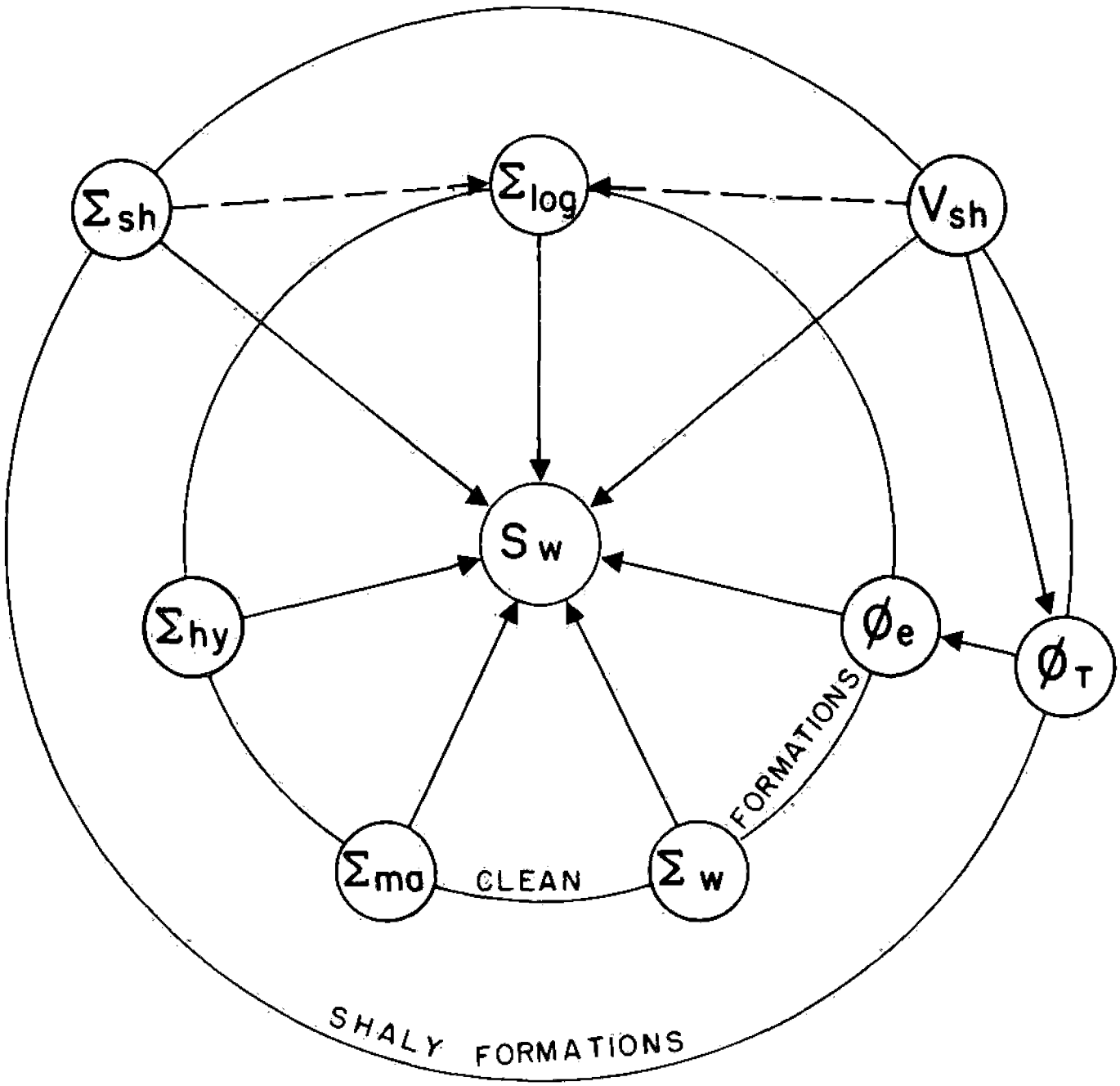

Fig. 3

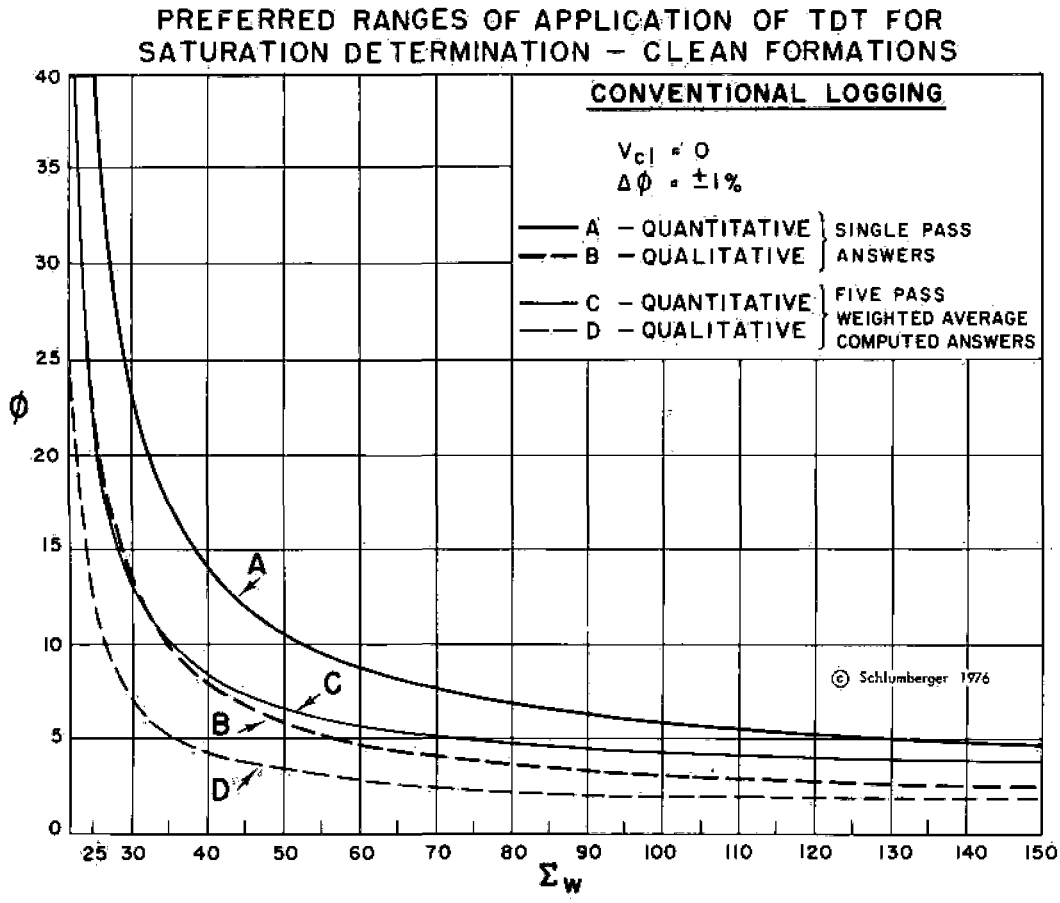
PREFERRED RANGES OF APPLICATION OF TDT FOR
SATURATION DETERMINATION – CLEAN FORMATIONS
CONVENTIONAL LOGGING
V_{cl} = 0
$\Delta\phi$ = ±1%
A – QUANTITATIVE } SINGLE PASS
B – QUALITATIVE } ANSWERS
C – QUANTITATIVE } FIVE PASS
D – QUALITATIVE } WEIGHTED AVERAGE
COMPUTED ANSWERS
© Schlumberger 1976
A
B
C
D
φ
Σ_w
0
5
10
15
20
25
30
35
40
25 30 40 50 60 70 80 90 100 110 120 130 140 150

Fig. 4

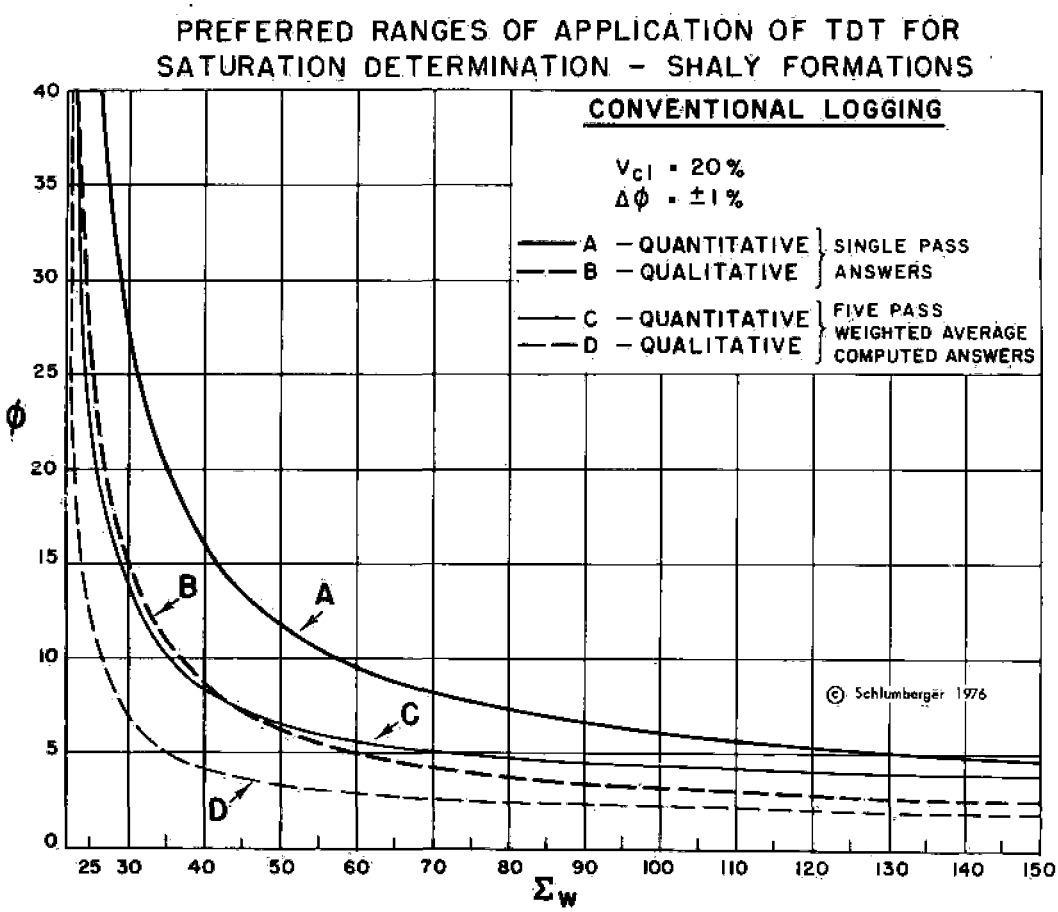
PREFERRED RANGES OF APPLICATION OF TDT FOR
SATURATION DETERMINATION – SHALY FORMATIONS
CONVENTIONAL LOGGING
V_{cl} = 20%
$\Delta\phi$ = ±1%
A – QUANTITATIVE } SINGLE PASS
B – QUALITATIVE } ANSWERS
C – QUANTITATIVE } FIVE PASS
D – QUALITATIVE } WEIGHTED AVERAGE
COMPUTED ANSWERS
© Schlumberger 1976
A
B
C
D
φ
Σ_w
0
5
10
15
20
25
30
35
40
25 30 40 50 60 70 80 90 100 110 120 130 140 150

Fig. 5

POROSITY AND APPARENT WATER SALINITY DETERMINATION FROM DUAL SPACING TDT-K

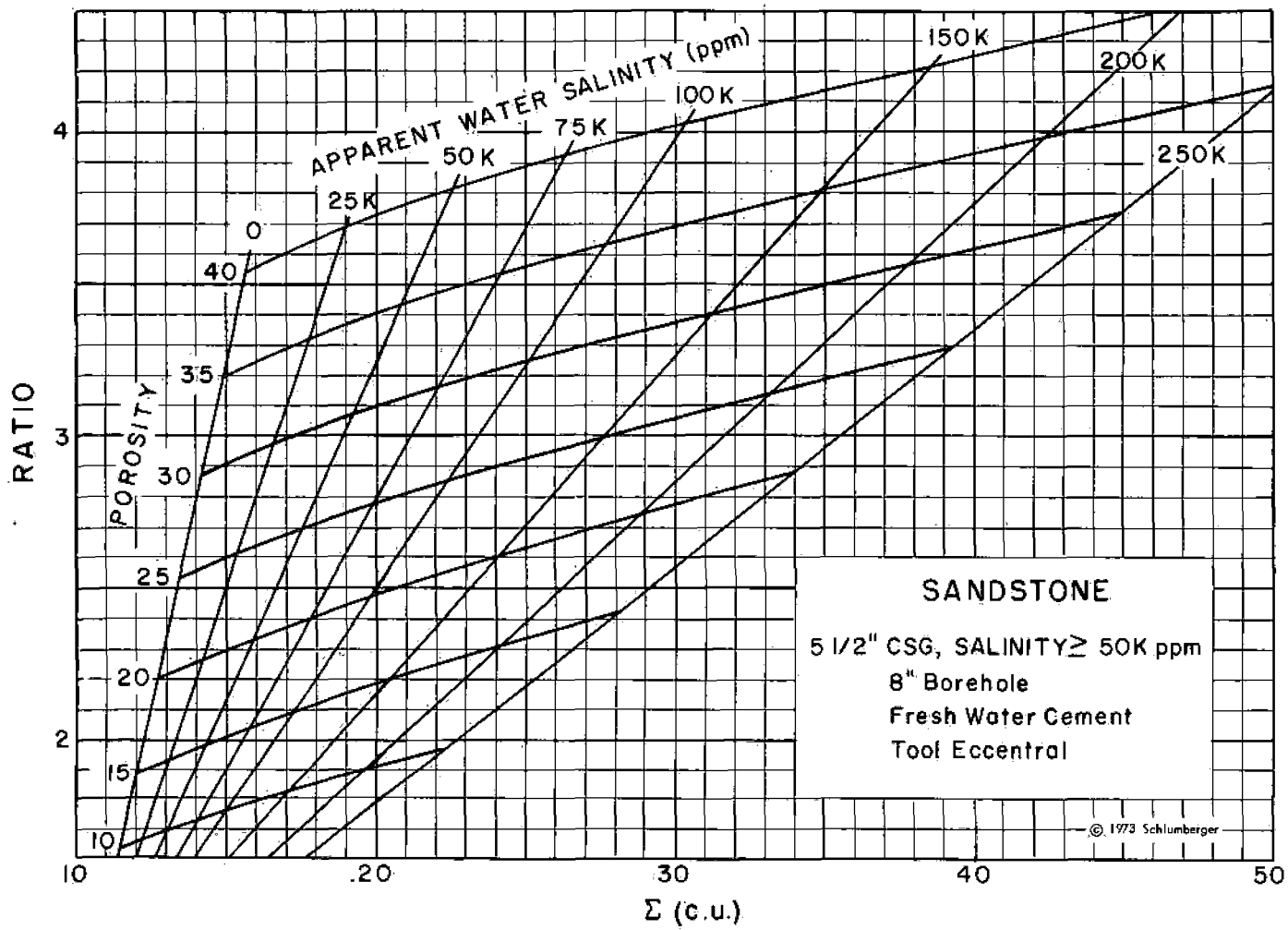

Fig. 6

POROSITY AND APPARENT WATER SALINITY DETERMINATION FROM DUAL SPACING TDT-K

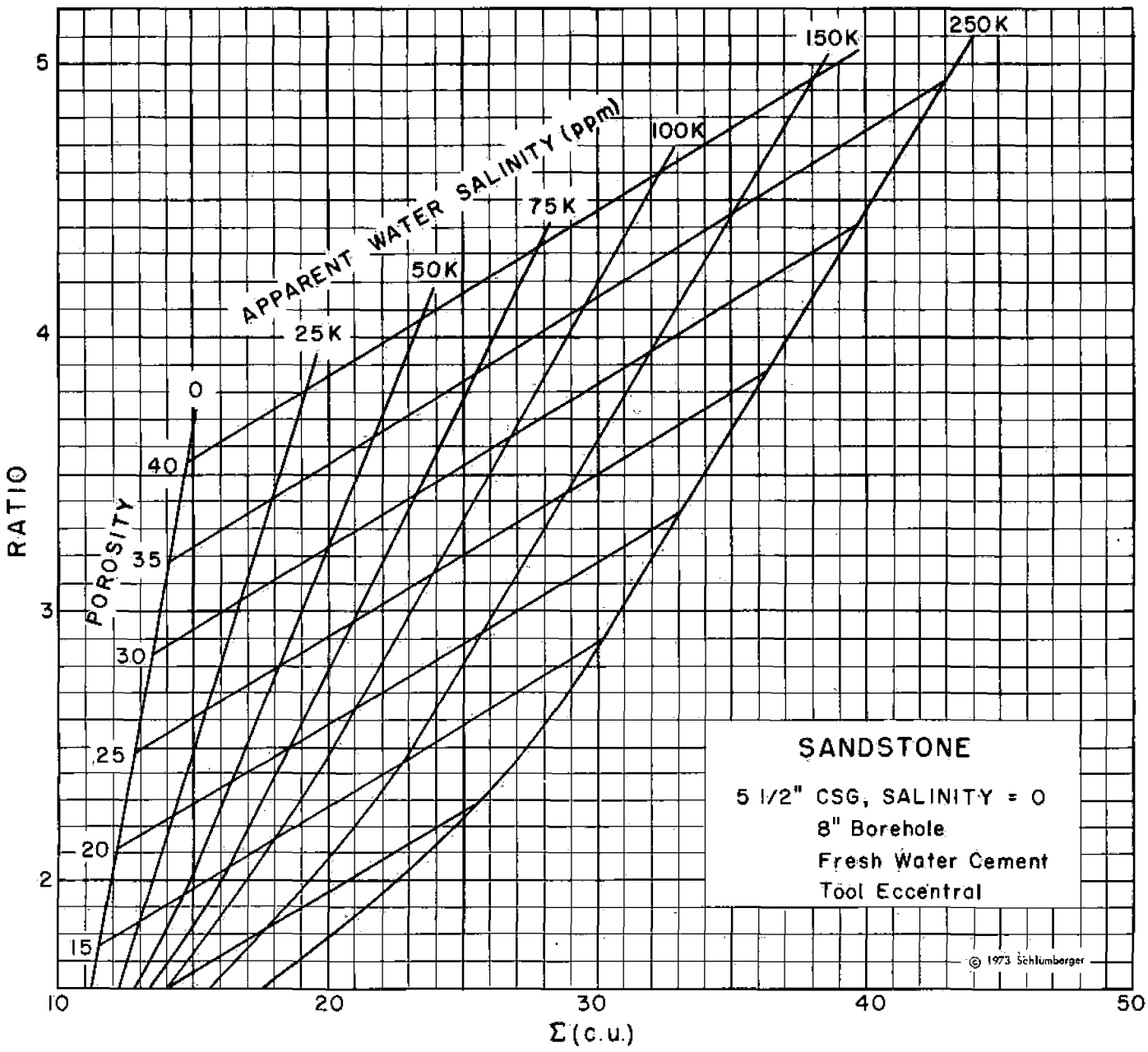

Fig. 7

POROSITY AND APPARENT WATER SALINITY DETERMINATION FROM DUAL SPACING TDT-K

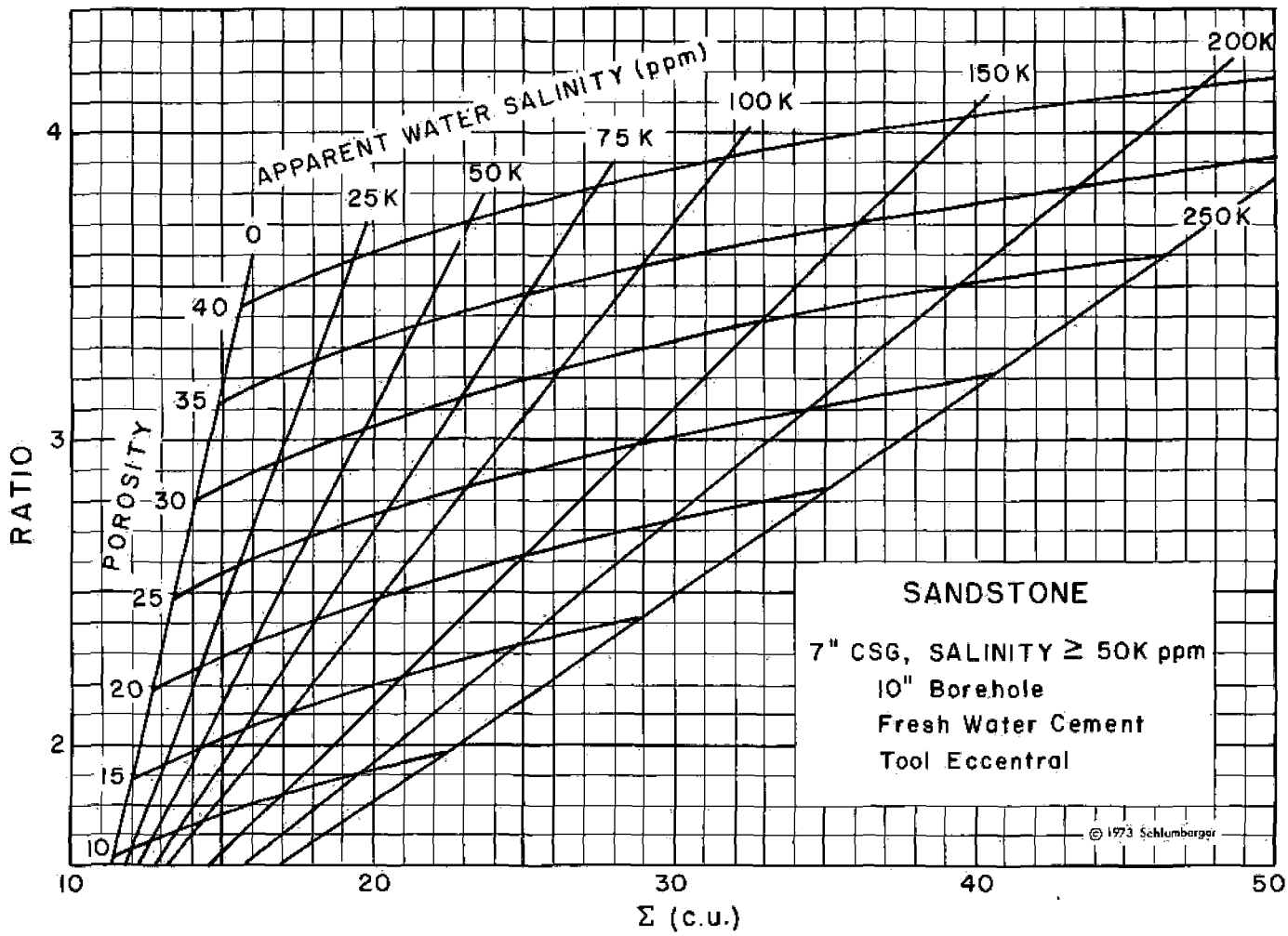

Fig. 8

POROSITY AND APPARENT WATER SALINITY DETERMINATION FROM DUAL SPACING TDT-K

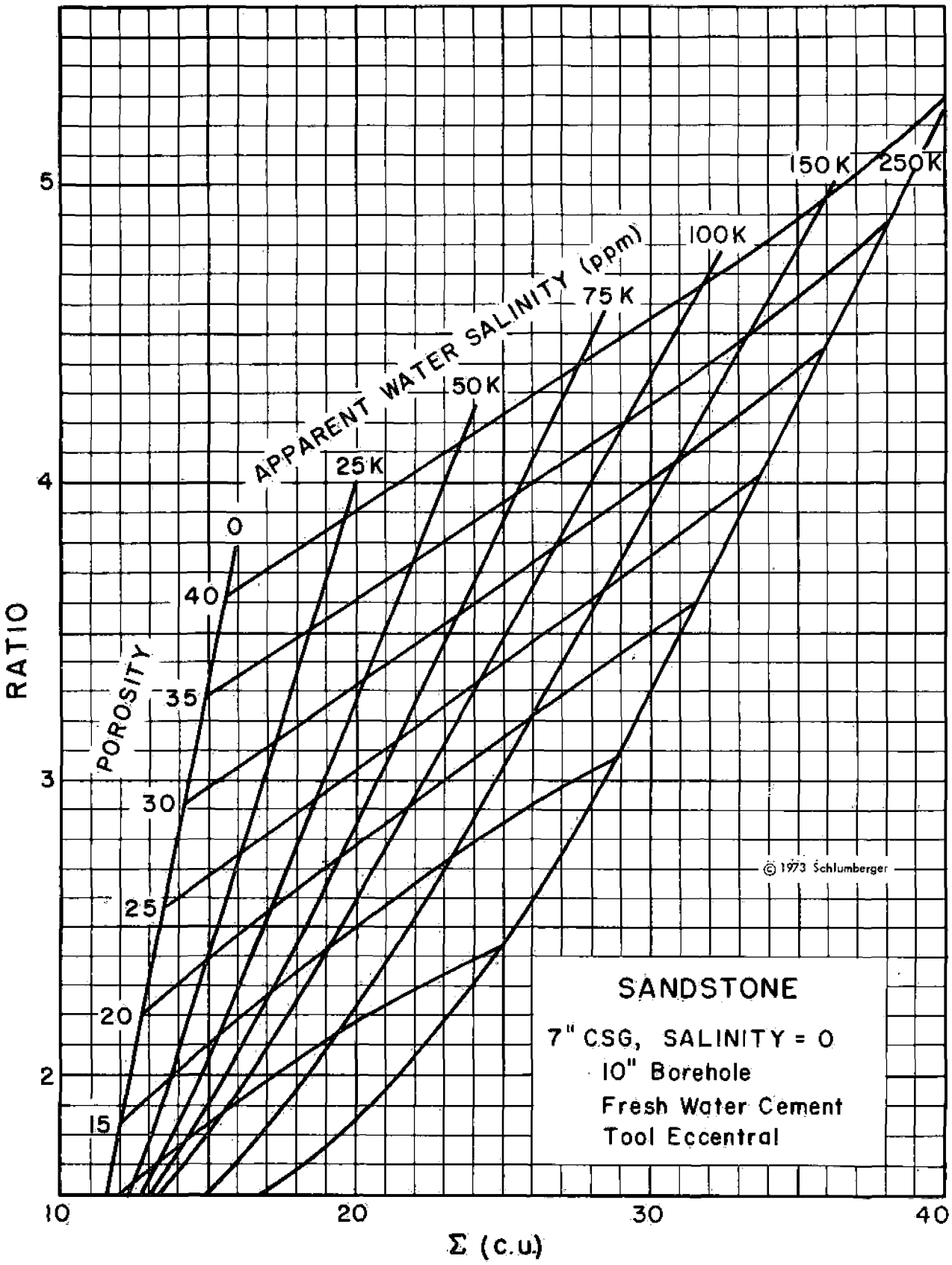

Fig. 9

POROSITY AND APPARENT WATER SALINITY DETERMINATION FROM DUAL SPACING TDT-K

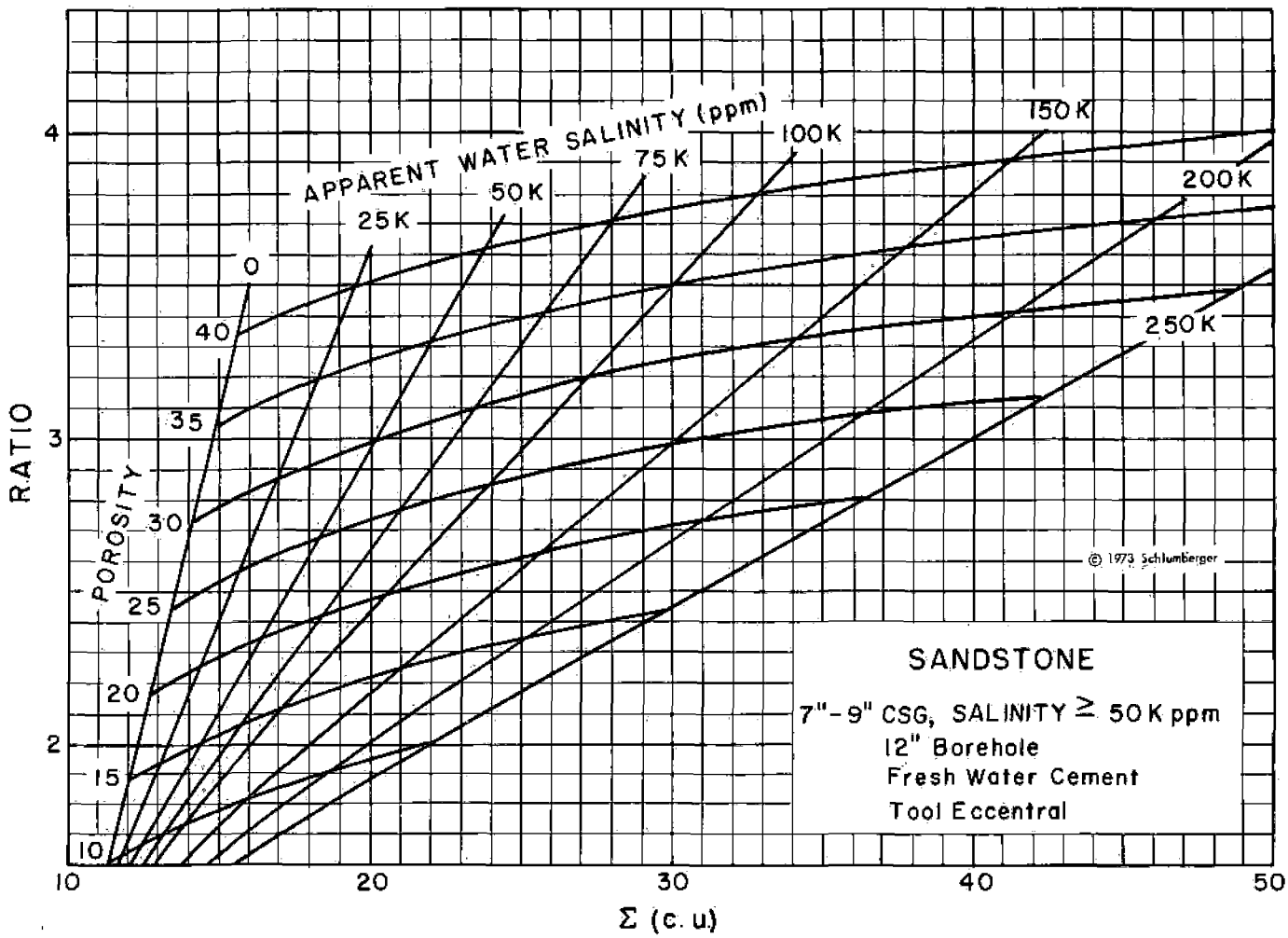

Fig. 10

POROSITY AND APPARENT WATER SALINITY DETERMINATION FROM DUAL SPACING TDT-K

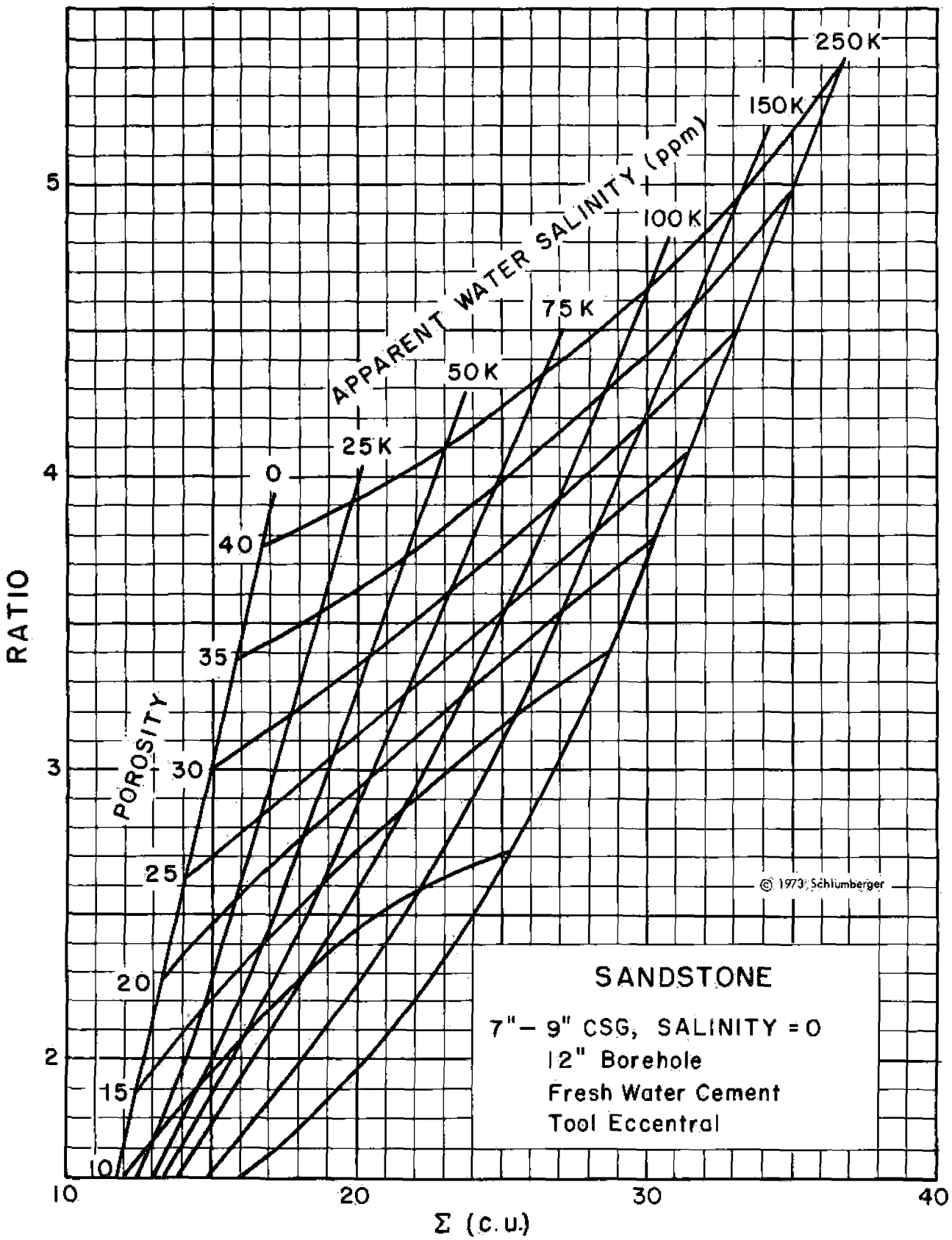

Fig. 11

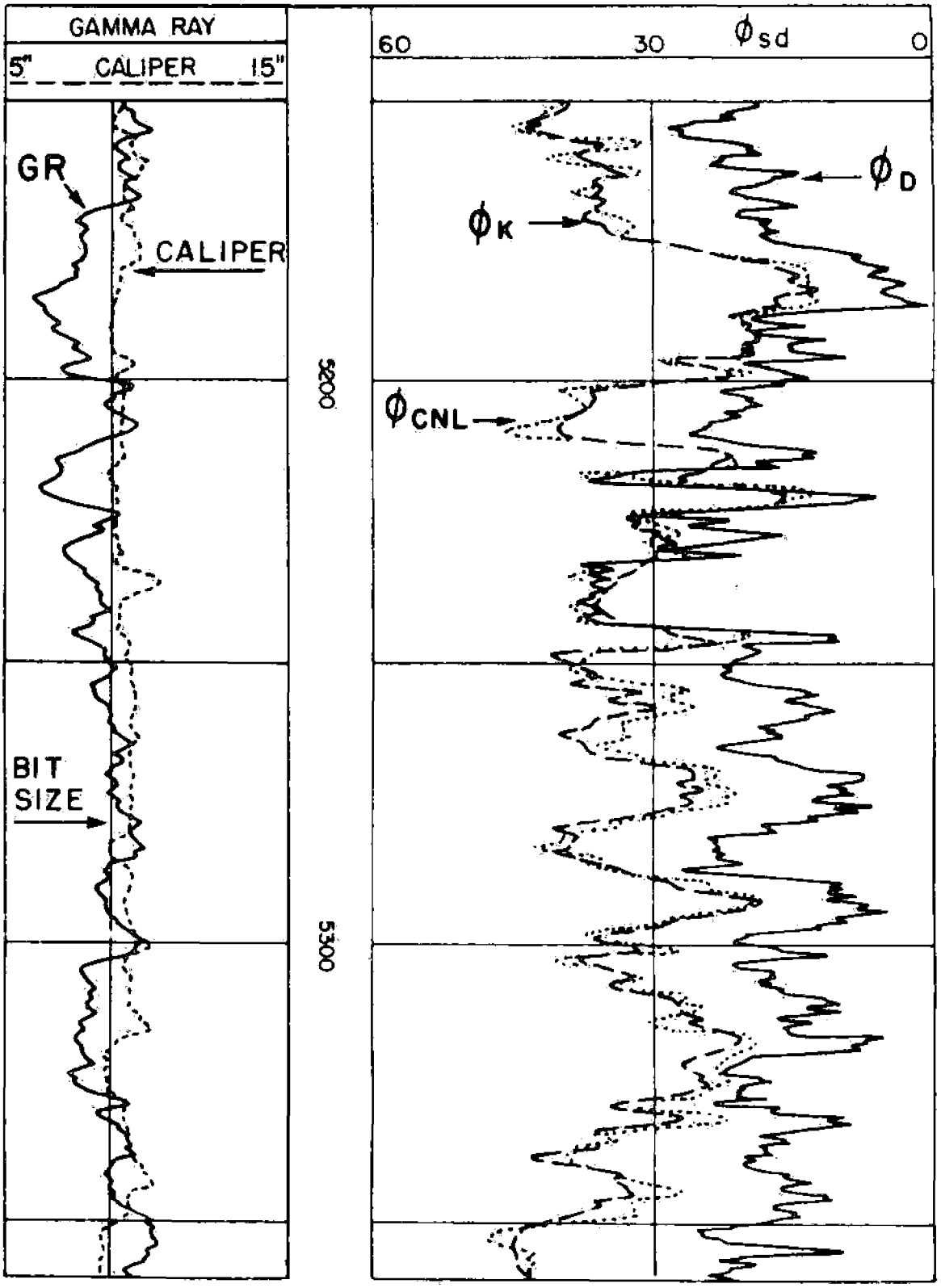
GAMMA RAY
5" CALIPER 15"
GR
CALIPER
BIT SIZE
5200
5300
60
30
ϕ_{sd}
0
ϕ_D
ϕ_K
ϕ_{CNL}

Fig. 12

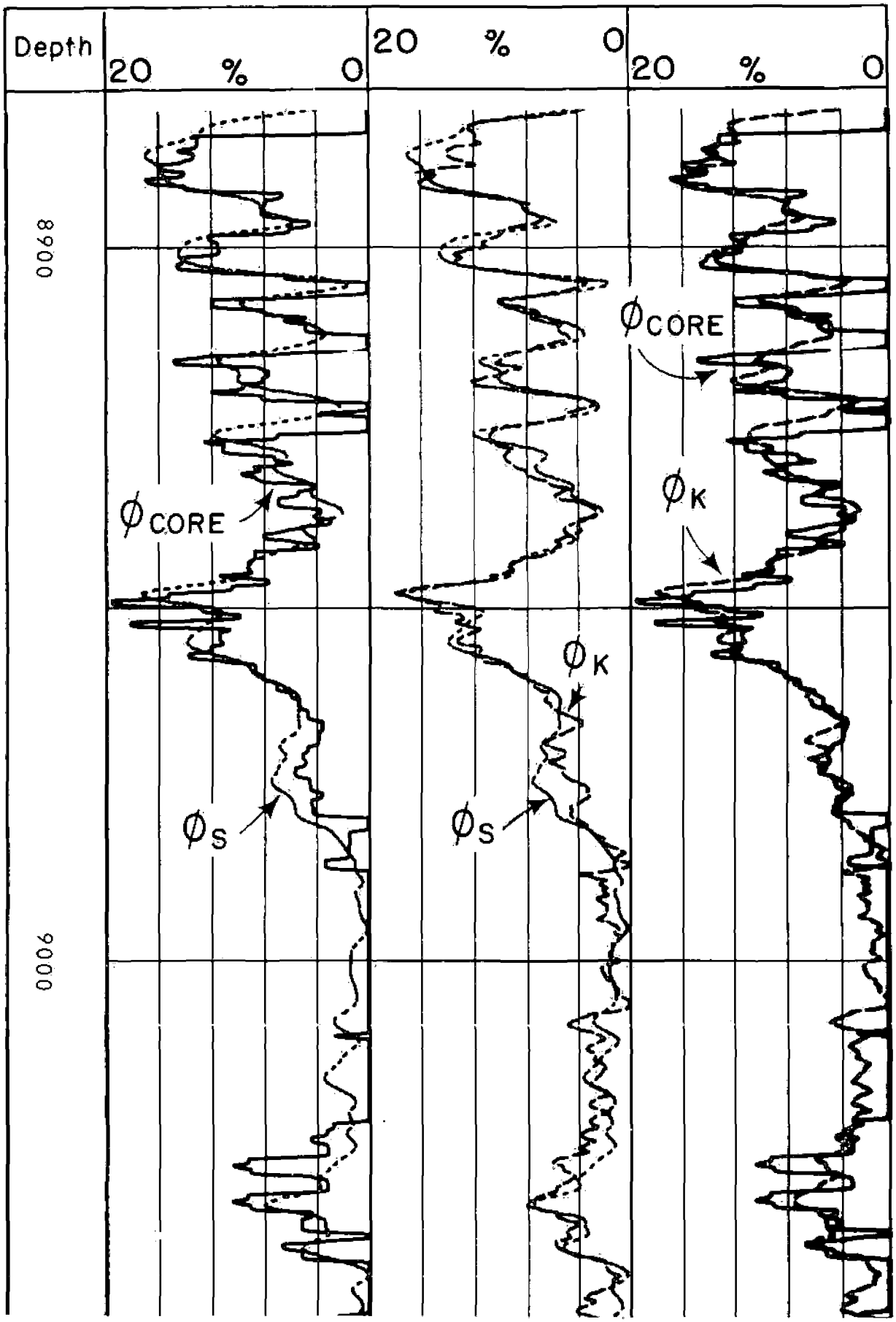

COMPARISON OF APPARENT POROSITY FROM CORE, SONIC, AND RATIO

Fig. 13

NEUTRON POROSITY EQUIVALENCE CURVES
Compensated Neutron Log (CNL)
or
TDT-K Porosity (ϕ_K)

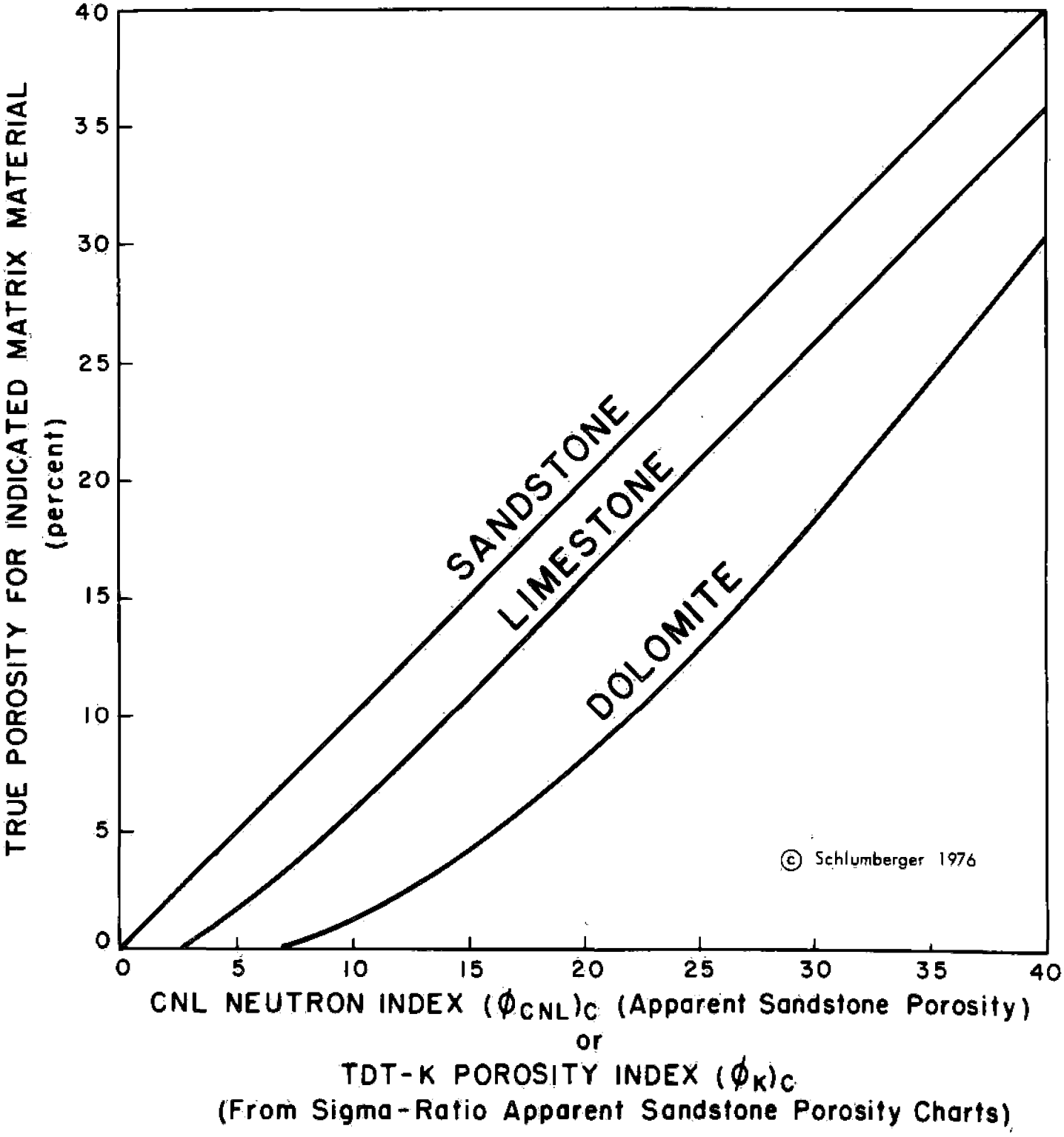

Fig. 14

TDT INTERPRETATION - SHALE % CHART

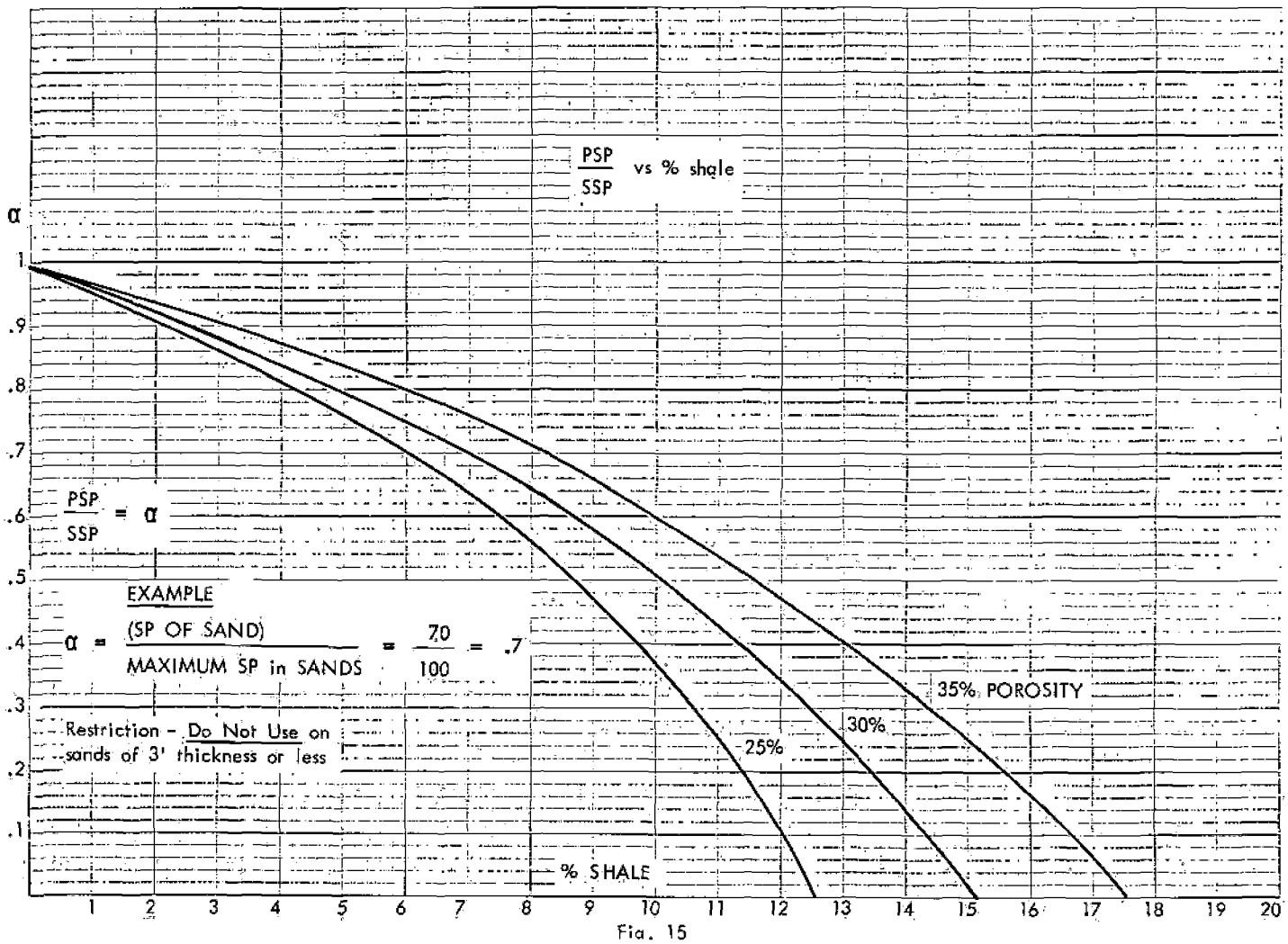

Fig. 15

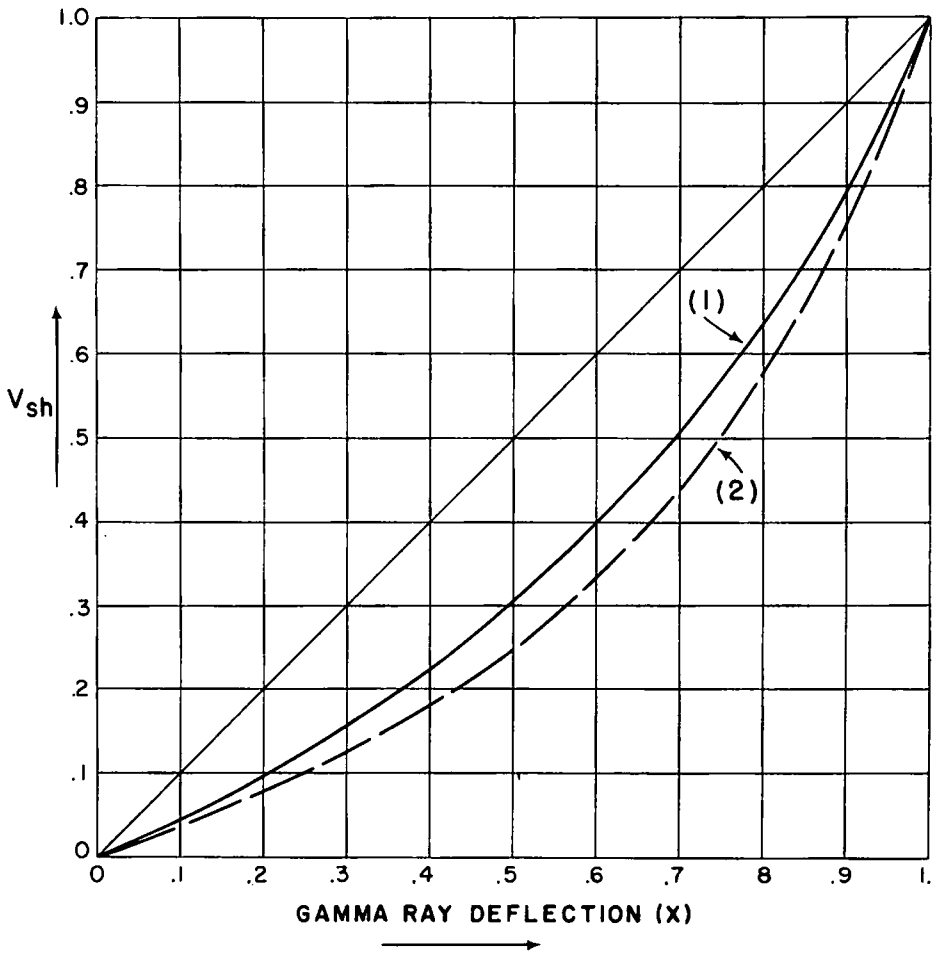

Fig. 16

Gamma Ray Deflection:

$$\frac{GR - GR_{clean}}{GR_{shale} - GR_{clean}} = X$$

(1) $V_{sh} = 1.7 - \sqrt{3.38 - (X + .7)^2}$

after Clavier et al, JPT - June 1971

(2) $V_{sh} = \frac{.5\,(X)}{1.5 - (X)}$

after Stieber, SPE 2961

Schlumberger

TDT LOG – HYDROCARBON CORRECTIONS

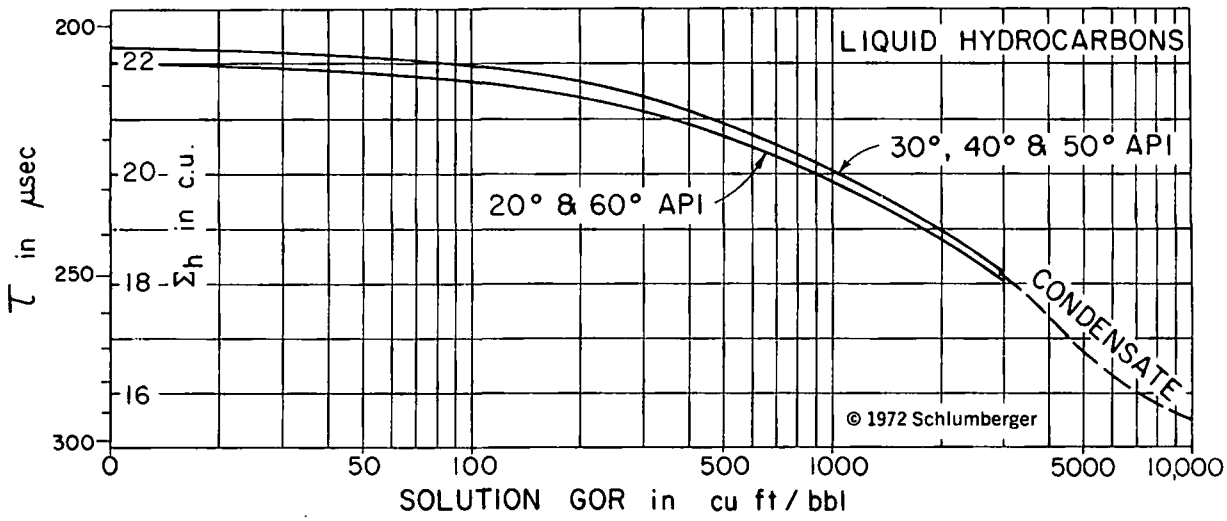

Fig. 17

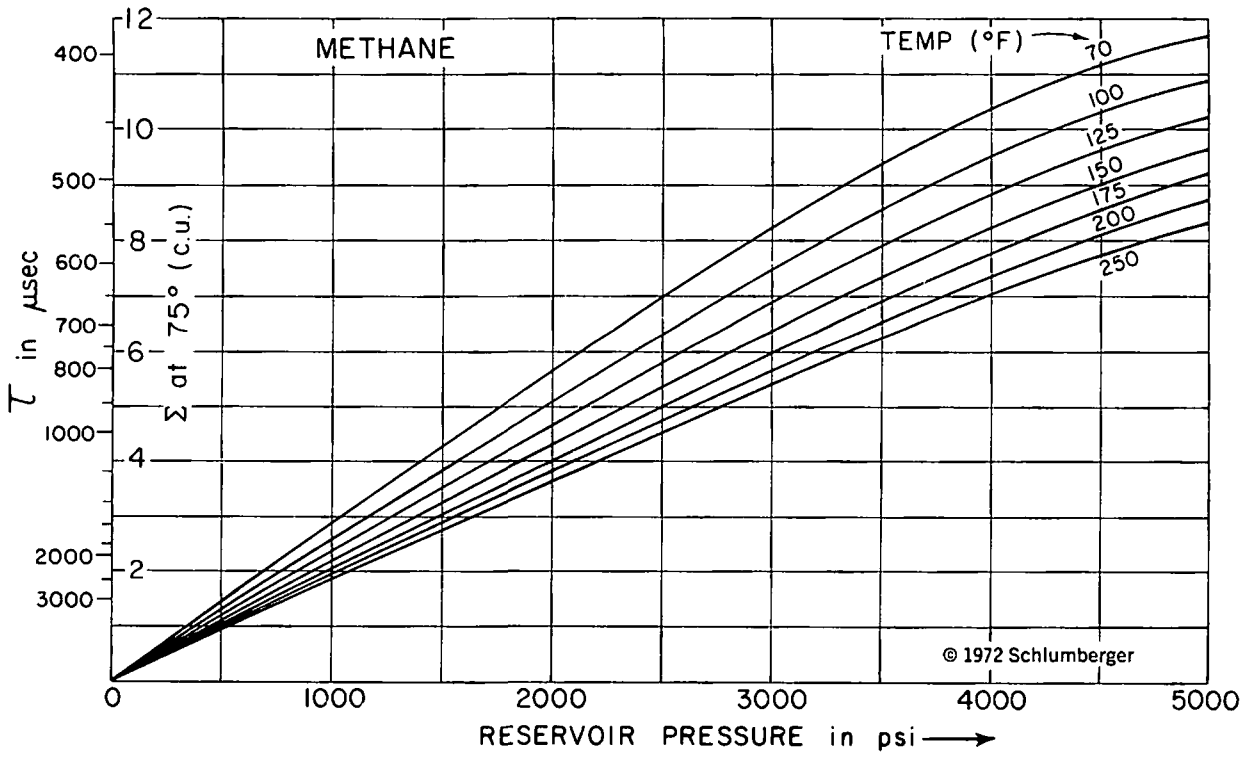

Fig. 18

Schlumberger

GRAPHICAL DETERMINATION OF S_w FROM THE TDT LOG (CLEAN FORMATIONS)

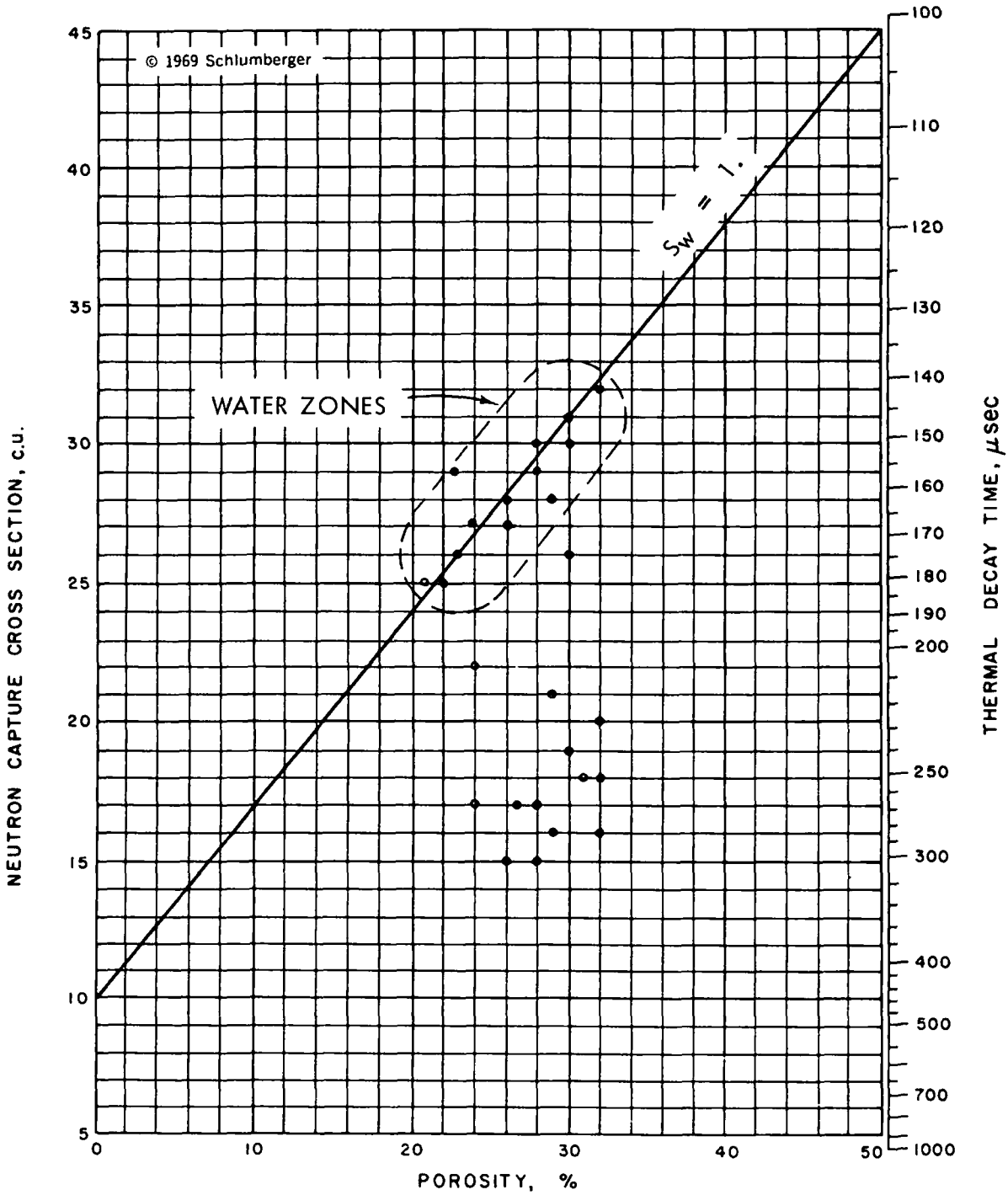

S_w may be determined graphically, in clean formations, by crossplotting Σ_{tog} versus ϕ. Σ_{ma} and Σ_w may be unknown, but are presumed to be constant over the interval studied. There must be some points for 100% water zones, and these must show a good variation in porosity. These water points define the S_w = 100% line; when extrapolated, this line intersects the zero-porosity axis at Σ_{ma}. The S_w = 0% line is drawn from Σ_{ma} at ϕ = 0% to Σ = ½ (Σ_{ma} + Σ_h) at ϕ = 50%. The vertical distance from S_w = 0% to S_w = 100% is divided linearly to find other lines of constant saturation. The effect of variable lithology is minimized if porosity is taken from a Neutron Log.

Fig. 19

Schlumberger

GRAPHICAL DETERMINATION OF S_W FROM THE TDT LOG (CLEAN FORMATIONS)

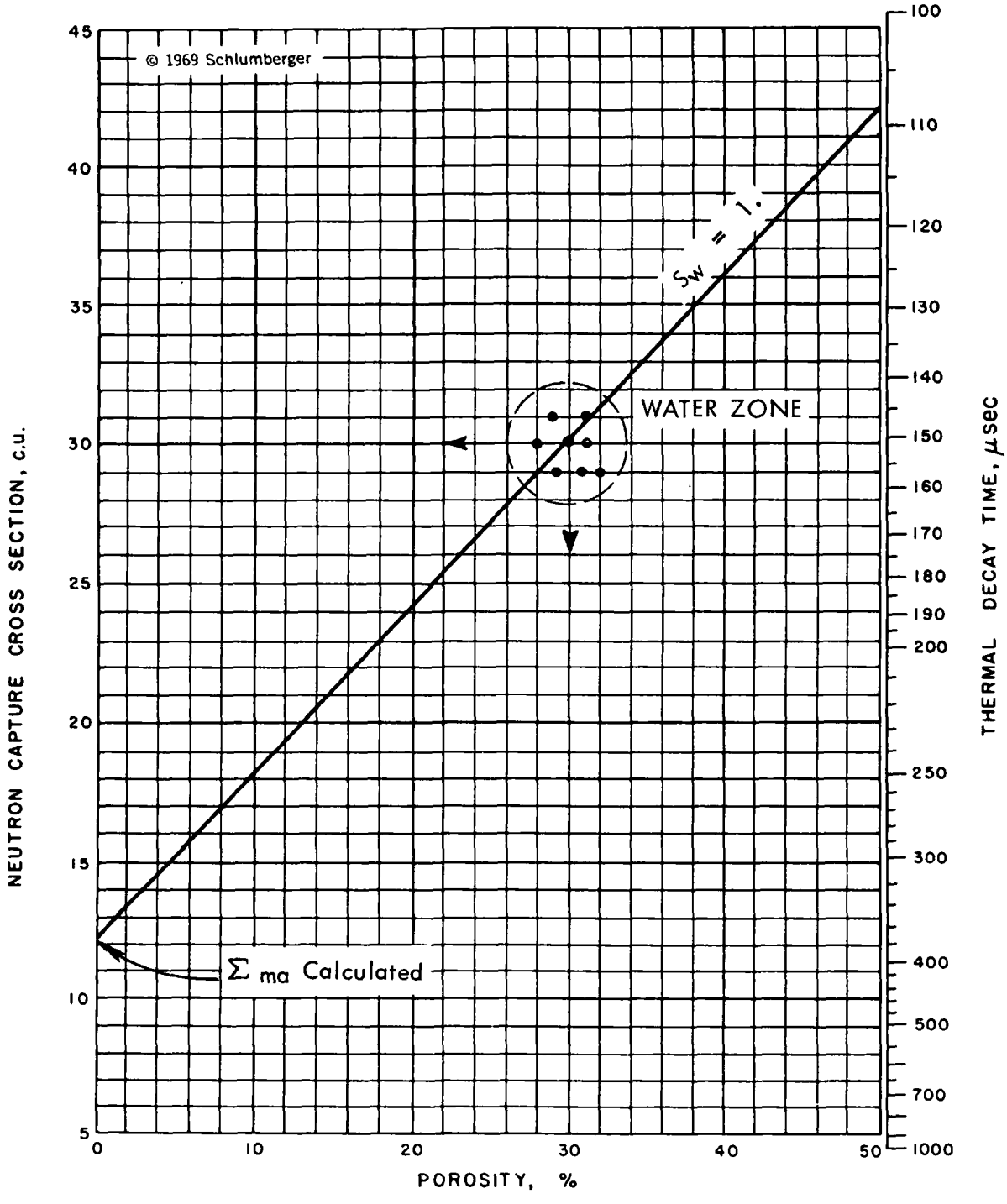

S_w may be determined graphically, in clean formations, by crossplotting Σ_{log} versus ϕ. Σ_{ma} and Σ_w may be unknown, but are presumed to be constant over the interval studied. There must be some points for 100% water zones, and these must show a good variation in porosity. These water points define the S_w = 100% line; when extrapolated, this line intersects the zero-porosity axis at Σ_{ma}. The S_w = 0% line is drawn from Σ_{ma} at ϕ = 0% to $\Sigma = \frac{1}{2}(\Sigma_{ma} + \Sigma_h)$ at ϕ = 50%. The vertical distance from S_w = 0% to S_w = 100% is divided linearly to find other lines of constant saturation. The effect of variable lithology is minimized if porosity is taken from a Neutron Log.

Fig. 20

TABLE 1

	DEPTH	POINT	Σ c.u.	COND mmhos/m	ϕ
ZONE A	9613	1	31.5	4600	.28
	9600	2	30	4000	.28
	9581	3	31	4900	.31
	9517	4	30	4000	.30
	9528	5	15	200	.31
	9230	6	29	3400	.31
ZONE B	8700	7	37	5600	.32
	8605	8	36	5000	.30
	8375	9	14	100	.29

Schlumberger

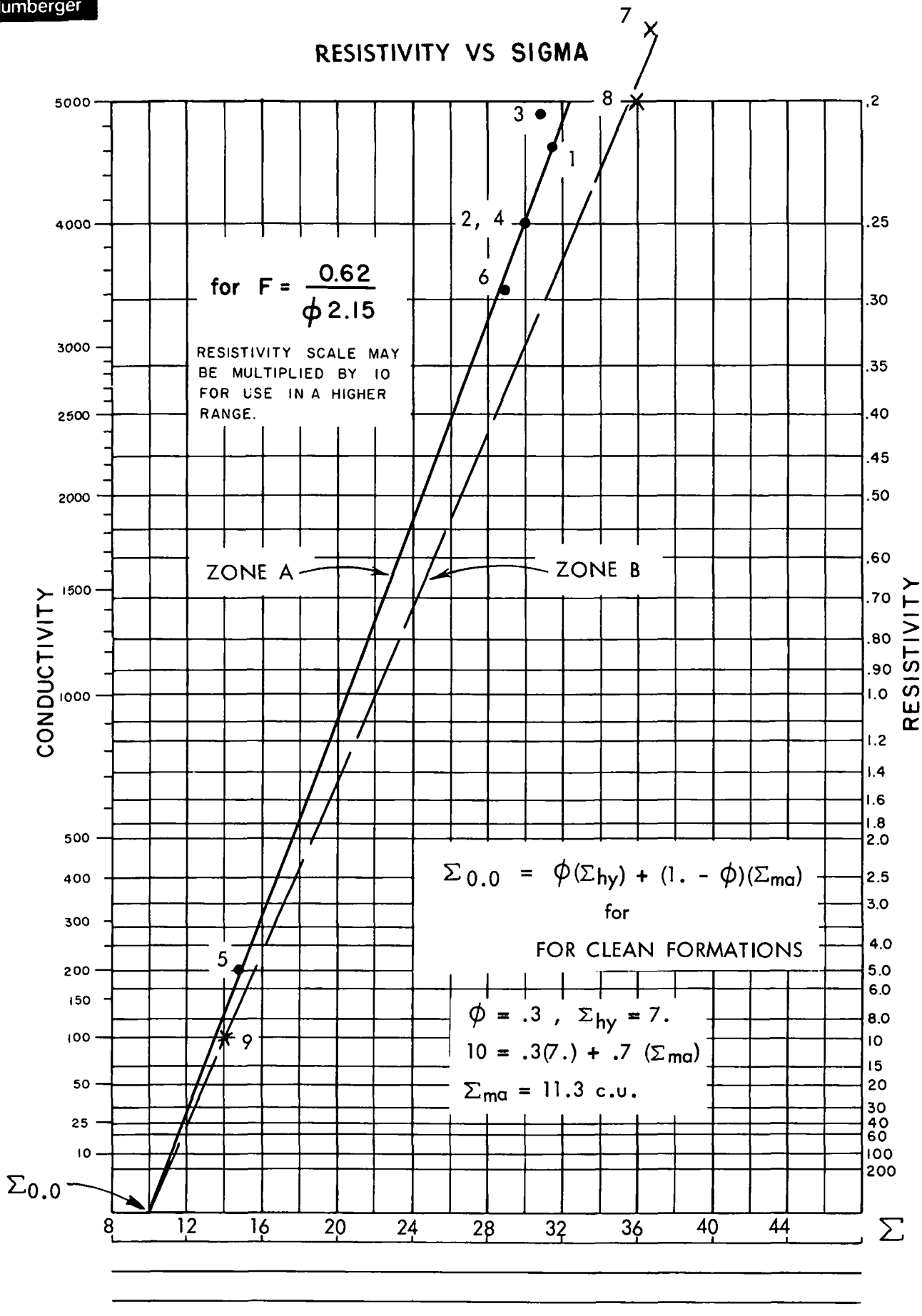

Fig. 21

Schlumberger

GRAPHICAL DETERMINATION OF S_w FROM THE TDT LOG (CLEAN FORMATIONS)

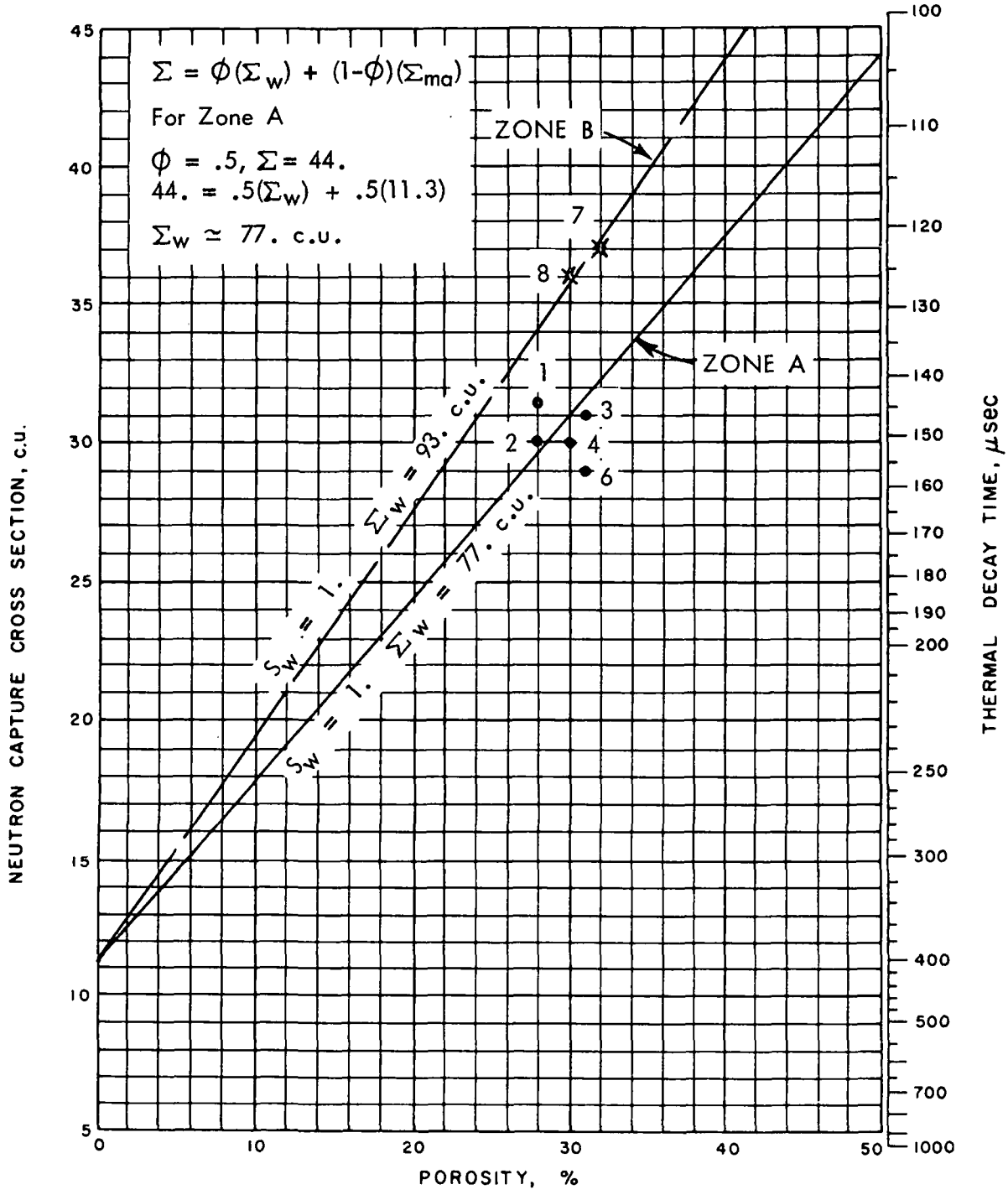

S_w may be determined graphically, in clean formations, by crossplotting Σ_{log} versus ϕ. Σ_{ma} and Σ_w may be unknown, but are presumed to be constant over the interval studied. There must be some points for 100% water zones, and these must show a good variation in porosity. These water points define the S_w = 100% line; when extrapolated, this line intersects the zero-porosity axis at Σ_{ma}. The S_w = 0% line is drawn from Σ_{ma} at ϕ = 0% to Σ = ½ (Σ_{ma} + Σ_h) at ϕ = 50%. The vertical distance from S_w = 0% to S_w = 100% is divided linearly to find other lines of constant saturation. The effect of variable lithology is minimized if porosity is taken from a Neutron Log.

Fig. 22

S_w DETERMINATION FROM THE TDT LOG

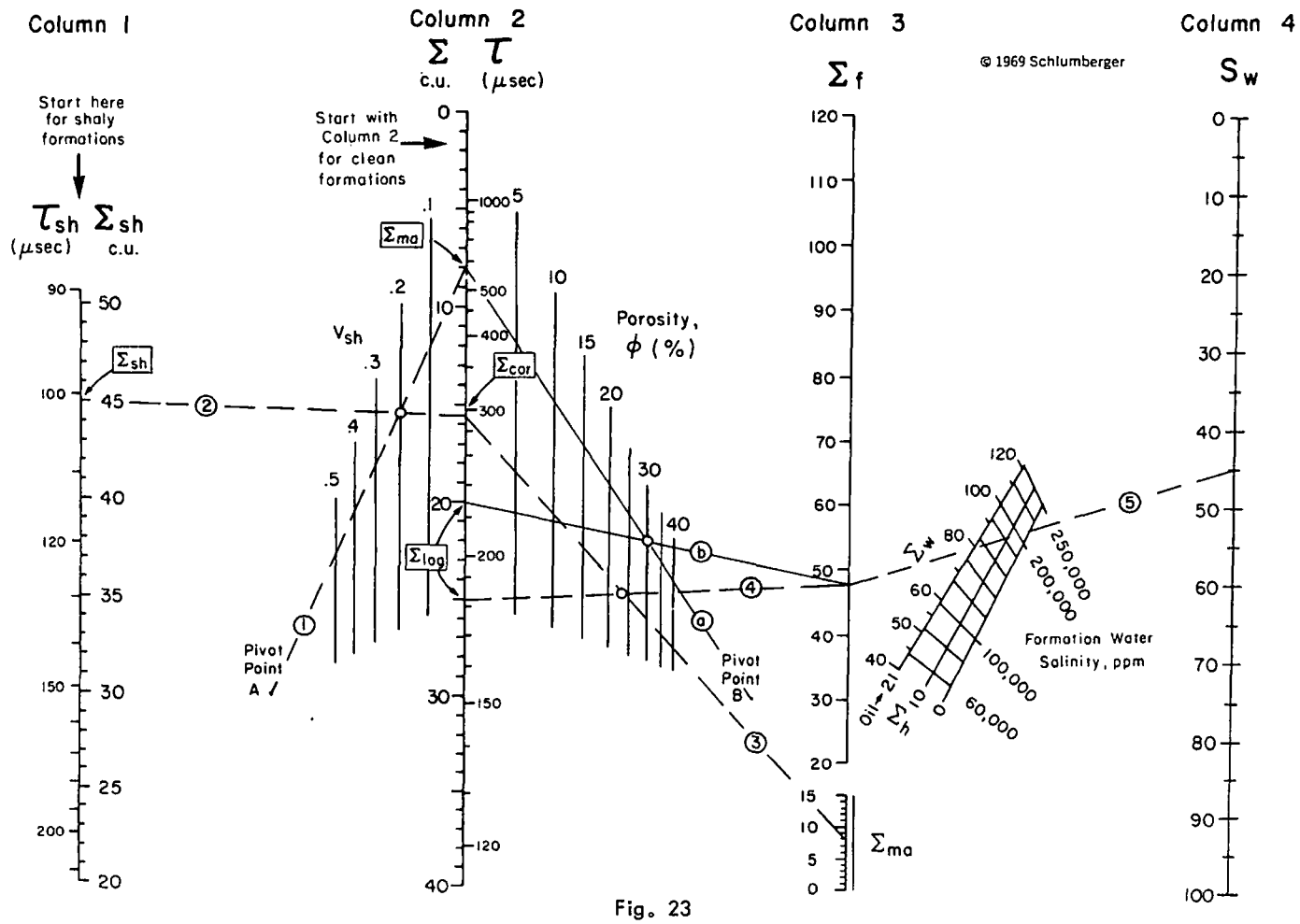

Fig. 23

Schlumberger

GRAPHICAL DETERMINATION OF S_w FROM THE TDT LOG (CLEAN FORMATIONS)

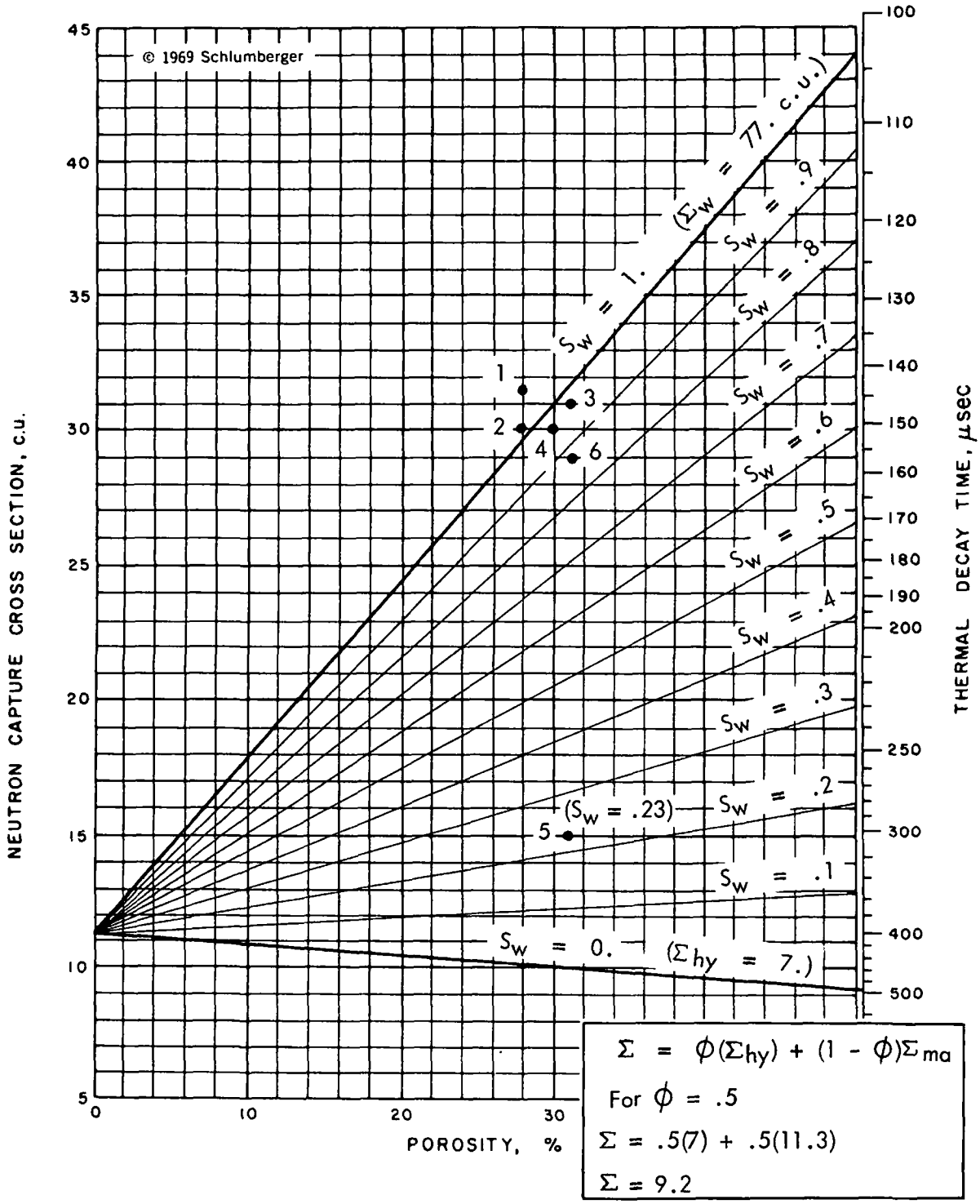

Fig. 24

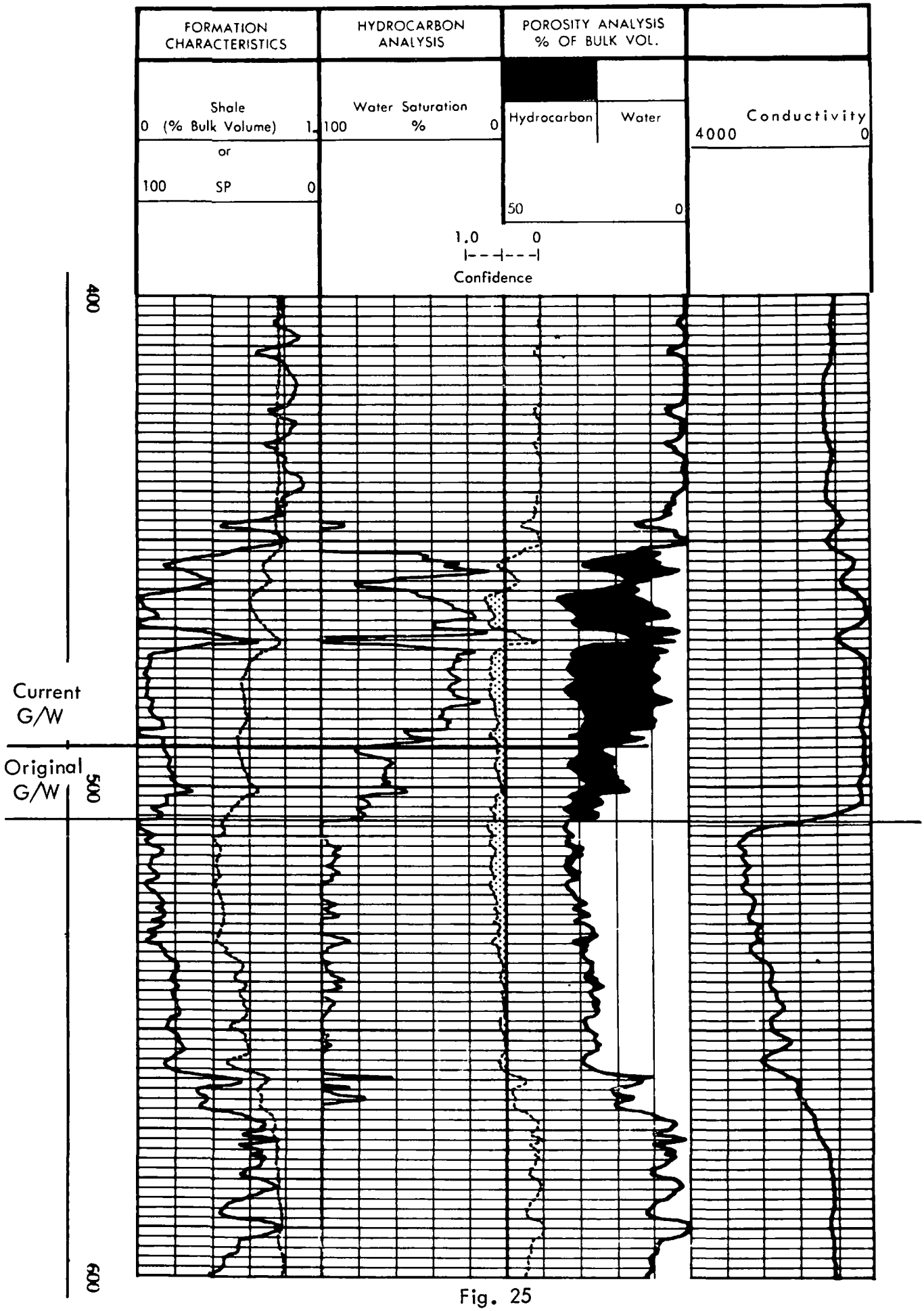
FORMATION CHARACTERISTICS
HYDROCARBON ANALYSIS
POROSITY ANALYSIS % OF BULK VOL.
Shale
0 (% Bulk Volume) 1
or
100 SP 0
Water Saturation
100 % 0
Hydrocarbon
Water
50 0
Conductivity
4000 0
1.0 0
Confidence
400
Current G/W
Original G/W
500
600

Fig. 25

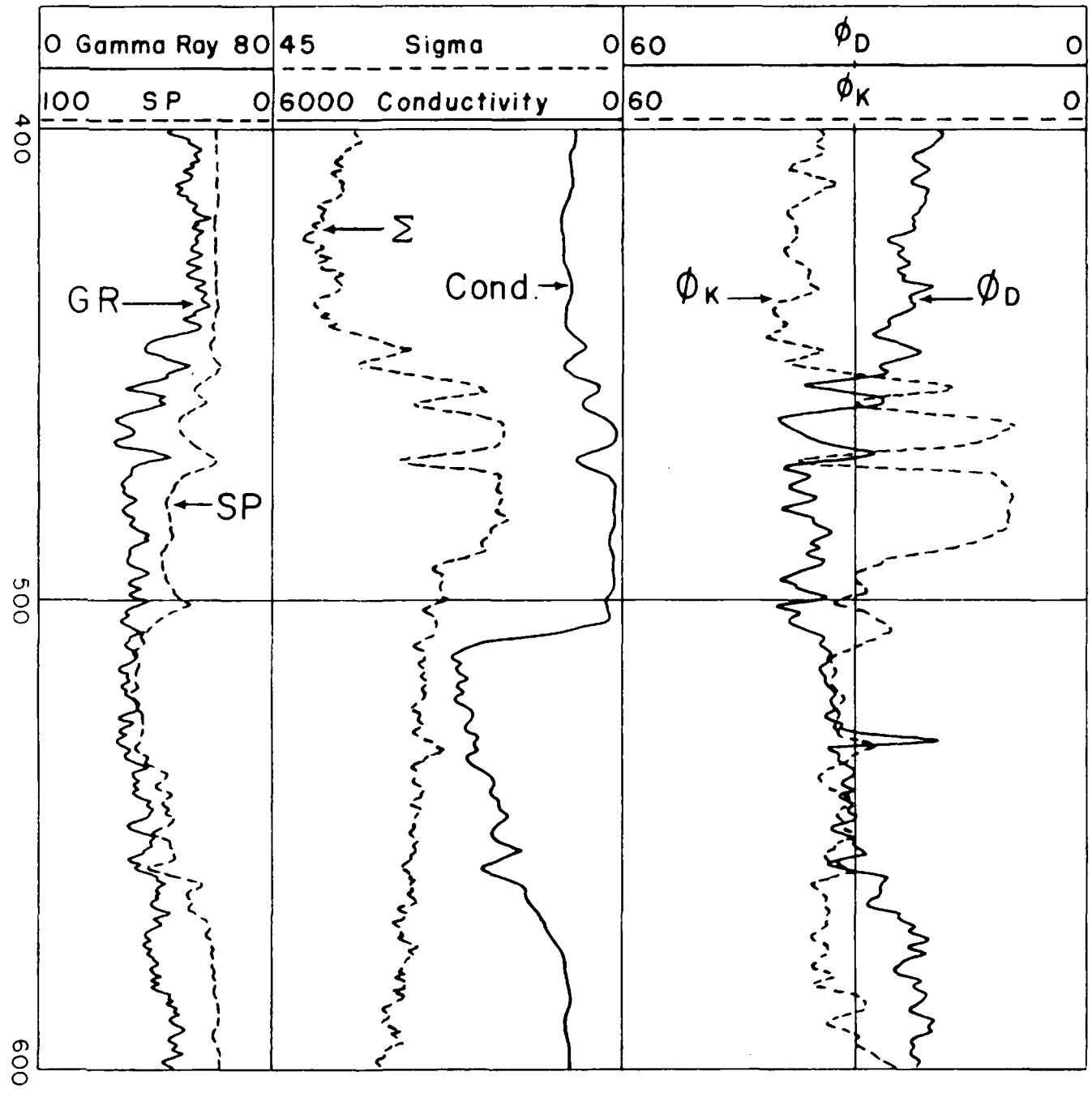
0 Gamma Ray 80
100 SP 0
45 Sigma 0
6000 Conductivity 0
60 ϕ_D 0
60 ϕ_K 0
400
500
600
GR
SP
Σ
Cond
ϕ_K
ϕ_D

Fig. 26

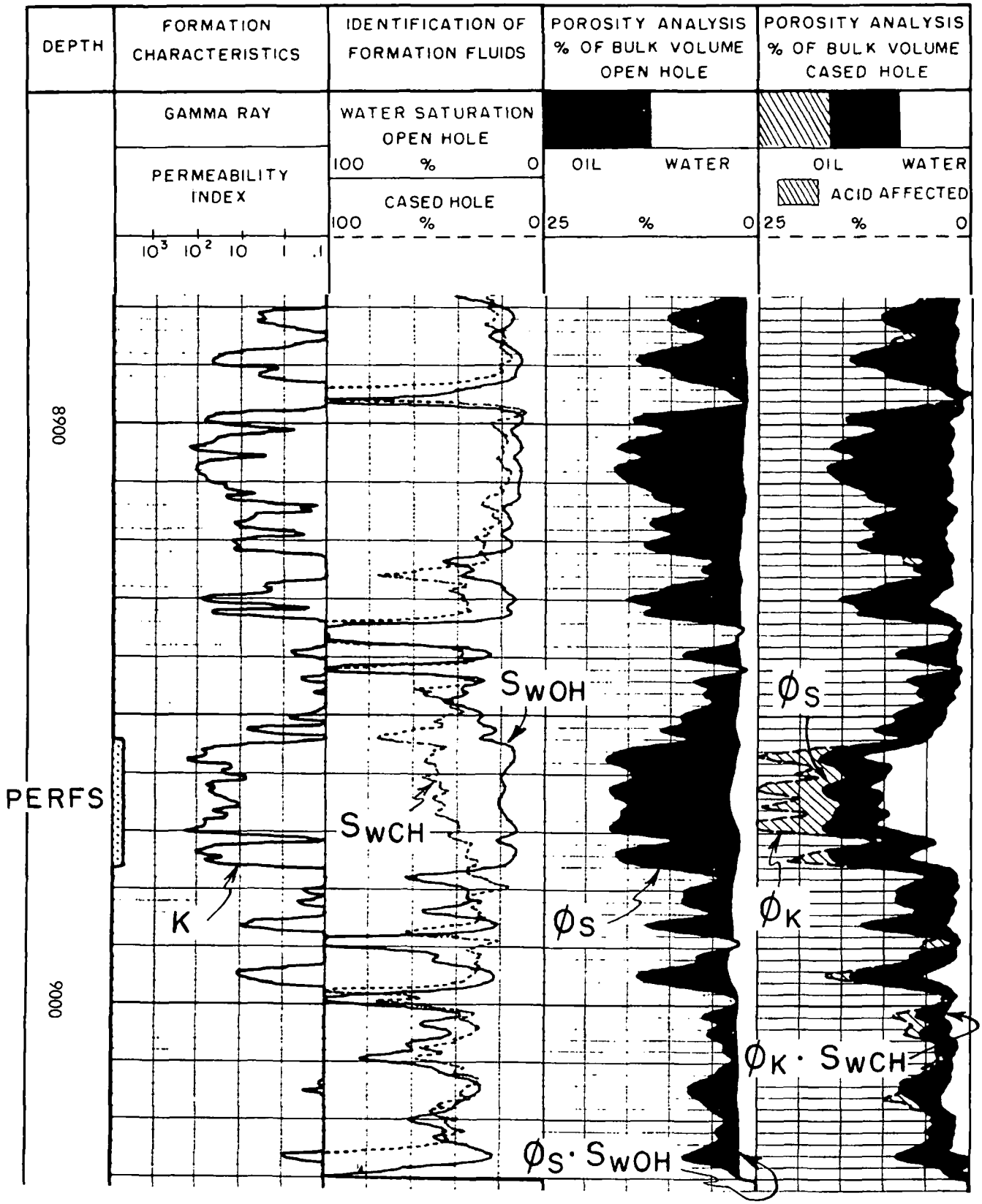
DEPTH
FORMATION CHARACTERISTICS
IDENTIFICATION OF FORMATION FLUIDS
POROSITY ANALYSIS % OF BULK VOLUME OPEN HOLE
POROSITY ANALYSIS % OF BULK VOLUME CASED HOLE
GAMMA RAY
PERMEABILITY INDEX
10^3 10^2 10 1 .1
WATER SATURATION OPEN HOLE
100 % 0
CASED HOLE
100 % 0
OIL WATER
25 % 0
OIL WATER
ACID AFFECTED
25 % 0
8900
9000
PERFS
K
S_{WCH}
S_{WOH}
ϕ_S
$\phi_S \cdot S_{WOH}$
ϕ_S
ϕ_K
$\phi_K \cdot S_{WCH}$

Fig. 27

Schlumberger

RESISTIVITY VS SIGMA

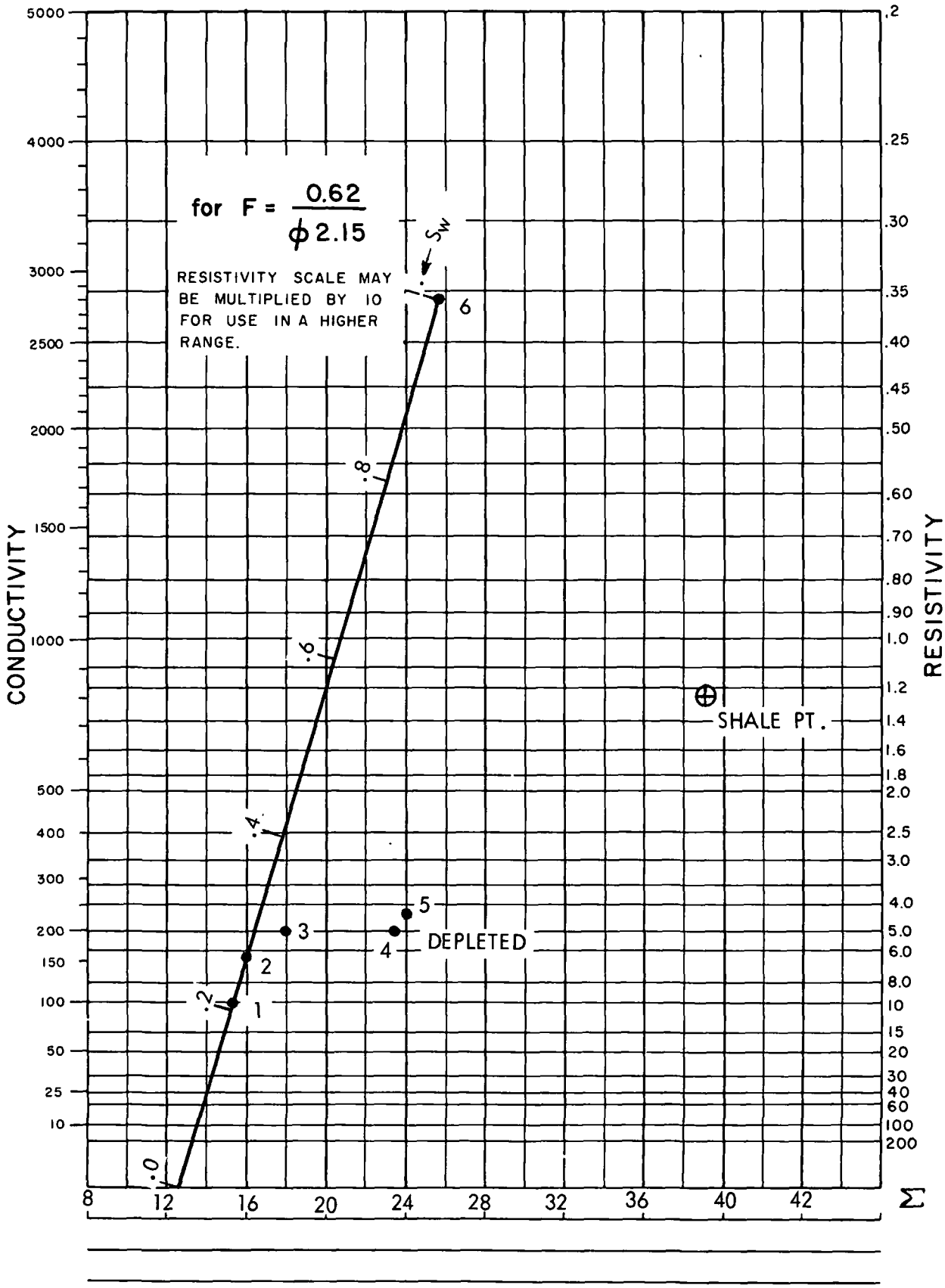

Fig. 28

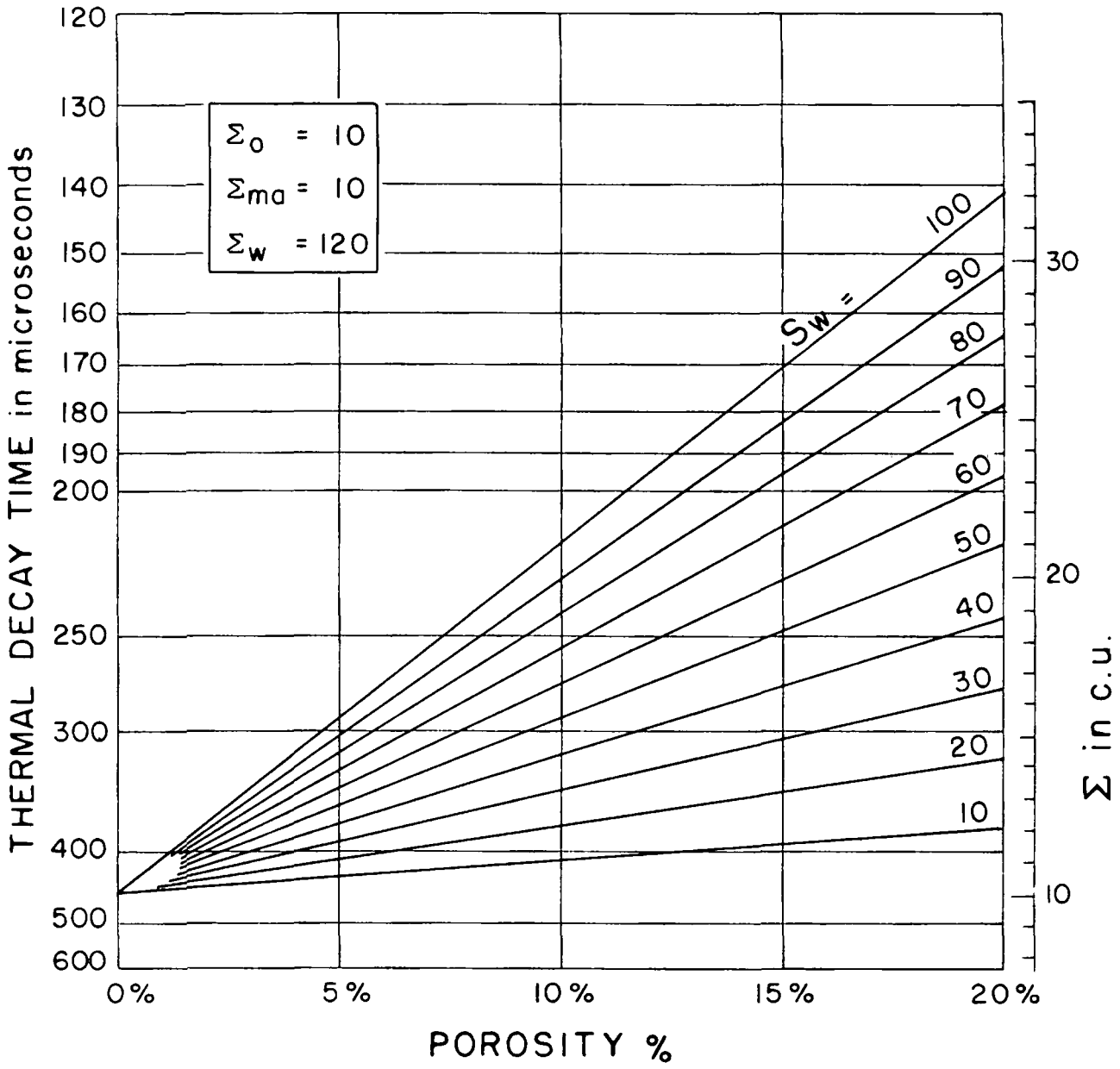
THERMAL DECAY TIME in microseconds
120
130
140
150
160
170
180
190
200
250
300
400
500
600
Σ_o = 10
Σ_{ma} = 10
Σ_w = 120
Sw =
100
90
80
70
60
50
40
30
20
10
0%
5%
10%
15%
20%
POROSITY %
30
20
10
Σ in c.u.

Fig. 29

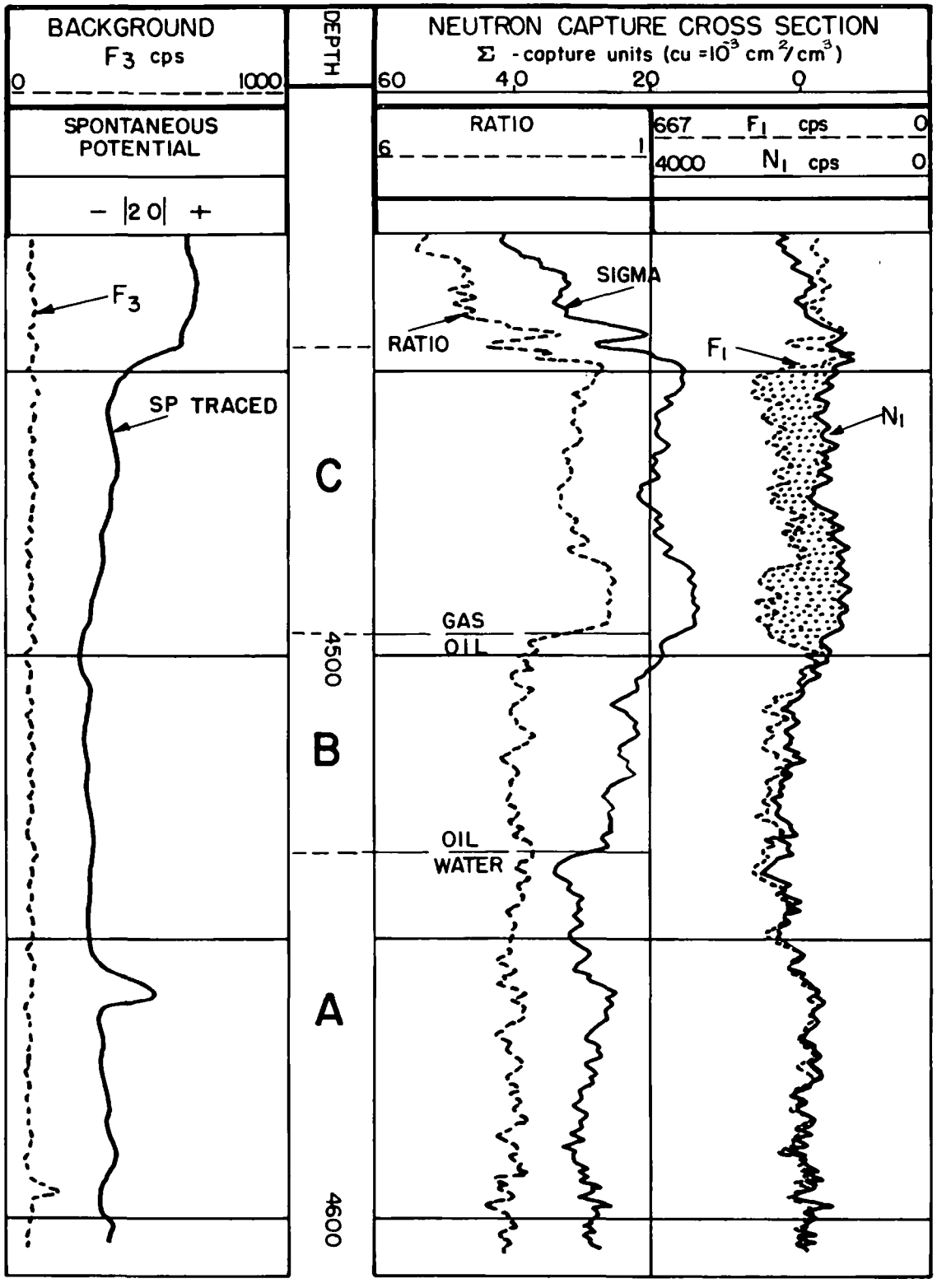
BACKGROUND
F3 cps
0
1000
SPONTANEOUS POTENTIAL
- |20| +
F3
SP TRACED
DEPTH
C
4500
B
A
4600
NEUTRON CAPTURE CROSS SECTION
Σ - capture units (cu =10^-3 cm^2/cm^3)
60
40
20
0
RATIO
6
1
667
F1 cps
0
4000
N1 cps
0
SIGMA
RATIO
F1
N1
GAS
OIL
OIL
WATER

Fig. 30

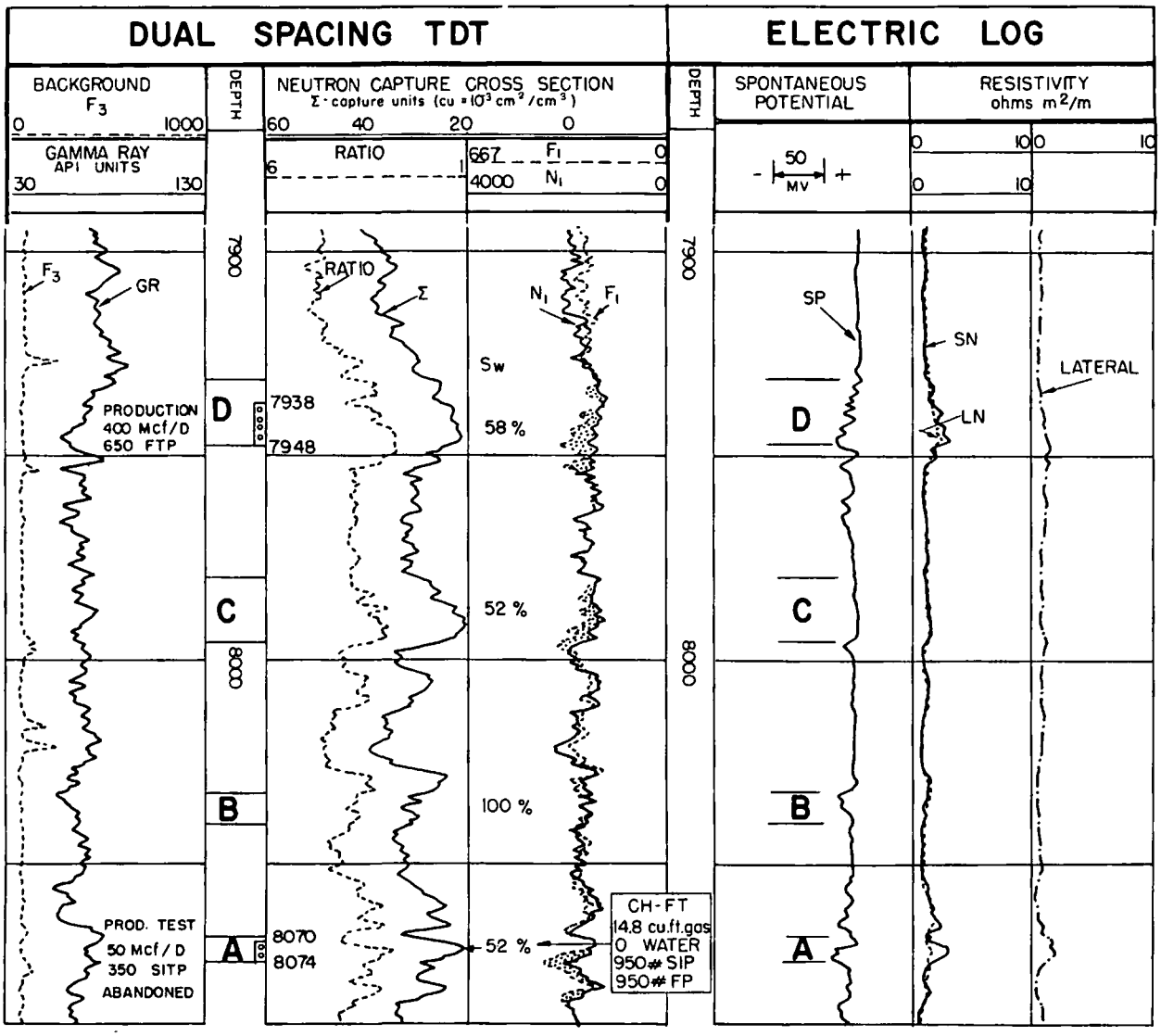
DUAL SPACING TDT
ELECTRIC LOG
BACKGROUND
F3
0
1000
GAMMA RAY
API UNITS
30
130
DEPTH
NEUTRON CAPTURE CROSS SECTION
Σ - capture units (cu = 10³ cm² / cm³)
60
40
20
0
RATIO
6
1
667
F1
0
4000
N1
0
DEPTH
SPONTANEOUS POTENTIAL
50
MV
RESISTIVITY
ohms m²/m
0
10
0
10
0
10
7900
8000
F3
GR
RATIO
Σ
N1
F1
Sw
SP
SN
LN
LATERAL
PRODUCTION
400 Mcf/D
650 FTP
D
7938
7948
58 %
C
52 %
B
100 %
PROD. TEST
50 Mcf/D
350 SITP
ABANDONED
A
8070
8074
52 %
CH-FT
14.8 cu.ft.gas
0 WATER
950# SIP
950# FP

Fig. 31

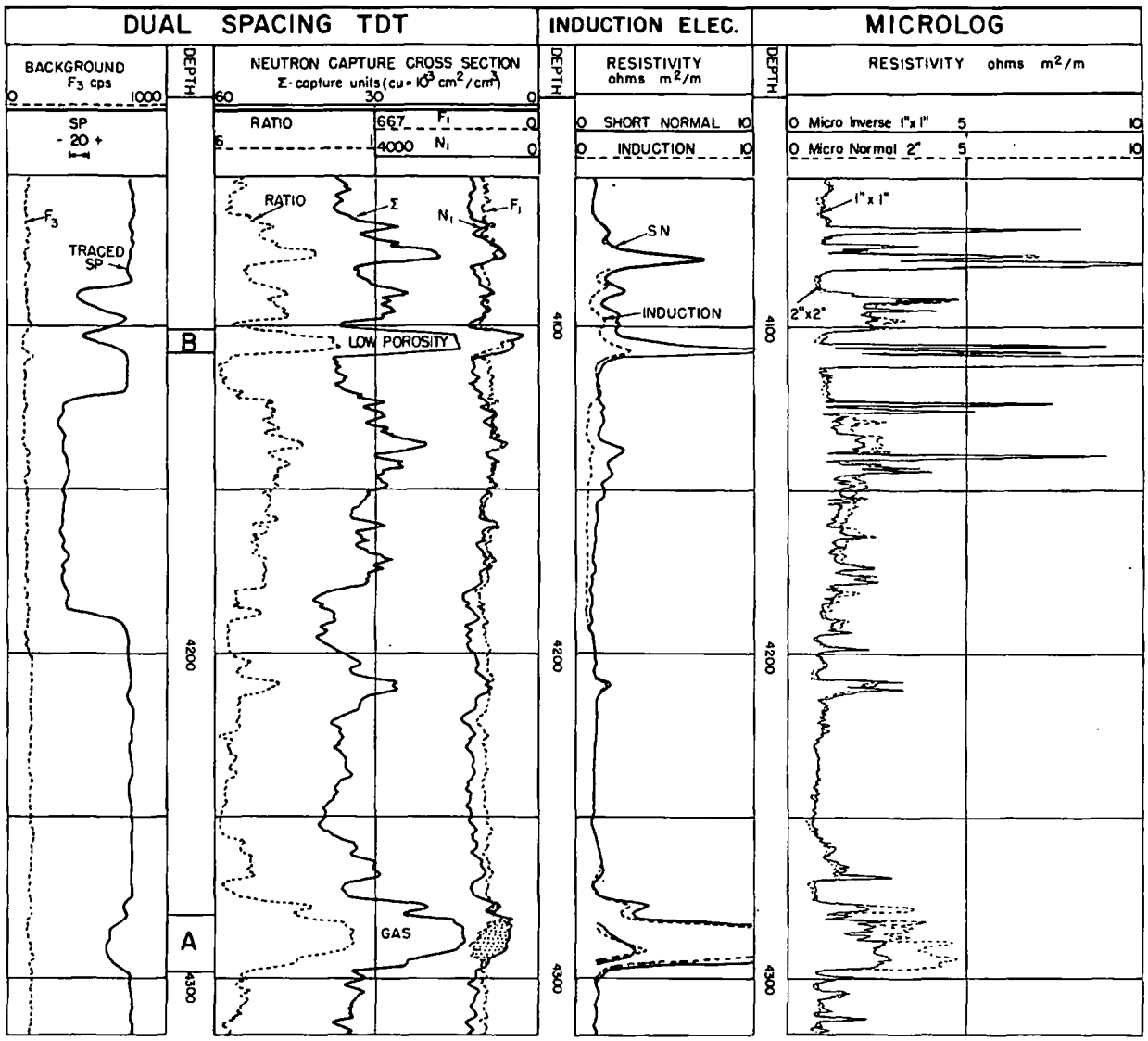
DUAL SPACING TDT
INDUCTION ELEC.
MICROLOG
BACKGROUND
F3 cps
0
1000
DEPTH
NEUTRON CAPTURE CROSS SECTION
Σ-capture units (cu = 10³ cm²/cm³)
60
30
0
SP
- 20 +
RATIO
6
667
F1
4000
N1
0
RESISTIVITY
ohms m²/m
0 SHORT NORMAL 10
0 INDUCTION 10
RESISTIVITY ohms m²/m
0 Micro Inverse 1"x1" 5 10
0 Micro Normal 2" 5 10
F3
TRACED SP
RATIO
Σ
N1
F1
SN
INDUCTION
1"x1"
2"x2"
B
LOW POROSITY
A
GAS
4100
4200
4300

Fig. 32

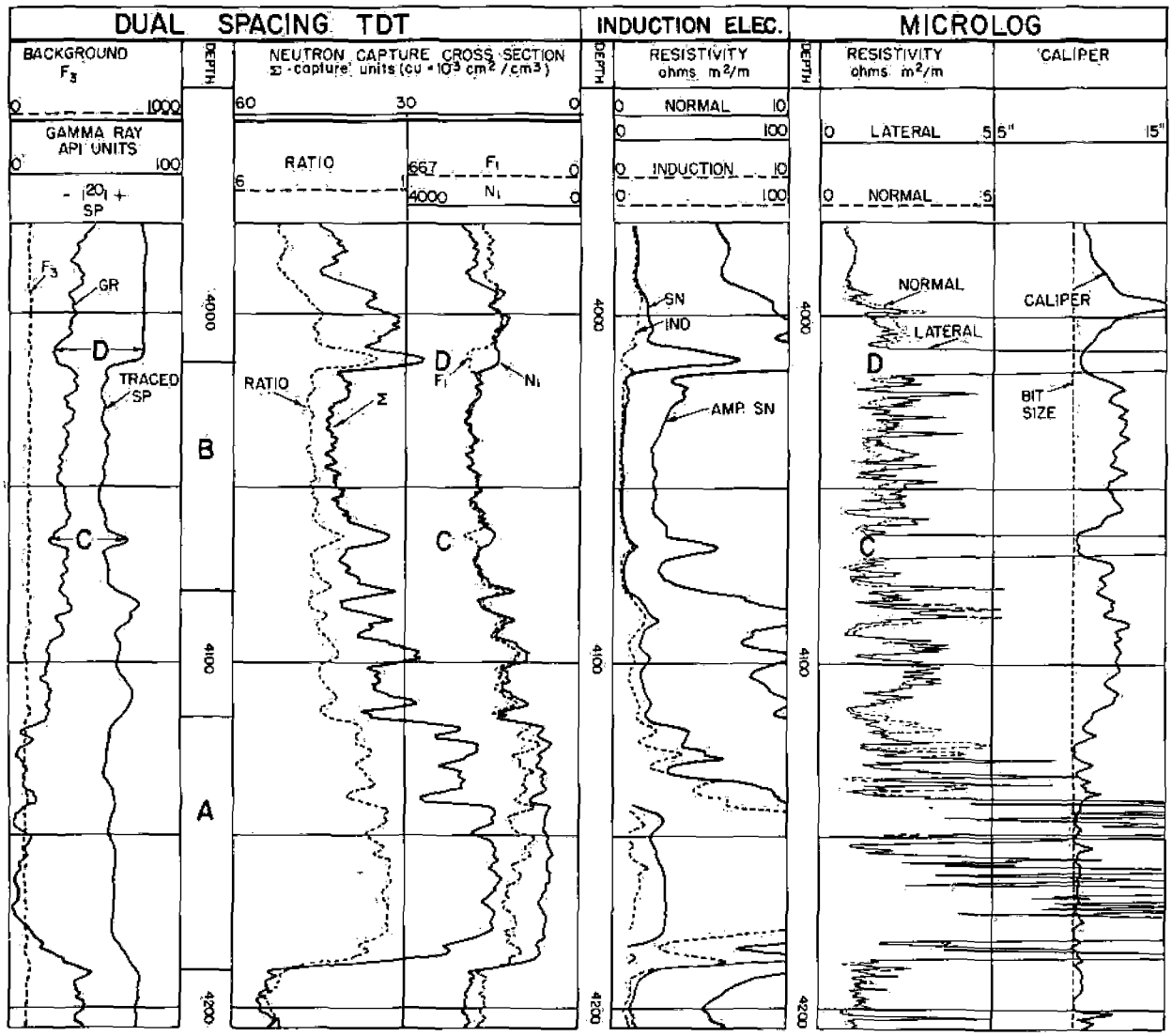
DUAL SPACING TDT
INDUCTION ELEC.
MICROLOG
BACKGROUND
F3
0
1000
GAMMA RAY
API UNITS
0
100
- 20 +
SP
DEPTH
NEUTRON CAPTURE CROSS SECTION
Σ - capture units (cu = 10³ cm² /cm³)
60
30
0
RATIO
6
1
667
F1
0
4000
N1
0
RESISTIVITY
ohms m²/m
0
NORMAL
10
0
100
0
INDUCTION
10
0
100
RESISTIVITY
ohms m²/m
0
LATERAL
5
0
NORMAL
5
CALIPER
5"
15"
F3
GR
D
TRACED
SP
C
B
A
RATIO
Σ
D
F1
N1
C
SN
IND
AMP SN
NORMAL
LATERAL
D
C
CALIPER
BIT
SIZE
4000
4100
4200

Fig. 33

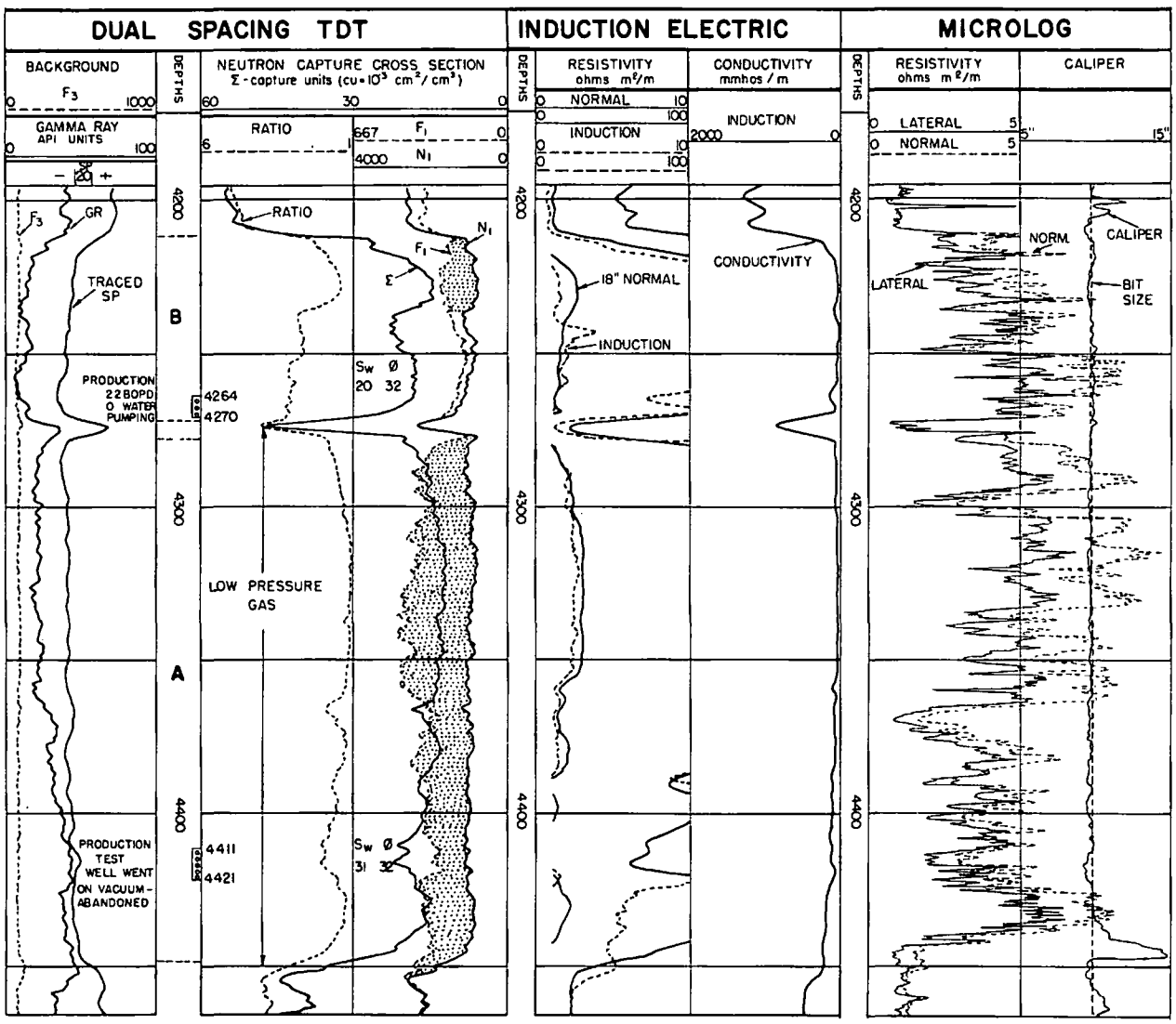
DUAL SPACING TDT
INDUCTION ELECTRIC
MICROLOG
BACKGROUND
F3
GAMMA RAY
API UNITS
GR
TRACED SP
PRODUCTION
22 BOPD
0 WATER
PUMPING
PRODUCTION
TEST
WELL WENT
ON VACUUM-
ABANDONED
DEPTHS
NEUTRON CAPTURE CROSS SECTION
Σ - capture units (cu • 10³ cm²/cm³)
RATIO
F1
N1
Σ
Sw Ø
4264
4270
4411
4421
LOW PRESSURE
GAS
B
A
RESISTIVITY
ohms m²/m
NORMAL
INDUCTION
CONDUCTIVITY
mmhos / m
18" NORMAL
CALIPER
LATERAL
NORM
BIT
SIZE
4200
4300
4400

Fig. 34

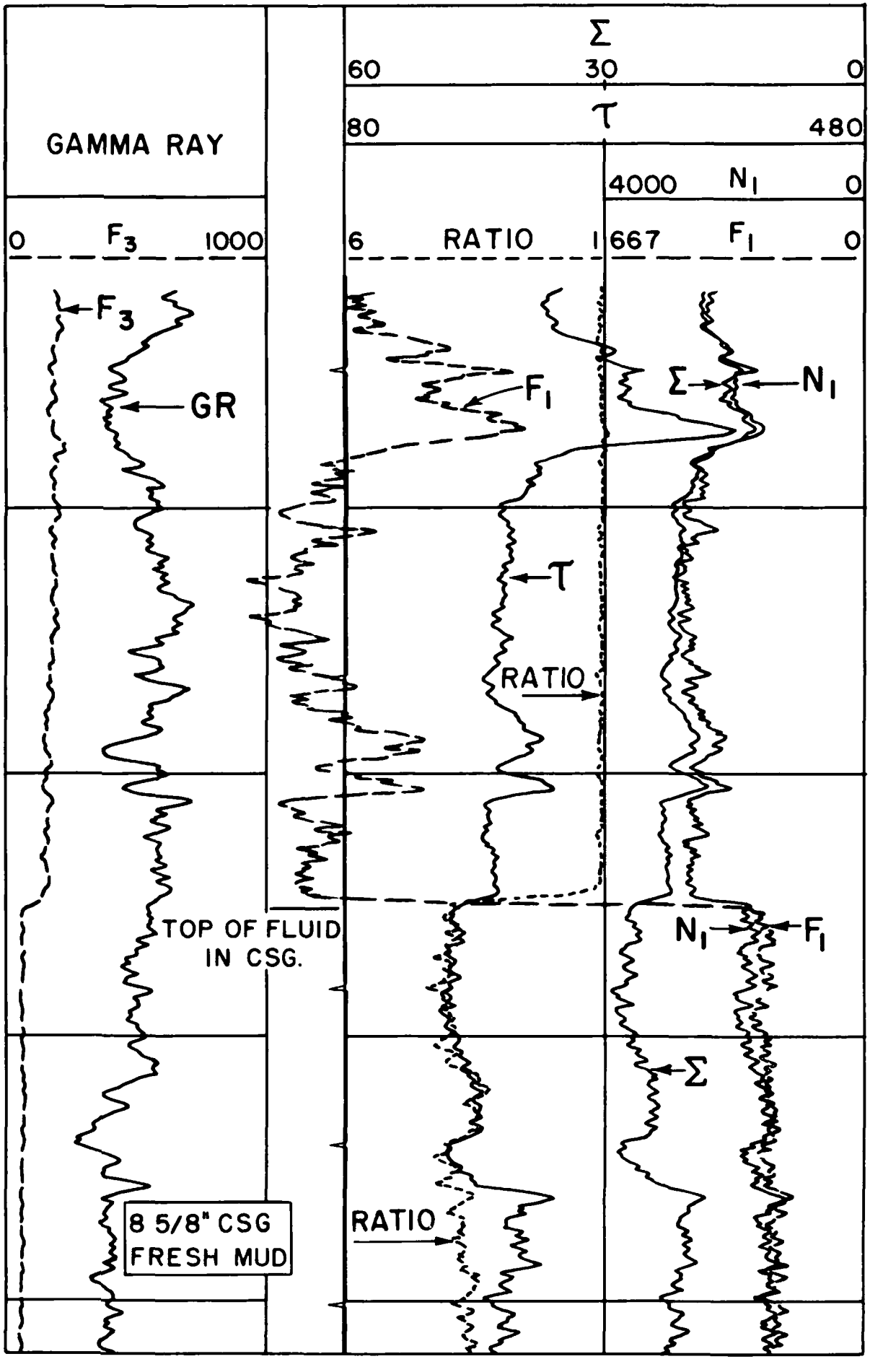
GAMMA RAY
0 F3 1000
Σ
60 30 0
τ
80 480
4000 N1 0
6 RATIO 1
667 F1 0
F3
GR
F1
Σ
N1
τ
RATIO
TOP OF FLUID
IN CSG.
N1
F1
Σ
RATIO
8 5/8" CSG
FRESH MUD

Fig. 35

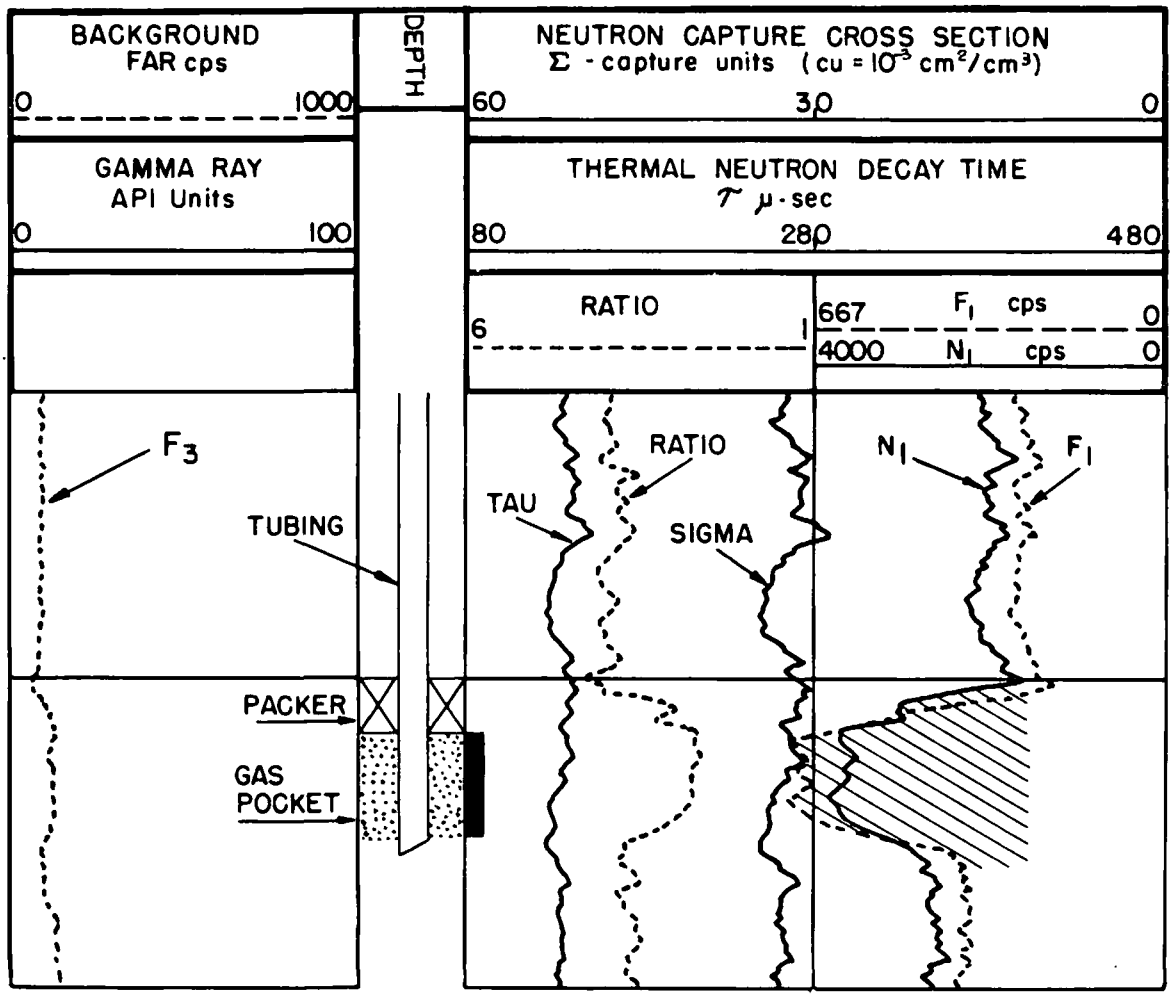
BACKGROUND
FAR cps
0
1000
DEPTH
NEUTRON CAPTURE CROSS SECTION
Σ - capture units (cu = 10⁻³ cm²/cm³)
60
30
0
GAMMA RAY
API Units
0
100
THERMAL NEUTRON DECAY TIME
τ μ-sec
80
280
480
RATIO
6
1
667 F1 cps 0
4000 N1 cps 0
F3
TUBING
PACKER
GAS
POCKET
TAU
RATIO
SIGMA
N1
F1

Fig. 36

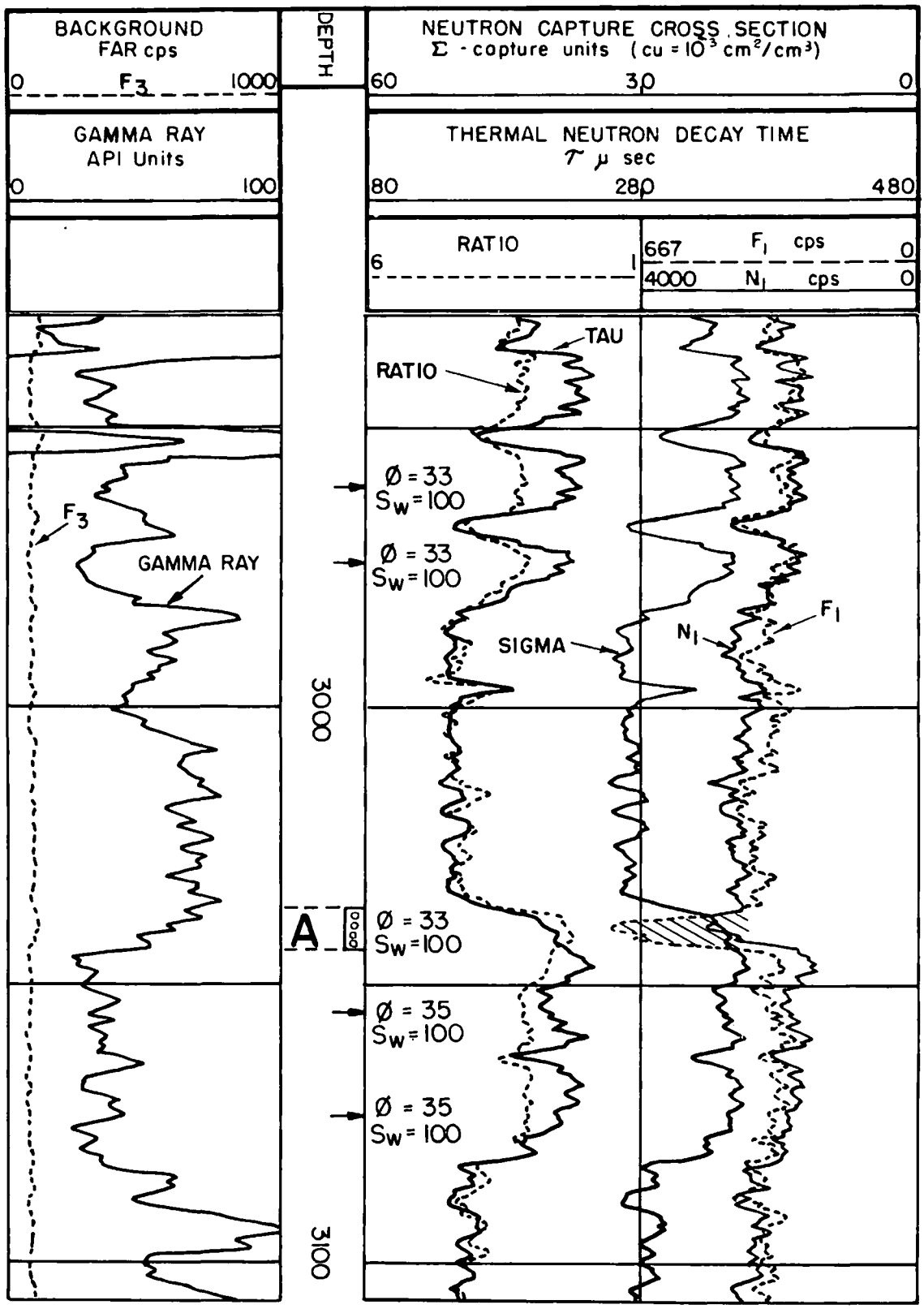
BACKGROUND
FAR cps
0
F3
1000
GAMMA RAY
API Units
0
100
DEPTH
NEUTRON CAPTURE CROSS SECTION
Σ - capture units (cu = 10³ cm²/cm³)
60
30
0
THERMAL NEUTRON DECAY TIME
τ μ sec
80
280
480
RATIO
6
1
667
F1 cps
0
4000
N1 cps
0
TAU
RATIO
Ø = 33
Sw = 100
Ø = 33
Sw = 100
F3
GAMMA RAY
SIGMA
N1
F1
3000
A
Ø = 33
Sw = 100
Ø = 35
Sw = 100
Ø = 35
Sw = 100
3100

Fig. 37

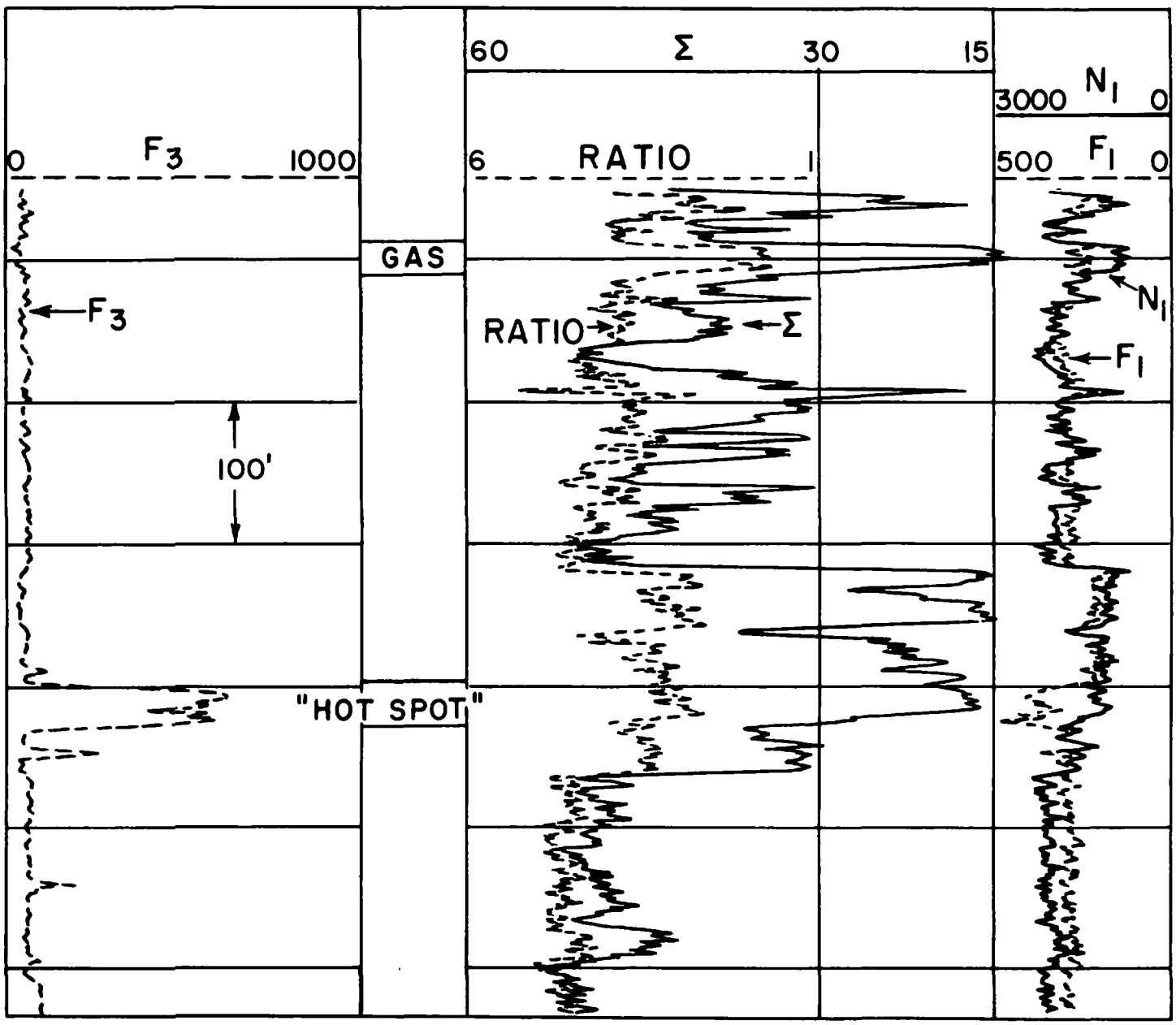
60
Σ
30
15
3000
N1
0
0
F3
1000
6
RATIO
1
500
F1
0
GAS
F3
RATIO
Σ
N1
F1
100'
"HOT SPOT"

Fig. 38

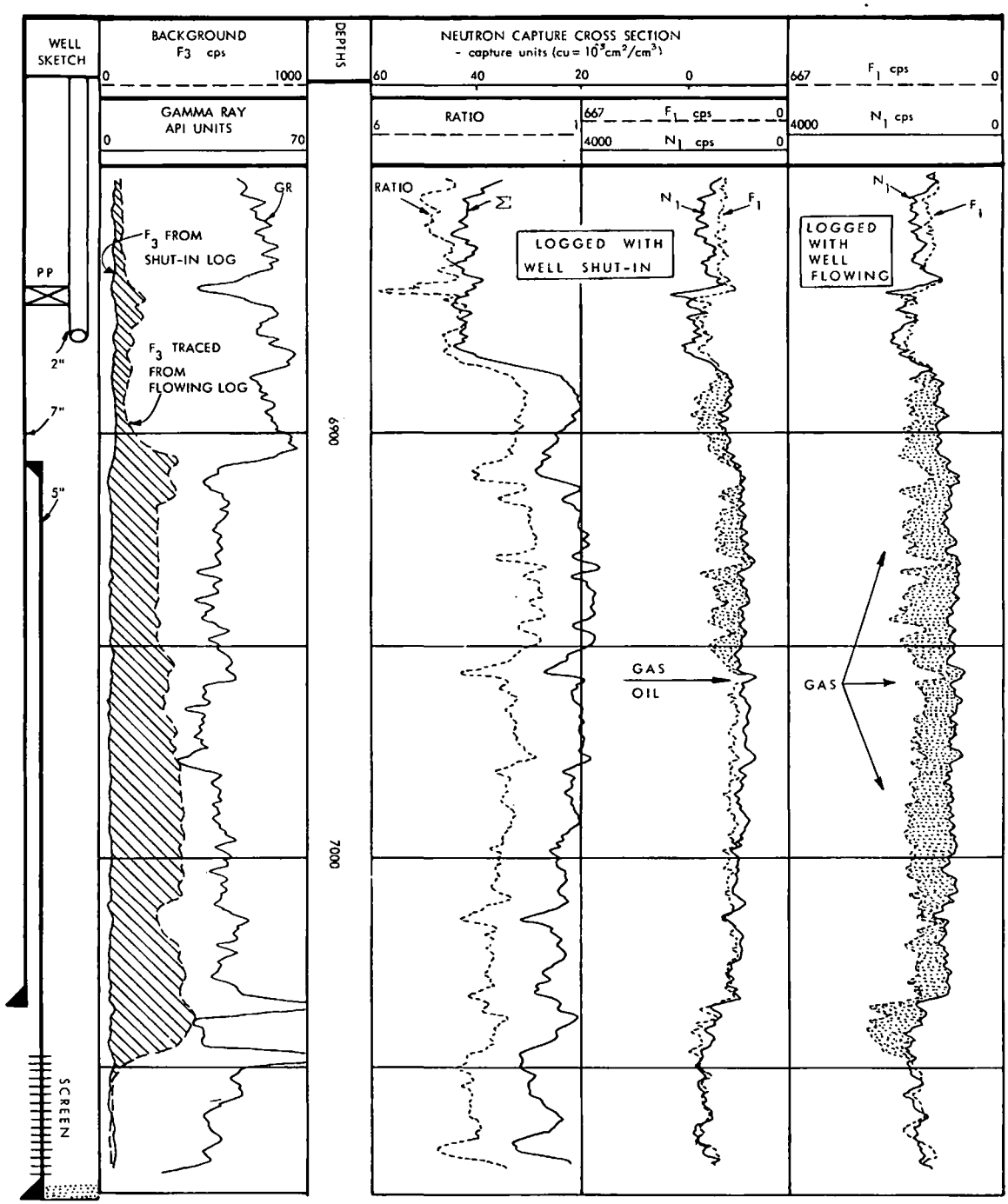
WELL SKETCH
BACKGROUND F3 cps
0
1000
GAMMA RAY API UNITS
0
70
DEPTHS
NEUTRON CAPTURE CROSS SECTION
- capture units (cu = 10^3 cm^2/cm^3)
60
40
20
0
667
F1 cps
0
6
RATIO
1
4000
N1 cps
0
GR
F3 FROM SHUT-IN LOG
F3 TRACED FROM FLOWING LOG
PP
2"
7"
5"
6900
7000
SCREEN
RATIO
N1
F1
LOGGED WITH WELL SHUT-IN
GAS
OIL
LOGGED WITH WELL FLOWING
GAS

Fig. 39

E-6

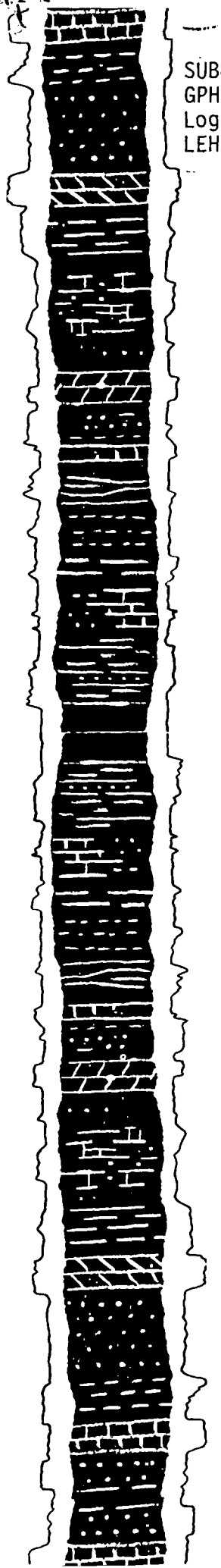

SUBJ
GPHYS
Log
LEH

LOGGING EMPTY HOLES

BY C. G. RODERMUND, R. P. ALGER,
AND J. TITTMAN

A reprint from THE OIL AND GAS JOURNAL of June 12, 1961 distributed
through the courtesy of Schlumberger Well Surveying Corporation

When the borehole contains only a gas, specialized logging methods are needed to get quantitative information on porosity and saturation. Here are some recommended programs that will give results in . . .

LOGGING EMPTY HOLES

BY C. G. RODERMUND, R. P. ALGER, AND J. TITTMAN
Schlumberger Well Surveying Corporatoin

POROSITY AND SATURATION, reduced to numbers, are what operators are looking for these days.

And more and more wells are being drilled with air or gas.

Put these two things together, and you have some new logging problems to cope with. When a well is drilled with a liquid, conventional resistivity-measuring tools can be used with good results. But with an empty hole, conditions are different, and new methods must be used.

The recent development of the density logging tool (Schlumberger's Gamma-Gamma Density Log) made it possible to prepare logging programs to suit all conditions involving wells drilled with air or gas.

Examples that follow are based on experience with cable-tool wells around Ohio and West Virginia, but the empty-hole programs can be applied to wells drilled with rotary tools, as long as other conditions are met.

Basic Logging Tools

The interpretation program for empty holes uses three basic logging tools: induction, neutron, and density logs.

Induction. The induction log is the only device capable of measuring resistivity in an empty borehole, and this condition enhances its ability to obtain R_t.

Neutron. The neutron log has long been the logging industry's only approach to the determination of porosity in empty boreholes. Under these conditions, log interpretation is usually done by an empirical scaling method. For the subsequent neutron-log study, a logarithmic porosity scale is applied between two control points. The shale deflection is used as 35% porosity, and a 2% porosity point is determined by the maximum neutron deflection in a dense carbonate. Gas-bearing carbonates may produce even larger deflections, but the density log will distinguish these from the dense zones.

Density. The Schlumberger Gamma-Gamma sonde (Fig. 1) is a device which measures, in situ, the bulk density of subsurface formations penetrated by a borehole. The name indicates the principle of operation: gamma rays are emitted by a source and, after having diffused through the formations, they are counted by a gamma-ray detector.

The principle is somewhat similar to that of the neutron sonde, but the big difference between the two tools is in the manner in which the emitted gamma rays and the neutrons interact with the formations. In neutron logging, the important effects are caused by collisions between the neutrons and hydrogen atoms. Gamma rays, on the other hand, interact with the electrons which are always present in each atom of formation. The density logging tool has been so designed that its response depends upon the electron density (electrons per cc.) in the formation, and not upon the nature of the atoms. This electron density is almost exactly proportional to the bulk density of the formation.

Fig. 2 shows how the counting rate varies with bulk density of the formation. Note that for the density-logging tool, the counting rate is approximately an exponential function of the bulk density. This means that the device has a constant density resolution irrespective of the value. Thus the fractional change in counting rate for a density change of 1 g/cc. is the same, whether the density is high or low. This property persists with respect to porosity, also.

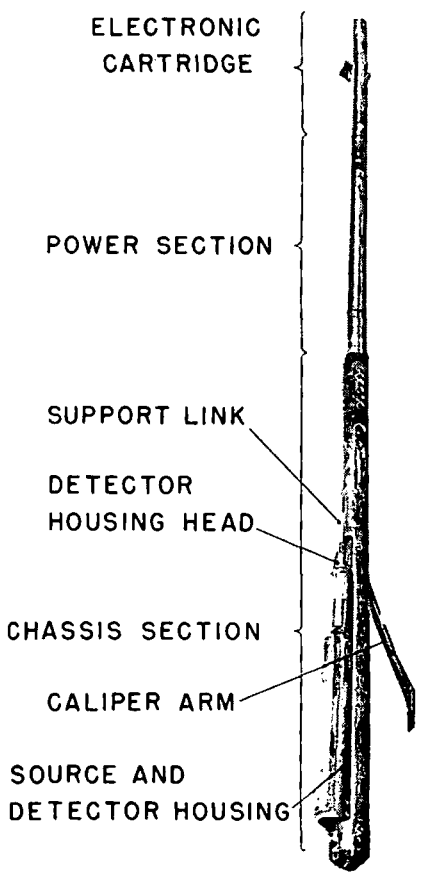

BULK DENSITY is measured with this Schlumberger Gamma-Gamma sonde. Fig. 1.

Paper presented at second annual meeting of Society of Professional Well Log Analysts, Dallas, May 17-19, 1961.

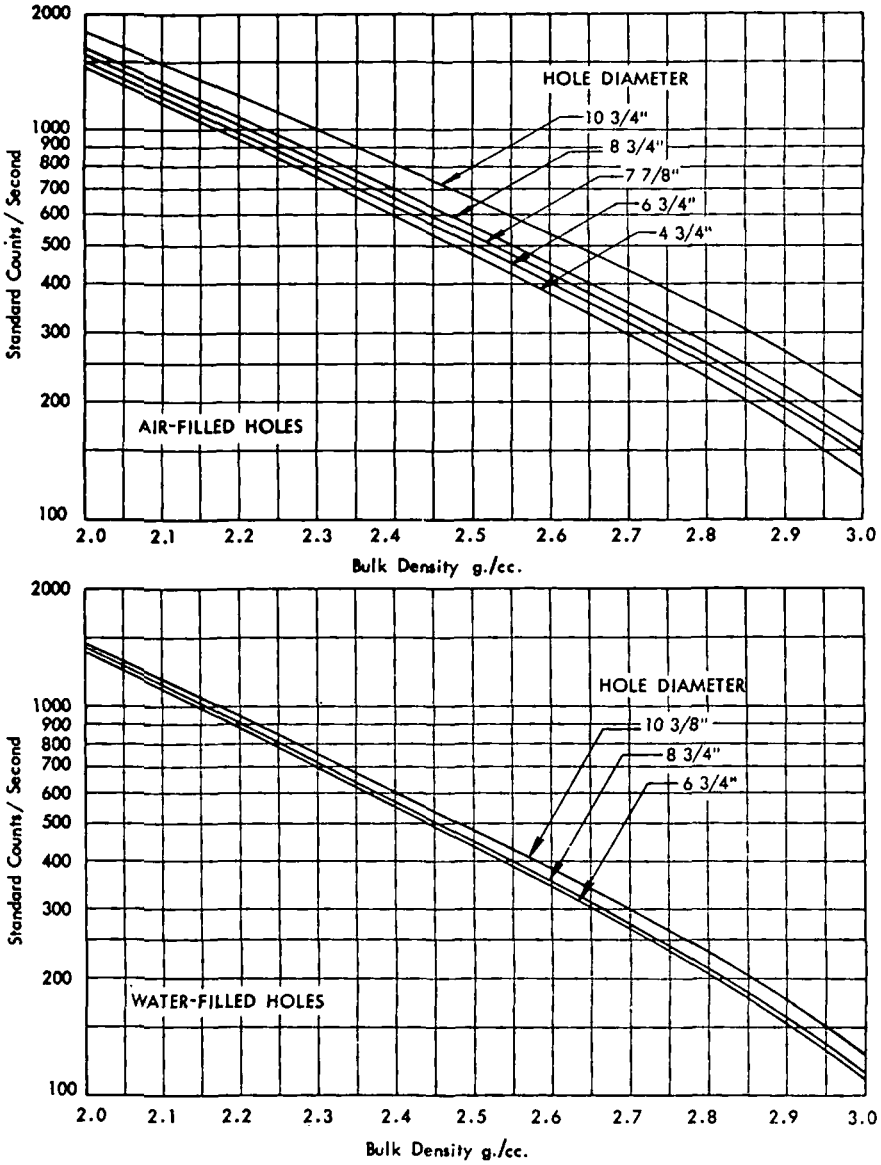

COUNTING RATE varies with bulk density of a rock formation, and with hole size as shown here. Fig. 2.

Associated Services

Gamma Ray. The gamma-ray log is used as the correlation device in each of the described methods. It also provides an indication of the accuracy of the interpretation since shaliness is always detrimental to any analysis. The neutron is quickly affected as shaliness increases, whereas the effect of shaliness on the density log is usually small and frequently unobservable.

Caliper. The density tool must make good contact with the wall of the hole. If, due to hole roughness or caving, there is gas between the articulated skid and the formation, the sonde will average it in and the apparent density will appear much too low. Therefore, a caliper log is essential to avoid errors in interpretation; preferably, it should be recorded simultaneously with the density log.

Knowledge of hole diameter is also needed for interpreting neutron and temperature surveys.

Temperature. The temperature survey is valuable for confirming low-density anomalies in that it pinpoints zones having sufficient permeability to produce gas without stimulation treatment. In favorable cases it can be used to determine the proportional production from two or more zones.[1]

Interpretation Techniques
Density-Hydrogen Index Method

Density tool response. The Schlumberger density tool is presently calibrated to read directly the bulk density of the formation. With the procurement of the bulk density, ρ_B, the role of the sonde is terminated. The interpretation procedure for porosity now depends on the introduction of correct grain and fluid densities. The bulk density is an average of the densities of the solids and the densities of the fluids contained in the pore spaces.

Consider a unit volume of formation, where the porosity, ϕ, is filled with fluids having a density of ρ_F. The remaining volume, $1-\phi$, represents the rock matrix whose grain density is ρ_G. Bulk density is then given by:

$$\rho_B = \phi\rho_F + (1 - \phi)\,\rho_G \qquad (1)$$

Solving for ϕ, we have:

$$\phi = \frac{\rho_G - \rho_B}{\rho_G - \rho_F} \qquad (2)$$

It can be seen that a quantitative porosity can now be derived with the knowledge of three parameters. Values for ρ_B are taken directly from the density log. Usually ρ_G can be obtained with sufficient accuracy from some prior knowledge of the type of formation being analyzed in empty-hole logging. ρ_F cannot be assumed as readily. Depending on the gas-to-liquid ratio, ρ_F will be either the average density of the liquids in the pore space or something less. If, for example, we have 70% liquid saturation with gas in the remainder of the pore space, ρ_F would be:

$$\rho_F = S_L\rho_L + S_g\rho_g \qquad (3)$$

(where S_L and S_g are the liquid and gas saturations, respectively)

then,

$$\rho_F = 0.7\rho_L + 0.3\rho_g$$

Density of formation water ranges from 0.95 g./cc. to 1.10 g./cc. approximately depending on temperature, pressure, and salinity. Average density of oil is slightly lower than these values and varies over an equally wide range. A simple calculation shows that errors due to these variations are negligible. Therefore, for simplicity and practical reasons, we use a value of unity for the term ρ_L. The gas density, ρ_g, for reservoirs producing gas into an empty hole approaches 0 g./cc. It follows then that

$$\rho_F = 0.7 \times 1 + 0.3 \times 0 = 0.7 \text{ g./cc.}$$

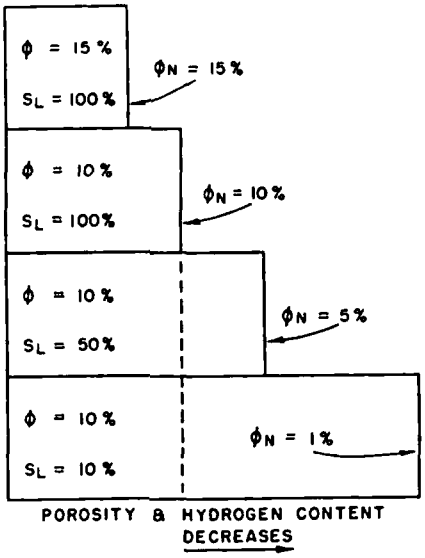

NEUTRON-DERIVED POROSITY approaches true porosity as liquid saturation approaches 100%. But as liquid saturation falls off, the hydrogen index decreases. Fig. 3.

In this special case, where the gas density is zero and the liquid density is unity, we always have the same interesting result:

$$\rho_F = S_L \qquad (4)$$

In any case, to determine the gas-to-liquid ratio it is necessary to have further information, which either the neutron or the induction log will supply.

Neutron response. The neutron logging device is primarily sensitive to the hydrogen content of the formation. Since in shale-free rocks the hydrogen present is generally in the form of the fluids in the pore space, it follows that as porosity varies, the hydrogen content of the formation will vary. The log is calibrated to read true porosity when the pore space is 100% liquid filled. Since oil and water have approximately the same hydrogen content per unit volume, the water-to-oil ratio makes no difference in the response to the tool. Difficulty arises when gas is also present. Since the gas occupies volume, but has both a very low hydrogen index and a low density, it alters the usual interpretation of both the density and neutron logs. As gas saturation increases, hydrogen content necessarily decreases and the hydrogen index, as given by the neutron log, decreases. In Fig. 3, zones A and B, both with 100% S_L, show 15% and 10% porosity, respectively. In these instances, the hydrogen index is the true porosity of each zone. Zones C and D indicate 10% porosity, but with a reduction in liquid saturation to 50% and then to 10%. It can be seen that as S_L approaches 100%, the hydrogen index (ϕ_N) approaches the true porosity. This relationship, in equation form, is:

$$S_L = \phi_N/\phi \qquad (5)$$

As explained previously, in a zone having $0.7 = S_L$ the ρ_F was also 0.7. Since we saw that $S_L = \rho_F$ in Equation 4 and since $S_L = \phi_N/\phi$, we can make a substitution in Equation 2 so that:

$$\phi = \frac{\rho_G - \rho_B}{\rho_G - (\phi_N/\phi)} \qquad (6A)$$

Solving for ϕ:

$$\phi = \frac{\rho_G - \rho_B + \phi_N}{\rho_G} \qquad (6B)$$

With this value of ϕ we can refer back to Equation 5 to obtain S_L.

It is now apparent that from data supplied by the density and neutron logs we can arrive at quantitative porosity and liquid saturation. This process is solved graphically by use of the chart shown on Fig. 4. By plotting ρ_B against ϕ_N, using the appropriate value of ρ_G, ϕ and S_g are read directly from the body of the chart.

Density, resistivity method. Another approach is possible when appropriate reservoir conditions exist; i.e., when water is the only liquid present in the pore space. Instead of Equation 5, a variation of the Archie relationship for S_w can be used.

$$S_w = (1/\phi)\sqrt{R_w/R_t} \qquad (7)$$

In this relationship we need R_t

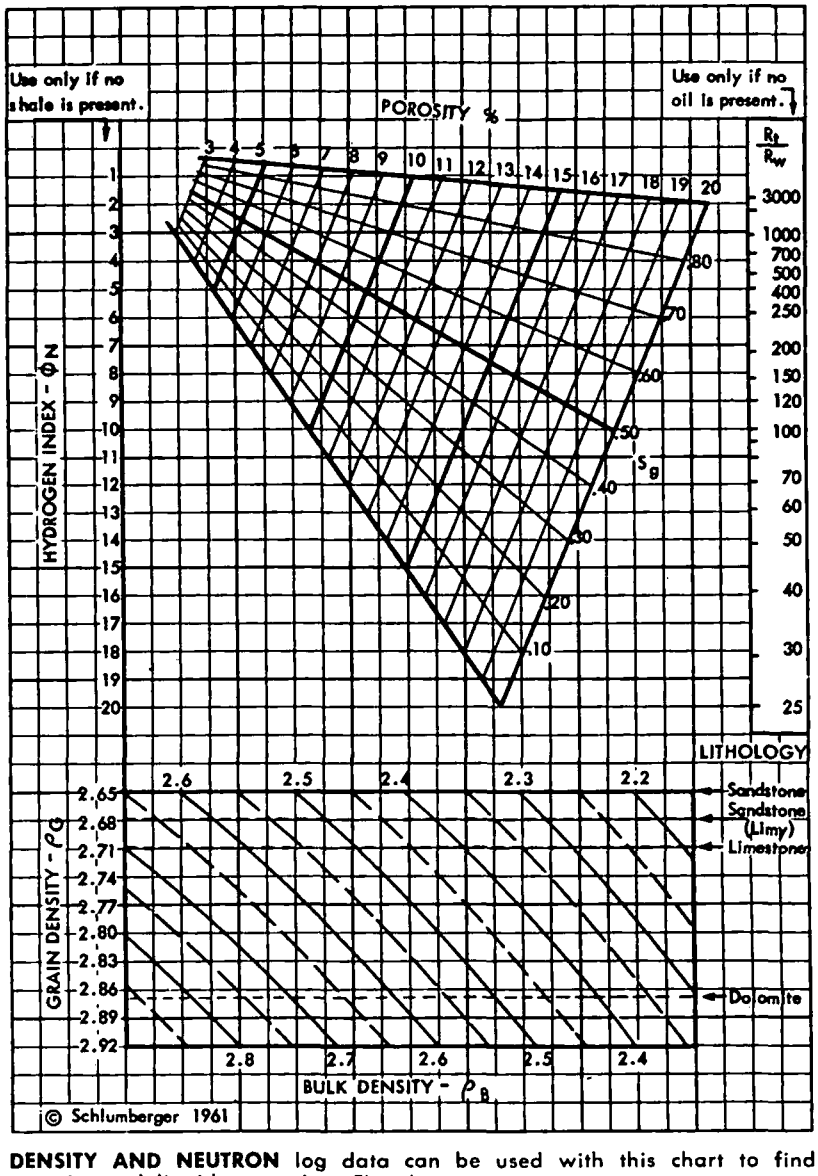

DENSITY AND NEUTRON log data can be used with this chart to find porosity and liquid saturation. Fig. 4.

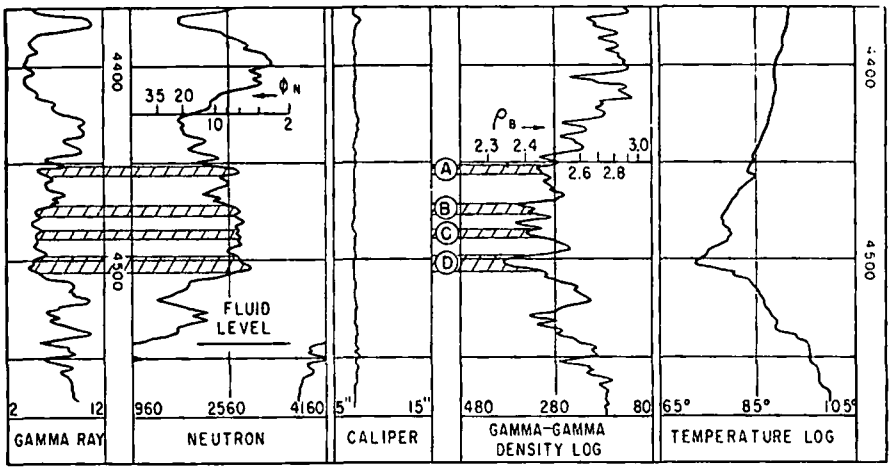

EXAMPLE 1—Application of the density-hydrogen index program.

and R_w information. R_w must be obtained from some prior knowledge of the area. R_t can be obtained quite accurately and with little correction from the induction log. When the only liquid present is water, we can see from Equation 4 that

$$\rho_F = S_w \qquad (8)$$

Substituting the value of S_w for ρ_F in Equation 2 we have:

$$\phi = \frac{\rho_G - \rho_B}{\rho_G - (1/\phi)\sqrt{R_w/R_t}} \qquad (9A)$$

Solving for ϕ:

$$\phi = \frac{\rho_G - \rho_B + \sqrt{R_w/R_t}}{\rho_G} \qquad (9B)$$

With this value of ϕ we can refer back to Equation 7 to obtain S_w. We should emphasize that Equation 9B is valid only if there is no oil in the pore space.

In some special cases it may be possible and advisable for the borehole to be filled with a few hundred feet of water. A focused resistivity log may then be used instead of the induction log. It gives better resistivity definition in thin beds and in highly resistive zones. Fig. 4 is also used to solve Equation 9. By plotting R_t/R_w versus ρ_B and ρ_G, ϕ and S_g data are obtained.

Applications of Above Techniques

Density-hydrogen index method. The density-hydrogen index method is used where gas saturation is primarily the information desired. Porosity and gas saturation data can be obtained regardless of the combination of the liquids present in the pore space.

This method has limitations where the neutron log is affected by shaliness. Under these circumstances the derived porosity is too high and the gas saturation is too low.

Density-resistivity method. In the density-resistivity method, gas saturation is still of primary interest. Here, however, it is required that the pore liquid be formation water. Since this method requires accurate resistivity values, use of the induction log is suitable when $R_t < 200$ ohm-m. If higher resistivities occur, a focused resistivity log may be used after spotting water in the hole. The effects of shaliness are less important with this method.

Density-hydrogen index-resistivity method. If a fractional analysis of all the fluids present is needed, it is necessary to provide R_t information from the induction or resistivity tools. With the true porosity obtainable through the density-hydrogen index plot, the use of R_t/R_w in Archie's Equation 7 will then provide S_w. Since we already have S_g, and now S_w, the S_o may be computed ($S_o = 1 - S_g - S_w$).

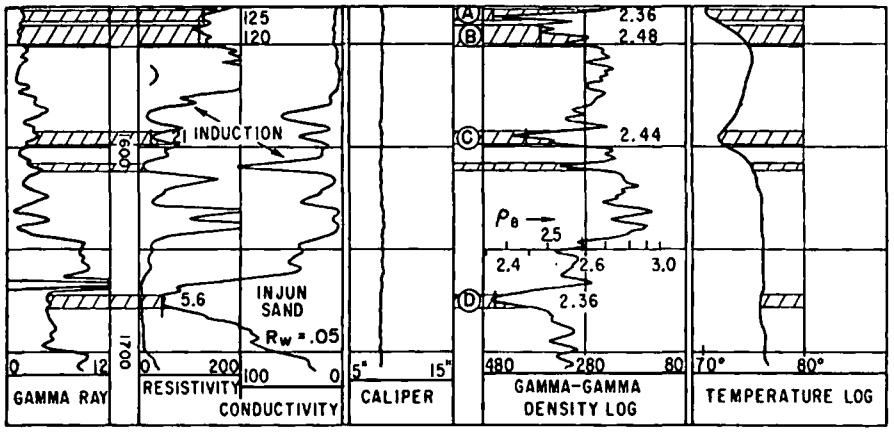

EXAMPLE 2—Application of the density-resistivity program.

Examples

Density-hydrogen index method. Example 1 is of a Clinton sandstone from a well in Ohio. In zone A the bulk density from the log is 2.44 g./cc. The neutron-derived index is 6%. On the basis of core analysis, the grain density of this sandstone has been found to be 2.68 g./cc.

Enter the bottom of the chart (Fig. 4) with the bulk density (2.44); proceed diagonally to the appropriate grain density (2.68). Move vertically to plot this point against the neutron index (6%). This location is at the intersection of the true porosity (11%) and the gas saturation (0.47) of this zone. Note that 53% of the fluids in the pore space are unaccounted for. Since this was primarily a gas field, even though some oil is produced, knowledge of oil saturation was not considered important. In any case, the gas saturation determination is independent of the amount of oil which may be present.

A summary of the interpretation of this formation is shown below:

Zone	ρ_G	ρ_B	ϕ_N	ϕ	S_g
A	2.68	2.44	6.0%	11.0%	0.47
B	....	2.41	6.0	12.3	0.52
C	....	2.40	6.0	12.5	0.53
D	....	2.34	4.5	14.0	0.68

On final completion this well had an open flow potential of 4 M.M.c.f.d.

Density - resistivity method. Example 2 shows logs from a well in West Virginia in a region where gas production is sometimes found in the base of the Big lime and in the Injun sandstone immediately below. The logs available are gamma ray, density, induction, and temperature.

Thus, the density-resistivity method may be used.

The grain density used in the Big lime is 2.75 g./cc. In zone A the bulk density is 2.36 g./cc. and R_t from the induction log is 125 ohm-m. R_w in this area is known to be 0.05 ohm-m, so that R_t/R_w becomes 2,500. The procedure is to enter the chart with the bulk density (2.36) then proceed diagonally to the proper grain density (2.75). This locates the abscissa value to plot against the ordinate value of R_t/R_w (2,500). The plotted point indicates a true porosity of 14.8% and a gas saturation of 0.87. We again point out that this system is applicable only if no oil is present in the pore space.

A summary of the interpretation of these logs is shown below:

Zone	ρ_G	ρ_B	R_t	R_w	R_t/R_w	ϕ	S_g
A	2.75	2.36	125.0	0.05	2,500	14.8	0.87
B	....	2.48	120.0	....	2,440	10.4	0.80
C	....	2.44	21.0	....	420	13.0	0.62
D	2.68	2.36	5.6	....	112	15.3	0.40

In this case the induction log helps select between two possible interpretations of the density and temperature surveys. For example, zone D could be impermeable, gas-filled beds, or high porosity, liquid-filled formations. The induction log by virtue of the small R_t reading indicates the latter condition. Actual production tests yielded large quantities of water plus a small amount of gas from zone D. Zones A, B, and C will become good producers.

Density-hydrogen index-resistivity method. Example 3 shows logs recorded through the Clinton sandstone. Included are gamma ray, density, neutron, and induction logs. These were run to achieve a complete analysis of all the fluids present.

In zone A, the bulk density is 2.34 g./cc. and the grain density is 2.68 g./cc. The neutron index is 8.0%. R_t is 68 ohm-m, and R_w is 0.04 ohm-m. Using the density and neutron data on Fig. 4, we get a true porosity of 15.5% and a gas saturation of 0.48. To distinguish between the two fluids, water and oil, we will use the derived true porosity (15.5%) together with the known R_w and the R_t from the induction log. Archie's Equation 7 gives water saturation (S_w) of 0.14.

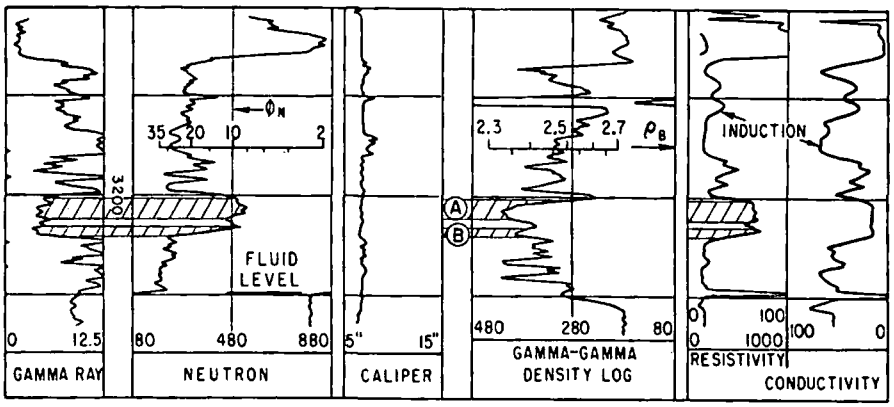

EXAMPLE 3—Application of the density-hydrogen index-resistivity program.

Oil saturation is then (1.00 − 0.48 − 0.14) or 0.38. Since there is oil in the pore space, we cannot enter Fig. 4 with R_t/R_w.

A summary of the interpretation of these logs is shown below:

Zone	ρ_G	ρ_B	ϕ_N	ϕ	S_g	R_t	R_w	S_w	S_o
A	2.68	2.34	8.0	15.5	0.48	68	0.04	0.14	0.38
B	2.68	2.36	9.0	15.0	0.44	70	0.04	0.14	0.42

Completion results for these zones show that 350,000 cu. ft. of gas per day is being delivered into the pipeline. The formation (or rock) pressure is reported as 800 psi. A small amount of oil is also produced.

Example 4 shows logs of the Clinton sand in Ohio. This is a case of particular interest because it uses the focused resistivity log instead of the induction log. In this instance, a slight amount of water was being produced from a formation above the Clinton. At the time the logs were run, the hole contained approximately 1,000 ft. of salt water. Since gas was being produced to the atmosphere, no invasion had occurred. The gas density in the reservoir is still sufficiently low to allow the use of these techniques. Another point of interest is that most of the sands in this well have only gas and water present. This gives us an opportunity to use both the density-hydrogen index and density-resistivity

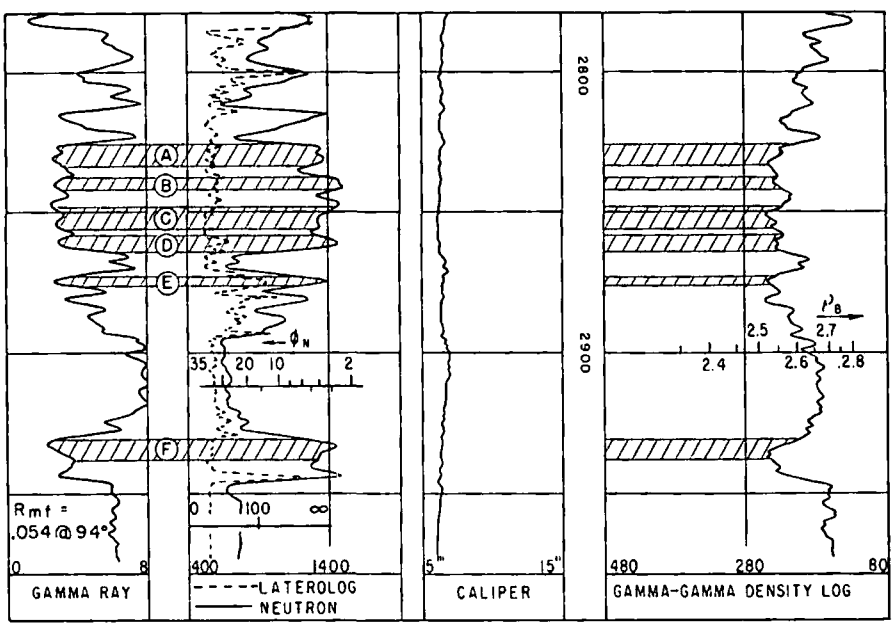

EXAMPLE 4—Program for water-loaded holes producing gas.

techniques on the same formations. The data have been tabulated in chart form so that comparison can be made. Note that these two methods give remarkably similar results except in the case of zone E. The logs show the presence of oil in this zone, which precludes the use of the density-resistivity method. Use of the two approaches to saturation could be said to provide a "saturation balance" technique.

Zone	ρ_G	ρ_B	R_t	R_w	R_t/R_w	ϕ_N
A	2.68	2.54	38	0.04	950	3.5
B	....	2.54	45	...	1,125	2.5
C	....	2.53	28	...	700	3.5
D	....	2.55	48	...	1,200	2.5
E	....	2.53	120	...	3,000	3.0
F	....	2.53	35	...	875	3.5

Zone—	A		B		C		D		E		F	
Method—	ϕ	S_g	ϕ	S_g	ϕ	S_g	ϕ	S_g	ϕ	S_g	ϕ	S_g
Density-hydrogen index..	6.5	0.45	6.1	0.59	6.9	0.49	5.8	0.56	6.7	0.55	6.9	0.49
Density-resistivity	6.5	0.49	6.3	0.51	7.0	0.43	6.0	0.50	6.2	0.72	6.9	0.50

Completion attempts yielded a small amount of water with a show of gas.

Use of Quantitative Data

When the appropriate conditions prevail, the values obtained for porosity and saturation permit computation of the reservoir fluids in place. For gas wells, the additional information such as temperature and rock pressure allows an estimation of producible reserves.

Another important application of quantitative data concerning porosity and water saturation is the estimation of the reservoir's ability to produce. Experience in the Clinton sandstone, for example, was used to construct Fig. 5. Here it is clearly seen that porosity information alone will not properly predict the productivity. A necessary condition for the use of Fig. 5 is the existence of irreducible water saturation; this situation, in fact, occurs in the Clinton sandstone. Similar charts could be made for other sandstones, or regions, provided that such gas zones are at irreducible water saturation.

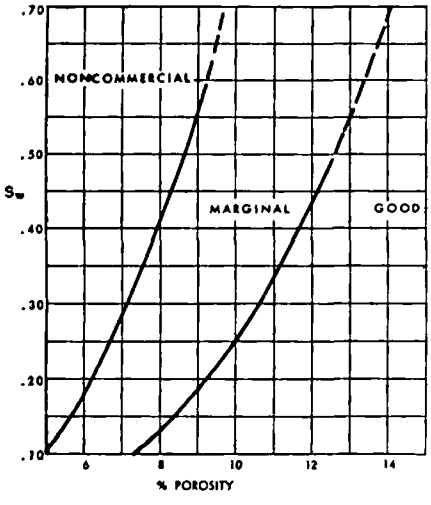

GAS-PRODUCTIVITY estimation for the Clinton sandstone. This chart was prepared from experience with several Clinton completions. Fig. 5.

Conclusions

An empty-hole logging program for the fractional analysis of reservoir fluids lacked a fundamental porosity tool until the advent of the density device. Now, by combining the bulk density of the formation with the hydrogen index, or with the true resistivity, the true porosity and fractional fluid saturations may be computed.

The accompanying table summarizes the proper conditions for log selection and the corresponding interpretation methods. Note that the neutron log and induction log are somewhat interchangable, particularly when gas is the only hydrocarbon present. In general, the induction log is preferable, since the neutron log is bothered by shaliness, and the hydrogen-index calibration is sometimes difficult. On the other hand, the density log is practically unaffected by shaliness, is readily calibrated, and works as well in empty as in mud-filled holes. It has, in fact, shown itself to be the key to all interpretations in empty-hole logging.

Symbols

1. Saturation terms, as fractions of pore space
   S_w = water saturation
   S_g = gas saturation (equals $1 - S_w - S_o$)
   S_o = oil saturation (equals $1 - S_w - S_g$)
   S_L = liquid (oil + water) (equals $1 - S_w$)
2. Density terms, given in g./cc.
   ρ_G = grain density of matrix
   ρ_B = bulk density; obtained from Gamma-Gamma Density Log
   ρ_L = liquid density, includes oil and water
   ρ_g = gas density
   ρ_F = average fluid density, includes water, oil, and gas
3. Porosity terms
   ϕ = True porosity of the formation
   ϕ_N = Hydrogen Index, as derived from neutron
4. Resistivity terms
   R_t = true resistivity of the formation
   R_w = resistivity of the formation water

Acknowledgments

The authors acknowledge the notable contribution of John S. Wahl to the design of the Schlumberger Gamma-Gamma Density sonde and to the development of interpretation methods for its logs. They also are indebted to W. E. Bachman and J. A. McGuire whose enthusiasm and technical ability helped develop and refine the field application of these logging programs. The authors are most grateful to the producing companies which have released the examples used as illustrations for this paper.

Reference

1. Kunz, K. S., and Tixier, M. P., "Temperature Surveys in Gas-Producing Wells": Petr. Tech., vol. 205, p. 111 f. (1955).

SUMMARY OF EMPTY-HOLE LOGGING PROGRAMS

Basic Logs	Hole Conditions	Formation Fluids	Interpretation Results	Remarks
Density plus Neutron	Empty, smooth	Gas + oil and/or water	ϕ, S_g (by chart)	Requires shale-free formations.
Density plus induction*	Empty, smooth and $R_t < 200$	(1) Gas + water (2) Oil + water	ϕ, S_g (by chart) ϕ, S_w (by Archie)	R_w must be known. Moderate shaliness tolerated.
Density plus neutron plus induction*	As above	Gas + oil + water	ϕ, S_g, S_o, S_w (by chart and Archie)	R_w must be known. Requires shale-free formation.
Auxiliary Logs:	Gamma ray and caliper are essential; temperature is very helpful.			

*Induction log may be replaced by a focused resistivity log if the hole is properly water-loaded. Water loading implies that a cable-tool hole or an air-drilled hole became partially filled with water: (a) Due to natural production of formation water, (b) Because water was spotted to partially control gas flow, (c) Because water was spotted to enable running a focused resistivity log, which is effective in highly resistive and/or thin beds.

GEOPHYSICS, VOL. 44, NO. 8 (AUGUST 1979); P. 1458–1462, 5 FIGS., 1 TABLE.

Short Note

A model for bottom-hole temperature stabilization

M. F. Middleton*

Bottom-hole temperature (BHT) stabilization is modeled assuming that the mud temperature in a deep well is uniform for several meters above its base and that the basal portion of the well was formed rapidly so that it may be considered to have formed "instantaneously". Therefore, knowledge of circulation time of the drilling fluids, which is required in many alternative methods of correction for BHT disturbance, is not necessary. Rectangular coordinates are used to describe the geometrical configuration of the well, which often departs from an ideal cylindrical shape due to caving of poorly consolidated formations. True formation temperature can be found by a simple curve-matching technique if several time-sequential BHT measurements are available. This technique is successfully applied to BHT data from a number of wells in the Moomba and Big Lake gas fields of the Cooper Basin, South Australia.

INTRODUCTION

The effect of circulating drilling fluids in deep wells is to bias measured bottom-hole temperatures (BHTs) to values some tens of degrees lower than true formation temperatures (Pirson, 1963; Kappelmeyer and Haenel, 1974, p. 183). Jaeger (1961) has shown that equilibrium temperature is reached within a day for the slow circulation rates required in diamond drilling, but he emphasized that it takes considerably longer to reach for the higher circulation rates required in rotary drilling.

Parasnis (1971), Dowdle and Cobb (1975), and Fertl and Winchmann (1977) devised methods of estimating true formation temperature by the extrapolation of time-sequential BHTs to infinite time. Cheremenski (1960) considered the zone of disturbance or "invaded zone" around the borehole in a method of correcting for disturbed thermal conditions; Bullard (1947) proposed a model for temperature recovery in deep wells based on the thermal decay of a line source. Such methods for correcting unstabilized BHT data incorporate the drilling or circulating time, which essentially accounts for the heat sink of the circulating fluids. However, the circulating time is often poorly known, with subsequent uncertainty in estimated formation temperature.

Jaeger (1961) has suggested that during rotary drilling the temperature of the circulating mud may be constant throughout large portions of the hole. A physical model is developed on this basis. The proposed model for thermal recovery assumes that the temperature of the circulating mud is constant over a distance of some tens of meters at the base of the well and that the final portion of the well is formed sufficiently rapidly to be considered as being formed instantaneously. Drilling rates in the range 2 to 10 minutes per meter are common for the basal section of a deep well; these rates indicate that the time of formation of the final few meters of the well is very much less than the time taken for thermal stabilization. Therefore, true formation temperature may be estimated without knowledge of the duration of drilling or circulating time. A further condition of the model is that the temperature probe is sufficiently re-

Manuscript received by the Editor July 5, 1978; revised manuscript received December 15, 1978.
* Dept. of Geology and Geophysics, The University of Sydney; presently Dept. of Geology, Univ. of Melbourne, Parkville, Victoria 3052 Australia.
0016-8033/79/0801—1458$03.00.

moved (a few well diameters) from the bottom of the well so that only radial flow of heat is significant. The physical model assumed is illustrated schematically in Figure 1.

The effect of the vertical geothermal gradient is neglected in the proposed scheme because the flow of heat during thermal recovery is essentially radial; the temperature difference across the 5-m vertical depth interval that may have an influence on the BHT is typically 0.15°C, whereas the temperature difference between the formation and the circulating fluids is of the order of tens of degrees.

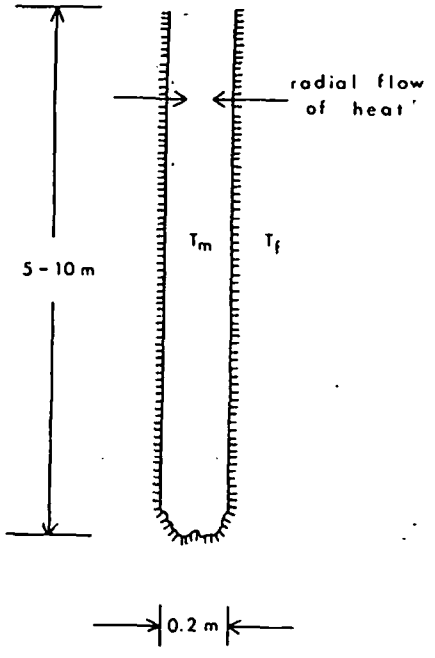

FIG. 1. Schematic diagram of the assumed physical model of the basal section of a borehole.

THEORY

Treatment of the problem of conductive heat transfer into a vertical, approximately cylindrical region of small diameter in rectangular coordinates leads to an expression for temperature which is very much simpler than the corresponding expression in cylindrical coordinates. Following the procedure of Carslaw and Jaeger (1959, p. 54–55), the temperature distribution $T(x, y, t)$ about a vertical cylinder of infinite length, which is initially zero temperature, can be expressed for time $t > 0$ as

$$T(x, y, t) = \frac{1}{4}\,\Delta T\left(\operatorname{erfc}\frac{a-x}{\tau} + \operatorname{erfc}\frac{a+x}{\tau}\right)\cdot \left(\operatorname{erfc}\frac{a-y}{\tau} + \operatorname{erfc}\frac{a+y}{\tau}\right), \quad (1)$$

where

$$\tau = (4kt)^{1/2}.$$

ΔT is the difference between the temperature of the infinite region outside the cylinder and the temperature of the interior of the cylinder, a is the radius of the cylinder, k is the thermal diffusivity, x, y are the Cartesian coordinates in the horizontal plane, and the infinite cylinder is defined by $|x| < a, |y| < a$. If measurement is made at the center of the hole ($x = 0$, $y = 0$), the temperature becomes a function of time only:

$$T(t) = \Delta T\left(\operatorname{erfc}\frac{a}{\tau}\right)^2. \quad (2)$$

In physical terms, ΔT is the difference between true formation temperature T_f and the temperature of the mud T_m circulating near the base of the well (Figure 1). Thus, the BHT, measured as a function of time after drilling of the well has been completed and circulation has ceased, may be written as

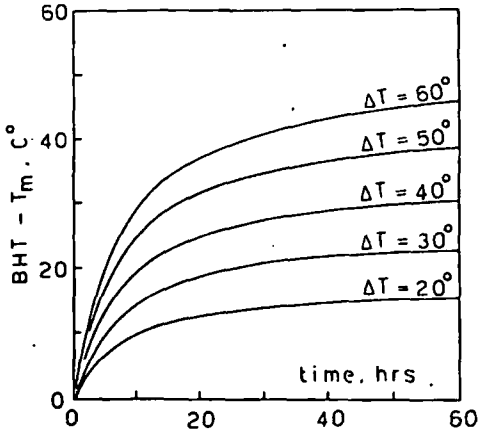

FIG. 2. Set of thermal stabilization curves, based on equation (3), which can be used for rapid determination of formation temperature by superposition on BHT-time data plotted at the same scale. Borehole radius and thermal diffusivity are assumed to be 10 cm and 0.01 cm²/sec, respectively.

$$\mathrm{BHT}(t) = T_m + \Delta T\left(\operatorname{erfc}\frac{a}{\tau}\right)^2, \qquad (3)$$

where $\Delta T = T_f - T_m$, and T_m is the temperature of the mud at the base of the hole when circulation has stopped. An implicit assumption of this model is that there are no sources or sinks of heat near the bottom of the well for $t > 0$.

A set of curves, based on equation (3), which can be used for rapid estimation of formation temperature by superposition on observed BHT-time (after end of circulation) data plotted at the same scale, is presented in Figure 2. Borehole radius a and thermal diffusivity k are assumed to be 10 cm and 0.01 cm²/sec, respectively. The field data plot, which is BHT versus time, is placed over Figure 2 with the vertical

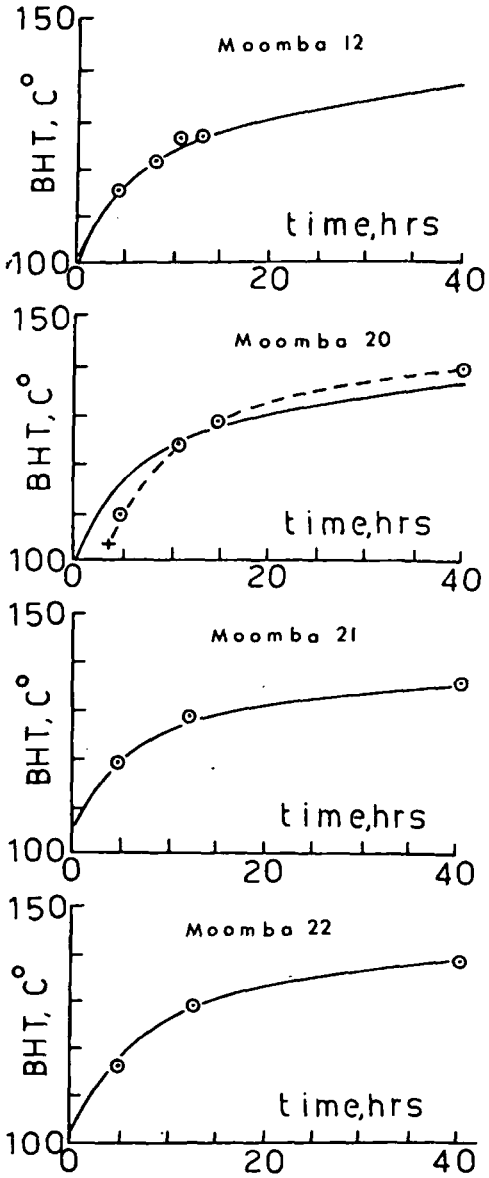

FIG. 3. BHT from wells in the Moomba field versus time after circulation ceases, with model curves.

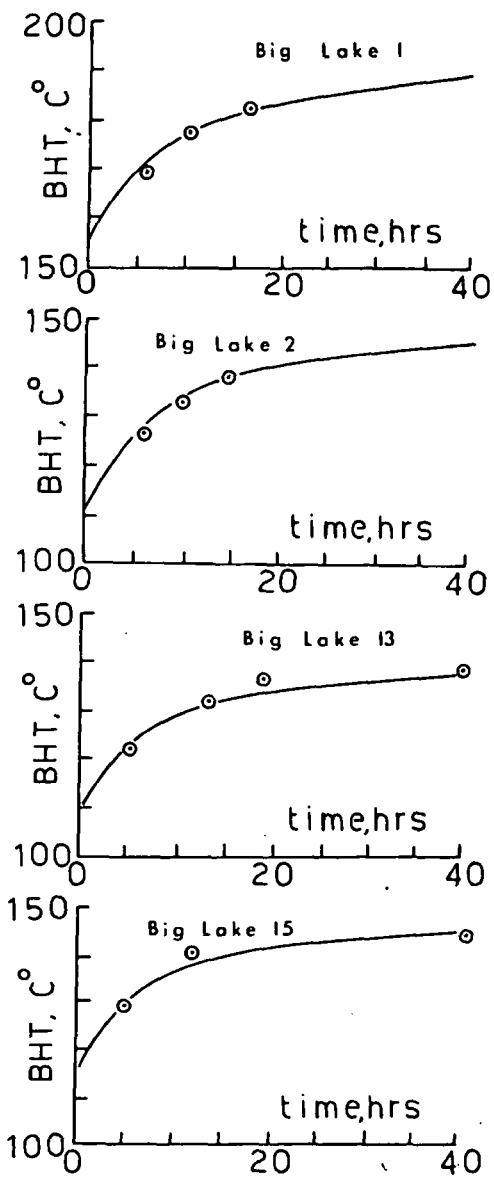

FIG. 4. BHT from wells in the Big Lake field versus time after circulation ceases, with model curves.

Table 1. Depths of BHT measurements and values of T_m and T_f for model curves in Figures 3 and 4.

Well	T_m(°C)	T_f(°C)	Depth (km)
Moomba 12	100	150	2.544
Moomba 20	100	150	2.486
Moomba 20	104*	154*	2.486
Moomba 21	106	146	2.476
Moomba 22	102	152	2.478
Big Lake 1	154	204	3.068
Big Lake 2	110	160	2.498
Big Lake 13	109	149	2.639
Big Lake 15	117	157	2.517

*—dashed curve in Figure 3.

axes superimposed. The curve best fitting the data gives ΔT, and T_m is the ordinate value on the field plot that corresponds to the origin in Figure 2 (BHT $- T_m = 0$, time = 0). Then T_f is given by

$$T_f = T_m + \Delta T.$$

This method is used to obtain T_m and T_f in Table 1 as well as the curves in Figures 3 and 4 in the following section.

RESULTS

The BHT stabilization model expressed as equation (3) is consistent with thermal recovery data from wells in the Moomba and Big Lake gas fields in the Cooper Basin in South Australia. More than 40 wells have been drilled in these two fields by rotary rigs to depths often exceeding 2.5 km; wells, in general, were spudded with a diameter of 44.5 cm, decreased to 31.1 cm in the central portion of the hole (typically between depths of 150 to 2000 m), and drilled to total depth with a diameter of 21.6 cm. The economic singificance of these fields has been discussed by Greer (1965), Kapel (1966), Martin (1967), and Thornton (1973). Data from four wells in the Moomba field are shown in Figure 3; model curves from Figure 2 are superimposed on the observed data. Comparable data for the Big Lake field are shown in Figure 4. Values of T_f and T_m for each model curve are tabulated in Table 1. Thermal diffusivity k is taken as 0.01 cm²/sec, which is typical for most

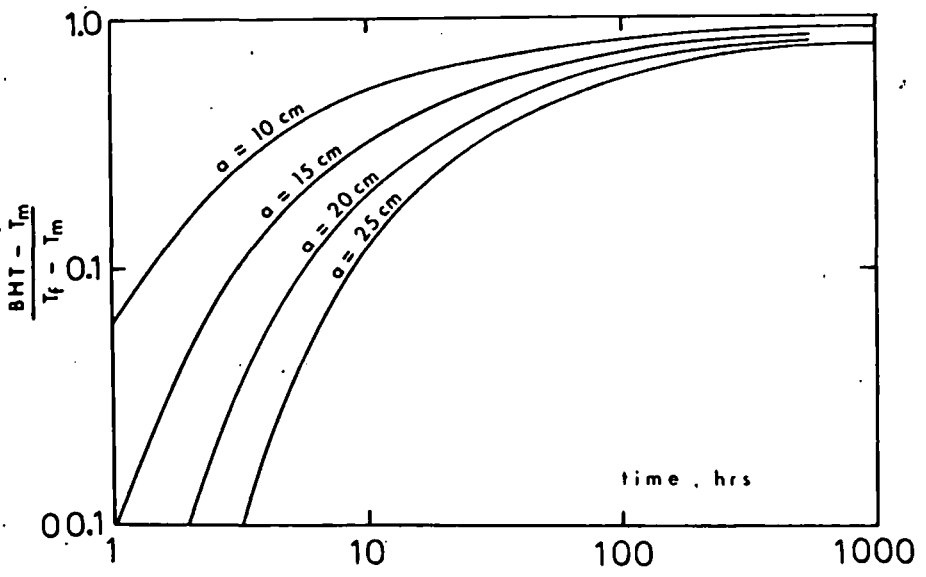

FIG. 5. Asymptotic behavior of the thermal stabilization model for various well radii a from equation (3).

sediments (Kappelmeyer and Haenel, 1974, p. 211; Carslaw and Jaeger, 1959, p. 497) and a radius of 10 cm is appropriate for all wells.

The data from Moomba 20 suggest that temperature stabilization did not commence until several hours after cessation of whole-well circulation. The dashed curve matched to these data (Figure 3) is based on the assumption that circulation at the base of the well did not cease until four hours after cessation of whole-well circulation; continued convection cells deep in the well can account for such an effect (Gretener, 1967). Although the dashed curve fits the data better than the solid curve, the quantity and accuracy of the data are not sufficient to permit distinction between models. The difference in T_f between both models is only 4°C, or 2.6 percent.

The asymptotic behavior of equation (3) is illustrated in Figure 5 for various well radii a. Clearly, after 72 hours the BHT has recovered to within 5 percent, and after 1000 hours (approximately 42 days) the BHT is within 1 percent of the true formation temperature, if T_f is assumed to be 150°C and T_m to be 100°C. These numbers are generally in agreement with those quoted by Kappelmeyer and Haenel (1974, p. 186).

CONCLUSIONS

The consistency of the temperature correction scheme represented by equation (3) with the data from the Moomba and Big Lake gas fields attests to the adequacy of the model for thermal recovery in deep wells. The qualifying conditions are essentially that (1) circulation of mud at the base of the hole stops almost immediately after drilling has ceased, (2) circulating groundwater does not disturb the thermal conditions after drilling has stopped, (3) measurement of BHT is made sufficiently far above the base of the hole (a few meters) that radial flow of heat only effectively occurs, and (4) the temperature of the mud in the bottom of the well (and preferably over several tens of meters) is approximately constant. These conditions are often physically realized in deep wells and enable reliable estimates of mud and true formation temperature to be obtained simply from a small number of time-sequential temperature measurements.

ACKNOWLEDGMENTS

Dr. D. A. Falvey, Dr. D. W. King, and Dr. D. W. Emerson of the University of Sydney offered useful suggestions in the preparation of this manuscript. I would like to thank Delhi International Oil Corporation for making these BHT data available.

REFERENCES

Bullard, E. C., 1947, The time necessary for a bore hole to attain temperature equilibrium: Month. Not. Roy. Astr. Soc., Geophys. suppl., v. 5, p. 127–130.

Carslaw, H. S., and Jaeger, J. C., 1959, Conduction of heat in solids: Oxford, Oxford University Press.

Cheremenski, G. A., 1960, Time of reestablishing the thermal conditions disturbed by drilling a borehole: Izv. Geophys. Ser., trans. R. B. Mudge, p. 1801–1805.

Dowdle, W. L., and Cobb, W. M., 1975, Static formation temperature from well logs—an empirical method: J. Petrol. Tech., v. 27, p. 1326–1330.

Fertl, W. H., and Winchmann, P. A., 1977, How to determine static BHT from well log data: World Oil, v. 183, p. 105–106.

Greer, W. J., 1965, The Gidgealpa gas field: APEA J., v. 5, p. 63–68.

Gretener, P. E., 1967, On the thermal instability of large diameter wells—an observational report: Geophysics, v. 32, p. 727–738.

Jaeger, J. C., 1961, The effect of the drilling fluid on temperatures measured in bore holes: J. Geophys. Res., v. 66, p. 563–569.

Kapel, A. J., 1966, The Coopers Creek Basin: APEA J., v. 6, p. 71–75.

Kappelmeyer, O., and Haenel, R., 1974, Geothermics with special reference to application: Stuttgart, Gebruder-Borntraeger.

Martin, C. A., 1967, Moomba—a South Australian gas field: APEA J., v. 7, p. 124–129.

Parasnis, D. S., 1971, Temperature extrapolation to infinite time in geothermal measurements: Geophys. Prosp., v. 19, p. 612–614.

Pirson, S. J., 1963, Handbook of well log analysis: New York, Prentice-Hall, Inc.

Thornton, R. C. N., 1973, Lithofacies study on the Toolachee-Gidgealpa-Moomba-Big Lake area, Cooper Basin, South Australia: APEA J., v. 13, p. 41–48.

1980 Midcon Professional Program ← presented at
Dallas Convention Center, November 4-6, 1980

A MICROPROCESSOR CONTROLLED BOREHOLE DEVIATION TOOL

Gary G. Olson
President
OWL Technical Associates, Inc.
1111 Delaware Avenue
Longmont, Colorado 80501

SUMMARY

Mineral logging equipment is described as it pertains to borehole deviation logging and the significance of deviation of a borehole from the perpendicular is discussed. The difficulty of obtaining deviation logs prior to the development of the modern micro processor controlled Deviation Survey tool is mentioned and the modern tool is described. Finally a comparison between minerals and petroleum logging is presented and instrument adaptations are suggested which would provide advantages to the petroleum logging industry.

INTRODUCTION

As we are all aware, the micro processor has touched nearly every aspect of our lives. Since its advent in the early 1970's, the micro processor has appeared in such diverse products as the traffic signal and the microwave oven; the home computer and the automobile. Many of us have grown accustomed to the presence of micro processors , but too often they are regarded as devices most suitable for laboratory environments or home hobbyists. We sometimes suspect that the micro processors used in traffic signals or microwave ovens only behave because they are specially designed by super engineers.

Micro processors are rumored to be unreasonably sensitive to static electricity; we are told that chips mysteriously 'blow' and signal nuclear invasions; and that the last place in the world to find a successful application would be in a Wyoming dust storm.

In this paper I will describe a successful application of a general purpose micro processor to control an instrument that is intended to be used in a nearly uncontrolled field environment. It is used with locally generated power in mobile data acquisition vehicles in all kinds of weather. It survives hundreds of miles of driving over dirt tracks and when it arrives at the job site it can easily be operated by non-scientific personnel. And best of all, many of these instruments have survived the static charges of countless Wyoming dust storms.

First I will quickly describe a typical logging truck. Since Deviation Logging is of principal interest in this paper, we will discuss the problems presented by a borehole's deviation from the vertical. For the most part, we will emphasize the problem from the point of view of non petroleum borehole drilling applications, especially in the area of minerals exploration.

In passing, we will briefly examine earlier attempts to cope with measuring borehole deviation. We will then describe and discuss a modern Borehole Deviation Survey instrument which features a micro processor which performs real time computations and presents data to the operator.

Finally we will discuss some of the salient differences between minerals and petroleum logging and suggest some instrument modifications which would fulfill the petroleum logging needs.

THE LOGGING TRUCK

In many mineral exploration programs, boreholes are drilled and data is taken from them either by collecting core (or cuttings) or by logging the holes with electronic instruments. In the case of cuttings or core, a borehole is evaluated by visual inspection of the samples and by laboratory analysis of ore percentage, etc. In the case of logging, a probe (or sonde) containing transducers is lowered into the borehole at the end of a cable which is paid out by a winch. The cable contains one or more electrical conductors so that the probe can communicate with uphole instrumentation which conditions the signal for presentation to the operator.

Most commonly in the United States, a specially outfitted truck or van is used for logging. In the mineral exploration industry, this vehicle is typically a four wheel drive van or light truck. It is equipped with an AC generator for powering the instrument systems and a winch system which accomodates 2500 to 6000 feet of armored cable with 1 to 4 electrical conductors. In the instrument bay, the logging vehicle ordinarily provides an analog strip chart recorder and a digital strip printer for recording logged data. Most of these vehicles are equipped to run a basic suite of logs embodying electrical and radioactivity measurements which are made in the borehole.

THE BOREHOLE DEVIATION PROBLEM

Borehole deviation from the vertical, if not deliberate, is caused principally by formation effects or driller technique. Whatever the cause, the bottom of a deviated hole is usually not beneath the origin or collar. In the extreme case, the bottom may not even be beneath our prospect, but our neighbor's!

If our well is to be a producing water well, for example, we should evaluate whether the hole is straight enough that we can expect good pump shaft life.

Perhaps the most important reason of all to know the deviation of a hole in mineral exploration is to determine the real position of the ore intercept. This becomes most especially important during ore reserve evaluation and mine design programs.

Now let us amplify a bit on the ore reserve and mine design concept. For simplicity, we will use a relatively stylized approach. Let us assume that an exploratory borehole is known to have intercepted an ore body through the use of some coring or logging technique.

Now let us assume that management has decided to evaluate the extent of the ore body for purposes of reserves estimation. Additional holes are drilled in the area and logged. These 'development' holes are ordinarily spaced on some uniform grid which allows mapping and reserves calculation.

Assuming that the ore body is of high quality and extensive enough, then the mine design proceeds. From knowledge of the overburden formations, the required angle of the sides and hence the surface extent of the mine can be determined such that the entire economical ore body can be removed without removing excessive overburden (See Figure 1).

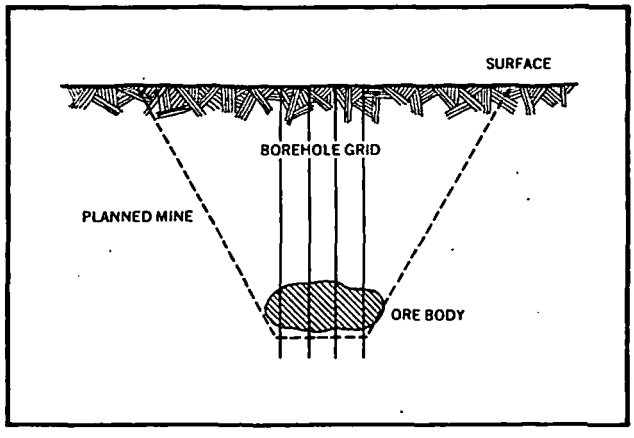

Figure 1. Ideal mine

If the boreholes are deviated significantly, then both the location and the depth of the ore body can be miscalculated. Since the borehole penetrates the ore body on a slant, the thickness is overestimated. Since the entire borehole slants, the true vertical depth to the ore body is overestimated. Worst of all, since the borehole isn't vertical, the ore isn't beneath the borehole pattern anyway.

Mines have actually been designed and constructed based upon the assumption that boreholes are straight (Figure 2). The chagrin of those involved is difficult to imagine.

When laterals are constructed in an underground mine to intercept the assumed location of the ore body, it is especially important to take borehole deviation into account in the development stage. Potential error is aggravated by the greater depths encountered in underground mine construction. For sake of completeness, it should be mentioned that lateral boreholes are often drilled and logged prior to extension of laterals. This helps to prevent disaster by permitting corrections to the mine design as the mine is being constructed.

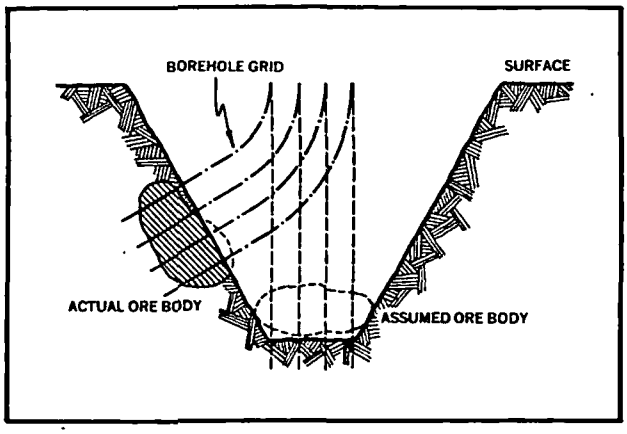

Figure 2. Non-ideal mine

OLD CAMERA AND FILM TOOL

Until a few years ago, only a small percentage of minerals exploration logged footage was also logged for deviation. Only when drilling in known or suspected problem conditions would the logging contractor be required to provide a deviation log. In order to provide such a log, the contractor would rent a version of a petroleum logging tool based upon camera and film.

In its 'multi shot' form, the camera and film tool records a photo of a hemispherical compass at known time intervals. The hemisphere is scribed with longitudinal lines of direction and latitudinal lines of inclination. The long axis of the tool is defined by a set of cross hairs, thus the inclination and direction of same can be determined for each photo. The tool must be motionless just before and during the exposure time, and the operator must keep a careful written record of the depth associated with each picture.

To be useful, a deviation log derived from a camera and film tool requires careful operator technique. To produce the deviation log, film developing facilities, a film reader, and hand (or calculator) computation of the individual points is required. This type tool's most important shortcoming for the mineral exploration industry is that there is no way for the operator to determine whether useable data have been obtained until after the film is developed. After several hours to a day, few mineral exploration boreholes can be reentered for logging again.

Modern Microprocessor Tool

Our company recognized the need for a direct reading deviation tool in the mineral logging industry approximately ten years ago. In late 1975, we judged that available transducers could be married with micro processor technology to produce such a tool. In 1977 we delivered the first prototypes and by now we have delivered tools throughout the western United States, and even have units working as far away as northwestern Africa and southeastern Asia.

Deviation surveys have become common place in the mineral logging industry within the past several years due to the availability of direct reading digital tools. We're firmly convinced that micro processor technology offers a rugged solution to many field instrumentation problems. The modern micro processor controlled tool is highly reliable in relatively unskilled hands and offers an extremely valuable additional log at a low incremental cost per hole.

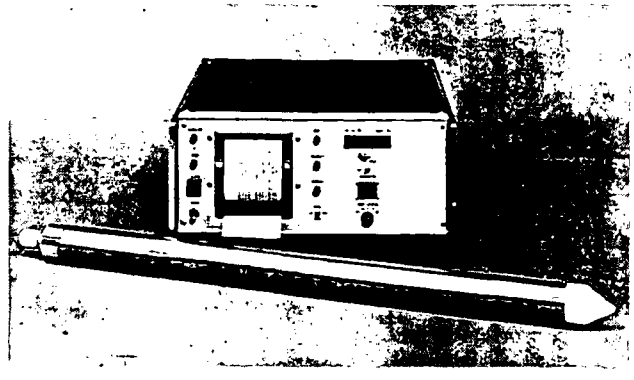

Figure 3. OWL Model 1275

Let us now examine our Model 1275 Micro Processor Controlled Borehole Deviation Survey Tool (See Figure 3). The heart of the system, of course, is the uphole electronics chassis which houses the micro processor, display, printer, and control switches. The micro processor receives variable data from the probe and winch systems, computes results, and sends data to the display. Data is also sent to the printer, either on command of the operator or automatically at selected depth intervals. Upon operator command, the processor also can compute the net directional bearing, the offset (or

closure) distance, and the true vertical depth of the probe, and send these data to the printer. Optionally, the micro processor also prepares the data in report format and sends it to the customer's page printer or recording device.

The downhole probe contains three transducers: X- and Y- axis inclinometers and a magnetic compass (See Figure 4). The probe also contains power and signal conditioning circuitry. An important feature of this probe is that data and power share a single electrical conductor. This feature makes it feasible to include other measurement parameters in the same probe string which use other available conductors.

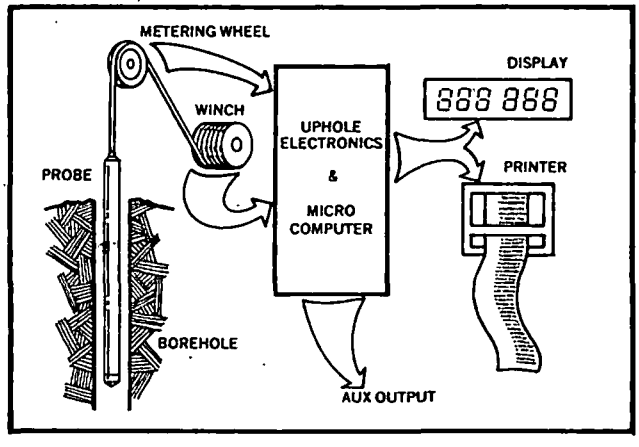

Figure 4. Model 1275 block diagram

The customers' logging winch systems each include a sheave or wheel of known circumference over which the cable passes enroute to or from the winch drum. Rotation of this 'metering wheel' signals the movement of cable by sending two pulse trains to the processor. The phase relationship between these pulse trains is used to determine whether the cable, thus the probe, is moving upward or downward in the borehole.

Visual LED displays are driven in a multiplex fashion by the processor system. The displays give the operator a continual visual presentation of the probe inclination and of the direction in which the probe is inclined.

Printed log information is recorded on an integral thermal strip printer. At depth intervals preselected by the operator, the processor system sends cable depth, probe inclination, and direction of inclination to the printer. The operator can also manually print at any time to record an ore intercept or the bottom of the hole, either of which may not come at a preselected interval.

An option frequently supplied with the tool is the capability of the processor to compute and print the probe position at any time. This is recorded on the printer as the directional bearing from the top of the hole to the probe, the offset distance to the probe, and the true vertical depth from the surface to the probe.

An optional serial output port can be furnished. This port provides data from the processor formatted into a report suitable for printing on an 80 column printer. The report-format data include a tabular presentation of cable depth, probe inclination and direction, true vertical depth, cumulative feet east or west and north or south, net closure distance and net bearing; along with suitable headings.

From the above discussion it can be seen that the processor performs a number of tasks, several of which may contend for the processor's attention at any point in time. The micro processor monitors completely asynchronous data from two sources, the downhole probe and the customer's cable length measuring system. It continually updates the display with the latest available probe inclination and direction and prints these data at selected cable length intervals.

The processor also maintains a running triangulation computation of the present probe position relative to the top of the borehole. Upon command it will print the directional bearing to the probe, the offset distance, and the true vertical depth from the top of the borehole to the probe's position.

MINERALS VERSUS PETROLEUM LOGGING

A few words are in order to compare minerals logging practices with those of petroleum logging, especially as the comparisons pertain to deviation logging.

Budget

Many mineral deposits present a rather small 'target', especially in comparison with hydrocarbon reservoirs. Accordingly, many boreholes must be drilled and logged in order to adequately define the deposit prior to mining. Indeed, thousands of holes are sometimes drilled during the development phase. Furthermore, the holes are drilled only for logging purposes. These considerations and others lead to a proportionately very small budget per hole. The effects of this low budget ripple throughout the mineral logging technology.

In contrast, most petroleum boreholes are drilled with the intent that they will become producing wells. They represent long term investments and accordingly boast a higher budget per hole.

Hole Size and Life

As suggested above, minerals boreholes are generally intended only for obtaining logging and sample information. A de facto U. S. standard hole size of 4 3/4 inches in diameter has developed, especially for the uranium and coal industry. This limits the maximum practical probe diameter to two inches. Further, since the holes have only a single purpose, namely to obtain data, generally little care is taken during drilling and the holes often collapse within a few hours.

Petroleum boreholes most often represent a long-term investment. An oil well might be expected to produce for 30 years. Therefore, the greatest of care is taken to design the drilling program to yield a permanent hole. It is of significantly larger diameter than a minerals borehole and usually much deeper.

When Surveyed

In minerals exploration, the borehole is usually drilled to completion and the drilling equipment is often removed prior to logging. Thus the entire deviation log must be obtained in one logging pass. It is often desirable to log other parameters during the same pass as well. Since the borehole probably won't exist a few hours from now, one must be able to immediately evaluate the log for reasonableness if he is to have the opportunity to relog the hole. For the same reasons, it is frequently desirable to log several parameters during the same logging pass.

Petroleum boreholes are often surveyed for deviation periodically during drilling. There may be no urgency about developing the log promptly, as the opportunity for further logging will usually present itself. Further, a 'single shot' configuration of the deviation tool may be adequate, since a knowledge of present deviation is often used to control future drilling of the same hole. Nevertheless, the potential for quickly surveying the entire drilled portion of the hole and obtaining a direct readout of the log shows potential for significant time savings.

Temperature and Pressure

The temperature in mineral exploration holes is almost always between 10 and 50 degrees centigrade, thus temperature stability and compensation are rarely a problem. Hydrostatic pressure on a probe rarely exceeds 200 atmospheres. Such pressures can be accomodated with pressure vessels of wall thickness. These temperature and pressure considerations favor relatively slim and inexpensive probe construction.

When extremely deep holes are encountered in petroleum drilling programs, very high temperatures and pressures are also encountered. Designing logging equipment to cope with these conditions inevitably increases the diameter and cost significantly, but represents a routine practice in the petroleum logging industry.

CONCLUSIONS

In the opening remarks, I mentioned that I would describe a successful application of a micro processor as a controller. By the way of concluding, let me indicate my perception of success. We have found the micro processor to be extremely reliable and hardy. Our instrument is routinely exposed to the vibration and shock of a motor vehicle moving on terrible roads. It is stored in the vehicle on sub-zero winter nights and locked up inside on the hottest of summer days.

We routinely burn in each new instrument for 100 to 200 hours. This period occasionally yields a few infant mortalities among all the integrated circuits. After the burn in period we've had only a scant handful of processor system failures. But for a couple of PROM's that dropped instructions, I think the only processor system failures have the very few peripheral chips that have mysteriously failed.

We have a three year track record of instrument performance, and we've had a modest share of transducer failures and mistreated equipment. From time to time we're embarrassed by quality control oversights. But we're not plagued with microprocessor problems.

Borehole deviation logging has become common place in the mineral exploration industry since the advent of direct reading digital deviation survey instruments. I submit that such instruments would not be possible without micro processor technology.

At least one of our customers is routinely offering deviation logging in oil and gas wells. He has taken pressure precautions and operates in non thermal wells in the depth range of 10,000 feet. I've offered a comparison between some aspects of the mineral and petroleum industry for your consideration.

Let me leave the reader with a challenge as a parting thought: We've only begun to think of micro processor applications in our mineral and petroleum logging industries. Properly applied, the micro processor offers solutions to problems that have plagued the industries for decades.

E-10

SUBJ
GPHYS
Log
MCD

MATRIX CHARACTERISTICS DEFINED BY POROSITY COMPUTATIONS

L. L. Raymer and W. P. Biggs
Schlumberger Well Surveying Corporation
Houston, Texas

Schlumberger E-10
1965

ABSTRACT

Accurate porosity determination is necessary for effective well evaluation. Several logging services are available for the computation of this necessary rock parameter; however, the interpretation of each is subject to inaccuracies caused by improper knowledge of the matrix or fluid characteristics. Since the various porosity devices, such as sonic, formation density, and neutron, are affected differently by matrix variations, combinations of logs from these tools frequently supply the data necessary for matrix identification.

When the matrix is composed of a single, but unknown, mineral, the mineral may be identified by a comparison of data from two appropriate porosity devices. In horizons containing a mixture of two known matrix minerals, this comparison may be used to determine the percentage of each. Once the rock matrix is identified, a reliable value of porosity can be computed.

Although the matrix may usually be identified through the use of any two porosity tools, better resolution is obtained with a proper selection. For example, in the sand and shale sequences of the Gulf Coast, the sonic and formation density logs are most appropriate. In predominantly carbonate areas, the neutron and formation density logs are generally recommended. Field examples show the relative efficiencies of the various combinations for different rock sequences.

INTRODUCTION

Formation porosity determinations have been improved and greatly simplified by the introduction and application of sonic, density, and neutron logging devices. The conditions under which each of these tools may be efficiently operated are well documented. A number of publications explain the various methods of using the logs to determine porosity. It is not the purpose of this paper to again treat these basic techniques; rather, it will be shown that the individual logs complement each other--that unknown or mixed matrix conditions may be solved by comparison of one porosity log with another.

While each of these three devices is responsive to porosity variations, each is also affected by matrix and fluid parameters. To accurately employ the individual logs for porosity determinations, it is necessary to assume values for these variable parameters. In many cases the formation characteristics are sufficiently well known to permit effective computations. On wells in which there is little knowledge of formation characteristics, errors in interpretation can result.

Although each device is affected by, for example, the mineral nature of the matrix, the effects on the devices are different. Through cross-plots of data from two porosity logs, the different effects can be resolved, and both porosity and matrix characteristics defined. Thus, for those wells in which formation characteristics are not well known, a judicious selection of two of the porosity-sensitive devices will enable more accurate computations--and greater confidence in the interpretation. The best combination of logs is the one in which the greatest resolution is possible--the one that most sharply differentiates between the lithologies that are more apt to be encountered. The following discussions illustrate the applicability of the various possible log combinations under a variety of field conditions.

DENSITY VS SONIC

The chart in Fig. 1 was prepared to facilitate the comparison of data from density and sonic logs. Characteristic responses of some of the more common matrix minerals are shown on a cross-plot of bulk density versus sonic transit time. These responses are indicated for various porosity values for each mineral. To construct the chart the density of the fluid in the zone investigated has been taken equal to 1.00 gm per cc. The grain densities and matrix velocities used for the various minerals are listed in Table I. To relate sonic transit time to porosity, the time-average formula was used, taking the fluid velocity as 5300 ft per sec.

TABLE I

Mineral	Grain Density gm/cc	Matrix Velocity ft/sec
Sandstone	2.65	18,000
Limestone	2.71	22,000
Dolomite	2.87	24,000
Anhydrite	2.98	20,000
Gypsum	2.35	19,000
Salt	2.03	15,000

A glance at Fig. 1 is sufficient to indicate that anhydrite, gypsum, and salt are readily distinguished one from another, and also from the more common reservoir rocks. While sandstone, limestone, and dolomite can be easily distinguished from the evaporite minerals, the resolution between these common reservoir rocks is less pronounced. As noted later, use of the sonic time-average relationship in carbonates often calls for fictitiously high fluid velocities, probably a result of the effect of vugular-type porosity.

Shale, because of wide variations in characteristics, is not plotted on this chart. In general, it may be stated that shales will usually exhibit density and sonic properties that will lead to a plot to the right of the line shown for dolomite.

Shaly Formations

The sandstone line in Fig. 1 will yield good values of porosity from either density or sonic data in clean and compacted sand formations. It is assumed, of course,

that the fluid and matrix characteristics used in the construction of the chart are appropriate. However, if the sand contains shale it is probable that corrections will have to be applied to the apparent values of porosity derived from either device. The density log, in most cases, indicates an apparent porosity in shaly sands that is close to the effective porosity of the zone. If the density of the shale is 2.65 gm/cc, the porosity indicated by the density log will be the effective porosity; for other shale densities errors will result.

The subject of shaly sand treatment through comparisons of density and sonic data was extensively covered in a recent paper.(1) In that paper, techniques were offered both for the solution of an interlaminated sand and shale model and for the solution of a sand with dispersed clay. For a more thorough treatment of this subject than will be presented here, it is recommended that the referenced paper be consulted.

Interlaminated sand and shale: One technique that has been effective in sand, shaly sand, and shale zones is a cross-plot of density and sonic data. Such a technique assumes interlaminated sand and shale beds, with the included shale having the same characteristics as the shale chosen for the control point. These comparisons are particularly helpful in wells drilled with oil-base muds, where the SP is not available. Even in wells drilled with water-base muds, however, the comparison of density vs sonic data affords a more accurate evaluation of porosity and shale content.

Since the density and sonic character of shale varies it is necessary to construct a cross-plot for each individual well and, possibly, for different geological horizons in a single well. The point for zero-porosity sand is plotted at the sand-grain density of 2.65 gm per cc and sand matrix transit time of 55.5 micro-seconds per foot. With this as an anchor point, a line is drawn through other porosity values as computed with the customary formulas. Then, from the sonic and density logs, an appropriate value of transit time and one of bulk density are chosen for the shales near the zone under study. These values are plotted to indicate a shale point. With these control points plotted, the data for zones under study are read from the logs and plotted. Applying a proportionality principle, the relative shale content and the effective porosity of each zone may then be graphically determined.

Portions of logs recorded in a Gulf Coast well are shown in Fig. 2. The well was drilled with a water-base, oil-emulsion mud. In addition to the Induction-Electrical Survey, both sonic and density logs were recorded. Density and transit-time values were read for twenty levels in the illustrated log sections. Fig. 3 is the cross-plot of data on the selected levels. The shale control point was located using a density value of 2.22 gm/cc and a transit-time value of 127 micro-sec/ft. Since the illustrated section is not sufficiently compacted for direct application of the time-average equation, the porosity scale for sonic measurements was corrected in the customary manner, using a $c\Delta tsh$ correction(2) of 120 micro-sec/ft. With the aid of the proportionality grid, the indicated values of effective porosity and per cent of shale content may be read for each plotted level.

Sands with dispersed clay: The paper by Alger, et al. offers a different approach for the treatment of sands with dispersed clay. As in the case of the

interlaminated sand and shale model, it is necessary to make several simplifying assumptions. First, it is assumed that the density of the clay is equal to the grain density for sand. On the basis of this assumption, the density log directly affords a value of effective porosity. The second assumption is that the clay and formation fluids occur as a slurry and, as such, exhibit a sonic velocity equal to that of the fluid alone. Thus, the sonic reading affords a value of total porosity that includes both the clay- and fluid-filled fractions of bulk volume. With both density- and sonic-derived values of porosity it is then possible to compute q, the fraction of intergranular space occupied by clay.

$$q = \frac{\phi_z - \phi}{\phi_z}$$

where ϕ_z = "total porosity," including volumes occupied by both clay and water. Value computed from sonic readings.

ϕ = effective porosity as determined from density log.

While the above assumptions are obviously oversimplifications, the technique has been found effective in dispersed-clay sands that are not extremely dirty. Experience indicates that a dispersed-clay sand exhibiting a value for q greater than 50 per cent will have too low a permeability for production.

Fig. 4 illustrates the graphical expression of the assumptions made in the dispersed-clay method. The plotted points are taken from the logs in Fig. 2 and are plotted with the same coordinates as on Fig. 3. The lines of effective porosity, which are based upon density-derived values, are horizontal. The lines corresponding to the various values of q converge at the sand matrix point.

The results of the plots are shown in Table II. For comparison, data are also shown on the analysis of cores (diamond core bit) and on the apparent porosities indicated individually by the density and sonic logs. At the cleaner levels all techniques are in close agreement. However, in the shalier zones the value of effective porosity obtained from the cross-plot in Fig. 3 is in much better agreement with core porosities than either of the values obtained directly from the individual logs. For example, at level 9 the sonic log indicates an apparent porosity of 38 per cent and the density log one of 32.5 per cent. This cross-plot indicates this zone to be shaly with an effective porosity of 25 per cent. This agrees more closely with the 23 per cent obtained from core analysis. It thus appears that this zone is more appropriately treated with the interlaminated method.

On the cross-plots, level 13 falls to the left of the clean sand line. This apparent discrepancy is caused by the limy nature of the interval. The interval corresponding to level 8 is also known to be limy.

Clean shale intervals are not always available for the definition of the shale point. The Gallup formation of the San Juan Basin is a silty shale with occasional

sand or lime streaks. The logs from a well in this section are shown in Fig. 5. In this case there was no attempt made to arbitrarily select a shale point. Instead, a number of levels were selected and the data were plotted. Following the plotting, it was apparent that a clean shale could be expected to have a density less than 2.50 gm/cc and a transit time greater than 94 micro-sec/ft. In the absence of more positive data, these values were used for the construction of the grid. The plot of the data is shown in Fig. 6.

While the exact position of the shale control point is somewhat dubious, there is no doubt that the bulk of levels are very shaly and have little or no effective porosity. Only the interval at level 9 is indicated to be relatively clean; this level exhibits an effective porosity slightly less than 10 percent. This value was confirmed by core analysis, and the well was completed at this level for 132 BOPD. The dispersed-clay technique also indicates that only level 9 might be productive.

Level 11, which plots below the line of zero effective porosity, is a shaly lime streak. The cross-plotting technique will work equally well for shaly carbonate sections. In such applications it is necessary to use matrix values appropriate for the carbonate. Such steps have been successfully employed in the study of shaly chalk sections.

Carbonates and Evaporites

The density vs sonic cross-plot is also useful in the definition of evaporites in sand or carbonate intervals. Sections of logs through such formations are shown in Fig. 7. The well in which these logs were recorded is located in Canada. The formations are predominately limestone and dolomite, with both salt and anhydrite intervals.

Data from the logs in Fig. 7 were used in the cross-plot of density vs sonic shown in Fig. 8. The plot clearly defines levels 22 and 24 as salt and levels 1, 2, 6, 16, 18, 19, 20, 21, and 23 as anhydrite. The remaining levels are readily indicated as carbonate beds; however, the distinction between limestone and dolomite is not pronounced. The lines corresponding to these matrix minerals are quite close to each other; small errors in correlating and reading the logs, and slight variations in matrix or fluid parameters, can materially affect the interpretation. A better distinction between limestone and dolomite is usually achieved with a comparison of density and neutron data.

DENSITY VS NEUTRON

A chart for comparison of density and neutron data is shown in Fig. 9. The chart is similar in construction and purpose to the chart comparing density and sonic data in Fig. 1. The same density values for matrix and fluid parameters were used.

In this case, however, a neutron index, ϕ_N, is plotted versus the density data This neutron index is the apparent porosity determined from neutron log departure

curves for a limestone matrix. By plotting the porosity index, such variables as source type, source-to-detector spacing, borehole size, and fluid type are already normalized. The relationships between limestone, sandstone, and dolomite have been determined experimentally in the laboratory. Special test formations containing blocks of known lithology and accurately measured porosity were employed.

A comparison of Fig. 9 with Fig. 1 shows that a much better distinction between limestone and dolomite exists on the density-neutron chart. The distinction between limestone and sandstone is also more pronounced. Salt zones are still readily identifiable on the density-neutron plot. While the distinction between dolomite and anhydrite is less pronounced, it is sufficient to identify the anhydrite beds.

Carbonates and Evaporites

Fig. 10 is a cross-plot of density and neutron data as taken from the logs in Fig. 7. The neutron index scale is computed for a 9-in. diameter borehole. The evaporite beds are again readily distinguished. The accuracy of resolution in the carbonate levels is shown in Table III by a comparison of results from the cross-plot with a description of cores. Also shown is the interpretation of lithology based on the density-sonic comparison in Fig. 8. While there are several discrepancies, the agreement is quite good between the core description and either of the log comparisons; the agreement is a little better with the density-neutron interpretation.

Limestone and Dolomite

The zone shown in the logs of Fig. 11 is normally referred to as a limestone. The comparison of density and neutron data in Fig. 12, however, indicates that the section is predominantly dolomite. The analysis of cores from portions of this section confirm the interpretation. While the extensive chemical analysis necessary for exact determination of degree of dolomitization was not performed, the grain densities of the cores were obtained. Since limestone grain density is 2.71 gm/cc and that for dolomite is approximately 2.87 gm/cc, the measured values of grain density provide a basis for mineral identification.

Table IV presents a comparison of interpretations from log and core data. From the plot in Fig. 12 the porosity and lithology for each level are indicated. Corresponding core data of porosity and grain density are tabulated. A lithological description based upon the value of grain density is also shown. Agreement between the two techniques is excellent.

If only one of the porosity logs were interpreted, and the sections were erroneously presumed to be limestone, considerable errors in porosity would result. The density interpretation would indicate very low values of porosity, whereas the neutron would result in values that are too high. For example, level 5 would appear to have a limestone porosity of only 7 per cent from the density measurements; it would appear to have a porosity greater than 16 per cent by the neutron. The comparison of density and neutron data is very efficient in carbonate zones.

In this example, the plot of density vs sonic data (not shown) was not efficient in the definition of lithology. It did show the need for unusually high apparent fluid velocity for the application of the time-average relationship between porosity and transit time. Present evidence suggests that abnormally high fluid velocities are related to the existence of vugular-type porosity. This problem, often encountered in carbonate formations is discussed in the previously referenced paper by Alger, Raymer, Hoyle, and Tixier. However, the sonic log has proved to be a most effective adjunct to resistivity logging for saturation determinations. In addition, since the sonic log affords a less clear-cut distinction between limestone and dolomite, it provides good average values of porosity in carbonate zones. It is also not so subject to deleterious effects resulting from irregular hole size, thick mud cake, and variation in type of borehole fluid as are the other porosity devices.

Carbonates, Shale, and Glauconite

Another example of lithological definition is taken from a well in Ohio. The logs shown in Fig.13 are from a section previously thought to be composed of carbonates and shales. Zones with high gamma-ray deflection were assumed to be shales. A cross-plot of density and neutron data, shown in Fig. 14, indicates that only level 6 is actually a shale; the other higher-radioactivity intervals are glauconite. The shales of this locale normally indicate higher densities and larger values of neutron index than are observed in the glauconite zones, which characteristically exhibit a density of 2.3 gm/cc and a neutron index of approximately 20 per cent. The porosities and lithologies of the carbonate levels are again defined by the cross-plot of density and neutron data.

Potash Exploration

An interesting application of the discussed techniques is the location and identification of evaporites in potash exploration. Fig. 15 shows portions of the logs recorded in a well drilled for such a purpose. The potash minerals are characterized by relatively high radioactivities and are normally found in close association with beds of salt and anhydrite. The five fairly common potassium minerals are sylvite, carnallite, polyhalite, langbeinite, and kainite.

Fig. 16 is a cross-plot of density and neutron data as taken from the logs in Fig. 15. The characteristic points for each of the pure evaporites are indicated on the plot. Since the potash minerals are rarely found in the pure state--they are normally found mixed with salt (halite)--it is to be expected that the mixtures will plot at some point between that for the pure mineral and the point for salt. From the plots on Fig.16 it is apparent that at least two potash minerals, sylvite and carnallite, are present and that a third, langbeinite, might be present. Since level 16, the possible langbeinite zone, is one of low radioactivity on the gamma ray, it is obviously not a zone of langbeinite. Although the stringer is too thin to be positively identified, it is probably anhydrite. This interpretation is confirmed by core analysis.

The mineralogical interpretations of the density vs neutron data are compared with the core analysis data in Table V. The percentages of potash minerals were

estimated on the basis of the proportional displacements of the plots from the point for halite. The comparison is again excellent.

SONIC VS NEUTRON

The third possible combination of porosity logs is that of sonic and neutron.(3) While this combination can afford excellent results, it is somewhat less reliable than the other combinations. A primary source of error is the fact that shale affects both the sonic and neutron responses in a similar manner. In each case the occurrence of shale appears as an increase in porosity; there is no resolution such as that afforded by the density log.

The characteristic relationships between the sonic and neutron data for various lithologies and porosities are shown in Fig. 17. The matrix and fluid conditions assumed in this case are the same as used in the other basic relationship charts (Figs. 1 and 9). From the chart, it is apparent that clean sandstones should be readily distinguished from carbonates. The evaporite minerals are not so well defined as in the other combinations. In particular, anhydrite leads to a plot confusingly close to the line for limestone.

Fig. 18 shows the portions of gamma ray, neutron, and sonic logs recorded in the Devonian section of a well in the Four Corners area. This section is known to contain sandstone, limestone, dolomite, and various mixtures of the three. Using the gamma ray recording to eliminate shale zones, the sonic and neutron data for 21 levels have been read and plotted on Fig. 19. All of the levels fall between the customary lines for sandstone and dolomite.

In such a case as this, with three matrix minerals and only two porosity logs for control, interpretation is less reliable than if only two minerals are involved. A mixture of sandstone and dolomite could very well plot on the characteristic line for limestone. If the matrix is composed of a single (but unknown) mineral, identification can be made; or, if the level contains two known matrix minerals (and only two) the comparison of log data enables the determination of the relative percentage of each. In any event, whether one, two, or three of the matrix minerals are involved, the porosity determined with the cross-plot is considerably more reliable than one based on a single log. For example, level 8 plots close to the limestone line, at a value of 6 per cent porosity; this porosity value is also appropriate for a mixture of sandstone and dolomite.

A comparison of the lithologies indicated by the cross-plot with those obtained from examination of cores is given in Table VI. In the description of the cores, the preponderant mineral is listed. For the cross-plot, the lithology is determined on the basis of proximity to the various identification lines. Matrix velocities used in the chart construction were 18,000 ft/sec for sandstone and 24,000 ft/sec for dolomite. However, matrix velocities for sandstone and dolomite of 19,000 and 23,000 ft/sec, respectively, would agree more closely with the points that plot farthest away from the limestone line. Such values are within the ranges that have been observed in field application of the sonic logs. The agreement between lithologies from the two methods of analysis is very good.

CONCLUSIONS

When the matrix of a formation is comprised of an unknown mineral, or a mixture of two known minerals, comparison of data from two suitable porosity logs will define the lithology and afford good values of porosity.

Three combinations of porosity logs are presently available for such studies. The selection of logs for the comparison should be based on the lithologies that are most likely to occur. For sand-shale or limestone-shale sequences the density vs sonic comparison is most effective. For limestone-dolomite sequences the density vs neutron cross-plot is best. The neutron with either density or sonic data is effective in sandstone-dolomite sequences. Common evaporites may be effectively identified by either the density vs sonic or the density vs neutron techniques.

The techniques discussed in this paper are exclusively directed toward the identification of the matrix and the determination of porosity. Since these are only part of the information required for formation evaluation, the various two-porosity-log combinations should not be considered complete logging programs. However, from the examples and methods given, it can be seen that a second porosity log materially increases the effectiveness of log interpretation and promotes greater confidence in the results thereby obtained.

REFERENCES

1. Alger, R. P., Raymer, L. L., Hoyle, W. R., and Tixier, M. P.: "Formation Density Log Applications in Liquid-Filled Holes," Journal of Petroleum Technology (March, 1963).

2. Tixier, M. P., Alger, R. P., and Doh, C. A.: "Sonic Logging," Journal of Petroleum Technology (May, 1959).

3. Chambliss, G. F.: "Devonian Lithology Identification Utilizing Porosity Logs," Four Corners Geological Society Third Field Conference, Moab, Utah, October 5, 1960.

TABLE II

Fig. 2 Example

Level	Apparent Sonic Porosity	Dispersed-Clay Method: Effective Porosity from Density	Dispersed-Clay Method: q	Laminated Method: Effective Porosity	Laminated Method: p	Lithology Description	Core Porosity
1	45.0	27.0	40	3.0	95	Sh	
2	37.5	30.0	17	18.5	40	Shy-Sd	
3	44.5	26.5	40	2.0	95	Sh	
4	45.5	29.0	36	7.0	85	Sh	
5	43.0	26.0	40	.0	95	Sh	
6	50.0	32.5	35	10.0	90	Sh	
7	41.0	29.0	23	13.0	60	V. Shy-Sd	
8	21.5	19.5	8	16.0	15	Lmy-Shy-Sd	17.0
9	38.0	32.5	11	25.0	30	Shy-Sd	23.0
10	34.0	30.5	9	25.0	20	Shy-Sd	28.5
11	40.0	35.0	10	28.0	30	Shy-Sd	29.3
12	39.0	32.5	12	25.0	30	Shy-Sd	24.3
13	15.0	17.5	-	20.0	-	Lmy-Sd	18.5
14	34.0	32.0	4	31.5	10	Shy-Sd	32.0
15	27.0	27.0	0	27.5	0	Sd	27.5
16	33.0	35.0	0	35.0	0	Sd	
17	34.0	34.0	0	34.0	0	Sd	
18	35.0	35.0	0	34.0	0	Sd	
19	34.0	34.0	2	34.0	0	Sd	
20	34.5	35.0	0	35.0	0	Sd	

TABLE III

Fig. 7 Example

Level	LITHOLOGY: Sonic-Density	LITHOLOGY: Core Description	LITHOLOGY: Density-Neutron
1	Anhy	Anhy	Anhy
2	Anhy	Anhy	Anhy
3	Ls	Ls	Ls
4	Lmy Dol	Dol	Ls Dol
5	Ls	Ls	Ls
6	Anhy	Anhy	Anhy
7	Ls	Dol Ls	Ls
8	Ls	Ls	Ls
9	Lmy Dol	Lmy Dol	Dol Ls
10	Lmy Dol	Lmy Dol	Dol Ls
11	Lmy Dol	Ls	Ls
12	Ls	Dol	Ls
13	Dol	Ls	Dol Ls
14	Dol	Ls	Dol Ls
15	Dol	Ls	Ls
16	Anhy	Anhy	Anhy
17	Ls	Ls	Ls
18	Anhy	Anhy	Anhy
19	Anhy	Anhy	Anhy
20	Anhy	Anhy	Anhy
21	Anhy	Anhy	Anhy
22	Salt	Salt	Salt
23	Anhy	Anhy	Anhy
24	Salt	Salt	Salt

TABLE IV

Fig. 11 Example

	Density-Neutron Plot		Core Analysis		
Level	Porosity	Lithology	Porosity	Grain Density	Lithology
1	2.0	Anhy			
2	1.5	Anhy			
3	12.5	Dol			
4	9.0	Dol	10.1	2.86	Dol
5	13.5	Dol	13.4	2.86	Dol
6	10.0	Lmy Dol	12.3	2.83	Lmy Dol
7	18.5	Dol	17.6	2.76	Dol Ls
8	17.5	Dol	16.5	2.88	Dol
9	8.5	Dol	8.6	2.84	Lmy Dol
10	18.0	Dol	16.8	2.89	Dol
11	9.5	Dol	9.5	2.87	Dol
12	13.5	Dol	13.4	2.87	Dol
13	7.5	Dol			
14	15.0	Dol			
15	8.0	Lmy Dol			
16	7.0	Anhy	4.0	2.95	Anhy
17	25.5	Lmy Dol	24.5	2.83	Lmy Dol
18	3.0	Anhy	2.8	2.94	Anhy
19	27.0	Dol	26.0	2.90	Dol
20	7.0	Lmy Dol	6.9	2.86	Dol
21	12.0	Lmy Dol	14.0	2.87	Dol
22	5.5	Lmy Dol	4.9	2.83	Lmy Dol

TABLE V

Fig. 15 Example

LITHOLOGY

Level	Density-Neutron Plot	Core Description
1	Halite	Halite
2	Halite - 40% Sylvite	Halite - 30-45% Sylvite
3	Halite - 40% Sylvite	Halite - 20-80% Sylvite
4	Halite - 50% Sylvite	Halite - 20-80% Sylvite
5	Halite	Halite
6	Halite - 35% Sylvite	Halite - 20-35% Sylvite
7	Halite	Halite
8	Halite - 35% Sylvite	Halite - 20-65% Sylvite
9	Halite - 70% Sylvite	Halite - 65% Sylvite
10	Halite	Halite
11	Halite - 20% Sylvite	Halite - 50% Sylvite
12	Halite	Halite
13	Halite - 60% Sylvite	Halite - 10-30% Sylvite
14	Halite - 10% Carnallite	Halite - 2-15% Carnallite
15	Halite - 20% Carnallite	Halite - 2-15% Carnallite
16	Anhydrite	Anhydrite
17	Halite - 5% Carnallite	Halite - 0-10% Carnallite
18	Halite	Halite
19	Halite	Halite - 2% Carnallite
20	Halite	Halite

TABLE VI

Fig. 18 Example

LITHOLOGY

Level	Sonic-Neutron Plot	Core Description
1	Dol	Dol
2	Ls	Ls
3	Dol	Dol
4	Ls	Ls
5	Dol	Dol
6	Dol	Dol
7	Ls	Dol
8	Ls	Ls
9	Dol	Dol
10	Dol Ls	
11	Ls	Dol
12	Ss	Ss
13	Ls	Ss
14	Ss	Ss
15	Ss	Ss
16	Ls	Ss
17	Ss Ls	Ss
18	Ss Ls	Ss
19	Ss	
20	Ss	Ss
21	Ss	Ss

SONIC - DENSITY

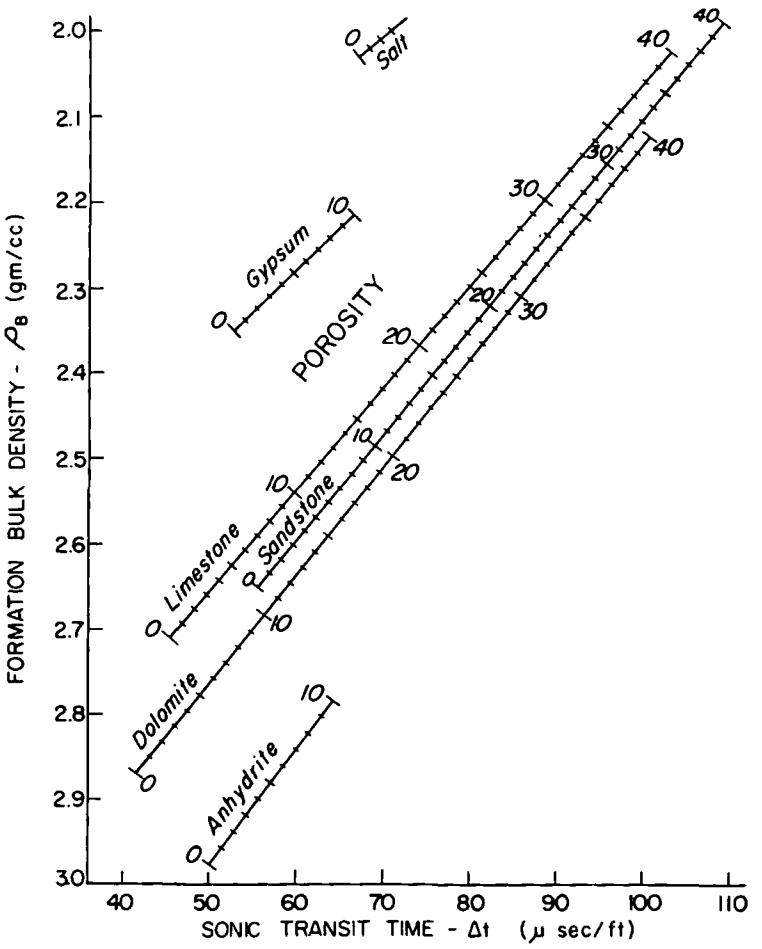

Fig. 1

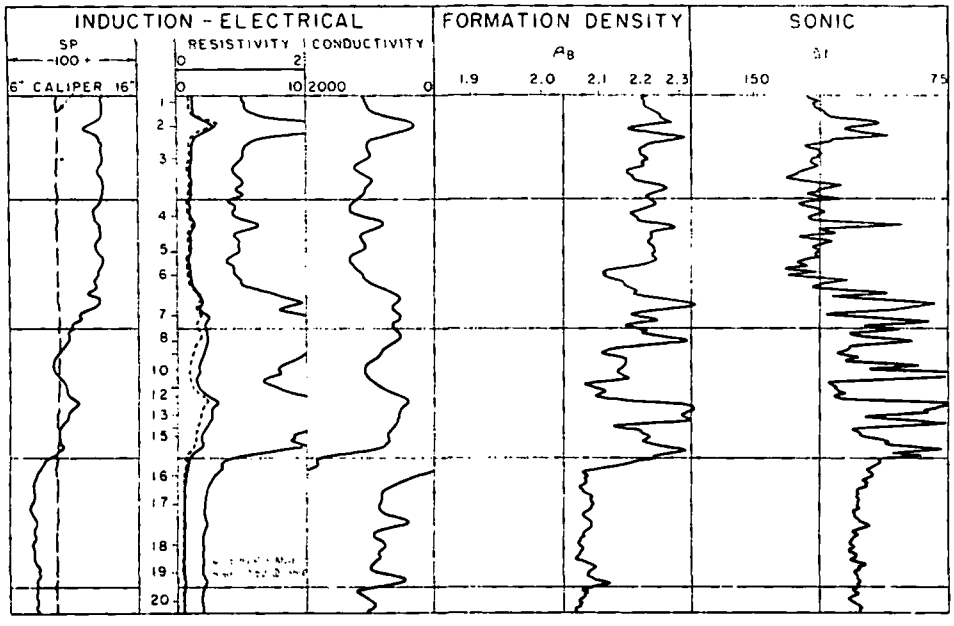
INDUCTION - ELECTRICAL
FORMATION DENSITY
SONIC
SP
-100 +
6" CALIPER 16"
RESISTIVITY
CONDUCTIVITY
0 2
0 10 2000 0
ρ_B
1.9 2.0 2.1 2.2 2.3
Δt
150 75
1 2 3 4 5 6 7 8 10 12 13 15 16 17 18 19 20

Fig. 2

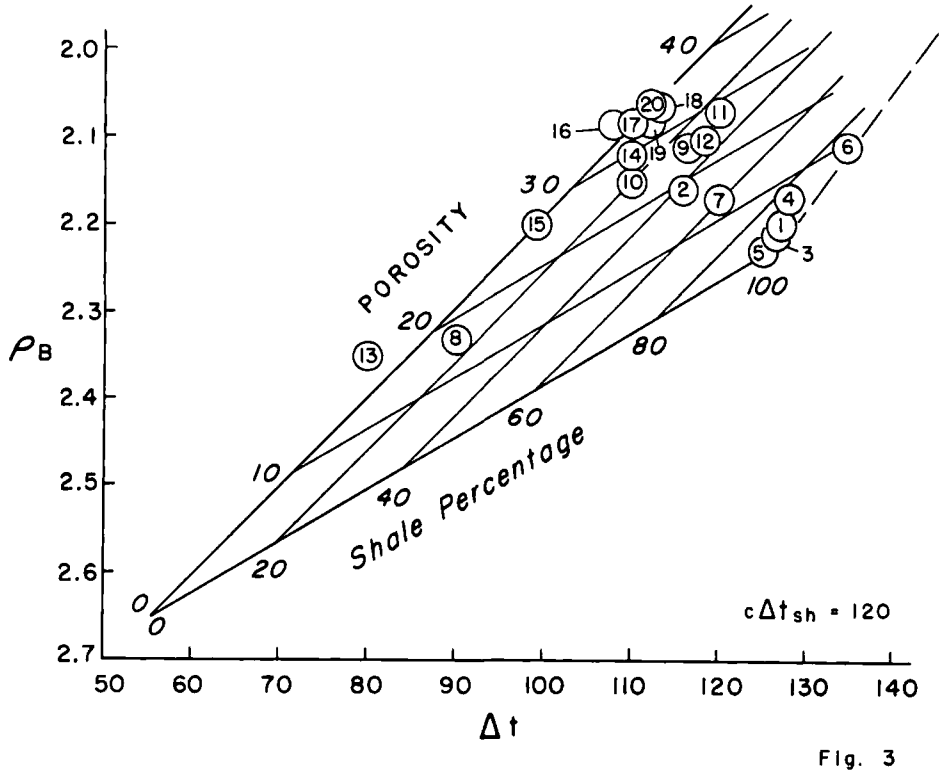
2.0
2.1
2.2
2.3
2.4
2.5
2.6
2.7
ρ_B
50 60 70 80 90 100 110 120 130 140
Δt
40
30
20
16
10
0
POROSITY
Shale Percentage
0
10
20
40
60
80
100
$c\Delta t_{sh} = 120$
20 18 11 17 16 14 19 9 12 10 2 7 6 4 1 5 3 15 8 13

Fig. 3

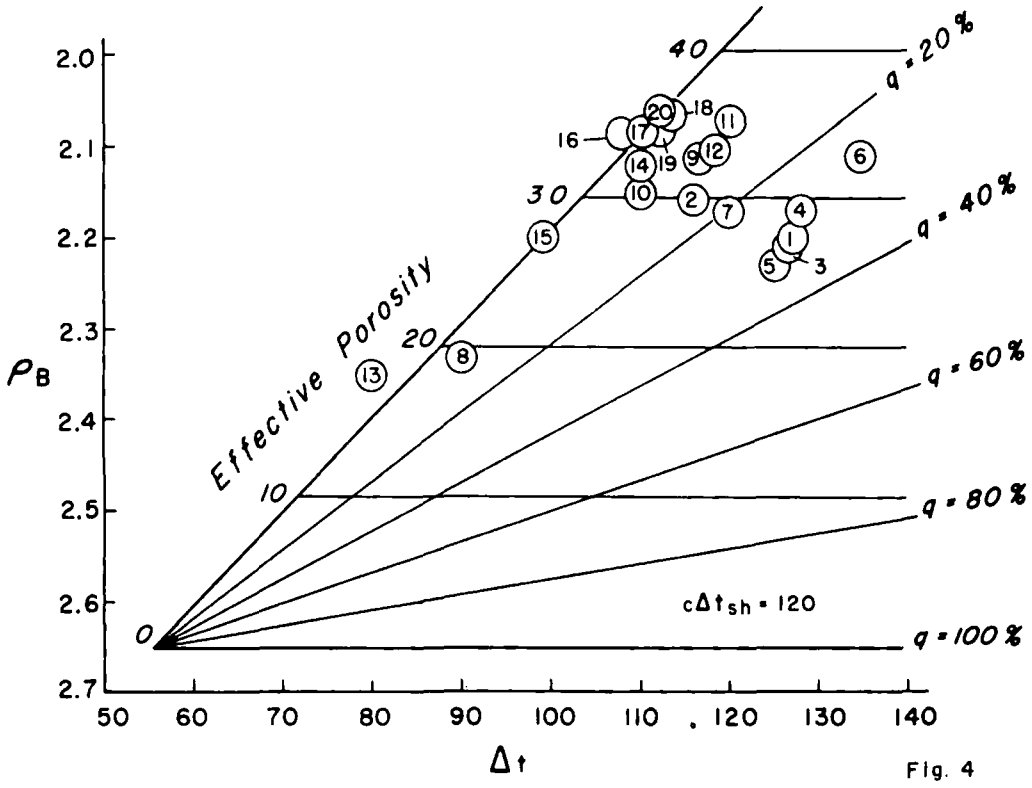
2.0
2.1
2.2
2.3
2.4
2.5
2.6
2.7
ρ_B
50
60
70
80
90
100
110
120
130
140
Δt
Effective Porosity
40
30
20
10
0
q = 20 %
q = 40 %
q = 60 %
q = 80 %
q = 100 %
$c\Delta t_{sh}$ = 120
1
2
3
4
5
6
7
8
9
10
11
12
13
14
15
16
17
18
19
20

Fig. 4

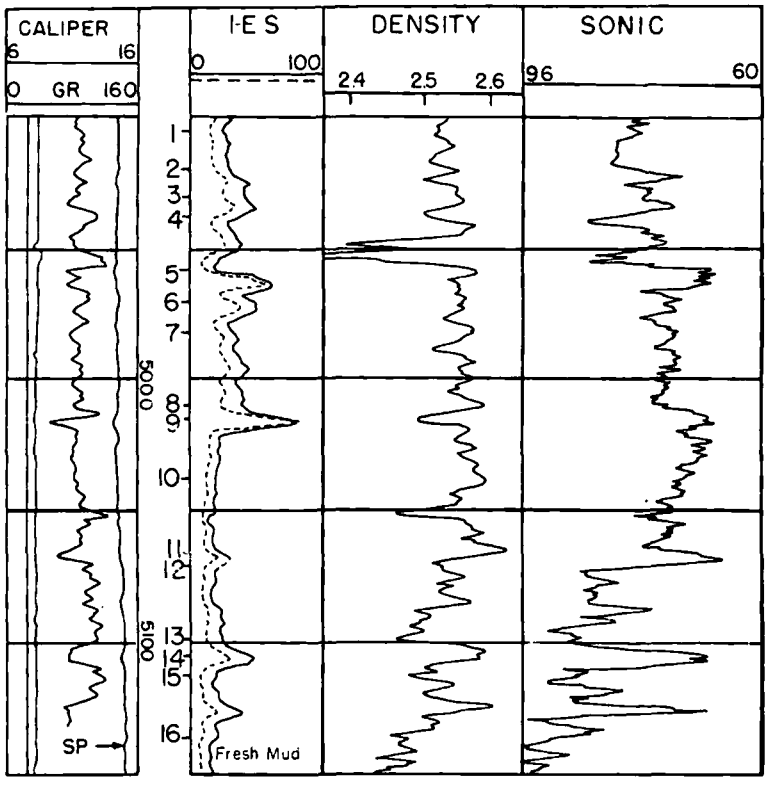
CALIPER
6
16
0 GR 160
I-E S
0
100
DENSITY
2.4
2.5
2.6
SONIC
96
60
5000
5100
SP
Fresh Mud

Fig. 5

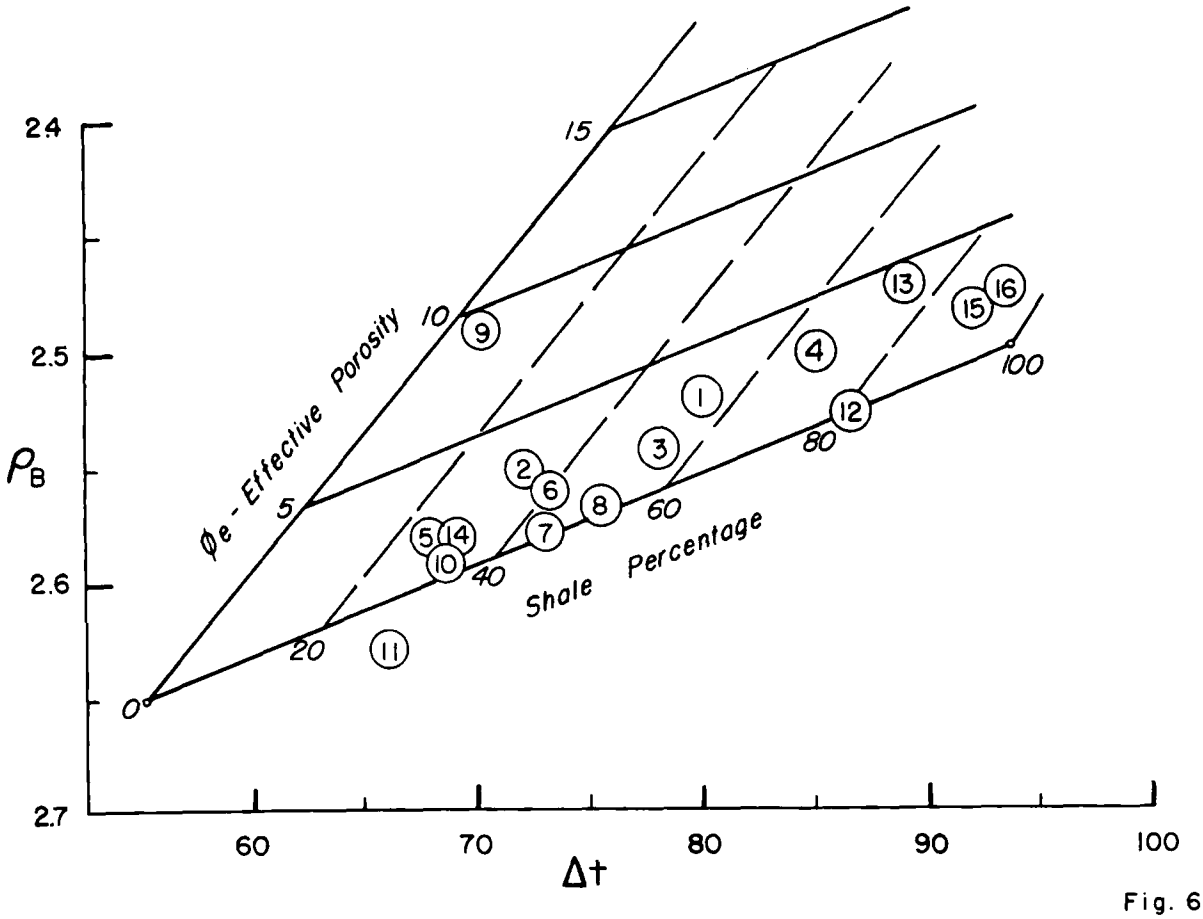
2.4
2.5
2.6
2.7
ρ_B
60
70
80
90
100
Δt
15
10
5
0
20
40
60
80
100
Øe - Effective Porosity
Shale Percentage
1
2
3
4
5
6
7
8
9
10
11
12
13
14
15
16

Fig. 6

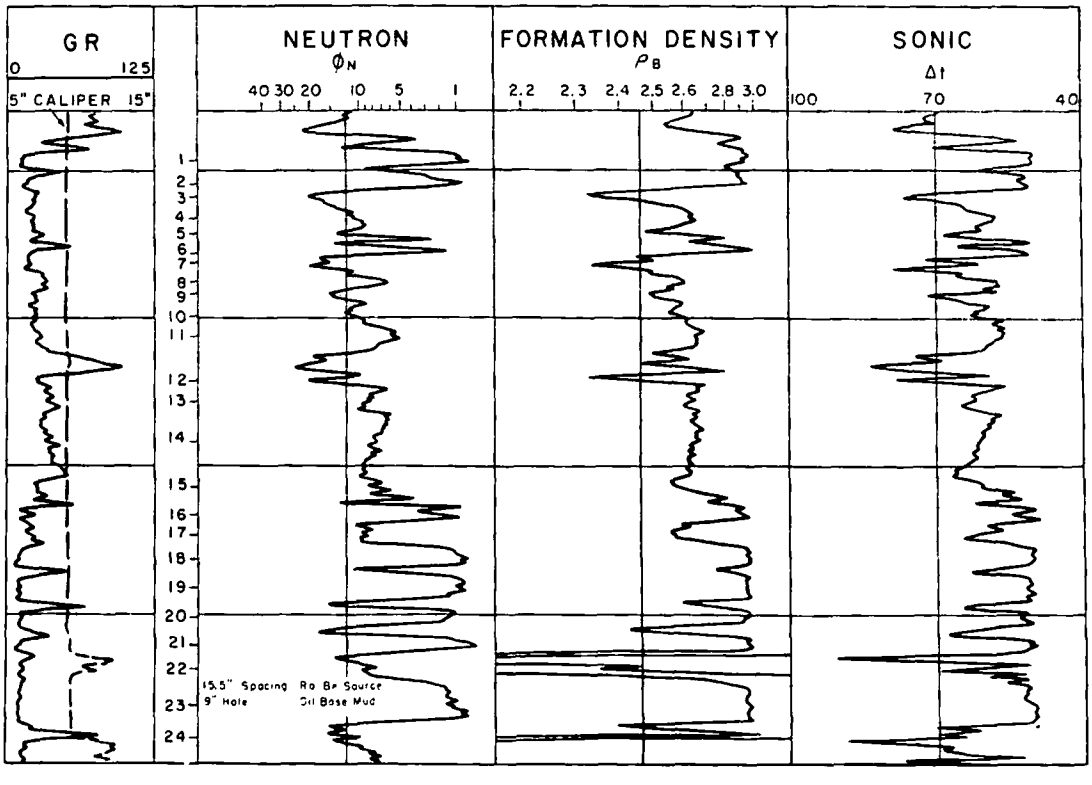
GR
0 125
5" CALIPER 15"
NEUTRON
ϕ_N
40 30 20 10 5 1
FORMATION DENSITY
ρ_B
2.2 2.3 2.4 2.5 2.6 2.8 3.0
SONIC
Δt
100 70 40
15.5" Spacing Ra Br Source
9" Hole Oil Base Mud

Fig. 7

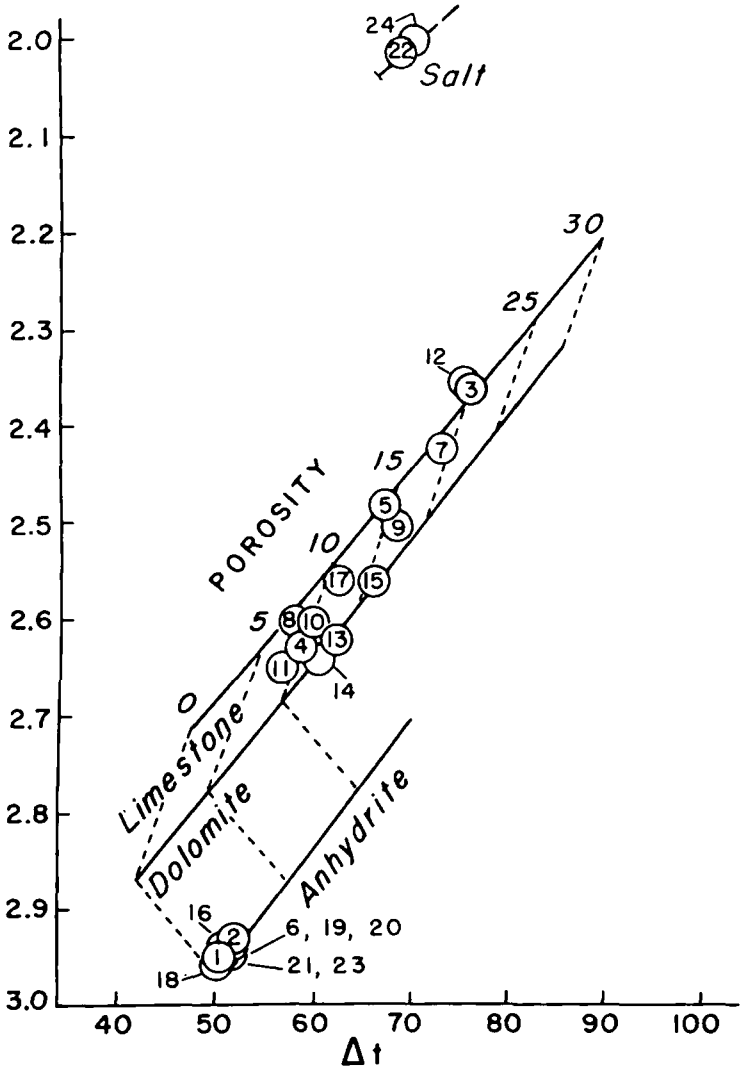
2.0
2.1
2.2
2.3
2.4
2.5
2.6
2.7
2.8
2.9
3.0
ρ_B
40
50
60
70
80
90
100
Δt
Salt
Limestone
Dolomite
Anhydrite
POROSITY
0
5
10
15
25
30
1
2
3
4
5
6, 19, 20
7
8
9
10
11
12
13
14
15
16
17
18
21, 23
22
24

Fig. 8

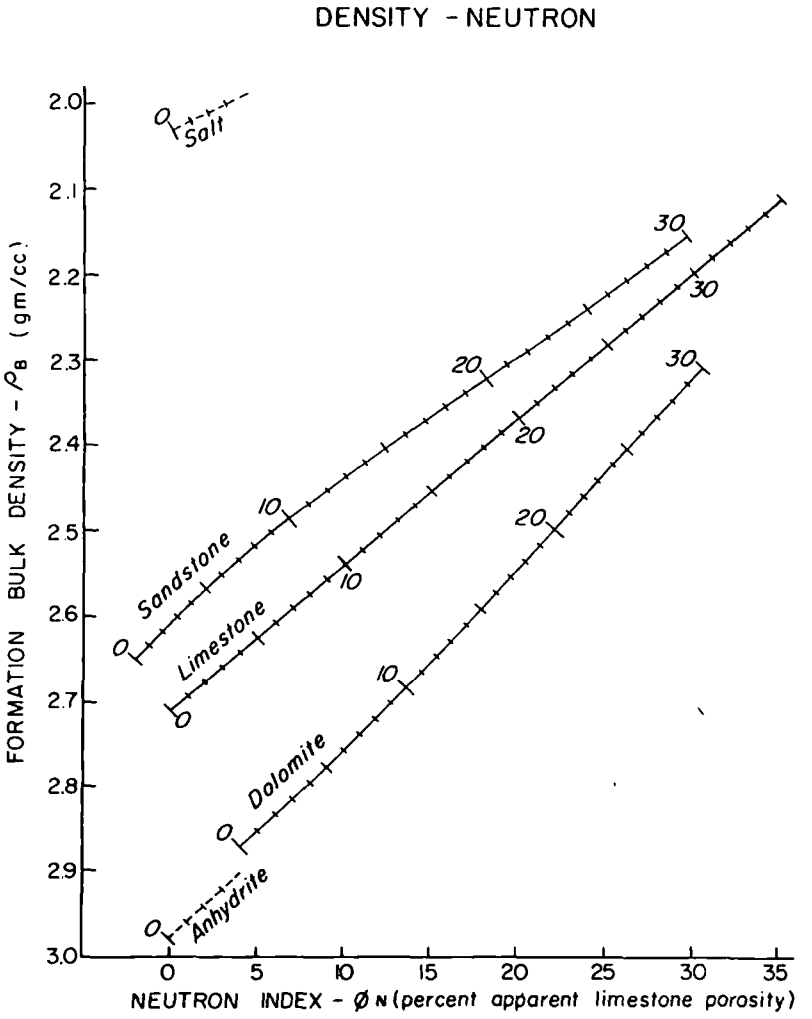
DENSITY - NEUTRON
FORMATION BULK DENSITY - ρ_B (gm/cc)
2.0
2.1
2.2
2.3
2.4
2.5
2.6
2.7
2.8
2.9
3.0
0
5
10
15
20
25
30
35
NEUTRON INDEX - ϕ_N (percent apparent limestone porosity)
Salt
Sandstone
Limestone
Dolomite
Anhydrite
0
10
20
30

Fig. 9

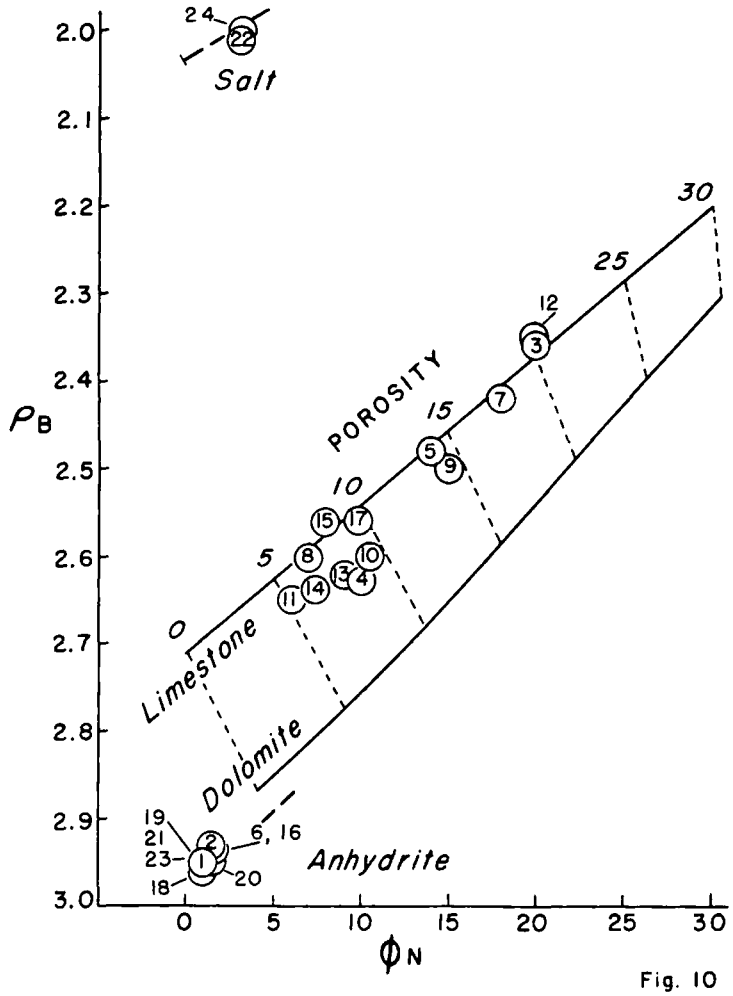
Salt
Limestone
Dolomite
Anhydrite
POROSITY
0
5
10
15
25
30
ρ_B
ϕ_N
2.0
2.1
2.2
2.3
2.4
2.5
2.6
2.7
2.8
2.9
3.0
0
5
10
15
20
25
30

Fig. 10

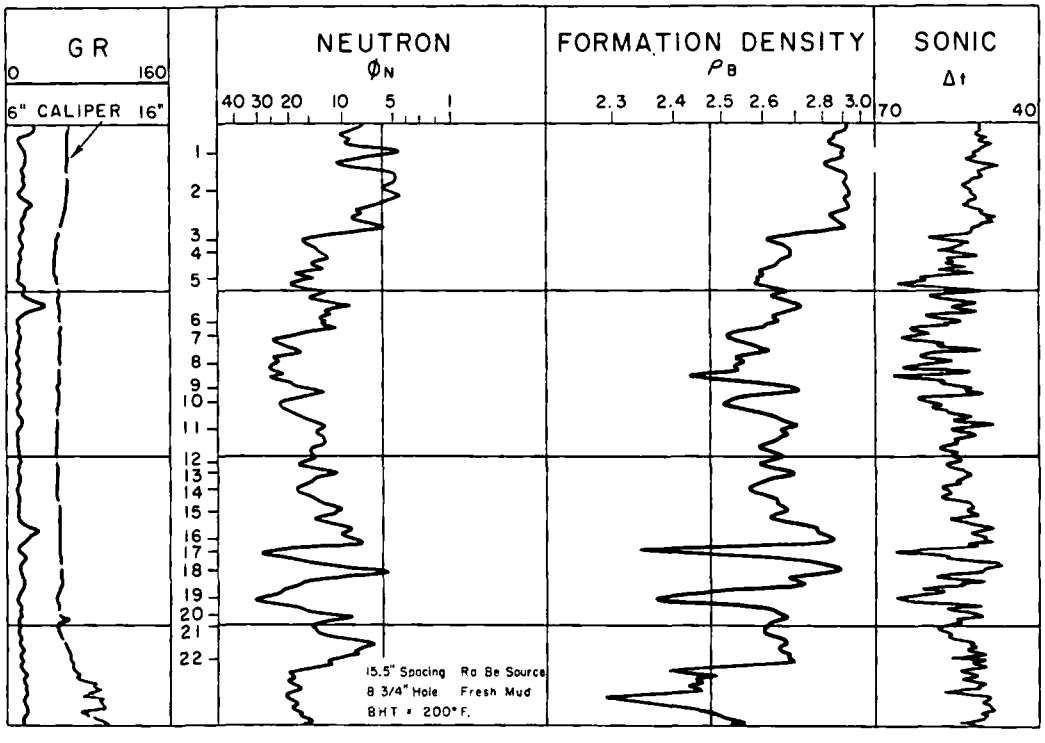
GR
0
160
6" CALIPER 16"
NEUTRON
ϕ_N
40 30 20 10 5 1
FORMATION DENSITY
ρ_B
2.3 2.4 2.5 2.6 2.8 3.0
SONIC
Δt
70
40
15.5" Spacing Ra Be Source
8 3/4" Hole Fresh Mud
BHT = 200°F.

Fig. 11

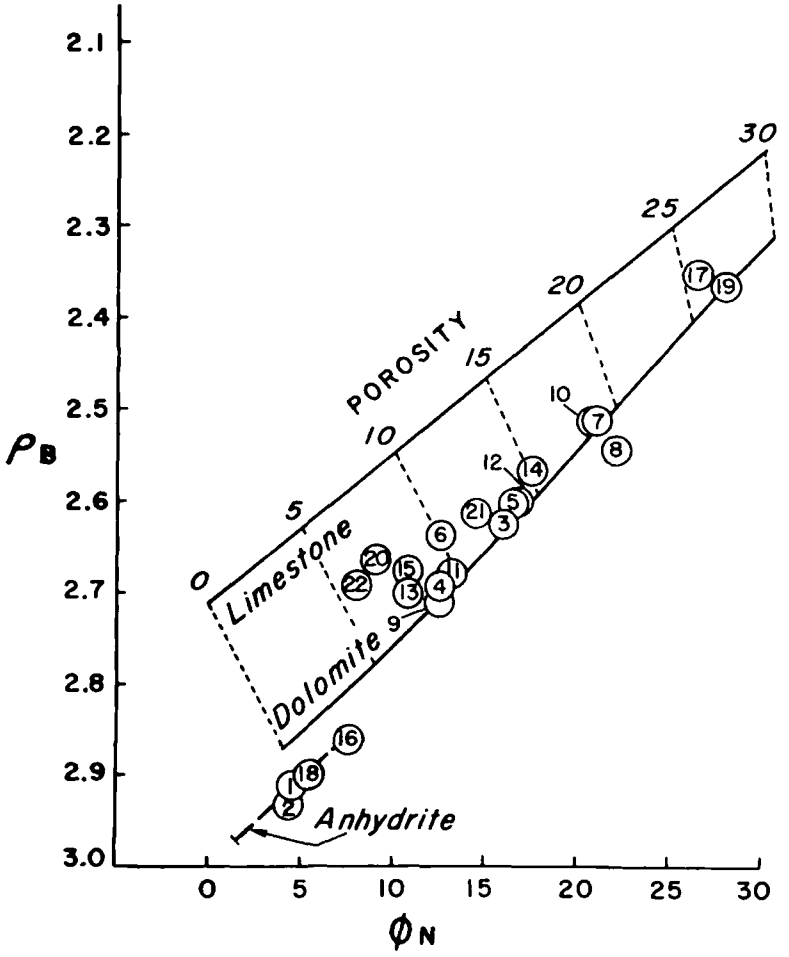
2.1
2.2
2.3
2.4
2.5
2.6
2.7
2.8
2.9
3.0
ρ_B
0
5
10
15
20
25
30
ϕ_N
POROSITY
Limestone
Dolomite
Anhydrite

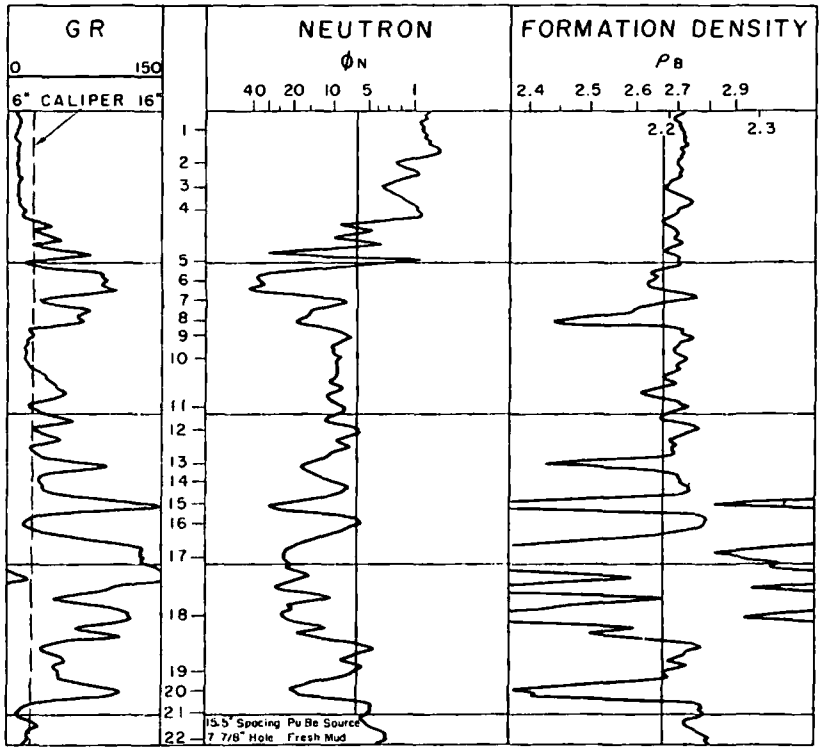
GR
0
150
6" CALIPER 16"
NEUTRON
ϕ_N
40 20 10 5 1
FORMATION DENSITY
ρ_B
2.4 2.5 2.6 2.7 2.9
2.2
2.3
15.5" Spacing Pu Be Source
7 7/8" Hole Fresh Mud

Fig. 13

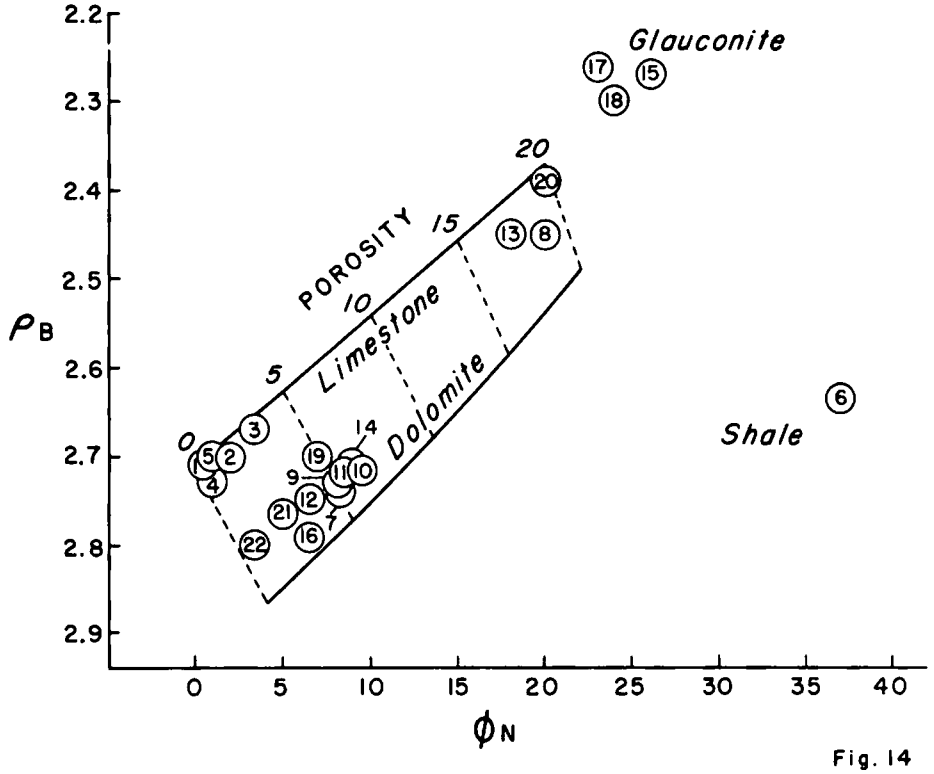
Glauconite
Shale
Limestone
Dolomite
POROSITY
0
5
10
15
20
ρ_B
ϕ_N

Fig. 14

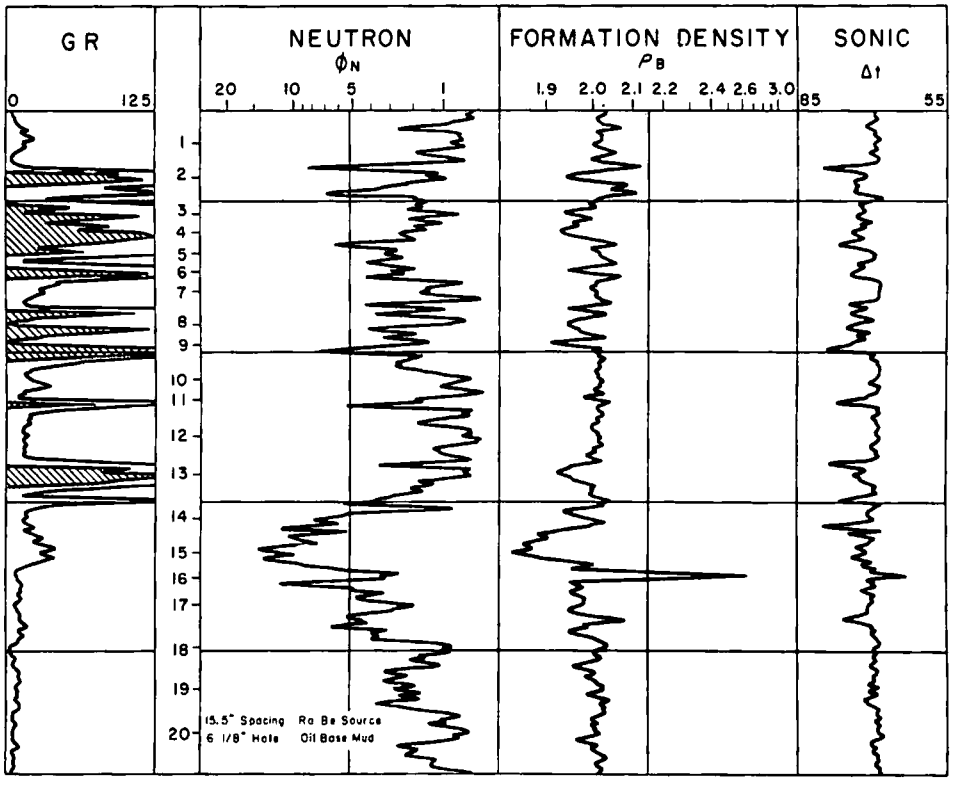
GR
0
125
NEUTRON
ϕ_N
20 10 5 1
FORMATION DENSITY
ρ_B
1.9 2.0 2.1 2.2 2.4 2.6 3.0
SONIC
Δt
85
55
15.5" Spacing Ra Be Source
6 1/8" Hole Oil Base Mud

Fig. 15

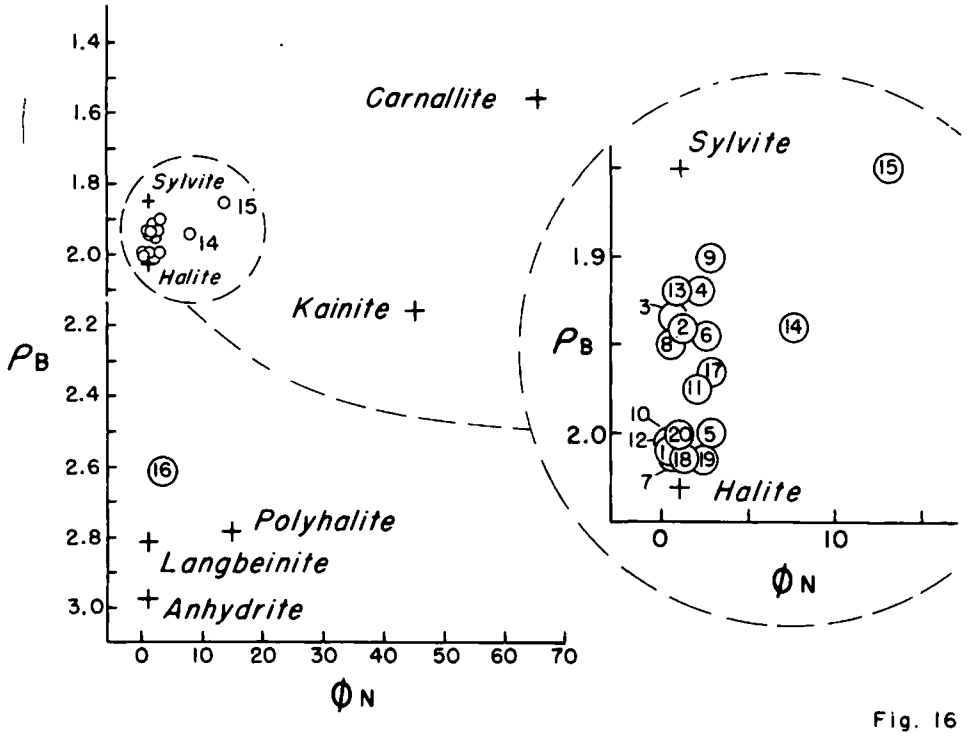

Fig. 16

SONIC - NEUTRON

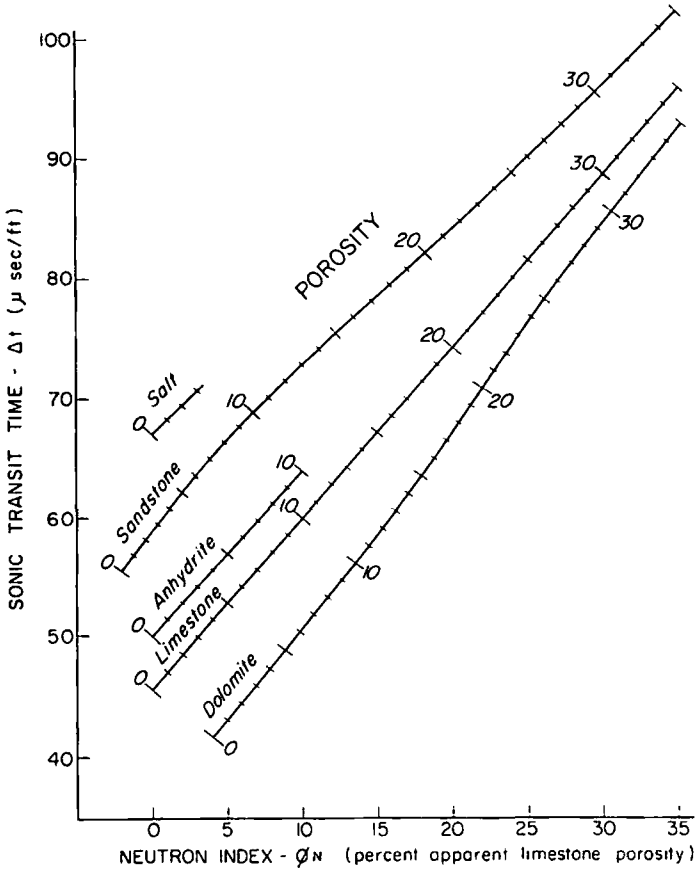

Fig. 17

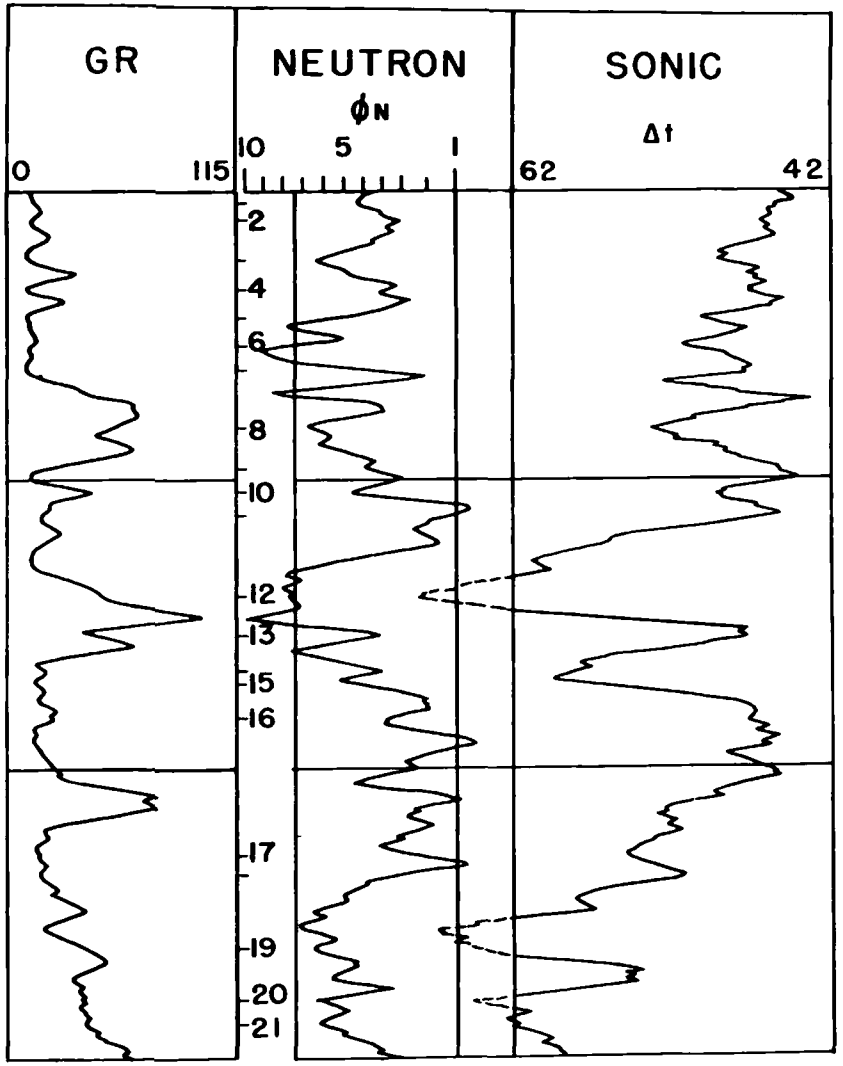
GR
0
115
NEUTRON
ϕ_N
10
5
1
SONIC
Δt
62
42
2
4
6
8
10
12
13
15
16
17
19
20
21

Fig. 18

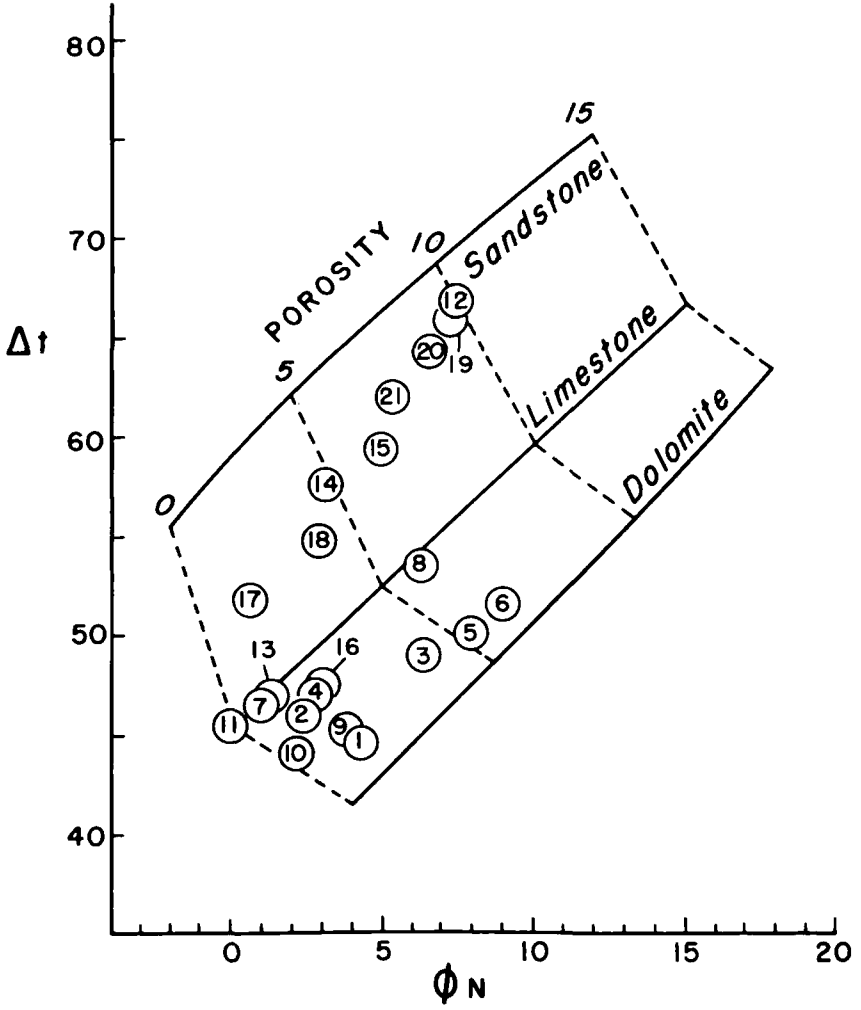
80
70
60
50
40
Δt
0
5
10
15
20
ϕ_N
POROSITY
0
5
10
15
Sandstone
Limestone
Dolomite
1
2
3
4
5
6
7
8
9
10
11
12
13
14
15
16
17
18
19
20
21

Fig. 19

in Journal of Petroleum Technology
July, 1973. p. 775-783

Mud Displacement with Cement Slurries

Charles R. Clark, SPE-AIME, Exxon Company, U.S.A.
L. Greg Carter, SPE-AIME, Halliburton Services

Introduction

One prerequisite for successful primary cementing is the complete displacement of drilling mud from the annular space. Much has been published[1-9] regarding proper techniques for maximum mud displacement efficiency. Yet, even after these techniques are properly applied, mud displacement efficiency often remains low. The objective of this study was to re-examine, under conditions closely simulating the down-hole environment, the relative importance of the driving forces available to displace drilling mud from the annulus. Fig. 1 illustrates the driving and resisting forces involved in the displacement of drilling mud with a cement slurry.

Test Equipment

The test facility (Fig. 2) consisted of a pneumatic trailer for storing bulk cement and a pneumatic handling system for delivering cement to a 4-bbl recirculating mixer. The cement slurry was mixed and pumped into a 25-bbl slurry heating and storage tank where retarders and friction reducers were added when needed to alter slurry properties.

Cement was circulated with three positive-displacement pumps. Two were connected to a variable speed motor that allowed pump rates to vary from 0.5 to 100 gal/min. The third pump was driven through two gear-reduction boxes on a two-speed motor that permitted rates up to 160 gal/min at pressures up to 200 psi. Mud was displaced with one positive-displacement pump.

Cement slurry, drilling mud, and test cell curing chamber were heated with steam coils located in the slurry tank, the mud-treating barrel, and the test cell curing chamber, respectively.

The simulated formation cores were made by compacting and heating a mixture of epoxy resin and sand inside 5½-in. casing. A 2.74-in. diameter hole was cast in the center of the 10-ft-long specimen to represent the wellbore. The center 7 ft of the external 5½-in. casing was removed to allow full exposure of the core permeability. The average water permeability of the cores was 400 md.

The test model consisted of a 1-in. OD pipe inside the 2.74-in. simulated formation wellbore. This configuration is scaled to model a 2⅞-in. tubingless completion in a 7⅞-in. hole (Fig. 3). The 10-ft sandstone core was placed in the apparatus depicted on Fig. 4. The 33-in. extension joint on the bottom contained straightening vanes to eliminate possible end effects. The core section and extension joint were encased within an annular filtration jacket to allow measurement of filtration through the core. On some tests, pressure taps were installed through the sandstone core to allow measurement of annular pressure drop across the middle 5 ft of the sandstone core.

Mud or cement was pumped down through the vertical standpipe into the extension joint, up through the sandstone core section, and out at the top of the cell. The exit line contained a plug valve to regulate pressure inside the core at 150 to 200 psi.

Mud displacement efficiency was studied under conditions simulating the borehole environment at 8,000 feet. Major findings were that the buoyant driving force resulting from the density difference between cement and mud has less effect on mud displacement than expected under such conditions and that pipe motion with scratchers substantially improves mud displacement, especially in areas of hole enlargement.

This created a differential from inside the wellbore out into the annular jacket. To maintain a high-temperature environment the entire test apparatus was submerged in a curing chamber.

The 1-in.-OD pipe simulating the casing string had weights attached to its lower end for stability and straightness. The top of the pipe was attached to a combination rotating and reciprocating head. It was possible to position the 1-in. pipe concentrically or eccentrically in the borehole.

Scale model slim-hole rotating or reciprocating scratchers were mounted on the center of the 1-in. pipe when tests called for pipe movement with scratchers.

Test Procedures

The following procedure was used in conducting all tests:

1. The curing hole and the annular filtration jacket were filled with water and heated to 125°F before the test began.
2. The drilling mud was heated to 125°F and circulated through the test cell for 1 hour at a differential pressure of 150 to 200 psi to build a filter cake.
3. The apparatus was shut in for 1 hour and 20 minutes under 150 to 200 psi differential pressure to simulate pulling of drillpipe and running of casing. The curing chamber temperature was maintained at 125°F during this phase.
4. Mud circulation was started and continued for 10 minutes under a differential pressure of 150 to 200 psi to simulate mud conditioning before cementing. (If pipe movement was employed in the test, it was started at this time.)
5. The drilling mud was displaced by the selected volume of cement slurry, which had been preheated to 125°F. (Pipe movement, when employed, was stopped when cement displacement was finished.)
6. The sample was closed in under pressure and gradually increased to a temperature of 200°F. This temperature was maintained throughout the waiting-on-cement period. The cement was allowed to remain in the curing chamber for 21 to 24 hours.
7. The core was removed from the test fixture and sawed into seven sections as shown on Fig. 5. In Sections 2 through 4, measurements were made of the minimum separation of pipe from the wall, and

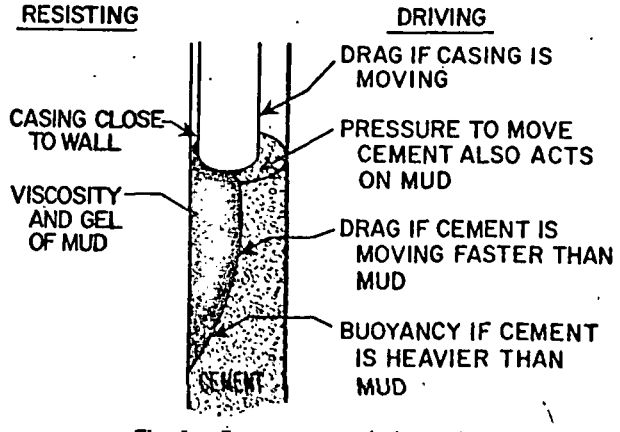

Fig. 1—Forces on mud channel.

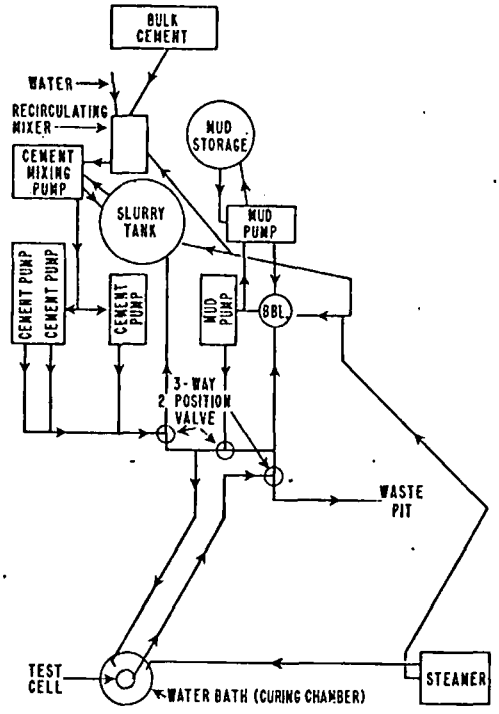

Fig. 2—Test facilities, mud displacement study.

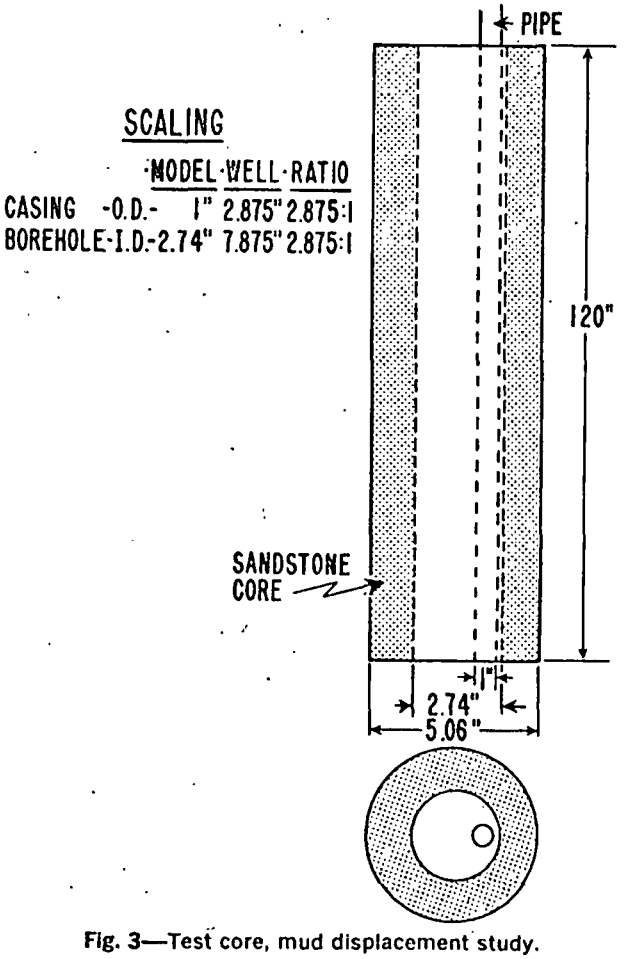

Fig. 3—Test core, mud displacement study.

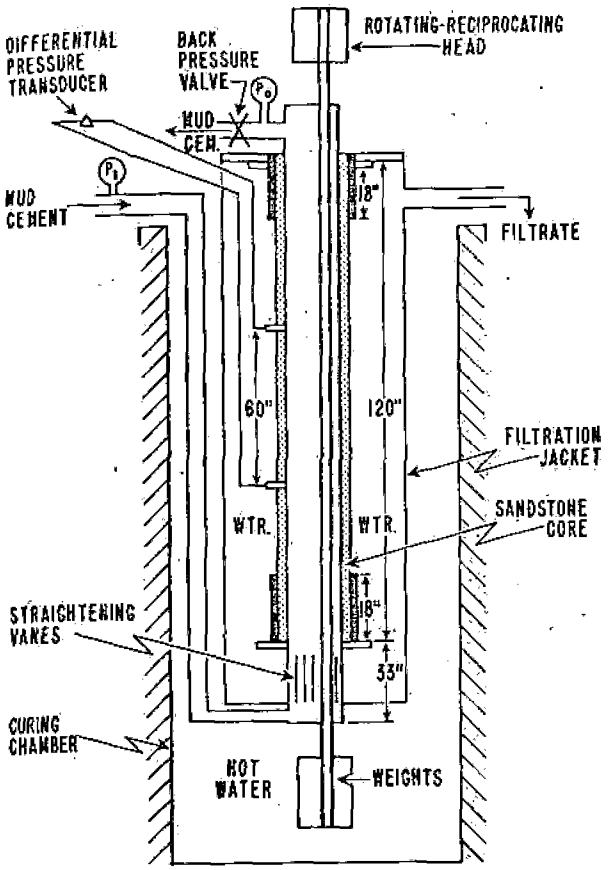

Fig. 4—Test apparatus, mud displacement study.

these sections were planimetered to determine the area of cement, pipe, and borehole.

Nine displacement tests were performed with cores containing simulated washed out sections. (See Fig. 6.) The cores with simulated washouts were sectioned as shown in the following table:

Cores with Washed-Out Sections

Section Number	Depth from Top (in.)	Hole Size (in.)
1	0 to 36	2.74
2	36 to 47	2.74
3A	47 to 54	3.25
3B	54 to 58	3.75
3C	58 to 61	3.75
3D	61 to 65	3.25
3E	65 to 74	2.74
3F	74 to 82	2.74
4	82 to 91	2.74
5	91 to 120	2.74

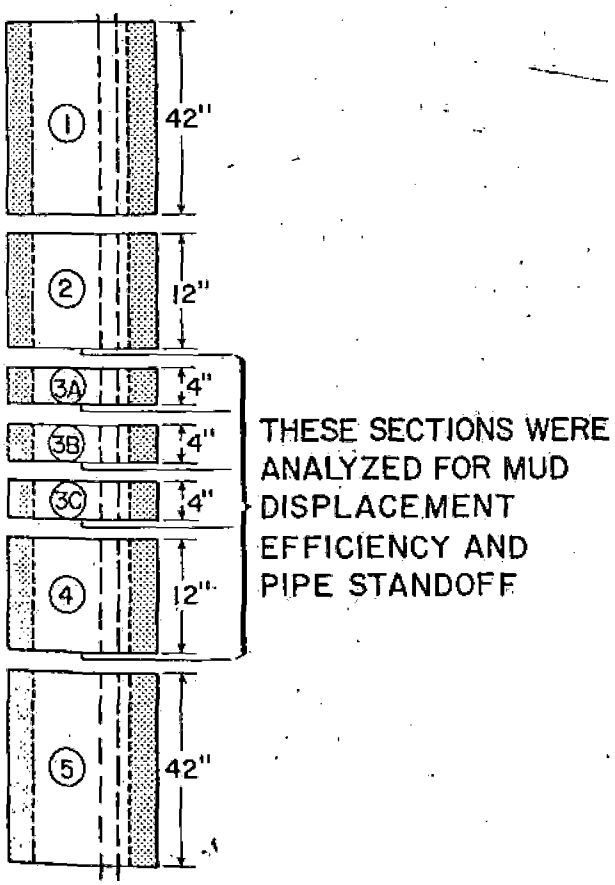

Fig. 5—Test evaluation, mud displacement study.

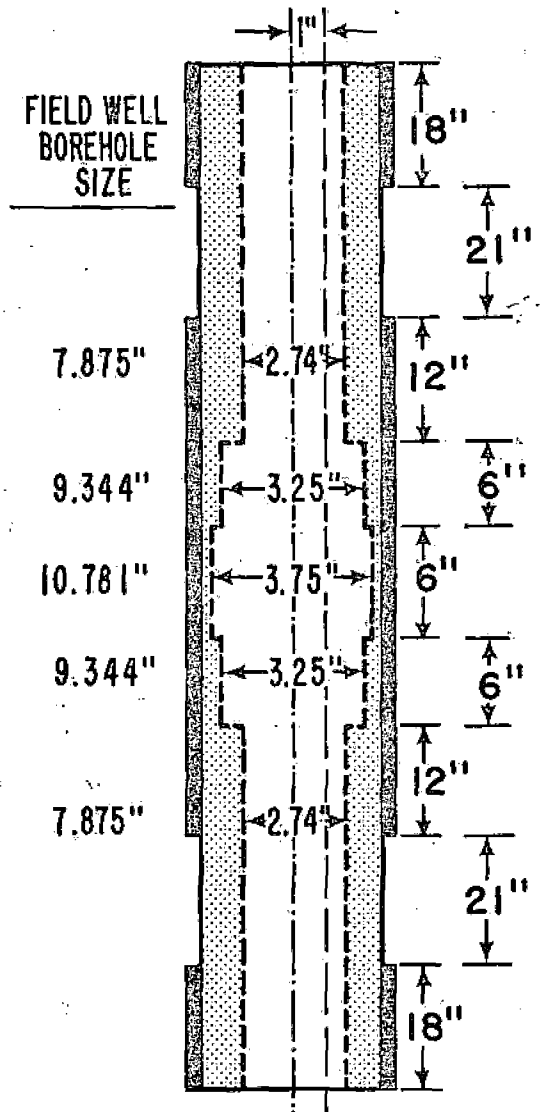

Fig. 6—Mud displacement study—cores with simulated washouts.

Test Evaluation Method

Displacement efficiency was determined for each test from the planimetered measurements of wellbore, pipe, and cement. The percent displacement efficiency was then calculated as illustrated in Fig. 7. The percent displacement efficiency for the uniform borehole tests was taken as the average of the values obtained on Sections 2, 3A, 3B, 3C, and 4. In the tests with washed out sections, the average value was taken on Sections 2 and 3E for the gauge borehole, from Sections 3A and 3D for the intermediate-size washout, and from Sections 3B and 3C for the largest hole size.

The fractional pipe standoff, defined as the minimum separation of the pipe and borehole wall (w_n) divided by the distance from the pipe to the borehole wall if the pipe were perfectly centered ($r_h - r_p$), was also determined in each test.

Criteria for Slurry Flow Regime

The mud displacement efficiency of thick cement slurries flowing in the laminar regime was compared with that of thin slurries flowing at a rate sufficient for turbulence to occur in at least some portion of an eccentric annulus. To establish slurry flow regime, a flow rate-pressure drop test was performed in a test cell with both thick and thin, 13.3 lb/gal, 8 percent gel cement slurries typical of those used in the mud displacement tests. (Test results are shown on Fig. 8.) As the slurries were pumped through the test cell at stabilized rates, annular frictional pressure drop was measured across the middle 5 ft of the sandstone core with a variable reluctance differential pressure transducer. For illustration purposes, the pressure drop observed across the 5-ft interval was converted to psi per 1,000 ft.

Also shown on Fig. 8 are data from three pressure-drop prediction methods: shear stress-shear rate, Power Law, and Reed slide rule equations. The specific equations used are shown below:

Shear Stress-Shear Rate

$$\Delta p = \frac{\tau\,(1{,}000)}{300\,(d_h - d_p)} \qquad \gamma = \frac{96\,v}{d_h - d_p}$$

Power Law

$$\Delta p = \frac{39\,v^2 f \rho}{d_h - d_p}\;; \quad N_{Re} = \frac{1.86 v^{(2-n')}\rho}{K'\left(\frac{96}{d_h - d_p}\right)^{n'}}$$

$$N_{Re} < 2{,}100; f = 16/N_{Re}$$

$$N_{Re} > 2{,}100; f = 0.00454 + 0.645\,(N_{Re})^{-0.7}$$

$$n' = 3.32 \log_{10}\left(\frac{\theta_{600}}{\theta_{300}}\right)$$

$$K' = \frac{\theta_{300}}{(511)^{n'}}$$

Reed Slide Rule

$$\Delta p = \frac{0.0765\,(\mu_{pl})^{0.18}(\rho)^{0.82}(q)^{1.82}}{(d_h - d_p)^3 (d_h + d_p)^{1.82}}$$

Use of the shear stress-shear rate equation simply requires plotting Model 35 Fann V-G meter dial readings vs reciprocal seconds on log-log paper for the slurry involved, determining from the graph the shear stress at the flow rate (sec^{-1}) of interest, and solving the equation for frictional pressure. No fluid model is involved. The Power Law Model equation is discussed in many technical articles.[10-12] The familiar Reed slide-rule equation is also discussed in the literature.[13] Since all the equations assume concentric pipe, the theoretical frictional pressure should be higher than that observed in the flow tests with the pipe positioned eccentrically.

Slurry 1 of Fig. 8 is a typical thick, high-yield-point slurry used in displacement tests. Slurry rheology was determined with a Fann Model 35 rotational viscometer.[14] The observed data are best matched by the shear stress-shear rate laminar flow equation and the Power Law equation. The Reed slide-rule equation, which assumes turbulent flow, gives a predicted pressure drop that is too low. The high-yield-point slurries, with one exception, were pumped at 25 gal/min in the displacement tests. Thus, it is concluded that these slurries were in laminar flow at this rate.

Slurry 2 is a thin, low-yield-point cement. At the lower flow rates, the observed pressure drop is best matched by the shear stress-shear rate and Power Law equations; and at the higher rates it is best matched by the Reed slide-rule turbulent flow equation and the Power Law equation. With the exception of one test, the thin slurries were pumped at a rate of 60 gal/min or higher in the displacement tests.

The transition from laminar to turbulent flow for concentric pipe occurs at approximately 44 gal/min, the rate at which the Reed slide rule predicts a higher pressure drop than the shear stress-shear rate equation. Therefore, with the pipe positioned eccentrically for the flow rate-pressure drop test and all subsequent displacement tests, turbulence occurred in the wide side of the annulus at rates less than 44 gal/min. McLean *et al.*,[1] in describing the transition from laminar to turbulent flow in an eccentric annulus state that it occurs over an extended range of flow rates, with turbulence first occurring on the wide side and slowly spreading to the narrow side. These authors report no rapid, distinct change in slope on the plot of pressure drop vs flow rate.

Throughout the remainder of the paper, slurry flow regime will be indicated. The method used to select flow regime was to calculate frictional pressure drop with the laminar flow shear stress-shear rate equation and the Reed slide-rule, turbulent flow equation. If the shear stress-shear rate equation gave the highest pressure drop prediction, the slurry was said to be in laminar flow. If the Reed slide-rule equation gave the highest prediction, the slurry was considered to be in turbulent flow, at least on the wide side of the eccentric annulus.

A few displacement tests were run with 13.5-lb/gal slurries. In these cases, the slurries without additives were more viscous than the comparable 13.3-lb/gal thick slurries. Therefore, they also should be in laminar flow at 25-gal/min displacement rates. Friction reducer was used to obtain a 13.5-lb/gal slurry with Fann dial readings comparable with the

13.3-lb/gal thin slurry shown on Fig. 8. The turbulent flow criteria previously described should apply to this slurry also.

Effect of Annular Pressure Drop and Drag Stress at the Cement/Mud Interface

To examine the effect of the driving forces, frictional pressure drop, and drag stress at the cement/mud interface during displacement, 15 tests were performed with cement and mud densities equal, and with no pipe motion. With the exception of three tests, 975 gal of slurry was used to displace the mud. This volume of slurry provides the same contact time as would be experienced by the casing shoe of the simulated field well if 600 sacks of 8-percent-gel cement were used. The effect of contact time on mud displacement is discussed later in the paper. Additional data pertinent to the mud displacement tests are shown in Table 1 for the 15 tests described, as well as 8 tests that will be discussed later and during which no pipe movement was used.

Fig. 9 illustrates the effect of annular pressure drop on mud displacement efficiency. These results indicate that for slurries flowing in the laminar regime, displacement efficiency was increased with increasing annular pressure drop as indicated by the line through Tests 1 through 7. Test 1 gave 44 percent efficiency with 8 psi/1,000 ft annular pressure drop and Test 7 resulted in 77 percent displacement efficiency with 174 psi/1,000 ft frictional pressure.

Tests 8 and 9, which had turbulent flow on the wide side of the annulus, resulted in displacement efficiencies of 65 and 78 percent, respectively. Test 2, which had a frictional pressure roughly equal to that of Test 8, gave only 55 percent displacement efficiency; and Test 5, which had approximately the same pressure drop as Test 9, gave only 60 percent displacement efficiency. Tests 2, 8, and 9 were performed with cement slurries that had similar rheology. The increasing pressure drop for these three tests was caused by increasing the flow rate from 60 to 90 to 120 gal/min. Had turbulence not developed in Tests 8 and 9, displacement efficiency should have increased along a trend of the line drawn through Tests 1 through 7.

Tests 10 through 12 indicate that higher mud displacement efficiency was possible at frictional pressure drops roughly equivalent to those of Tests 2, 8, and 9. Examination of the six-speed Fann rheology data shown on Table 2 reveals that the slurries used in Tests 10 through 12 were thinner than those used in Tests 2, 8, and 9. This indicates that a greater degree of turbulence was achieved in Tests 10 through 12, thus greater drag stress was imposed at the cement/mud interface than experienced with the thicker slurries of Tests 2, 8, and 9. In fact, if mud and cement rheology, geometric configuration, and other test conditions could have been precisely duplicated, a single characteristic line should describe displacement efficiency with increasing flow rate for *a particular cement slurry rheology*.

Test 13, also a very thin slurry, exhibits high displacement efficiency because of 31-percent pipe standoff (see Table 1 for pipe standoff in each test).

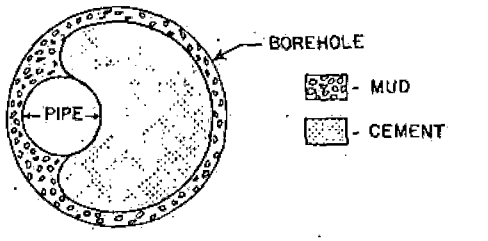

$$\text{DISPLACEMENT EFFICIENCY, \%} = \frac{\text{CEMENT AREA}}{\text{BOREHOLE AREA - PIPE AREA}}(100)$$

$$\therefore \text{DISPLACEMENT EFFICIENCY, \%} = \frac{\text{CEMENT AREA}}{\text{ANNULUS AREA}}(100)$$

Fig. 7—Displacement efficiency—planimeter measurement.

CLASS H + 8% gel

SLURRY NO.	TYPE	DENSITY PPG	FANN READINGS—#/100FT.² 600	300	200	100	6	3	μ_{pl} CP.	ϕ #/100FT.²	ADDITIVES
1	THICK	13.3	49	42	40	36	28	15	7	35	NONE
2	THIN	13.3	23	13	11	8	5	5	10	3	RETARDER

◇—◇ SHEAR RATE-SHEAR STRESS EQUATION [ASSUMING CONCENTRIC PIPE]
△—△ POWER LAW EQUATION
□—□ REED SLIDE RULE EQUATION
○—○ OBSERVED EXPERIMENTALLY [ECCENTRIC]

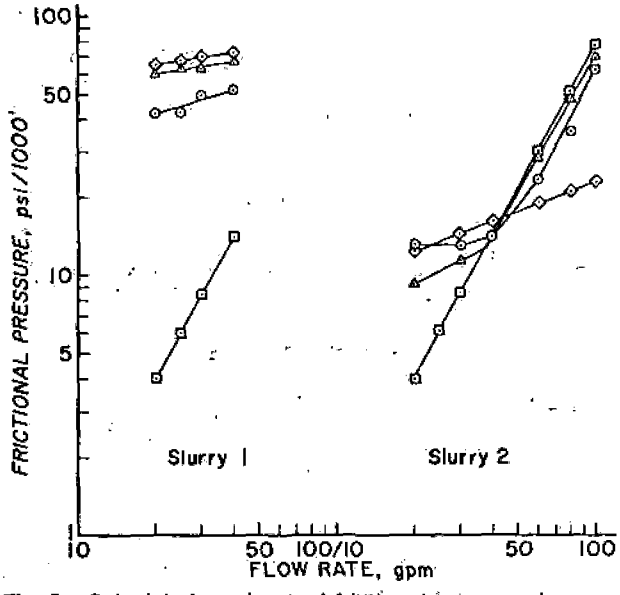

Fig. 8—Calculated vs observed frictional pressure drop.

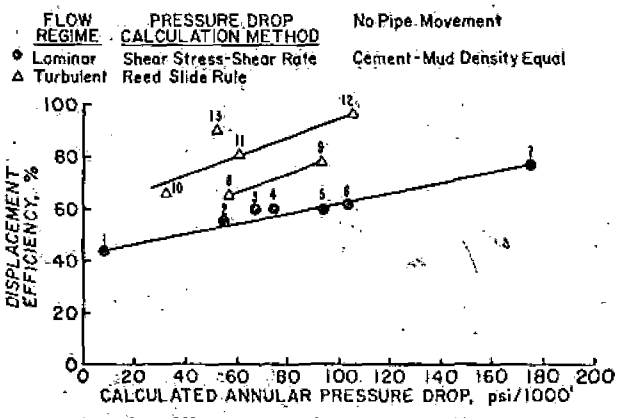

Fig. 9—Effect of annular pressure drop on displacement efficiency.

This re-emphasizes the importance of centralizing the pipe for mud removal.

Three important points should be recognized from Fig. 9:

1. At equal annual pressure drops, a slurry with turbulence occurring in some portion of the annulus will give greater mud displacement efficiency than a slurry in laminar flow.

2. The slope of the lines describing displacement efficiency as a function of pressure drop for slurries in turbulent flow is steeper than that shown for slurries in laminar flow. Thus, for a given increase in annular pressure drop, a slurry in turbulent flow will give a greater increase in displacement efficiency.

3. Annular pressure drop is not the only driving force occurring in Tests 1 through 13. If it were, only one line would appear on Fig. 9. The other driving force involved is either drag stress or erosion at the cement/mud interface.

To evaluate further the relative importance of the driving forces, frictional pressure, and drag stress at the cement/mud interface, two specially designed tests were performed. Fig. 10 illustrates the geometric configuration for these two tests. A metal plate was attached to the middle 6 ft of the line pipe. The plate was open at both ends so that mud could flow through the narrow side of the annulus. Subsequently, when a cement slurry was pumped through the test cell, cement could displace mud on the narrow side of the annulus only by virtue of the pressure drop across the 60-ft length. Drag stress by the faster moving cement in the wide side of the annulus could not act on the mud because of the presence of the metal sheath.

Fig. 11 compares a conventional displacement test (Test 12) with the two tests run with the metal sheath in place. A thin slurry was pumped at 120 gal/min in all three tests. Pipe motion was not used.

In Test 12, 96 percent of a thick drilling mud (plastic viscosity = 52 cp, yield point = 18 lb/100 sq ft) was displaced by the flowing cement. In Test 14 with the metal plate in place, cement preferentially flowed on the wide side of the annulus. The 103 psi/1,000 ft pressure gradient exerted by the flowing slurry was insufficient to move the thick mud behind the fin. It is recognized that the additional surface area introduced by the presence of the metal plate made it more difficult to displace mud from

TABLE 1—MUD DISPLACEMENT STUDY, EFFECT OF ANNULAR PRESSURE DROP
(No Pipe Movement)

Test No.	Flow Properties of Mud* μ_{pl} (cp)	Flow Properties of Mud* ϕ (lb/100 sq ft)	Standoff (percent)	Flow Properties of Cement μ_{pl} (cp)	Flow Properties of Cement ϕ (lb/100 sq ft)	Density Difference** (lb/gal)	Cement Rate (gal/min)	Average Annular Velocity (ft/min)	Slurry Volume (gal)	Contact Time (minutes)	Calculated Frictional Pressure† (psi/1,000 ft)	Displacement Efficiency (percent)
1	41	36	11	10	0	0	25	95	975	39	8 - lam.	44
2	35	47	4	5	26	0	60	225	975	16	55 - lam.	55
3	58	24	2	8	34	0	25	95	15	0.60	67 - lam.	60
4	58	40	4	9	42	0	25	95	975	39	74 - lam.	60
5	42	26	11	8	69	0	5	20	195	39	94 - lam.	60
6	57	23	8	9	57	0	25	95	6	0.23	103 - lam.	62
7	74	67	10	10	97	0	25	95	975	39	174 - lam.	77
8	24	34	6	6	24	0	90	340	975	11	57 - turb.	65
9	45	27	4	4	23	0	120	455	975	8	93 - turb.	78
10	56	21	6	8	1	0	60	225	15	0.25	32 - turb.	66
11	25	40	2	9	4	0	90	340	975	11	61 - turb.	81
12	52	18	17	10	−1	0	120	455	975	8	105 - turb.	96
13	43	17	31	10	−3	0	80	305	975	12	52 - turb.	90
14	54	30	9	11	0	0	120	455	975	8	103 - turb.	—‡
15	25	5	13	9	1	0	120	455	975	8	107 - turb.	—‡
16	43	24	13	10	125	3	5	20	195	39	137 - lam.	70
17	43	21	8	13	77	3	25	95	975	39	140 - lam.	73
18	47	20	7	8	−1	3	120	455	975	8	107 - turb.	95
19	49	22	7	11	−1	3	60	225	975	16	31 - turb.	78
20	58	24	3	8	2	0	60	225	6	0.10	28 - turb.	56
21	41	21	21	12	1	0	60	225	2,340	39	31 - turb.	80
22	33	20	26	11	1	0	90	340	3,510	39	63 - turb.	95
23	42	23	0	12	2	0	120	455	480	4	108 - turb.	95

*Water and 8 percent gel with barite added for 13.3 density. 10.5 lb/gal mud used in Tests 16 through 19. Ten minutes gel strengths generally were 40 to 70 lb/100 sq ft.
**Cement density minus mud density.
†Larger value of shear stress-shear rate (laminar) or Reed slide rule (turbulent) predictions.
‡Special tests—see text on effect of drag stress at the cement mud interface.

TABLE 2—MUD DISPLACEMENT TESTS, EFFECT OF CEMENT SLURRY RHEOLOGY

Test No.	Slurry Fann Readings (lb/100 sq ft) 600	300	200	100	6	3	Rate (gal/min)	Flow Regime	Displacement Efficiency (percent)
2	36	31	30	27	17	12	60	laminar	55
8	36	30	29	26	15	10	90	turbulent	62
9	31	27	26	23	13	9	120	turbulent	78
10	17	9	7	5	3	2	60	turbulent	66
11	21	12	10	7	4	4	90	turbulent	81
12	19	9	7	4	3	2	120	turbulent	96

the narrow side of the annulus. However, the result suggests that the 96-percent displacement efficiency achieved in Test 12 was related to the drag stress that the cement exerts on the mud in the narrow side of the annulus.

Test 15 was a repeat of Test 14 except that thin drilling mud was used (plastic viscosity = 25 cp, yield point = 5 lb/100 sq ft). Note that the annular pressure drop of the flowing cement was sufficient to make the mud flow in the narrow annulus and be replaced by cement. This interates the importance of maintaining a thin, well conditioned mud for successful primary cementing. Note also that in Test 15 the faster flowing slurry on the wide side removed more mud filter cake on the wide side of the annulus than the low-velocity cement removed on the narrow side.

Effect of Cement-Mud Density Difference

Fig. 12 duplicates Fig. 9, except that 4 additional tests have been plotted: Tests 16 through 19. In these tests, the density of the cement was 3 lb/gal heavier than the density of the mud being displaced. If buoyancy were fully effective, these tests would have 156 psi/1,000 ft additional driving force available for mud removal (52 psi/1,000 ft per pound per gallon density difference). However, Fig. 12 illustrates that mud displacement efficiency for these tests, with the exception of Test 19, was essentially the same as for the comparable tests without density difference. If Test 19 were plotted at 187 psi/1,000 ft pressure gradient (31 + 156), mud removal in excess of 95 percent would be expected instead of the 78-percent efficiency observed. Therefore, it appears that the buoyant driving force has a greatly reduced effect under conditions simulating wellbore conditions.

Previous investigators[1,5,6,9] performed laboratory experiments that indicated cement-mud density difference was a significant driving force. However, to our knowledge, these experiments were performed at ambient temperature with models that used impermeable pipe to simulate the wellbore. A permeable medium at elevated temperature was used to represent the wellbore in the tests described here. Thus, mud trapped in the narrow portion of the eccentric annulus lost water from its structure by filtration and was less mobile than mud containing all of its original water. The mud had also undergone gellation due to high temperature. For buoyancy to be fully effective the mud must be mobile. Jones and Berdine,[8] using a laboratory model with alternating impermeable and permeable intervals, reported excellent mud removal in the impermeable sections and thick mud cake in the permeable intervals when cement-mud density differences of 5 to 6 lb/gal were used. They drew no conclusions regarding the driving force of cement-mud density difference. We believe that cement should be heavier than the mud being displaced but not necessarily that the density difference should be the maximum possible. More mud removal is achieved at a reduced cement-mud density difference by displacing the cement at a higher rate. This approach permits maximum realization of the two principal driving forces: frictional pressure drop and drag stress at the cement/mud interface.

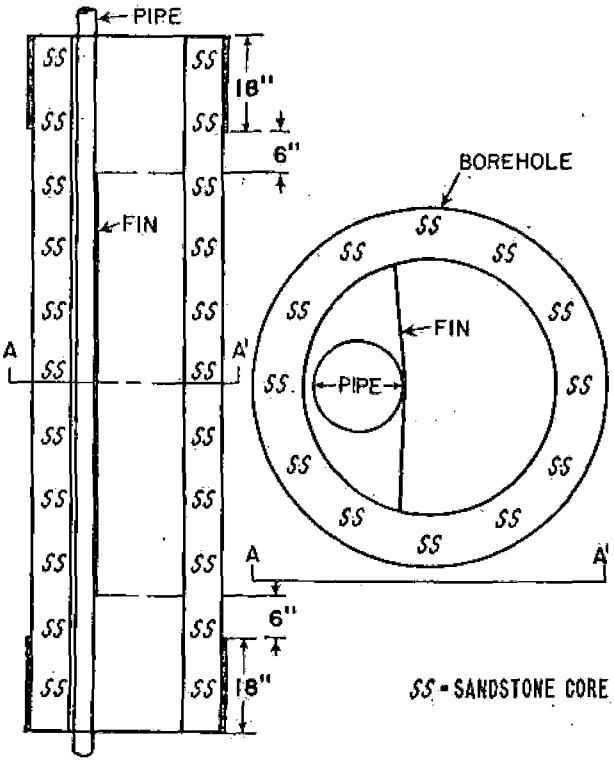

Fig. 10—Test cell configuration for evaluating drag stress at the cement/mud interface.

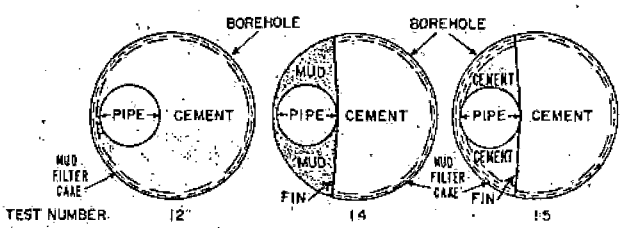

TEST NUMBER	12	14	15
CEMENT			
RATE, q pm	120	120	120
μpl, cp	10	11	9
ϕ, #/100ft²	-1	0	1
Δp, psi/1000	105	103	107
DENSITY, ppg	13.3	13.3	13.3
MUD			
μpl, cp	52	54	25
ϕ, #/100ft²	18	30	5
DENSITY, ppg	13.3	13.3	13.3
PIPE STAND OFF, %	17	9	13
PIPE MOTION	NONE	NONE	NONE

Fig. 11—Effect of drag stress at the cement/mud interface.

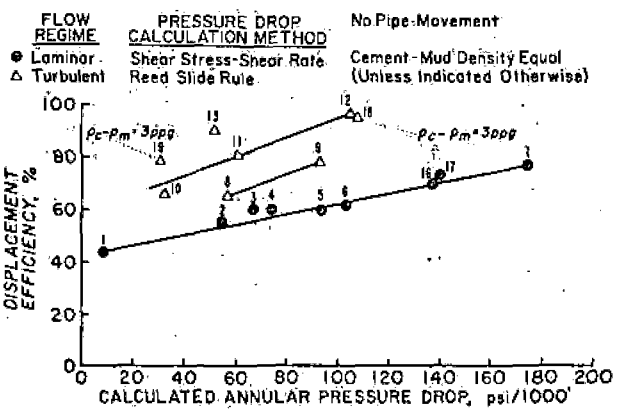

Fig. 12—Effect of cement-mud density difference on displacement efficiency.

Effect of Contact Time

From the limited data developed, it appears that contact time has an effect on displacement efficiency with slurries in turbulent flow. (Contact time is defined as the period of time required for the cement slurry to move through the test cell.) Brice and Holmes[4] reported improved primary cementing success in field applications when contact times were greater than 10 minutes for slurries in turbulent flow. Fig. 13, a duplicate of Fig. 9 with plots of four additional tests (Tests 20 through 23), illustrates the effect of contact time on displacement efficiency. Tests 20, 10, and 21, thin slurries in turbulent flow, with approximately 30 psi/1,000 ft frictional pressure drop, show increased efficiency with contact time increasing from 0.1 to 39 minutes. Test 22 shows a 15 percent improvement in displacement efficiency over Test 11, with 28 minutes of additional exposure. However, it should be recognized that Tests 21 and 22 had greater pipe standoff than the comparative tests. Test 23 with 4 minutes' contact time exhibited the same efficiency as Test 12, which had 8 minutes' contact time. Apparently, only 4 minutes' contact time was needed with the high frictional pressure drop (105 psi/1,000 ft) for effective mud removal.

Contact time seems to have little effect on displacement efficiency for thick slurries in laminar flow. Tests 3 through 6 reveal that increasing contact time from 0.2 to 39 minutes had little effect on displacement efficiency in this flow regime.

Effect of Pipe Movement and Scratchers

Tests were conducted using gauge and washed-out sections to evaluate displacement efficiency as a function of flow regime and pipe movement, with and without scratchers. These data are presented in Table 3.

Gauge Hole

Investigation disclosed that the best displacement efficiency in both flow regimes was achieved when the pipe was placed in motion. This is exhibited in Tests 24 through 27 for pipe movement vs Test 3 and 10 for no pipe movement. Pipe movement employing rotation may be better than movement employing reciprocation (see Tests 24 through 27), but it is well to recognize that this difference in displacement efficiency is only 4 to 7 percent. At this point it should be noted that in all tests utilizing reciprocation, pipe reciprocation was limited to axial motion only and there was no lateral translation as would probably be experienced in a field well.

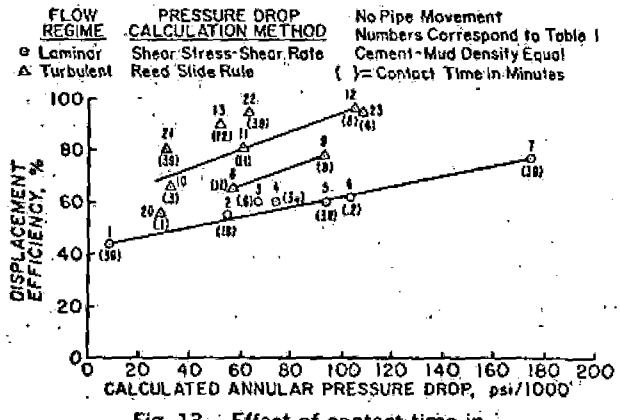

Fig. 13—Effect of contact time in displacement efficiency.

Washed-Out Hole

The two sizes of washed out sections are shown in Fig. 6. Because of the method used to fabricate the cores with washed out sections and to give added strength to the sandstone, the external casing was left in place in the area surrounding the washout. Mud filter cake could be deposited in this area only by water filtration through vertical permeability. Therefore, this should reasonably duplicate hole enlargement in a low-permeability shale formation. All previous displacement tests were made with cores that would permit direct deposition of mud filter cake in the middle 7 ft of the 10-ft specimen.

As shown in Table 3 for Tests 28 through 36, displacement efficiency decreased with increasing hole size. Pipe movement (Tests 30 through 33), as would be expected, resulted in greater displacement efficiencies than no pipe movement (Tests 28 through 29). Contrary to observations made in tests run with gauge-hole cores, displacement efficiency in the large washout was better when pipe was reciprocated than when it was rotated. However, this improved efficiency — Tests 32 and 33 vs Tests 30 and 31 — was only 5 to 6 percent. The important observation is that pipe movement, either rotation or reciprocation, improved mud displacement.

The highest displacement efficiency was attained in Tests 34 through 36, which included pipe movement and the use of scratchers. The rotating scratchers were 18 in. long with ¾-in.-long cable spikes and were placed in the washed out section only. The reciprocating scratcher was moved only in the washed out area. Significant observations made in the scratcher tests were that cement penetrated the narrow side of the annulus as expected, and that there was an improvement in mud removal on the wide side, even though the end of the scratcher arms fell short of the borehole wall by more than 1 in. The improved displacement is attributed to breaking of the gelled mud and flow stream disturbances by the scratcher arms.

Conclusions

The following conclusions are drawn from this laboratory investigation.

1. Pipe movement, either rotation or reciprocation, is a major driving force for mud removal.
2. A well conditioned mud greatly increases mud displacement efficiency.
3. Pipe centralization significantly aids mud displacement.
4. The buoyant driving force resulting from cement-mud density difference has less effect on mud displacement than expected under conditions simulating the down-hole environment.
5. Drag stress at the cement/mud interface can

TABLE 3—MUD DISPLACEMENT STUDY, EFFECT OF PIPE MOVEMENT AND SCRATCHERS
(Cement density = mud density = 13.3 lb/gal; slurry volume = 15 gal.)

Test No.	Flow Properties of Mud μ_{pl} (cp)	Flow Properties of Mud ϕ (lb/100 sq ft)	Pipe Standoff* (percent) G	I	L	Flow Properties of Cement μ_{pl} (cp)	Flow Properties of Cement ϕ (lb/100 sq ft)	Cement Rate gal/min	Flow Regime	Pipe Movement**	Displacement Efficiency (percent) 2.74-in. Borehole	3.25-in. Borehole	3.75-in. Borehole
3	58	24	2	—	—	8	34	25	lam.	None	60	—	—
10	56	21	6	—	—	8	1	60	turb.	None	66	—	—
24	54	20	9	—	—	5	48	25	lam.	rot. - 16	84	—	—
25	49	20	21	—	—	8	2	60	turb.	rot. - 16	83	—	—
26	34	24	16	—	—	5	25	25	lam.	rcp. - 1.5	77	—	—
27	48	27	15	—	—	11	9	60	turb.	rcp. - 1.5	79	—	—
28	40	26	9	18	40	8	33	25	lam.	None	63	47	37
29	40	30	10	30	42	8	6	60	turb.	None	69	63	55
30	40	26	9	14	39	6	39	25	lam.	rot. - 16	79	79	62
31	39	26	11	27	35	11	5	60	turb.	rot. - 16	75	71	62
32	43	26	6	21	32	6	37	25	lam.	rcp. - 1.5	78	76	68
33	42	25	14	41	54	9	6	60	turb.	rcp. - 1.5	87	85	67
34	63	24	25	44	52	6	53	25	lam.	rot. - 16†	93	90	89
35	63	22	45	63	61	10	0	60	turb.	rot. - 16†	92	89	88
36	61	24	5	26	38	11	0	60	turb.	rcp. - 1.5†	90	87	80

*G = 2.74-in. hole; I = 3.25-in. hole; L = 3.75-in. hole.
**rot. = rotation in rpm.
rcp. = reciprocation in ft/sec.
†Scratchers used.

be a significant driving force for mud removal when the cement slurry is in turbulent flow in some part of the annulus.

6. Pipe motion with scratchers substantially improves mud displacement, especially in areas of hole enlargement.

Nomenclature

d_h = hole diameter, in.
d_p = pipe diameter, in.
f = Fanning friction factor, dimensionless
K' = fluid consistency index, lb-sec$^{n'}$/sq ft
n' = fluid-flow behavior index, dimensionless
N_{Re} = Reynolds number, dimensionless
Δp = annular frictional pressure drop, psi/1,000
q = bulk flow rate, gal/min
v = bulk velocity, ft/sec
γ = shear-rate, sec^{-1}
θ_3 = Fann dial reading at 300 rpm, lb/sq ft
θ_6 = Fann dial reading at 600 rpm, lb/sq ft
μ_{pl} = plastic viscosity, cp
ρ = density, lb/gal
τ = shear stress, lb/100 sq ft
ϕ = yield point, lb/100 sq ft

Acknowledgments

We wish to express our appreciation to Exxon Co. U.S.A., and to Halliburton Services for permission to publish this paper. Appreciation is also extended to those in the two organizations who contributed many valuable suggestions. A special thanks is given to Halliburton Services personnel, E. Riggle, Jr., C. L. Couch, and L. Sanders, who helped obtain much of the data, and D. W. Harriman who designed the test apparatus.

References

1. McLean, R. H., Manry, C. W. and Whitaker, W. W.: "Displacement Mechanics in Primary Cementing," *J. Pet. Tech.* (Feb., 1967) 251-260; *Trans.*, AIME, **240.**
2. Howard, G. C. and Clark, J. B.: "Factors to be Considered in Obtaining Proper Cementing of Casing," *Drill. and Prod. Prac.*, API (1948) 257.
3. Childers, M. A.: "Primary Cementing of Multiple Casing," *J. Pet. Tech.* (July, 1968) 751-762; *Trans.*, AIME, **243.**
4. Brice, J. W., Jr., and Holmes, R. C.: "Engineering Casing Cementing Programs Using Turbulent Flow Techniques," *J. Pet. Tech.* (May, 1964) 503-508.
5. Ross, W. M. and Wahl, W. W.: "Slow Flow Cementing—A Primary Cementing Technique Using Low Displacement Rates," paper SPE 1234, presented at SPE-AIME 40th Annual Fall Meeting, Denver, Colo., Oct. 3-6, 1965.
6. Ross, W. M.: "Low-Rate Displacement Solves Tough Cementing Jobs," *Pet. Eng.* (Nov., 1965) 74-79.
7. Teplitz, A. J. and Hassebrock, W. E.: "An Investigation of Oil-Well Cementing," *Drill. and Prod. Prac.*, API (1946) 76.
8. Jones, P. H. and Berdine, D.: "Oil-Well Cementing—Factors Influencing Bond Between Cement and Formation," *Drill. and Prod. Prac.*, API (1940) 45.
9. Parker, P. N.: "Cementing Successful at Low Displacement Rates," *World Oil* (Jan., 1969) 93-95.
10. Slagle, Knox A.: "Rheological Design of Cementing Operations," *J. Pet. Tech.* (March, 1962) 323-328; *Trans.*, AIME, **255.**
11. Savins, J. G.: "Generalized Newtonian (Pseudoplastic) Flow in Stationary Pipes and Annuli," *Trans.*, AIME (1958) **213**, 325-332.
12. Melton, L. L. and Saunders, C. D.: "Rheological Measurements of Non-Newtonian Fluids," *Trans.*, AIME (1957) **210**, 196-201.
13. McCray, A. W. and Cole, F. W.: *Oilwell Drilling Technology*, U. of Oklahoma Press, Norman (1959) 264.
14. *Testing Oil-Well Cements and Cement Additives*, 17th Ed., API RP 10B (April, 1971). **JPT**

Paper (SPE 4090) was presented at SPE-AIME 47th Annual Fall Meeting, held in San Antonio, Tex. Oct. 8-11, 1972.